

University of St Andrews



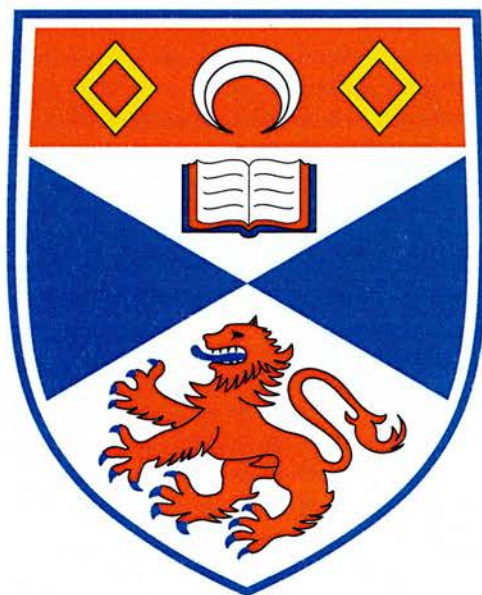
Full metadata for this thesis is available in
St Andrews Research Repository
at:

<http://research-repository.st-andrews.ac.uk/>

This thesis is protected by original copyright

MHD Wave Propagation in the Neighbourhood of Magnetic Null Points

James Alexander McLaughlin



Thesis submitted for the degree of Doctor of Philosophy
of the University of St Andrews

1 November 2005



Th F134

Abstract

This Thesis looks at the properties and behaviour of MHD waves in the neighbourhood of 2D null points in a variety of magnetic configurations and under various physical assumptions. This gives an indication of wave propagation in the Sun's corona. The work aims to contribute to the understanding of how plasma waves behave in complicated magnetic structures by focusing on wave propagation entering from a boundary. We use both numerical and analytical techniques throughout the Thesis.

We initially consider a simple 2D X-point in a $\beta = 0$ plasma. For the fast magnetoacoustic (MA) wave, it is found that a refraction effect focuses the wave at the null point, causing current density to accumulate there and that this build-up is exponential in time. Ohmic dissipation will extract the energy in the wave at this point. This illustrates that null points play an important role in the rapid dissipation of fast MA waves and suggests the location where wave heating will occur in the corona. We conclude that fast wave heating will naturally occur at $\beta = 0$ null points.

The Alfvén wave behaves in a different manner in that it propagates along the field lines and the wave energy is dissipated along the separatrices. In 2D, the Alfvén waves are decoupled from the MA waves and the value of the plasma β is unimportant to its behaviour. However, the phenomenon of dissipating the majority of the wave energy at a specific place is a feature of both wave types.

We also investigate the nature of the fast and Alfvén waves in a 2D pair of null points and in a two dipole magnetic configuration (still $\beta = 0$ plasma). For the two null points pair, we find the fast wave is attracted to the null points and splits so that a proportion of the wave energy goes to each null point. For the two dipole configuration, we find that the fast wave splits and a fraction of the wave is focused at the null. The rest of the wave has its propagation influenced by the null, but manages to escape our numerical box (taking its wave energy with it). In both configurations, we find the Alfvén wave is again confined to the field lines it starts on and accumulates along the separatrices.

We also consider the behaviour of both fast and slow MA waves in a simple 2D X-point for a non-zero β plasma. We find that moving from a cold to a warm plasma introduces many new effects and discuss the importance of the location of the $c_s^2 = v_A^2$ layer. We find that the system displays two competing phenomena; a refraction effect caused by the varying Alfvén speed and a non-zero sound speed at the null which allows the fast wave to pass through.

Finally, we look at the behaviour of the Alfvén wave near a 2D null point with a non-uniform density profile. It is found that each fluid element is again confined to its starting field line, but now each element travels at its own speed. This causes the wave front to distort from its original shape as it propagates, but we find no evidence of phase mixing in the system; the energy is still extracted near the separatrices.

Declaration

I, James McLaughlin, hereby certify that this thesis, which is approximately 70,000 words in length, has been written by me, that it is the record of work carried out by me and that it has not been submitted in any previous application for a higher degree.

Name: James McLaughlin **Signature:**

Date: 19/12/05

I was admitted as a research student in October 2002 and as a candidate for the degree of Doctor of Philosophy in October 2003; the higher study for which this is a record was carried out in the University of St Andrews between 2002 and 2005.

Name: James McLaughlin **Signature:**

Date: 19/12/05

I hereby certify that the candidate has fulfilled the conditions of the Resolution and Regulations appropriate for the degree of Doctor of Philosophy in the University of St Andrews and that the candidate is qualified to submit this thesis in application for that degree.

Name: Alan Hood **Signature:**

Date: 19/12/05

In submitting this thesis to the University of St Andrews I understand that I am giving permission for it to be made available for use in accordance with the regulations of the University Library for the time being in force, subject to any copyright vested in the work not being affected thereby. I also understand that the title and abstract will be published, and that a copy of the work may be made and supplied to any bona fide library or research worker.

Name: James McLaughlin **Signature:**

Date: 19/12/05

Acknowledgements

Thanks to:

- My supervisor, Alan Hood, for all his advice, suggestions and encouragement over the three years of my PhD. It has been an interesting and difficult journey, but I couldn't have wished for a better guide.
- My parents and brothers. They may not have always understood the work I was doing, but they have always understood my reasons for doing it.
- My long suffering office mates, Gavin Donnelly and Duncan McGregor, for all their help and banter during my PhD. Three years together in the same office is a long time! Whether they meant to or not, they made my days interesting and eventful.
- To all the friends who have come into and out of my life here in St Andrews, particularly the friends I made through Gannochy House. Special mention must also go to Lynda Boothroyd and Ben Hood (but for *very* different reasons).
- My internal and external examiners, Bernie Roberts and Michael Ruderman, for all their constructive comments and helpful suggestions.

Finally, I would like to acknowledge the financial assistance from the Particle Physics and Astronomy Research Council (PPARC). Thanks guys, I really enjoyed those conferences!

Contents

Contents	i
1 Introduction	1
1.1 The Sun	1
1.1.1 Interior structure of the Sun	2
1.1.2 Atmospheric structure of the Sun	3
1.1.3 Solar Facts	4
1.2 Solar MHD Theory	4
1.2.1 MHD Equations	5
1.2.2 Induction Equation	6
1.3 Perturbation Theory	8
1.3.1 Equilibrium State	8
1.3.2 Considering small perturbations	8
1.3.3 Magnetic tension and magnetic pressure	9
1.4 Topology	10
1.5 MHD waves	11
1.5.1 Properties of waves	11
1.5.2 MHD wave modes	11
1.5.3 MHD waves in uniform magnetic field embedded in inhomogenous media	12
1.5.4 MHD waves in uniform magnetic field embedded in a homogenous media	15
1.5.5 The Alfvén wave	15
1.5.6 The Magnetoacoustic waves	16
2 The behaviour of MHD waves in the neighbourhood of null points	18
2.1 Aims of this Thesis	19
2.1.1 Thesis outline	19
2.2 Linearised Equations	20

2.2.1	Special Coordinate System	20
2.2.2	Dimensionless quantities	21
2.2.3	Simplification under $\beta = 0$	22
2.3	Numerical Methods	23
2.3.1	Numerical Schemes	24
2.3.2	CFL Condition	27
2.4	WKB approximation	28
2.4.1	Introduction to the WKB theory	28
2.4.2	Application to MHD waves	29
2.4.3	Characteristics	29
2.4.4	Derivation of Charpit's equations	30
2.4.5	Charpit's Equations	31
2.4.6	Alternative derivation	31
3	Behaviour of Fast MA Wave near a 2D null point in a $\beta = 0$ plasma	33
3.1	Introduction	33
3.2	Basic equations and set-up	35
3.3	Fast Magnetoacoustic Wave (in cartesian coordinates)	36
3.3.1	Numerical simulation results	37
3.3.2	WKB approximation	39
3.3.3	Current accumulation	44
3.4	Fast Magnetoacoustic Wave (in polar coordinates)	47
3.4.1	Numerical simulation	48
3.4.2	Analytical work : Klein-Gordon and Bessel functions	50
3.4.3	WKB approximation	53
3.5	Asymmetric Pulse	55
3.6	Conclusions	57
4	Behaviour of Alfvén Wave near a 2D null point	58
4.1	Basic equations and set-up	58
4.2	Numerical simulation	60
4.3	Analytical work	62
4.3.1	D'Alembert solution	62
4.3.2	WKB approximation	65
4.4	Behaviour of j_x and j_z	67

4.5	Conclusions	70
5	MHD wave propagation in the neighbourhood of two null points	72
5.1	Introduction	72
5.2	Basic Equations and set-up	74
5.3	Fast Waves in the neighbourhood of two null points	76
5.3.1	Upper Boundary	77
5.3.2	Analytical Results : WKB approximation	79
5.3.3	Side Boundary	84
5.3.4	Analytical Results	86
5.4	Alfvén Waves in the neighbourhood of two null points	90
5.4.1	Two null points connected by a separator	90
5.4.2	Case 1 : Upper Boundary	90
5.4.3	Case 2 : Side Boundary	96
5.4.4	Two null points not connected by a separator	100
5.4.5	Case 3 : Upper Boundary	100
5.4.6	Case 4 : Side Boundary	106
5.5	Conclusions	110
5.6	Including the effects of resistivity	112
6	Behaviour of MHD waves in the neighbourhood of two dipoles	114
6.1	Introduction	114
6.2	Basic Equations and set-up	115
6.2.1	Alfvén speed profile	117
6.3	Fast Waves	118
6.4	Simulation One	119
6.5	Simulation Two	121
6.5.1	Numerical simulation	121
6.5.2	WKB approximation	125
6.6	Simulation Three	130
6.6.1	Numerical simulation	130
6.6.2	WKB approximation	133
6.7	Alfvén Waves	137
6.7.1	Numerical simulation	137
6.7.2	WKB approximation	140

6.8	Conclusions	143
7	Magnetoacoustic mode coupling in the neighbourhood of a null point	145
7.1	Introduction	145
7.2	Basic equations and set-up	146
7.3	Plasma β	148
7.4	Polar coordinates ($\beta_0 = 0.25$ system)	150
7.4.1	Numerical Simulation : v_{\perp}	150
7.4.2	Numerical Simulation : v_{\parallel}	155
7.4.3	Interpreting the waves we see in v_{\perp} and v_{\parallel}	157
7.4.4	Small β_0 expansion	158
7.5	Mode conversion across the $c_s^2 = v_A^2$ layer	160
7.6	Cartesian coordinates ($\beta_0 = 0.25$ system)	161
7.6.1	Numerical Simulation : v_{\perp} ($\beta_0 = 0.25$)	161
7.6.2	Numerical Simulation : v_{\parallel} ($\beta_0 = 0.25$)	165
7.6.3	Current ($\beta_0 = 0.25$)	168
7.7	Cartesian coordinates ($\beta_0 = 2.25$ system)	171
7.7.1	Numerical Simulation : v_{\perp} ($\beta_0 = 2.25$)	171
7.7.2	Numerical Simulation : v_{\parallel} ($\beta_0 = 2.25$)	175
7.7.3	Current ($\beta_0 = 2.25$)	175
7.8	Analytical work : WKB approximation	178
7.9	Conclusions	183
8	Phase mixing of Alfvén waves near a 2D null point	185
8.1	Introduction	185
8.2	Basic Equations	186
8.3	D'Alembert solution	188
8.4	Density profiles	188
8.5	Case 1 : Uniform Density ($\lambda = 0$)	190
8.5.1	Numerical Simulation	190
8.5.2	Analytical Solution	192
8.6	Case 2 : Weakly non-uniform Density ($\lambda = 3$)	193
8.6.1	Numerical Simulation	193
8.6.2	Analytical Solution	195
8.7	Case 3 : Strongly non-uniform Density ($\lambda = 30$)	197

8.7.1	Numerical Simulation	197
8.7.2	Analytical Solution	199
8.8	Case 4 : Non-uniform Density $\rho_0 = [1 + 30(xz)^2]^{-1}$	202
8.8.1	Numerical Simulation	202
8.8.2	Analytical Solution	204
8.9	Conclusion	207
9	Summary and Further Work	208
9.1	Summary	208
9.2	Further Work	211
9.2.1	Non-linear wave behaviour	211
9.2.2	3D wave propagation near null points	212
9.2.3	MHD disturbances in observed magnetic fields	212
	Appendix A: Derivation of equation (3.4)	213
	Appendix B : Contents of CD-ROM	215
	Bibliography	217

Chapter 1

Introduction

Give me the splendid silent sun with all his beams full-dazzling.

— Walt Whitman (1819 - 1892)

1.1 The Sun

The Sun is a middle aged, ordinary star of spectral type G2 and absolute magnitude 4.8. It is one of 200,000 million stars that make up our galaxy, lying in one of the spiral arms about 100,000 parsecs from the Galactic Centre. The age of the Sun is about 4.6×10^9 years. Its mass is approximately 300,000 times the Earth's, i.e. 1.99×10^{30} kg. The distance between the Sun and the Earth is 1.5×10^8 km; which is denoted as one astronomical unit. The radius of the Sun is 6.96×10^5 km. It has a surface temperature of approximately 5780K, but the solar atmosphere, the **corona**, is much hotter, $T \approx 10^6$ K (Priest 1982; Lang 2001)

In the interior, solar material is compressed under its own gravitational attraction making the central temperatures and pressures high enough for nuclear reactions to take place. This supplies energy to the core, from the conversion of hydrogen into helium via nuclear fusion, which then continuously leaks outwards and is eventually radiated into space. A new area of solar physics, **helioseismology** (which is the study of the propagation of pressure waves in the Sun) has dramatically enhanced our knowledge of the inner workings of the Sun.

The Sun is a variable star; its brightness changes constantly, especially in ultraviolet and x-ray wavelengths. The Sun generates the solar wind; a continual outflow of plasma. Rapid variations of solar wind can disrupt communications and navigation, damage satellites, interrupt power distribution on Earth and even affect astronauts and aircraft passengers. Slower changes contribute to

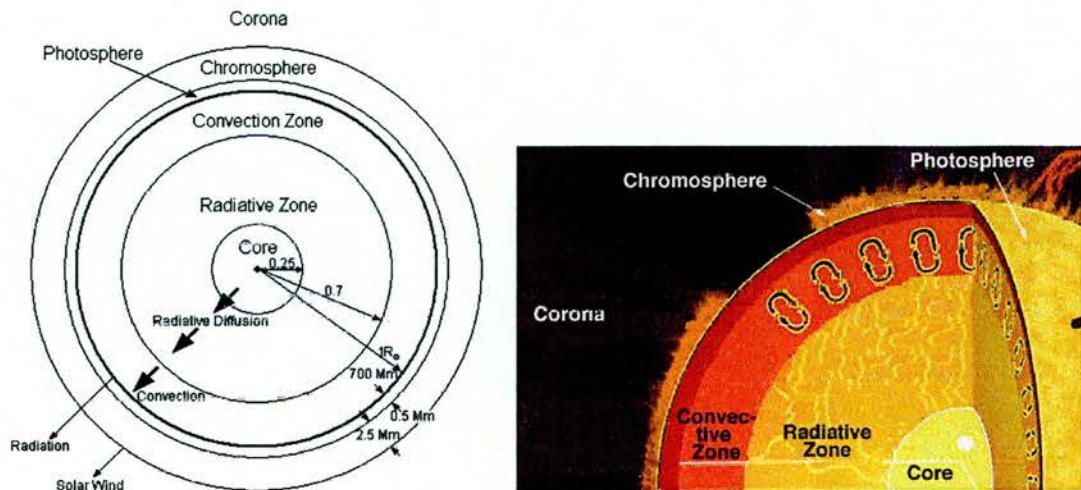


Figure 1.1: The structure of the Sun. *Left* shows a simple description of the different regions of the solar interior and exterior. *Right* shows simplistic interior of the Sun and satellite data of exterior of Sun.

climate change as well. Since the 1970s there has been a massive leap in our understanding of the physics of the Sun, brought about by advances in observations from a series of satellite missions, supplemented by ground based telescopes.

1.1.1 Interior structure of the Sun

Solar material is compressed under its own gravitational attraction. The central temperatures and densities are so high that nuclear fusion reactions take place. This supplies the energy that travels outwards via several different types of energy transport and is eventually radiated into space. Thus, energy is generated at its core and then transferred to the solar surface and beyond. The structure of the Sun is split into zones which each designation coming from the primary energy transfer mechanism at work there.

The nuclear core is the central region where nuclear reactions occur at a temperature believed to be around $1.5 \times 10^7 K$. As we move away from the centre, density decreases and so the fusion reactions are less prevalent. Photons from the core (taking energy with them) travel outwards through a region called the **radiative zone**. Photons produced in the core take millions of years to travel through this zone due to continuous absorption and emission (small mean free path). Each absorption and re-emission reduces the photon energy and hence increases its wavelength. The radiative zone stretches from roughly a quarter of a solar radius to 0.7 solar radii. At this point, the temperature has dropped enough to allow atomic recombination to start and the plasma begins to absorb the photons (they can no longer radiate freely). Now convection becomes the primary process for transporting the energy to the solar surface. This is called the **convection zone**. These zones can be seen in Figure 1.1.

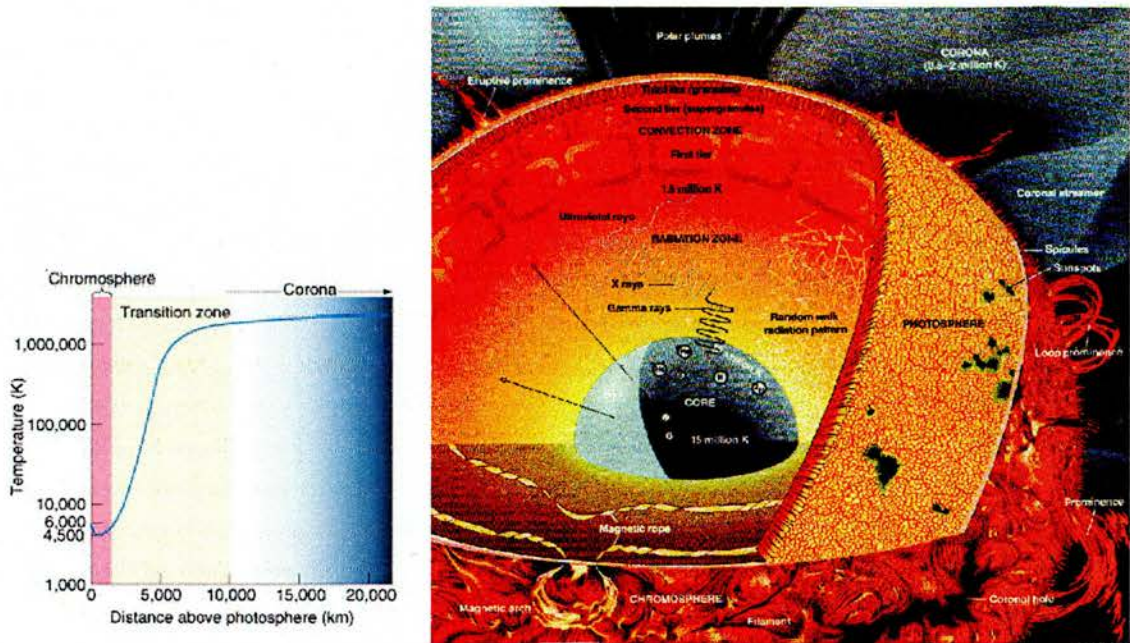


Figure 1.2: The structure of the Sun. *Left* shows simplistic interior of the Sun and satellite data of exterior of Sun. *Right* shows more complicated interior of the Sun and other solar phenomena.

1.1.2 Atmospheric structure of the Sun

The solar surface we see is called the **photosphere**. It is a thin layer occurring where radiation, produced in the core, is more likely to escape into space than be absorbed. By this region, the energy of the photons has decreased from X-ray and γ -ray levels down to visible light wavelengths. The temperature of the photosphere is about $5780K$. Above the photosphere is a layer called the **chromosphere**. Here, the temperature rises to about $20,000K$ and at these higher temperatures hydrogen emits light that gives off a reddish color (H_{α} emission). Above this, there is the **transition region**. The transition region is an irregular layer of the Sun's atmosphere that separates the cool chromosphere from the much hotter outer atmosphere of the Sun. In this thin region, an amazing increase in temperature occurs; temperature soar from tens of thousands to millions of degrees Kelvin.

The Sun's outer atmosphere is called the **corona**. Because it is so very hot (millions of degrees) the coronal gas emits low-energy X-rays. There are also large loop structures that indicate where the ionised gas flows along magnetic fieldlines. It is still a mystery why the corona is so hot compared to the much cooler chromosphere. It is, however, clear that the magnetic field plays a key role. There are many theories on how to heat the corona, such as reconnection models and wave heating models. In one such model, the magnetic field in a loop is twisted by photospheric motions at its base. If the twisting happens slowly, it generates a steady electric current that heats up the coronal gas (Ruzmaikin & Berger 1998). It does not take much energy to do this, because

the coronal gas is so thin that it has a small heat capacity.

The different regions of the Sun's atmosphere are defined by the temperature in that region, and hence are irregular and dynamic strata. These regions can be seen in Figure 1.2.

1.1.3 Solar Facts

age 4.6×10^9 years

mass $M_{\odot} = 1.99 \times 10^{30}$ kg

radius $R_{\odot} = 6.96 \times 10^5$ km

surface temperature 5785 K

mean density 1.4×10^3 kg m⁻³

mean distance from Earth 1 AU = 1.50×10^8 km

surface gravity $g_{\odot} = 274$ m s⁻²

equatorial rotation period 26 days

composition 90% H, 10% He, 0.1% other elements

The above values are taken from Priest (1982).

1.2 Solar MHD Theory

Magnetohydrodynamics (MHD) unites two disciplines; *electromagnetism* and *fluid dynamics*. MHD is a relatively new area, approximately seventy years old, but has been developing quickly since the 1950s when it was realised that MHD gave a good description of plasmas in the Sun as well as other stars and the interstellar medium (a plasma is a highly ionised gas in which electrons and atomic nuclei move freely). The Sun acts as a laboratory, illustrating astrophysical MHD. The magnetic field has several effects:

- it exerts a force
- it can store energy
- it acts as a thermal blanket
- it provides stability

1.2.1 MHD Equations

The following equations are from electromagnetism and continuum mechanics. Together they are called the **magnetohydrodynamic equations** and are used in the study of the interaction between a magnetic field and a plasma.

Equation of Motion

$$\rho \left[\frac{\partial \mathbf{v}}{\partial t} + (\mathbf{v} \cdot \nabla) \mathbf{v} \right] = -\nabla p + \mathbf{j} \times \mathbf{B} + \rho \mathbf{g} , \quad (1.1)$$

Mass Conservation

$$\frac{\partial \rho}{\partial t} + \nabla \cdot (\rho \mathbf{v}) = 0 , \quad (1.2)$$

Adiabatic Energy Equation

$$\frac{\partial p}{\partial t} + \mathbf{v} \cdot \nabla p = -\gamma p \nabla \cdot \mathbf{v} , \quad (1.3)$$

Ideal Gas Law

$$p = \frac{R}{\hat{\mu}} \rho T , \quad (1.4)$$

Ampère's Law

$$\mu \mathbf{j} = \nabla \times \mathbf{B} , \quad (1.5)$$

Solenoidal Condition

$$\nabla \cdot \mathbf{B} = 0 , \quad (1.6)$$

Faraday's Law

$$\frac{\partial \mathbf{B}}{\partial t} = -\nabla \times \mathbf{E} , \quad (1.7)$$

Ohm's Law

$$\frac{\mathbf{j}}{\hat{\sigma}} = \mathbf{E} + \mathbf{v} \times \mathbf{B} . \quad (1.8)$$

Here \mathbf{v} is fluid velocity, ρ is density, p is pressure, \mathbf{B} is the magnetic induction (usually called the magnetic field), \mathbf{E} is electric field, g is gravitational acceleration, \mathbf{j} is the electric current density, T is the temperature, μ is the magnetic permeability ($4\pi \times 10^{-7} \text{Hm}^{-1}$), R is the universal gas

constant ($R = 8.314510 \text{ JK}^{-1}\text{mol}^{-1}$), $\hat{\mu}$ is the mean atomic weight (average mass per particle in units of mass of a proton), $\hat{\sigma}$ is electric conductivity and γ is the ratio of specific heats (usually $\gamma = \frac{5}{3}$ for a monoatomic gas). We have also considered the inviscid equation of motion for simplicity.

1.2.2 Induction Equation

In solar MHD, we eliminate the electric field \mathbf{E} and the electric current density \mathbf{j} and work with the *primary variables*, \mathbf{B} and \mathbf{v} . We eliminate \mathbf{E} from equation (1.7) using equations (1.5) and (1.8) to obtain:

$$\frac{\partial \mathbf{B}}{\partial t} = -\nabla \times \left(-\mathbf{v} \times \mathbf{B} + \frac{\nabla \times \mathbf{B}}{\mu \hat{\sigma}} \right). \quad (1.9)$$

We let $\eta = (\mu \hat{\sigma})^{-1}$, where η is known as the **magnetic diffusivity**. In this Thesis, we assume η to be constant. Equation (1.9) can be expressed as

$$\frac{\partial \mathbf{B}}{\partial t} = \nabla \times (\mathbf{v} \times \mathbf{B}) + \eta \nabla^2 \mathbf{B}. \quad (1.10)$$

This is known as the **Induction Equation**.

Here we have used $\nabla \times (\nabla \times \mathbf{B}) = \nabla (\nabla \cdot \mathbf{B}) - \nabla^2 \mathbf{B}$ and $\nabla \cdot \mathbf{B} = 0$.

Magnetic Reynolds number

The **magnetic Reynolds number**, R_m is defined as:

$$R_m = \frac{L \bar{v}}{\eta} \quad (1.11)$$

where L is a typical length scale for the plasma, \bar{v} is a typical plasma velocity and η is the magnetic diffusivity. R_m is a measure of the size of the advection term, $\nabla \times (\mathbf{v} \times \mathbf{B})$, compared to the size of the diffusion term, $\eta \nabla^2 \mathbf{B}$. On the Sun, R_m is normally very large because L and \bar{v} are typically large. When \bar{v} is equal to the Alfvén speed, R_m becomes the Lundquist number, S . The Lundquist number is the ratio of the diffusion time to the Alfvén time.

By considering a large magnetic Reynolds number, $R_m \gg 1$, the induction equation, (1.10), simplifies to:

$$\frac{\partial \mathbf{B}}{\partial t} = \nabla \times (\mathbf{v} \times \mathbf{B}) .$$

Then the **frozen-flux theorem** of Alfvén (1942) applies. A proof can be found in Priest (1982).

Alfvén's Theorem

In a perfectly conducting fluid ($R_m \rightarrow \infty$), magnetic field lines move with the fluid; the field lines are *frozen* into the plasma.

Scale height

The **scale height**, H_0 , is defined as:

$$H_0 = \frac{p_0}{\rho_0 g} ,$$

where p_0 is a typical pressure and ρ_0 is a typical density in the system. It gives a measure of how quickly quantities vary in the system under the effect of gravity. Thus, by considering typical length scales that are much less than the scale height, $L \ll H_0$ we can ignore the gravitational forces in the system. A full explanation of the scale height can be found in Priest (1982). In this Thesis, all the problems considered will ignore gravitational effects.

Plasma β

We define the ratio of the gas pressure to the magnetic pressure as:

$$\beta = \frac{p_0}{B_0^2/2\mu} \tag{1.12}$$

This ratio, β , is called the **plasma β** . In the majority of the corona, the magnetic pressure is much greater than the gas pressure, and so the plasma β is much smaller than unity. Hence, we may ignore the gas pressure (relative to the effect of the magnetic pressure) and take $\beta = 0$ as a good approximation. However, there are places where this approximation breaks down, such as at null points (Section 1.4) and we have to consider the effects of plasma pressure (Chapter 7 considers this issue). Note also that although $\beta = 0$ is a good approximation in the corona, β may be much higher and irregular in the lower atmosphere, such as in the Chromosphere (Section 1.1.2).

1.3 Perturbation Theory

Perturbation theory is a mathematical method that is used to find an approximate solution to a problem which cannot be solved exactly by starting from the exact solution of a related problem. Perturbation theory is applicable if the problem at hand can be formulated by adding a “small” term to the mathematical description of the exactly solvable problem. Perturbation theory leads to an expression for the desired solution in terms of a power series in some “small” parameter that quantifies the deviation from the exactly solvable problem. The leading term in this power series is the solution of the exactly solvable problem, while further terms describe the deviation in the solution, due to the deviation from the initial problem.

1.3.1 Equilibrium State

We will now consider an equilibrium state, such that the system is steady ($\frac{\partial}{\partial t} = 0$) and $\mathbf{v} = \mathbf{0}$. Applying this to equations (1.1), (1.2) and (1.3) results in the following **equilibrium state**:

$$\mathbf{B} = \mathbf{B}_0(\mathbf{r}), \quad \rho = \rho_0(\mathbf{r}), \quad p = p_0(\mathbf{r}), \quad \left(\frac{1}{\mu} \nabla \times \mathbf{B}_0 \right) \times \mathbf{B}_0 = \nabla p_0, \quad (1.13)$$

where \mathbf{r} is a position vector such as $\mathbf{r} = (x, y, z)$.

1.3.2 Considering small perturbations

Let us now consider small perturbations to our equilibrium (small deviations from our solvable equilibrium system) :

$$\mathbf{B} = \mathbf{B}_0 + \epsilon \mathbf{b}(x, y, z, t), \quad (1.14)$$

$$\mathbf{v} = \mathbf{0} + \epsilon \mathbf{v}_1(x, y, z, t), \quad (1.15)$$

$$\rho = \rho_0 + \epsilon \rho_1(x, y, z, t), \quad (1.16)$$

$$p = p_0 + \epsilon p_1(x, y, z, t). \quad (1.17)$$

where ϵ is a very small number ($\epsilon \ll 1$) and, thus, the above equations signify small changes to the equilibrium state. As in standard perturbation theory, we substitute (1.14) – (1.17) into equations (1.2), (1.1), (1.3) and (1.10), expand in powers of ϵ and neglect terms of the order ϵ^2 and above. This results in the following linearised perturbation equations:

$$\frac{\partial \mathbf{b}}{\partial t} = \nabla \times (\mathbf{v}_1 \times \mathbf{B}_0) + \eta \nabla^2 \mathbf{b}, \quad (1.18)$$

$$\rho_0 \frac{\partial \mathbf{v}_1}{\partial t} = -\nabla p_1 + \left(\frac{1}{\mu} \nabla \times \mathbf{b} \right) \times \mathbf{B}_0, \quad (1.19)$$

$$\frac{\partial \rho_1}{\partial t} = -\nabla \cdot (\rho_0 \mathbf{v}_1) , \quad (1.20)$$

$$\frac{\partial p_1}{\partial t} = -\gamma p_0 (\nabla \cdot \mathbf{v}_1) . \quad (1.21)$$

1.3.3 Magnetic tension and magnetic pressure

Recall the quantity $\frac{1}{\mu} (\nabla \times \mathbf{B}_0) \times \mathbf{B}_0$ from equation (1.13). We can rewrite this term:

$$\frac{1}{\mu} (\nabla \times \mathbf{B}) \times \mathbf{B} = \frac{1}{\mu} (\mathbf{B} \cdot \nabla) \mathbf{B} - \nabla \left(\frac{1}{2\mu} \mathbf{B} \cdot \mathbf{B} \right) .$$

Here, the first term $\frac{1}{\mu} (\mathbf{B} \cdot \nabla) \mathbf{B}$ represents the effect of **magnetic tension** parallel to \mathbf{B} of magnitude $\frac{\mathbf{B}^2}{\mu}$ per unit area. It gives a magnetic tension force if the fieldlines are curved.

The second term $\nabla \left(\frac{1}{2\mu} \mathbf{B} \cdot \mathbf{B} \right)$ represents the effect of **magnetic pressure** of magnitude $\frac{\mathbf{B}^2}{2\mu}$. This gives a magnetic pressure force when \mathbf{B} varies with position. It exerts the same pressure in all directions (isotropic).

Thus, equation (1.19) can also be written as:

$$\rho_0 \frac{\partial \mathbf{v}_1}{\partial t} = -\nabla p_1 - \frac{1}{\mu} \nabla (\mathbf{B}_0 \cdot \mathbf{b}) + \frac{1}{\mu} [(\mathbf{B}_0 \cdot \nabla) \mathbf{b} + (\mathbf{b} \cdot \nabla) \mathbf{B}_0] . \quad (1.22)$$

These two alternative forms will be useful later.

1.4 Topology

It is clear that the magnetic field plays an essential role in understanding the myriad of phenomena in the solar corona. We can use *topology* nomenclature to reduce a complicated mess of field-lines to something more understandable. A complex magnetic field configuration can have many different components. In 2D, a general magnetic configuration contains *separatrix curves* (separatrices), which split the plane into topologically distinct regions, in the sense that all the field lines in one region start at a particular source and end at a particular sink. Separatrices intercept at *magnetic null points*¹. Null points are single-point locations where the magnetic field vanishes, $\mathbf{B} = 0$. Magnetic topologies with such singular points are common in the presence of multiple magnetic sources. A magnetic fieldline that joins two null points (itself a special type of separatrix) is called a *separator*. Thus, instead of showing all the magnetic field lines in a region, we can just show these aspects of importance; such a picture of the magnetic structure is called the *skeleton* of the field.

In 3D, we have similar properties, now with *separatrix surfaces* separating the volume into topologically different regions. They intersect each other at a separator. Figure (1.3) shows an example of these topological features in 2D (left) and 3D (right) (see also Priest & Forbes 2000; Aschwanden 2004).

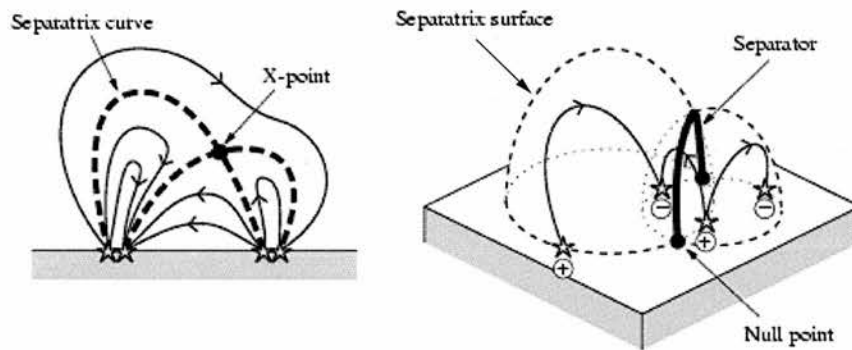


Figure 1.3: The definitions of X-points, separatrix curves, separatrix surfaces and separators in a 2D (left) and 3D (right) context.

The existence of null points is predicted on theoretical grounds and their importance lies in the fact that the Alfvén speed (Section 1.5.2) is actually zero at that point. This important consequence will be utilised later. Potential field extrapolations, using photospheric magnetograms to provide the field distribution on the lower boundary, suggest that there are always likely to be null points in the corona. The number of such points depends on the magnetic complexity of the photospheric

¹In fact, there are two different types of magnetic neutral points, one at the intersection of separatrix curves (X-point), the other at the center of a magnetic island (O-point).

flux distribution. Detailed investigations of the coronal magnetic field, using such potential field calculations, can be found in Beveridge *et al.* (2002) and Brown & Priest (2001).

1.5 MHD waves

1.5.1 Properties of waves

A wave is a time-varying quantity that is also a function of position. It is a disturbance, either continuous or transient, travelling through a medium by virtue of the elastic nature of the medium. In cartesian coordinates, wave equations are partial differential equations of the form:

$$\frac{\partial^2 U}{\partial t^2} = c^2 \left(\frac{\partial^2 U}{\partial x^2} + \frac{\partial^2 U}{\partial y^2} + \frac{\partial^2 U}{\partial z^2} \right) = c^2 \nabla^2 U, \quad (1.23)$$

or its counterpart in different dimensions. The solution represents the propagation of displacements as waves with velocity c . For transverse waves propagating through a medium it is given by $c = \sqrt{\frac{\text{tension}}{\text{density}}}$.

Waves possess a **frequency** (ω) and a **wavevector** (\mathbf{k}) which is related to wavelength. **Dispersion relations** relate the frequency with which the waves oscillate in time to the wavevector, i.e. the spatial length scales of the wave. These relations are of the form $\omega = \omega(\mathbf{k})$. Dispersion relations can be used to define two important quantities, namely the **phase speed** and the **group velocity**.

$$c_{\text{phase speed}} = \frac{\omega}{|\mathbf{k}|}, \quad c_{\text{group velocity}} = \frac{\partial \omega}{\partial \mathbf{k}}.$$

The phase speed gives the speed of an individual wave. The group velocity gives the speed and direction of the transport of information and energy. If we also consider a compressible medium, then we can define the **sound speed** as:

$$c_s = \sqrt{\frac{\gamma p_0}{\rho_0}} \quad (1.24)$$

where p_0 and ρ_0 are the equilibrium pressure and density in the system and γ is the ratio of specific heats (as in Section 1.2.1).

1.5.2 MHD wave modes

In magnetohydrodynamics, the magnetic tension (Section 1.3.3) provides an elastic restoring force, such that we would expect waves to propagate along uniform magnetic field lines with

speed:

$$v_A = \sqrt{\frac{\text{magnetic tension}}{\text{density}}} = \sqrt{\frac{\frac{B_0^2}{\mu}}{\rho_0}} = \frac{B_0}{\sqrt{\mu\rho_0}}, \quad (1.25)$$

where v_A is called the **Alfvén speed**. Transverse waves travelling at this speed along magnetic field lines are called **Alfvén waves**.

If we also include pressure fluctuations, the Alfvén wave still remains, but the sound speed and Alfvén speed can now couple together to give *magnetoacoustic waves* (MA waves). These can take two separate forms, the higher frequency mode is known as the **fast magnetoacoustic wave** and the lower frequency mode is known as the **slow magnetoacoustic wave**. However, since the three types of MHD mode are so important in this Thesis, we will now look at them more mathematically.

1.5.3 MHD waves in uniform magnetic field embedded in inhomogenous media

We begin by examining waves in a magnetically structured atmosphere (ignoring gravity)². Considering the equilibrium state (in the same way as in Section 1.3.1) but for a simpler system where all the quantities may only vary in x :

$$\mathbf{B}_0 = B_0(x) \hat{\mathbf{z}}, \quad p_0 = p_0(x), \quad \rho_0 = \rho_0(x). \quad (1.26)$$

This represents a plasma with pressure p_0 and density ρ_0 exposed to a unidirectional magnetic field B_0 aligned with the z -axis.

Recall that our equilibrium equations (1.13) tell us that $\frac{1}{\mu} (\mathbf{B}_0 \cdot \nabla) \mathbf{B}_0 - \nabla \left(\frac{1}{2\mu} \mathbf{B}_0 \cdot \mathbf{B}_0 \right) = \nabla p_0$ and hence with the quantities above:

$$\frac{d}{dx} \left(p_0 + \frac{B_0^2}{2\mu} \right) = 0 \quad (1.27)$$

Recall the linearised perturbation equations (1.18), (1.20) – (1.22):

$$\begin{aligned} \frac{\partial \mathbf{b}}{\partial t} &= \nabla \times (\mathbf{v}_1 \times \mathbf{B}_0), \\ \rho_0 \frac{\partial \mathbf{v}_1}{\partial t} &= -\nabla \left[p_1 + \frac{1}{\mu} (\mathbf{B}_0 \cdot \mathbf{b}) \right] + \frac{1}{\mu} [(\mathbf{B}_0 \cdot \nabla) \mathbf{b} + (\mathbf{b} \cdot \nabla) \mathbf{B}_0], \\ \frac{\partial \rho_1}{\partial t} + (\mathbf{v}_1 \cdot \nabla) \rho_0 &= -\rho_0 (\nabla \cdot \mathbf{v}_1), \end{aligned}$$

²This section closely follows the work of Roberts (1985)

$$\frac{\partial p_1}{\partial t} = -\gamma p_0 (\nabla \cdot \mathbf{v}_1) .$$

Here we have rearranged the equations so that the plasma pressure and magnetic pressure term $\frac{1}{\mu} (\mathbf{B}_0 \cdot \mathbf{b})$ are together and have taken $\eta = 0$ for simplicity. We can also combine the last two equations as:

$$\frac{\partial p_1}{\partial t} + (\mathbf{v}_1 \cdot \nabla) p_0 = \frac{\gamma p_0}{\rho_0} \left[\frac{\partial \rho_1}{\partial t} + (\mathbf{v}_1 \cdot \nabla) \rho_0 \right] .$$

We can also write $c_s^2 = \frac{\gamma p_0}{\rho_0}$ as a background sound speed (as defined in section 1.5.1). Here $c_s = c_s(x)$, velocity takes the form, $\mathbf{v}_1 = (v_x, v_y, v_z)$ and perturbed magnetic field takes the form $\mathbf{b} = (b_x, b_y, b_z)$.

There has been a great deal of research into the theory of MHD waves. Papers of mention include Edwin & Roberts (1982, 1983), Rae & Roberts (1982, 1983), Roberts, Edwin & Benz (1984), Roberts (1985, 1991, 2004), Nakariakov & Ofman (2001), Goossens *et al.* (2002) and Roberts & Nakariakov (2003). These works have shown it is beneficial to construct the *total pressure* quantity. Thus the *total perturbed pressure* of our system is:

$$p_T = \text{plasma pressure} + \text{magnetic pressure} = p_1 + p_m = p_1 + \frac{(\mathbf{B}_0 \cdot \mathbf{b})}{\mu} \quad (1.28)$$

Thus, equation (1.27) tells us that the *total equilibrium pressure* in the system is constant.

Our linearised perturbation equations can now be rearranged to form the quantities:

$$\begin{aligned} \rho_0 \left(\frac{\partial^2}{\partial t^2} - v_A^2 \frac{\partial^2}{\partial z^2} \right) \mathbf{v}_\perp + \nabla_\perp \left(\frac{\partial p_T}{\partial t} \right) &= 0 \\ \left(\frac{\partial^2}{\partial t^2} - c_s^2 \frac{\partial^2}{\partial z^2} \right) v_\parallel - c_s^2 \nabla_\perp \cdot \frac{\partial \mathbf{v}_\perp}{\partial z} &= 0 \end{aligned} \quad (1.29)$$

where $\mathbf{v}_\perp = (v_x, v_y, 0)$ and $\mathbf{v}_\parallel = v_\parallel \hat{\mathbf{z}} = (0, 0, v_z)$ are the velocities perpendicular and parallel to the equilibrium field $\mathbf{B}_0 = (0, 0, B_0(x))$ and $\nabla_\perp = \left(\frac{\partial}{\partial x}, \frac{\partial}{\partial y}, 0 \right)$. $v_A^2(x)$ is the Alfvén speed, as defined in Section (1.5.1). We can also write equations for the total pressure and magnetic pressure perturbations:

$$\begin{aligned} \frac{\partial p_T}{\partial t} &= -\rho_0 \left[c_s^2 \frac{\partial v_\parallel}{\partial z} + (c_s^2 + v_A^2) \nabla_\perp \cdot \mathbf{v}_\perp \right] \\ \frac{\partial p_m}{\partial t} &= \frac{\partial}{\partial t} (\mathbf{B}_0 \cdot \mathbf{b}) = v_x \frac{dp_0}{dx} - \rho_0 v_A^2 \nabla_\perp \cdot \mathbf{v}_\perp \end{aligned} \quad (1.30)$$

where we have used the fact that $\nabla \cdot \mathbf{v} = \nabla_\perp \cdot \mathbf{v}_\perp + \frac{\partial}{\partial z} v_\parallel$ and equation (1.27).

We can solve these equations using *normal mode analysis*. We can look for a harmonic solution by introducing the Fourier components:

$$\begin{aligned} v_x &= v_x(x) e^{i(\omega t - k_y y - k_z z)} , & v_y &= v_y(x) e^{i(\omega t - k_y y - k_z z)} , \\ v_z &= v_z(x) e^{i(\omega t - k_y y - k_z z)} , & p_T &= p_T(x) e^{i(\omega t - k_y y - k_z z)} . \end{aligned}$$

Note we cannot Fourier analyse in the x -direction because we do not have constant coefficients in that variable. These forms are substituted into equations (1.29) and (1.30) and then v_y and v_z are eliminated. This gives a pair of coupled ODEs in terms of $v_x(x)$ and $p_T(x)$:

$$\begin{aligned} \frac{dp_T}{dx} + i \frac{\rho_0}{\omega} (\omega^2 - k_z^2 v_A^2) v_x &= 0 , \\ (\omega^2 - k_z^2 v_A^2) (\omega^2 - k_z^2 c_T^2) \frac{dv_x}{dx} + i \frac{\omega}{\rho_0 (c_s^2 + v_A^2)} (\omega^2 - \omega_S^2) (\omega^2 - \omega_F^2) p_T &= 0 , \end{aligned} \quad (1.31)$$

where ω_S and ω_F satisfy:

$$\omega_S^2 + \omega_F^2 = (k_y^2 + k_z^2) (c_s^2 + v_A^2) , \quad (\omega_S \omega_F)^2 = k_z^2 (k_y^2 + k_z^2) c_s^2 v_A^2 . \quad (1.32)$$

We have also introduced a new important speed, the **tube speed**, c_T , where:

$$c_T = \frac{c_s v_A}{\sqrt{c_s^2 + v_A^2}} . \quad (1.33)$$

We can combine our two ODEs together to a single equation for one variable. Once we know v_x , we will know p_T and vice versa. Eliminating p_T yields:

$$\frac{d}{dx} \left[\frac{\rho_0 (c_s^2 + v_A^2) (\omega^2 - k_z^2 v_A^2) (\omega^2 - k_z^2 c_T^2)}{(\omega^2 - \omega_S^2) (\omega^2 - \omega_F^2)} \frac{d}{dx} v_x \right] + \rho_0 (\omega^2 - k_z^2 v_A^2) v_x = 0 . \quad (1.34)$$

This equation describes the behaviour of MHD waves in an inhomogeneous medium with an applied magnetic field $B_0 \hat{z}$. It is a complicated equation with a very rich structure.

The equation has two singularities; an *Alfvén singularity* occurring when $\omega^2 = k_z^2 v_A^2$ and a *cusp singularity* when $\omega^2 = k_z^2 c_T^2$. These singularities occur due to the anisotropic nature of the MHD waves. Also, the locations where $\omega^2 = \omega_F^2$ or $\omega^2 = \omega_S^2$ are not singularities, but *cut-off points*. These locations indicate where the waves change between oscillatory and evanescent behaviour, indicating locations of wave trapping or reflection. This is especially important in coronal loop studies (Edwin & Roberts 1982; 1983; Roberts 1991; Nakariakov & Ofman 2001).

1.5.4 MHD waves in uniform magnetic field embedded in a homogenous media

We now consider a further simplification to equation (1.34); we consider all the coefficients in equations (1.29) -(1.31) to be constants (equivalent to removing x dependence of the equilibrium quantities). Thus, equation (1.34) simplifies to:

$$\rho_0 (\omega^2 - k_z^2 v_A^2) \left[\frac{\rho_0 (c_s^2 + v_A^2) (\omega^2 - k_z^2 v_A^2) (\omega^2 - k_z^2 c_T^2)}{(\omega^2 - \omega_S^2) (\omega^2 - \omega_F^2)} \frac{d^2}{dx^2} v_x + v_x \right] = 0 .$$

We may now Fourier analyse in the x -direction (we now have constant coefficients), such that $v_x \propto e^{-ik_x x}$. Substituting into the above equation gives:

$$(\omega^2 - k_z^2 v_A^2) [\omega^4 - \omega^2 (c_s^2 + v_A^2) k^2 + k^2 k_z^2 c_s^2 v_A^2] = 0 , \quad (1.35)$$

where $k^2 = k_x^2 + k_y^2 + k_z^2$. This is the general **dispersion relation** for MHD modes. There are three roots to consider.

This dispersion relation describes the interaction between plasma pressure, magnetic pressure and magnetic tension. To aid in our discussion of the three roots, we note that from equations (1.18) – (1.22), we have the quantities:

$$p_m = \frac{(\omega^2 - k_z^2 v_A^2)}{\omega^2} \left(\frac{v_A}{c_s} \right)^2 p_1 , \quad (1.36)$$

$$p_T = \frac{(\omega^2 - k_z^2 c_T^2)}{\omega^2} \left(\frac{c_s^2 + v_A^2}{c_s^2} \right) p_1 = \frac{\rho_0}{\omega} (\omega^2 - k_z^2 v_A^2) \frac{v_x}{k_x} , \quad (1.37)$$

$$p_1 = \rho_1 c_s^2 = \rho_0 \omega \frac{v_z}{k_z} , \quad (1.38)$$

1.5.5 The Alfvén wave

One root of the dispersion relation (1.35) is given by:

$$\omega^2 = k_z^2 v_A^2 = k^2 v_A^2 \cos^2 \theta , \quad (1.39)$$

where θ is the angle the wavevector $\mathbf{k} = (k_x, k_y, k_z)$ makes with the magnetic field $B_0 \hat{\mathbf{z}}$. This is the **Alfvén wave**, named after the work of Alfvén (1942). It has $c_{\text{phase speed}} = \pm v_A$ and $\mathbf{c}_{\text{group velocity}} = \pm v_A \hat{\mathbf{z}}$. From equations (1.36) - (1.38), we see that under this solution, p , p_m , p_T , v_z and ρ are all zero. Thus, propagation of the Alfvén wave is an incompressible wave and occurs transverse to the applied magnetic field. We can also see that the Alfvén wave is unable to propagate across the magnetic field ($\theta = \frac{\pi}{2} \Rightarrow \omega = 0$). The Alfvén wave is driven by the magnetic tension force and is akin to the transverse wave on an elastic string.

We can also write the solution as:

$$\mathbf{v}_{\text{Alfvén}} = \frac{v_y}{k_x} (-k_y, k_x, 0) .$$

1.5.6 The Magnetoacoustic waves

If we look for a different root to the dispersion relation (i.e. $\omega^2 \neq k_z^2 v_A^2$), equation (1.35) reduces to:

$$\omega^4 - \omega^2 (c_s^2 + v_A^2) k^2 + k^2 k_z^2 c_s^2 v_A^2 = 0 . \quad (1.40)$$

This may be solved such that:

$$\frac{\omega^2}{k^2} = \frac{1}{2} (c_s^2 + v_A^2) \pm \frac{1}{2} \sqrt{(c_s^2 + v_A^2)^2 - 4 c_s^2 v_A^2 \cos^2 \theta} . \quad (1.41)$$

The two roots of this equation correspond to the **fast magnetoacoustic** (higher frequency) and **slow magnetoacoustic** modes (lower frequency), as mentioned in Section (1.5.2).

When propagating along the field ($\theta = 0$) and $\omega_{\text{fast}}^2 = k^2 v_A^2$ and $\omega_{\text{slow}}^2 = k^2 c_s^2$. When propagating perpendicular to the field ($\theta = \frac{\pi}{2}$), the fast wave achieves its greatest speed, whereas the slow wave cannot propagate. More precisely, $\omega_{\text{slow}}^2 = k^2 c_T^2 \cos^2 \theta$ as $\theta \rightarrow \frac{\pi}{2}$. Thus, the slow wave (and the Alfvén wave) cannot propagate across field lines whereas the fast wave can.

It can also be shown (e.g. Roberts 1985) that the velocity fields of both magnetoacoustic (MA) modes are of the form:

$$\mathbf{v}_{\text{fast}} = \frac{v_x}{k_x} (k_x, k_y, \lambda^F k_z) , \quad \mathbf{v}_{\text{slow}} = \frac{v_x}{k_x} (k_x, k_y, \lambda^S k_z) \quad (1.42)$$

where

$$\lambda^F = \frac{c_s^2 (k_x^2 + k_y^2)}{(\omega_{\text{fast}}^2 - k_z^2 c_T^2)} , \quad \lambda^S = \frac{c_s^2 (k_x^2 + k_y^2)}{(\omega_{\text{slow}}^2 - k_z^2 c_T^2)}$$

where the S and F superscripts indicates the form of ω^2 from equation (1.41), i.e. fast or slow frequency solution (where $\omega_{\text{slow}} < \omega_{\text{fast}}$).

Figure 1.4 shows a graphical representation of the phase speeds for the three MHD modes. Here, we can clearly see the anisotropic nature of the slow and Alfvén waves and the (almost) isotropic form of the fast mode. We see that the speed of the Alfvén wave lies between that of the slow and fast waves, although the phase speeds for both the slow and fast waves depend upon the angle between the direction of propagation and the equilibrium magnetic field.

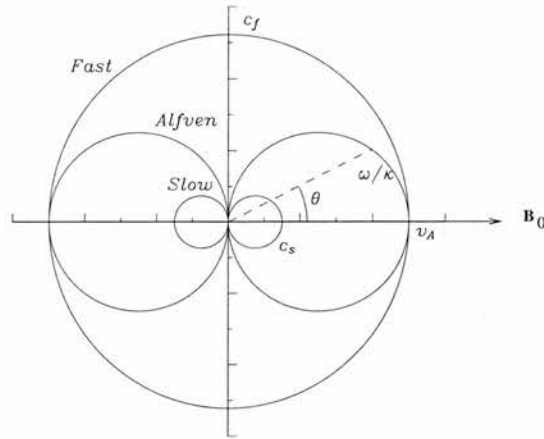


Figure 1.4: Polar plot showing the phase speeds of the three types of MHD mode ($v_A > c_s$ here).

We can look at equations (1.36) - (1.38) to see how these quantities interrelate in the magnetoacoustic modes. For the slow wave, p_m and p_1 are *out of phase*, but for the fast wave these quantities are always *in phase*. The slow and fast waves compress the gas (as ordinary sound waves do) and bend the magnetic field lines. The Alfvén waves just bend the fieldlines without compressing the gas. Since Alfvén waves are incompressible, they do not lose energy as quickly (the MA modes compress the gas which uses up energy). Also, by taking scalar products with equation (1.35), it can be shown that $\mathbf{v}_{\text{Alfvén}}$, \mathbf{v}_{slow} and \mathbf{v}_{fast} are all orthogonal.

We can also consider what happens in a zero β -plasma, in which there is no gas pressure perturbations and hence $c_s = 0$. In this case, $\omega^2 = k^2 v_A^2$ for the fast wave, so this mode propagates isotropically at speed v_A . For this reason, it is sometimes referred to as a *compressional Alfvén wave*, though this is not the anisotropic Alfvén wave of Section (1.5.5). The slow mode vanishes in a zero β -plasma.

Finally, for a high β -plasma $c_s \gg v_A$ and the fast wave behaves akin to a sound wave, whereas the slow wave would obey $\omega^2 = k_z^2 v_A^2$. Again, this is discussed further in Section 7.5.

Chapter 2

The behaviour of MHD waves in the neighbourhood of null points

The coronal heating problem remains one of the key unsolved problems in solar physics. As mentioned in Sections 1.1.1 and 1.1.2, energy is generated in the core of the Sun, with temperatures of millions of degrees. This energy then travels outwards through the material of the Sun via radiation and (then) convection. At the photosphere, visible light is emitted from material at a temperature of about 6000 K. Then mysteriously (and counter intuitively), the temperature starts to rise again. The temperature increase is slow at first in the chromosphere (which has a temperature of tens of thousands of degrees), then there is a massive increase through the transition region until we reach the corona, which has a value of several million degrees. This is the crux of the mystery; how can we go from a cool photosphere to a hot corona?

The corona is dominated by the magnetic field and it is generally believed that the energy to heat the corona must somehow come from this (stored) magnetic energy. There are, however, many rival theories ranging from reconnection models involving a change in the magnetic connectivity (with heat coming from *nanoflares*), and wave heating models involving *phase mixing* and *resonant absorption*.

Wave heating models rely on the generation of small length scale wave motions in the corona. Recently, SOHO and TRACE observations (two satellites taking measurements of the Sun) have shown clear evidence of magnetohydrodynamic waves in the solar atmosphere. It is still unclear whether there is sufficient energy in these waves to heat the whole corona, but their dissipation will certainly contribute to the overall energy budget. It is this fundamental process – the propagation of disturbances in a non-uniform plasma – that this Thesis will investigate.

2.1 Aims of this Thesis

This Thesis looks at how MHD waves behave when they travel into magnetic structures. There are theoretical models of wave motions that should occur in the Sun's corona (see Section 1.5.4) and recent observations have shown that heating in the corona occurs in specific parts of the magnetic topology (Longcope & Cowley 1996; Priest *et al.* 2002; Priest, Longcope & Heyvaerts 2005). Thus there is a need for a detailed theory on how plasma waves behave in complicated magnetic configurations. This Thesis aims to provide work that will contribute to such a theory. This work may also have applications in coronal seismology (Roberts, Edwin & Benz, 1983; 1984; Nakariakov *et al.*, 1999). MHD wave – topology interactions are also a fundamental plasma process that is occurring all the time and hence worth investigating for its own merit.

2.1.1 Thesis outline

This Thesis begins an investigation into the relationship of MHD waves and magnetic topology. Throughout the next six chapters, we investigate the properties and behaviour of MHD waves in the neighbourhood of two-dimensional null points in a variety of magnetic configurations and under various physical assumptions. This work will add to the understanding of the propagation of plasma disturbances in a non-uniform media. The rest of this chapter will introduce several tools (such as numerical techniques and the WKB approximation) that will be used in the course of this Thesis.

Chapter 3 will investigate the behaviour of the fast magnetoacoustic wave in the neighbourhood of a single 2D null point, in a $\beta = 0$ plasma. Both numerical and analytical techniques are used in order to gain a better understanding of this process. The build-up of current in this magnetic configuration will also be studied.

Chapter 4 will investigate the behaviour of the Alfvén wave in the neighbourhood of a single 2D null point. This chapter complements the work of Chapter 3. Again, both numerical and analytical techniques are used and we look at the formation of current.

Chapter 5 again looks at the behaviours of the fast magnetoacoustic wave and Alfvén wave, but now in a more complicated geometry with two null points. This chapter aims to see if the behaviour observed in Chapters 3 and 4 still persist in the different magnetic configuration.

Chapter 6 looks at the behaviour of the fast and Alfvén waves in a more realistic magnetic geometry. Like Chapter 5, Chapter 6 compares and contrasts itself to Chapters 3 and 4.

Chapter 7 considers the behaviour of both fast and slow waves in a $\beta \neq 0$ plasma. We look at the propagation and coupling of the two modes in a single 2D null point magnetic configuration. We

do not look into the nature of the Alfvén wave in such a $\beta \neq 0$ plasma as it is unaffected by the inclusion of pressure effects.

Chapter 8 again looks at the behaviour of the Alfvén wave near a 2D null point, but now with a non-uniform density profile. Numerical and analytical techniques are used to see if phase mixing now plays an important role.

Chapter 9 provides a summary of the work done and key results of this Thesis. Appendix A provides the derivation of equation (3.4). Appendix B details the contents of the CD-ROM that is attached to the back cover of this Thesis. The CD-ROM contains movies of some of the figures shown in the Thesis.

2.2 Linearised Equations

2.2.1 Special Coordinate System

The investigations carried out in this Thesis are done so in a two-dimensional geometry in the x and z plane. Thus, equilibrium quantities like magnetic field and density are of the form $\mathbf{B}_0 = \mathbf{B}_0(x, z)$, $\rho_0 = \rho_0(x, z)$. To aid in MHD mode detection and interpretation, we work in a special coordinate system where we consider the velocity to have components parallel and perpendicular to the equilibrium magnetic field. We saw in Section 1.5.6 that the fast and slow waves have very different behaviours in the directions perpendicular and parallel to the magnetic field.

In the case of a $\beta = 0$ plasma, $c_s^2 = 0$ and so the slow wave disappears. Also, equations (1.29) decouple under $c_s^2 = 0$ to give $\frac{\partial^2}{\partial t^2} v_{\parallel} = 0$, and since we do not have flows in our equilibrium we take $v_{\parallel} = 0$. Thus, the fast wave only has a perpendicular velocity component for a $\beta = 0$ plasma.

We will be looking at $\beta = 0$ scenarios in Chapters 3 – 6 and hence choosing a coordinate system that splits the velocity field up into a perpendicular and a parallel component makes good sense (to aid identification and interpretation). Such a coordinate system for \mathbf{v}_1 is given by:

$$\mathbf{v}_1 = \mathcal{V}_{\parallel} \left(\frac{\mathbf{B}_0}{\sqrt{\mathbf{B}_0 \cdot \mathbf{B}_0}} \right) - \mathcal{V}_{\perp} \left(\frac{\nabla A_0}{\sqrt{\mathbf{B}_0 \cdot \mathbf{B}_0}} \right) + v_y \hat{\mathbf{y}} \quad (2.1)$$

where $\mathbf{A} = (0, A_0, 0)$ is the vector potential ($\mathbf{B}_0 = \nabla \times \mathbf{A}$) and A_0 is its y -component. The terms in brackets are unit vectors (as is $\hat{\mathbf{y}}$). This splits the velocity into parallel and perpendicular components. This will make our MHD mode detection and interpretation easier later (e.g. since the slow wave is primarily field aligned, etc.). To aid the numerical calculation, the primary variables we will work with are $v_{\perp} = \sqrt{\mathbf{B}_0 \cdot \mathbf{B}_0} \mathcal{V}_{\perp}$ and $v_{\parallel} = \sqrt{\mathbf{B}_0 \cdot \mathbf{B}_0} \mathcal{V}_{\parallel}$.

Using this special choice of coordinates, we can rewrite equations (1.18), (1.19) and (1.21) as:

$$\rho_0 \frac{\partial v_{\perp}}{\partial t} = -(\mathbf{B}_0 \cdot \mathbf{B}_0) \left(\frac{1}{\mu} \nabla \times \mathbf{b} \right) + \nabla A_0 \cdot \nabla p_1, \quad (2.2)$$

$$\rho_0 \frac{\partial v_{\parallel}}{\partial t} = -(\mathbf{B}_0 \cdot \nabla) p_1, \quad (2.3)$$

$$\rho_0 \frac{\partial v_y}{\partial t} = \frac{1}{\mu} (\mathbf{B}_0 \cdot \nabla) b_y, \quad (2.4)$$

$$\frac{\partial b_x}{\partial t} = [(\nabla v_{\perp} \times \hat{y}) \cdot \hat{x}] + \eta \nabla^2 b_x, \quad (2.5)$$

$$\frac{\partial b_y}{\partial t} = (\mathbf{B}_0 \cdot \nabla) v_y + \eta \nabla^2 b_y, \quad (2.6)$$

$$\frac{\partial b_z}{\partial t} = [(\nabla v_{\perp} \times \hat{y}) \cdot \hat{z}] + \eta \nabla^2 b_z, \quad (2.7)$$

$$\frac{\partial p_1}{\partial t} = -\gamma p_0 \left[\nabla \cdot \left(\frac{\mathbf{B}_0 v_{\parallel}}{\mathbf{B}_0 \cdot \mathbf{B}_0} \right) - \nabla \cdot \left(\frac{v_{\perp} \nabla A}{\mathbf{B}_0 \cdot \mathbf{B}_0} \right) \right], \quad (2.8)$$

where we have used $\mathbf{B}_0 = \nabla \times \mathbf{A} = \nabla A_0 \times \hat{y}$ and $\frac{\partial}{\partial y} = 0$. We do not consider equation (1.20) as once ρ_0 and \mathbf{v}_1 are known, ρ_1 is known.

2.2.2 Dimensionless quantities

We now consider a change of scale to simplify our equations, where we let * denote a dimensionless quantity. This section will assume the quantities are in cartesian form, but the method is equally valid for all coordinate systems (including polar coordinate systems which will be used later).

We now consider a change of scale to non-dimensionalise; let $\mathbf{v}_1 = \bar{v} \mathbf{v}_1^*$, $v_{\perp} = B_0 \bar{v} v_{\perp}^*$, $v_{\parallel} = B_0 \bar{v} v_{\parallel}^*$, $\mathbf{B}_0 = B_0 \mathbf{B}_0^*$, $\mathbf{b} = B_0 \mathbf{b}^*$, $x = L x^*$, $z = L z^*$, $p_1 = p_0 p_1^*$, $\nabla = \frac{1}{L} \nabla^*$, $t = \bar{t} t^*$, $A_0 = B_0 L A_0^*$, $\rho_0 = \bar{\rho} \rho_0^*$ and $\eta = \eta_0$, where we let * denote a dimensionless quantity and \bar{v} , B_0 , L , p_0 , \bar{t} , $\bar{\rho}$, μ and η_0 are constants with the dimensions of the variable they are scaling. Typical values of B_0 in the corona range from $\sim 10 - 50$ Gauss for quiet Sun regions, $\sim 100 - 300$ Gauss for active regions and $\sim 2000 - 3000$ Gauss for sunspots, and typical length scales in the corona are $L \sim 50 - 200$ Mm (Priest 1982; Aschwanden 2004).

We then set $B_0 / \sqrt{\mu \bar{\rho}} = \bar{v}$ and $\bar{v} = L / \bar{t}$ (this sets \bar{v} as a sort of constant background Alfvén speed). We also set $\frac{\eta_0 \bar{t}}{L^2} = R_m^{-1}$, where R_m is the magnetic Reynolds number (Section 1.2.2), and set $\beta_0 = \frac{2\mu p_0}{B_0^2}$, where β_0 is related to the plasma beta (see Section 7.3). Thus, we can easily revert back to our dimensionally correct quantities. Once we impose B_0 and ρ_0 , we will know v_A and so \bar{v} , and then when we impose L we know the correct timescale for our system. For an Alfvén speed of, say, 1000 km s^{-1} and length scale of 10^7 m , our time would then be measured in units of 10 seconds.

This process non-dimensionalises equations (2.2) – (2.8), and under these scalings, $t^* = 1$ (for example) refers to $t = \bar{t} = L/\bar{v}$; i.e. the time taken to travel a distance L at the background Alfvén speed. Thus, the non-dimensionalised equations are:

$$\begin{aligned}
\rho_0^* \frac{\partial}{\partial t^*} v_{\perp}^* &= -(\mathbf{B}_0^* \cdot \mathbf{B}_0^*) (\nabla^* \times \mathbf{b}^*) + \frac{\beta_0}{2} \nabla^* A_0^* \cdot \nabla^* p_1^*, \\
\rho_0^* \frac{\partial}{\partial t^*} v_{\parallel}^* &= -\frac{\beta_0}{2} (\mathbf{B}_0^* \cdot \nabla^*) p_1^*, \\
\rho_0^* \frac{\partial v_y^*}{\partial t^*} &= (\mathbf{B}_0^* \cdot \nabla^*) b_y^*, \\
\frac{\partial b_x^*}{\partial t^*} &= [(\nabla^* v_{\perp}^* \times \hat{\mathbf{y}}) \cdot \hat{\mathbf{x}}] + \frac{1}{R_m} \nabla^{2*} b_x^*, \\
\frac{\partial b_y^*}{\partial t^*} &= (\mathbf{B}_0^* \cdot \nabla^*) v_y^* + \frac{1}{R_m} \nabla^{2*} b_y^*, \\
\frac{\partial b_z^*}{\partial t^*} &= [(\nabla^* v_{\perp}^* \times \hat{\mathbf{y}}) \cdot \hat{\mathbf{z}}] + \frac{1}{R_m} \nabla^{2*} b_z^*, \\
\frac{\partial p_1^*}{\partial t^*} &= -\gamma \left[\nabla^* \cdot \left(\frac{\mathbf{B}_0^* v_{\parallel}^*}{\mathbf{B}_0^* \cdot \mathbf{B}_0^*} \right) - \nabla^* \cdot \left(\frac{v_{\perp}^* \nabla^* A_0^*}{\mathbf{B}_0^* \cdot \mathbf{B}_0^*} \right) \right], \tag{2.9}
\end{aligned}$$

These are the linearised, non-dimensionalised, perturbation equations in our choice of coordinate system. This Thesis will utilise these equations to investigate the behaviour of MHD waves in a magnetised, inhomogeneous plasma.

2.2.3 Simplification under $\beta = 0$

If we assume $\beta = 0$ for our system, then equations (2.9) simplify greatly. Under the $\beta = 0$ assumption, the plasma pressure plays no part in the dynamics of the system, and so the linearised equation of mass continuity (equation 1.20) has no influence on the momentum equation (equation 1.19), and so in effect the plasma is arbitrarily compressible (Craig & Watson 1992). The slow wave also vanishes (Section 1.5.6) and so we do not need to work out the equation for v_{\parallel} either. Thus, equations (2.9) reduce to:

$$\rho_0^* \frac{\partial v_{\perp}^*}{\partial t^*} = -(\mathbf{B}_0^* \cdot \mathbf{B}_0^*) (\nabla^* \times \mathbf{b}^*), \tag{2.10}$$

$$\frac{\partial b_x^*}{\partial t^*} = -\frac{\partial}{\partial z^*} v_{\perp}^* + \frac{1}{R_m} \nabla^{2*} b_x^*, \quad \frac{\partial b_z^*}{\partial t^*} = \frac{\partial}{\partial x^*} v_{\perp}^* + \frac{1}{R_m} \nabla^{2*} b_z^*. \tag{2.11}$$

$$\rho_0^* \frac{\partial v_y^*}{\partial t^*} = (\mathbf{B}_0^* \cdot \nabla^*) b_y^*, \tag{2.12}$$

$$\frac{\partial b_y^*}{\partial t^*} = (\mathbf{B}_0^* \cdot \nabla^*) v_y^* + \frac{1}{R_m} \nabla^{2*} b_y^*. \tag{2.13}$$

Note also that under a 2D geometry, equations (2.10) and (2.11) decouple from equations (2.12) and (2.13).

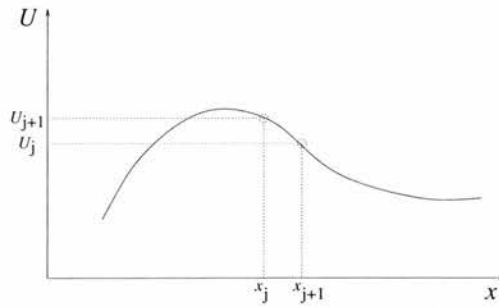


Figure 2.1: Approximation of the gradient

2.3 Numerical Methods

Not all equations can be solved analytically. However, we can use computers to obtain approximate results to equations. We can use the computer to approximate functions and equations on a numerical grid, where the accuracy of our approximation is directly related to the resolution of our mesh. Hence, using computers allows us to solve problems that cannot be solved analytically (or at least cannot be readily solved analytically) and so allow us to investigate more complicated, elaborate models with more realistic physical parameters. Numerical models, coupled with a deeper understanding of non-linear processes, help us to explain the features that are being seen.

In order to illustrate the basic ideas, consider a function $u(x)$ that is only known at discrete grid points. Let the value of u at point x_j be u_j . The neighbouring point on the grid is $u_{j+1} = u(x_{j+1})$ and so on. Thus, we can build up a graph of the behaviour of the function using these discrete points. When the resolution is good enough, i.e. the spacing between x_j and x_{j+1} is small enough, the behaviour will appear to be a smooth function. To the mathematician, the discrete point representation's real worth is in approximating derivatives. From the definition of a derivative, we know it is the gradient of the tangent to the function $u(x)$. We can approximate the derivative at the point x_j by:

$$\frac{du}{dx_j} \approx \frac{u_{j+1} - u_j}{x_{j+1} - x_j}. \quad (2.14)$$

This is the gradient between the point (x_j, u_j) and (x_{j+1}, u_{j+1}) . This can be seen in Figure 2.1. We consider the numerical grid to be uniform and we take:

$$x_{j+1} = x_j + \delta x.$$

There are several ways of working out the gradient using these discrete points. The form used in equation (2.14) is called a *forward difference* since it uses the point in front of x_j to work out the gradient at x_j . Similarly, a *backwards difference* would use the point behind x_j , i.e. x_{j-1} to

work out the same gradient at x_j . We can also use adjacent points, x_{j+1} and x_{j-1} to work out the gradient at the centre point, x_j . This is known as a *central difference*. We can form more complicated differences by using more adjacent points. All our approximations have truncation errors, based on how small the width of the grid is. Forward and backwards differences have a truncation error, worked out by comparing the Taylor expansion of the original equation to our discrete approximation, that is proportional to δx . We call this *first order accurate*. The central difference has a truncation error that is proportional to δx^2 , due to cancellations in the Taylor expansion, and we call this *second order accurate*. You can see how accuracy improves as δx , i.e. the grid spacing, becomes smaller and smaller. Of course, the accuracy of the higher order approximations improves at a faster rate.

2.3.1 Numerical Schemes

There are several numerical schemes that can be employed to solve mathematical equations (most often differential equations). Some of these are mentioned below, with an illustrative example involving the advection equation:

$$\frac{\partial u}{\partial t} + v \frac{\partial u}{\partial x} = 0 \quad , \quad (2.15)$$

for $u = u(x, t)$ and v is constant.

Lax Method

The Lax Method uses a forward time and centred space method, but replaces one of the terms with the average value of the neighbouring points. Using equation (2.15) as an example, this method takes the form:

$$u_j^{n+1} = \frac{1}{2} (u_{j+1}^n + u_{j-1}^n) - \frac{v\delta t}{2\delta x} (u_{j+1}^n - u_{j-1}^n) \quad .$$

The Lax Method is an explicit one-step method that is second order accurate in space and first order accurate in time.

Leapfrog Method

The Leapfrog Method is similar to the Lax method, but involves discretising the time step using the midpoint method.

$$u_j^{n+1} = u_j^{n-1} - \frac{v\delta t}{2\delta x} (u_{j+1}^n - u_{j-1}^n)$$

This is an explicit one-step method that is second order accurate in both space and time. There is no numerical diffusion, but there is a possibility the even and odd timesteps can become uncoupled leading to an alternating instability. It also requires us to know or calculate u_j^0 and u_j^1 to start the scheme.

Lax-Wendroff Method

The Lax-Wendroff scheme is obtained by Taylor expanding the function about the time level $n + 1$ in terms of the time level n and replacing the temporal derivatives with spatial derivatives obtained by differentiating the original PDE. For the advection equation, (2.15), this method takes the form:

$$u_j^{n+1} = u_j^n - \frac{v\delta t}{2\delta x} (u_{j+1}^n - u_{j-1}^n) + \frac{v^2\delta t^2}{2\delta x^2} (u_{j-1}^n - 2u_j^n + u_{j+1}^n) .$$

This method is an explicit one-step method that is second order accurate in space and in time. The example above has a three point stencil, but can be easily extended to a five-point stencil (utilising u_{j-2}^n and u_{j+2}^n for example). In practice when solving wave equations, we introduce a second variable to convert second order differential equations into two (coupled) first order equations. Each of these can then be discretised according to the method above.

Beam-Warming Method

The Beam-Warming Method uses the same format as the Lax-Wendroff Method, but uses one-sided approximations to the spatial derivatives:

$$u_j^{n+1} = u_j^n - \frac{v\delta t}{2\delta x} (3u_j^n - 4u_{j-1}^n + u_{j-2}^n) + \frac{v^2\delta t^2}{2\delta x^2} (u_j^n - 2u_{j-1}^n + u_{j-2}^n) .$$

MacCormack Method

The MacCormack method is a variation of the Lax-Wendroff scheme that can be expressed as a Predictor-Corrector scheme. A Predictor-Corrector scheme is a two-step method that involves simultaneously solving coupled equations that describe that PDE we wish to solve in real space and in predictor space. The scheme uses half steps and estimates the values at the half timestep and half spatial step in predictor space. This is called the predictor step. These values are then used to compute the values at the whole time-step and whole spatial-step in real space. For our advection equation example, we use a forward difference for the spatial step in the predictor stage and a backwards difference for the spatial step in the corrector stage (although one can swap these).

The predictor step is:

$$u_{j+\frac{1}{2}}^{n+\frac{1}{2}} = u_j^n - \frac{v\delta t}{\delta x} (u_{j+1}^n - u_j^n) .$$

The corrector step is:

$$u_j^{n+1} = \frac{1}{2} \left(u_{j+\frac{1}{2}}^{n+\frac{1}{2}} + u_j^n \right) - \frac{v\delta t}{2\delta x} \left(u_{j+\frac{1}{2}}^{n+\frac{1}{2}} - u_{j-\frac{1}{2}}^{n+\frac{1}{2}} \right) .$$

There exists an intimate relationship between the MacCormack and Lax-Wendroff methods; the MacCormack scheme reduces to the Lax-Wendroff after rearrangement and so the MacCormack method is used when the second temporal derivatives in the Taylor expansion are too time consuming to work out.

We will use the two-step Lax-Wendroff Method several times throughout this Thesis. Although the method suffers from strong numerical diffusion, it is simple to implement and adequate for the simulations of linear MHD waves in this Thesis.

Runge-Kutta Method

The Runge-Kutta method propagates a solution over an interval by combining derivative information from several trial intervals to match a Taylor series expansion up to some high order. The use of mid-points also cancels out the lower-order error terms, so the method is $\mathcal{O}(h^{n+1})$ accurate if a n^{th} order scheme is used. The most widely used version of the method is the fourth-order Runge-Kutta method:

$$\begin{aligned} k_1 &= hf'(x_n, y_n), & k_2 &= hf'\left(x_n + \frac{h}{2}, y_n + \frac{k_1}{2}\right), \\ k_3 &= hf'\left(x_n + \frac{h}{2}, y_n + \frac{k_2}{2}\right), & k_4 &= hf'(x_n + h, y_n + k_3), \\ y_{n+1} &= y_n + \frac{k_1}{6} + \frac{k_2}{3} + \frac{k_3}{3} + \frac{k_4}{6} + \mathcal{O}(h^5) \end{aligned}$$

This method is reasonably simple and robust. We will also be using this numerical scheme several times throughout this Thesis.

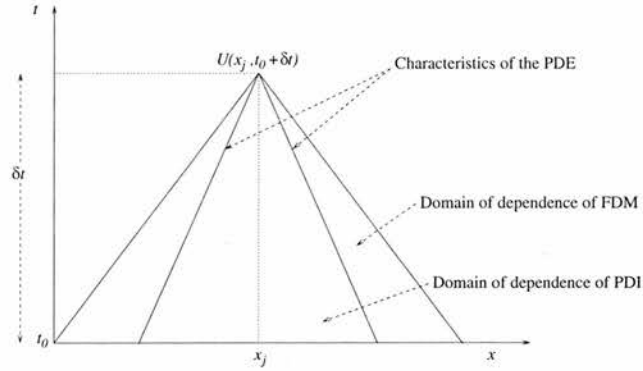


Figure 2.2: The CFL condition.

2.3.2 CFL Condition

The CFL condition states that the domain of dependence of the numerical scheme (or finite difference method; FDM) should include the domain of dependence of the PDE, as shown in Figure (2.2).

The domain of dependence of a numerical scheme is the set of all points for which some initial data could possibly have affected the solution at some later fixed point (say $U(x, t + \delta t)$). The domain of dependence of the PDE is the set of all points bounded by the characteristics of the PDE. If the information in the system propagates at a maximum speed v , then the CFL condition is

$$c = \left| \frac{v \delta t}{\delta x} \right| \leq 1.$$

This states that over a single timestep, the characteristic we trace back must lie within one grid point of x_j .

A numerical method that violates the CFL condition uses data from outside the cone of influence to produce a solution. Hence this will not be the true solution and may result in an instability (i.e. a solution tending to infinity). The condition is named after Courant, Friedrichs and Levy who wrote a fundamental paper that was essentially the first paper on stability and convergence of finite difference methods for PDEs (Courant, Friedrichs & Levy 1928).

2.4 WKB approximation

This section describes one of the most important tools we will be implementing in this Thesis; the **WKB approximation**.

The WKB approximation is an asymptotic approximation technique which can be used when a system contains a large parameter. It is very useful for solving differential equations. It is named after *Wentzel, Kramers and Brillouin*, who pioneered its use in quantum mechanics (around 1927). Section 2.4.1 is based on a lecture course by Hood (2003). Section 2.4.3 is based on the work of Bender & Orszag (1978) and Evans, Blackledge & Yardley (1999). Various parts of the theory in Section 2.4.6 can be found in Murray (1927) and Sneddon (1957),

2.4.1 Introduction to the WKB theory

Consider the equation

$$\frac{d^2y}{dx^2} + \lambda^2 f(x)y = 0, \quad \text{where } \lambda \gg 1 \quad \text{and } y = y(x). \quad (2.16)$$

This solution is oscillatory in x if $f(x) > 0$ and exponential if $f(x) < 0$. If $f(x)$ is a constant, the general solution is

$$y(x) = Ae^{i(\lambda\sqrt{f})x} + Be^{-i(\lambda\sqrt{f})x} \quad \text{where } A, B \text{ are constants}.$$

This suggests that in order to capture the correct behaviour as $\lambda \rightarrow \infty$, we should include this rapid exponential oscillatory behaviour by changing the dependent variable from $y(x)$ to $Y(x, \lambda)$ where $y = e^{i\lambda Y}$. Substituting this form into (2.16) gives:

$$\begin{aligned} i\lambda \left(\frac{d^2Y}{dx^2} \right) e^{i\lambda Y} - \lambda^2 \left(\frac{dY}{dx} \right)^2 e^{i\lambda Y} + \lambda^2 f(x) e^{i\lambda Y} &= 0, \\ \Rightarrow \left[- \left(\frac{dY}{dx} \right)^2 + f(x) \right] + \frac{i}{\lambda} \left[\frac{d^2Y}{dx^2} \right] &= 0. \end{aligned}$$

This suggests we can expand Y in a power series of powers of λ^{-1} that is valid as $\lambda^{-1} \rightarrow 0$. The approximation comes from solving iteratively in powers of λ^{-1} .

Hence, we set $Y = Y_0 + \frac{1}{\lambda}Y_1 + \dots$. Collecting the same powers of λ^{-1} together gives a series of differential equations. Thus we have

$$y = e^{i\lambda Y} = e^{i[\lambda Y_0 + Y_1 + \mathcal{O}(\frac{1}{\lambda})]} = e^{i\lambda Y_0} e^{iY_1} + \mathcal{O}\left(\frac{1}{\lambda}\right);,$$

where we have used the Taylor expansion $e^{\mathcal{O}(\frac{1}{\lambda})} = 1 + \mathcal{O}(\frac{1}{\lambda})$. These solutions are called the *WKB solutions*. It can be shown that equation (2.16) can be represented as:

$$y = \frac{c_1}{\sqrt[4]{f(x)}} \exp \left[i\lambda \int \sqrt{f(x)} dx \right] + \frac{c_2}{\sqrt[4]{f(x)}} \exp \left[-i\lambda \int \sqrt{f(x)} dx \right] + \mathcal{O} \left(\frac{1}{\lambda} \right)$$

for $f(x) > 0$, and

$$y = \frac{c_3}{\sqrt[4]{-f(x)}} \exp \left[\lambda \int \sqrt{-f(x)} dx \right] + \frac{c_4}{\sqrt[4]{-f(x)}} \exp \left[-\lambda \int \sqrt{-f(x)} dx \right] + \mathcal{O} \left(\frac{1}{\lambda} \right)$$

for $f(x) < 0$. Here, c_1 , c_2 , c_3 and c_4 are constants determined by the boundary conditions. Note that the WKB solutions will fail near a zero of $f(x)$; such a point is called a *turning point* or *transition point* (there is a change in the nature of the solution at such a point).

2.4.2 Application to MHD waves

In this Thesis, the WKB approximation is applied to second-order, linear ordinary differential equations¹. The above explanation was concerned with the variable $y(x)$. In this Thesis, one of the primary variables is v_{\perp} and we will be looking for WKB solutions of the form $v_{\perp} = e^{i\phi(x,z)} e^{-i\omega t}$, where ω and ϕ are considered to be our large parameters (we could also consider $\phi = \omega\phi_0$ if we only wanted one large parameter). Performing this substitution and then making the WKB approximation $\omega \approx \phi \gg 1$ will lead to a first-order, non-linear PDE of the (general) form $\mathcal{F} \left(\phi, x, z, \frac{\partial\phi}{\partial x}, \frac{\partial\phi}{\partial z} \right) = 0$. This can be solved using the method of characteristics.

The WKB method can be used when a wave propagates through a background medium which varies on some spatial scale which is much longer than the wavelength of the wave. Thus, the method is appropriate for use in our investigations.

2.4.3 Characteristics

The **method of characteristics** is a way of solving partial differential equations (PDEs) by providing a link between a non-linear PDE and a system of ordinary differential equation (ODEs). For a PDE of the form $\mathcal{F} \left(\phi, x, z, \frac{\partial\phi}{\partial x}, \frac{\partial\phi}{\partial z} \right) = 0$, consider the phase space comprising of the independents (x, z) , the dependent, $\phi(x, z)$ and the partial derivatives of the dependent with respect to the independents $(\frac{\partial\phi}{\partial x}, \frac{\partial\phi}{\partial z})$. A **characteristic** is a line in this phase space along which the PDE degenerates into an ODE. If s is a parameter along the characteristic, the quantity $\frac{d\mathcal{F}}{ds}$ is zero along such a line. The **characteristic curves** are defined as the curves in the phase space along which the highest partial derivatives are not uniquely defined.

¹If we were considering an equation with a first-order derivative, we could always perform a substitution to convert the equation to a second-order equation.

2.4.4 Derivation of Charpit's equations

Consider a general non-linear, first-order PDE of the form:

$$\mathcal{F}(u, x, z, p, q) = 0 \quad (2.17)$$

where $u = u(x, z)$ is the dependent variable, $p = \frac{\partial u}{\partial x}$ and $q = \frac{\partial u}{\partial z}$. Let us assume our variables depend upon an independent parameter s , such that

$$\frac{dx}{ds} = \mathcal{F}_p \quad \text{and} \quad \frac{dz}{ds} = \mathcal{F}_q \quad (2.18)$$

There exists the partial derivative relation:

$$\frac{du}{ds} = \frac{\partial u}{\partial x} \frac{dx}{ds} + \frac{\partial u}{\partial z} \frac{dz}{ds} = p \frac{dx}{ds} + q \frac{dz}{ds} \quad (2.19)$$

Substituting equation (2.18) into this relation gives:

$$\frac{du}{ds} = p\mathcal{F}_p + q\mathcal{F}_q \quad ,$$

which with (2.18) yields the characteristic equations:

$$\frac{dx}{\mathcal{F}_p} = \frac{dz}{\mathcal{F}_q} = \frac{du}{p\mathcal{F}_p + q\mathcal{F}_q} = ds \quad (2.20)$$

In addition,

$$\frac{dp}{ds} = \frac{\partial p}{\partial x} \frac{dx}{ds} + \frac{\partial p}{\partial z} \frac{dz}{ds} = \frac{\partial p}{\partial x} \mathcal{F}_p + \frac{\partial p}{\partial z} \mathcal{F}_q = \frac{\partial p}{\partial x} \mathcal{F}_p + \frac{\partial q}{\partial x} \mathcal{F}_q \quad , \quad (2.21)$$

since $\frac{\partial p}{\partial z} = \frac{\partial^2 u}{\partial x \partial z} = \frac{\partial q}{\partial x}$. Differentiating $\mathcal{F}(u, x, z, \frac{\partial u}{\partial x}, \frac{\partial u}{\partial z}) = 0$ with respect to x gives:

$$\frac{\partial \mathcal{F}}{\partial x} + \frac{\partial \mathcal{F}}{\partial u} p + \frac{\partial \mathcal{F}}{\partial p} \frac{\partial p}{\partial x} + \frac{\partial \mathcal{F}}{\partial q} \frac{\partial q}{\partial x} = 0 \quad .$$

Substituting into equation (2.21) gives:

$$\frac{dp}{ds} = - \frac{\partial \mathcal{F}}{\partial x} - p \frac{\partial \mathcal{F}}{\partial u} \quad (2.22)$$

In a similar fashion:

$$\frac{dq}{ds} = - \frac{\partial \mathcal{F}}{\partial z} - q \frac{\partial \mathcal{F}}{\partial u} \quad (2.23)$$

2.4.5 Charpit's Equations

Thus, equations (2.20), (2.22) and (2.23) give **Charpit's Equations** for the characteristics, where s is a variable measured along a given characteristic. The five equations are:

$$\frac{du}{ds} = p\mathcal{F}_p + q\mathcal{F}_q \quad (2.24)$$

$$\frac{dp}{ds} = -\frac{\partial\mathcal{F}}{\partial x} - p\frac{\partial\mathcal{F}}{\partial u} \quad (2.25)$$

$$\frac{dq}{ds} = -\frac{\partial\mathcal{F}}{\partial z} - q\frac{\partial\mathcal{F}}{\partial u} \quad (2.26)$$

$$\frac{dx}{ds} = \frac{\partial\mathcal{F}}{\partial p} \quad (2.27)$$

$$\frac{dz}{ds} = \frac{\partial\mathcal{F}}{\partial q} \quad (2.28)$$

These five ordinary differential equations are subject to the initial conditions $u = u_0(s)$, $x = x_0(s)$, $z = z_0(s)$, $p = p_0(s)$ and $q = q_0(s)$ at $s = 0$.

These generalised characteristic equations were first used by Paul Charpit in 1784. It seems that Lagrange also found these equations in 1779, but the method is attributed to Charpit who perfected it.

2.4.6 Alternative derivation

Since Charpit's relations are of such fundamental importance to this Thesis, it is important that they are fully understood. To this end, here is an alternative derivation of the relations.

Charpit's equations provide a method of solving the PDE $\mathcal{F}(u, x, z, \frac{\partial u}{\partial x}, \frac{\partial u}{\partial z}) = 0$. The fundamental idea is the introduction of a second PDE; $\mathcal{G}(u, x, z, \frac{\partial u}{\partial x}, \frac{\partial u}{\partial z}) = 0$, where \mathcal{G} gives a second (different) relation between u , x , z , p and q . Since u depends upon x and z , it follows that:

$$\frac{du}{ds} = p\frac{dx}{ds} + q\frac{dz}{ds}. \quad (2.29)$$

Thus, we can eliminate p and q from (2.29) using \mathcal{F} and \mathcal{G} . This will give a solvable ODE for u , x and z .

A method of finding the relation \mathcal{G} must now be devised. Firstly, we assume we know the form for \mathcal{G} . On differentiating \mathcal{F} and \mathcal{G} with respect to x and z , the following equations appear:

$$\frac{\partial \mathcal{F}}{\partial x} + \frac{\partial \mathcal{F}}{\partial u} p + \frac{\partial \mathcal{F}}{\partial p} \frac{\partial p}{\partial x} + \frac{\partial \mathcal{F}}{\partial q} \frac{\partial q}{\partial x} = 0, \quad (2.30)$$

$$\frac{\partial \mathcal{G}}{\partial x} + \frac{\partial \mathcal{G}}{\partial u} p + \frac{\partial \mathcal{G}}{\partial p} \frac{\partial p}{\partial x} + \frac{\partial \mathcal{G}}{\partial q} \frac{\partial q}{\partial x} = 0, \quad (2.31)$$

$$\frac{\partial \mathcal{F}}{\partial z} + \frac{\partial \mathcal{F}}{\partial u} q + \frac{\partial \mathcal{F}}{\partial p} \frac{\partial p}{\partial z} + \frac{\partial \mathcal{F}}{\partial q} \frac{\partial q}{\partial z} = 0, \quad (2.32)$$

$$\frac{\partial \mathcal{G}}{\partial z} + \frac{\partial \mathcal{G}}{\partial u} q + \frac{\partial \mathcal{G}}{\partial p} \frac{\partial p}{\partial z} + \frac{\partial \mathcal{G}}{\partial q} \frac{\partial q}{\partial z} = 0. \quad (2.33)$$

Eliminating $\frac{\partial p}{\partial x}$ between (2.30) and (2.31) and eliminating $\frac{\partial q}{\partial z}$ between (2.32) and (2.33) gives:

$$\left(\frac{\partial \mathcal{F}}{\partial x} \frac{\partial \mathcal{G}}{\partial p} - \frac{\partial \mathcal{F}}{\partial p} \frac{\partial \mathcal{G}}{\partial x} \right) + p \left(\frac{\partial \mathcal{F}}{\partial u} \frac{\partial \mathcal{G}}{\partial p} - \frac{\partial \mathcal{F}}{\partial p} \frac{\partial \mathcal{G}}{\partial u} \right) + \frac{\partial q}{\partial x} \left(\frac{\partial \mathcal{F}}{\partial q} \frac{\partial \mathcal{G}}{\partial p} - \frac{\partial \mathcal{F}}{\partial p} \frac{\partial \mathcal{G}}{\partial q} \right) = 0 \quad (2.34)$$

$$\left(\frac{\partial \mathcal{F}}{\partial z} \frac{\partial \mathcal{G}}{\partial q} - \frac{\partial \mathcal{F}}{\partial q} \frac{\partial \mathcal{G}}{\partial z} \right) + q \left(\frac{\partial \mathcal{F}}{\partial u} \frac{\partial \mathcal{G}}{\partial q} - \frac{\partial \mathcal{F}}{\partial q} \frac{\partial \mathcal{G}}{\partial u} \right) + \frac{\partial p}{\partial z} \left(\frac{\partial \mathcal{F}}{\partial p} \frac{\partial \mathcal{G}}{\partial q} - \frac{\partial \mathcal{F}}{\partial q} \frac{\partial \mathcal{G}}{\partial p} \right) = 0 \quad (2.35)$$

Adding (2.34) and (2.35) together, and realising $\frac{\partial q}{\partial x} = \frac{\partial^2 u}{\partial x \partial z} = \frac{\partial p}{\partial z}$ (so the last terms cancel), gives:

$$\begin{aligned} \left(\frac{\partial \mathcal{F}}{\partial x} + p \frac{\partial \mathcal{F}}{\partial u} \right) \frac{\partial \mathcal{G}}{\partial p} + \left(\frac{\partial \mathcal{F}}{\partial z} + q \frac{\partial \mathcal{F}}{\partial u} \right) \frac{\partial \mathcal{G}}{\partial q} + \left(-p \frac{\partial \mathcal{F}}{\partial p} - q \frac{\partial \mathcal{F}}{\partial q} \right) \frac{\partial \mathcal{G}}{\partial u} \\ + \left(-\frac{\partial \mathcal{F}}{\partial p} \right) \frac{\partial \mathcal{G}}{\partial x} + \left(-\frac{\partial \mathcal{F}}{\partial q} \right) \frac{\partial \mathcal{G}}{\partial z} = 0. \end{aligned} \quad (2.36)$$

This is a linear equation of the first-order which \mathcal{G} must satisfy. Consider the derivative of \mathcal{G} with respect to parameter s :

$$\frac{d\mathcal{G}}{ds} = \frac{dp}{ds} \frac{\partial \mathcal{G}}{\partial p} + \frac{dq}{ds} \frac{\partial \mathcal{G}}{\partial q} + \frac{du}{ds} \frac{\partial \mathcal{G}}{\partial u} + \frac{dx}{ds} \frac{\partial \mathcal{G}}{\partial x} + \frac{dz}{ds} \frac{\partial \mathcal{G}}{\partial z} = 0. \quad (2.37)$$

Comparing like terms in (2.36) and (2.37) and multiplying by -1 gives the relations:

$$\frac{dp}{-\frac{\partial \mathcal{F}}{\partial x} - p \frac{\partial \mathcal{F}}{\partial u}} = \frac{dq}{-\frac{\partial \mathcal{F}}{\partial z} - q \frac{\partial \mathcal{F}}{\partial u}} = \frac{du}{p \frac{\partial \mathcal{F}}{\partial p} + q \frac{\partial \mathcal{F}}{\partial q}} = \frac{dx}{\frac{\partial \mathcal{F}}{\partial p}} = \frac{dz}{\frac{\partial \mathcal{F}}{\partial q}} = ds.$$

These relations are **Charpit's relations**, identical to equations (2.24) – (2.28).

Chapter 3

Behaviour of Fast MA Wave near a 2D null point in a $\beta = 0$ plasma

3.1 Introduction

The coronal heating problem remains a key unsolved problem in solar physics. As mentioned previously, there are rival heating theories ranging from reconnection models involving *nanoflares* and wave heating models involving *phase mixing* and *resonant absorption*. The reconnection models either require the formation of many current sheets, due to random photospheric boundary motions that braid the magnetic field, or the collapse of null points. The wave heating models rely on the generation of small length scale wave motions in the corona. There is clear evidence from SOHO and TRACE observations of slow MHD waves (Berghmans & Clette 1999; De Moortel *et al.* 2000), fast MHD waves (Nakariakov *et al.* 1999) and non-thermal line broadening due to Alfvén waves (Harrison *et al.* 2002). This chapter is concerned with the propagation of fast MHD waves in the neighbourhood of a simple 2D null point in a $\beta = 0$ plasma.

As detailed in Section 1.4, null points are locations in a magnetic configuration where the field strength is zero, and hence the Alfvén speed (Section 1.5.2) is zero. The fact that null points are a weakness in the magnetic field has been used to investigate how they collapse in response to boundary motions. This has been investigated by Craig and co-workers and other authors using analytical and numerical approaches (Craig & McClymont 1991; Hassam 1992; Vekstein & Bian 2005). The basic aim is to move the field lines passing through the boundary in a particular manner in order to perturb the field. The resulting field perturbations cause the null point to collapse to form a current sheet in which reconnection can release magnetic energy. In these models the boundary motions move the field lines but do not return them to their original positions. Thus, the Poynting flux induced by the imposed motion (and then fixing the field after the motion

is complete) accumulates at the resulting current sheet and provides the energy released in the reconnection. However, if the boundary motions are simply due to the passing of incoming waves through the boundary, then it is not clear that the null point need collapse and form a current sheet. If this is the case, then it is not clear if the energy in the wave, again due to the Poynting flux through the boundary, will dissipate or simply pass through one of the other boundaries.

Waves in the neighbourhood of 2D null points have been investigated by various authors. Bulanov and Syrovatskii (1980) provided a detailed discussion of the propagation of fast and Alfvén waves using cylindrical symmetry. In their paper, harmonic fast waves are generated and these propagate towards the null point. However, the assumed cylindrical symmetry means that the disturbances can only propagate either towards or away from the null point. Craig and Watson (1992) mainly consider the radial propagation of the $m = 0$ mode (where m is the azimuthal wavenumber) using a mixture of analytical and numerical solutions. In their investigation, the outer radial boundary is held fixed so that any outgoing waves will be reflected back towards the null point. This means that all the energy in the wave motions is contained within a fixed region. They show that the propagation of the $m = 0$ wave towards the null point generates an exponentially large increase in the current density and that magnetic resistivity dissipates this current in a time related to $\log \eta$. Their initial disturbance is given as a function of radius.

In this chapter, we are interested in generating the disturbances at the boundary rather than internally. Craig and McClymont (1991; 1993) investigate the normal mode solutions for both $m = 0$ and $m \neq 0$ modes with resistivity included. Again they emphasise that the current builds up as the inverse square of the radial distance from the null point. However, attention has been restricted to a circular reflecting boundary. The experiments carried out in this chapter will investigate wave propagation in a $\beta = 0$ plasma in the neighbourhood of a simple 2D null point but for more general disturbances, more general boundary conditions and single wave pulses. This allows us to concentrate on the transient features that are not always apparent using normal mode analysis. Galsgaard *et al.* (2003) looked at a particular type of wave disturbance for a symmetrical 3D null. They investigated the effect of rotating the field lines around the spine and found that a twist wave (essentially an Alfvén wave) propagates in towards the null. They found that while the helical Alfvén wave spreads out, coupling due to the field geometry generates a fast wave that focuses on the null and wraps around it. This wrapping effect is analysed in more detail here for the simpler 2D null.

The propagation of fast magnetoacoustic waves in an inhomogeneous coronal plasma has been investigated by Nakariakov and Roberts (1995) who showed how the waves are refracted into regions of low Alfvén speed. In the case of null points, one of the aims of this and the next chapter is to see how this refraction proceeds when the Alfvén speed actually drops to zero.

3.2 Basic equations and set-up

In this chapter, we will investigate the behaviour of a linear, fast magnetoacoustic wave in the neighbourhood of a simple 2D null point. This chapter is based on the paper by McLaughlin & Hood (2004).

The basic magnetic field structure is taken as a simple 2D X-type neutral point. The aim of studying waves in a 2D configuration is one of simplicity. The individual effects are much easier to identify when there is no coupling between the fast and Alfvén modes. However, the extension to 3D is relatively straightforward. The modes will become coupled but their evolution is predictable from the 2D case. Therefore, the magnetic field is taken as

$$\mathbf{B}_0 = \frac{B_0}{L} (x, 0, -z), \quad (3.1)$$

where B_0 is a characteristic field strength and L is the length scale for magnetic field variations. This magnetic field can be seen in Figure (3.1). Obviously this particular choice of magnetic field is only valid in the neighbourhood of the null point located at $x = 0, z = 0$. Such restrictions will be addressed later in Chapter 6 (with a more realistic magnetic configuration).

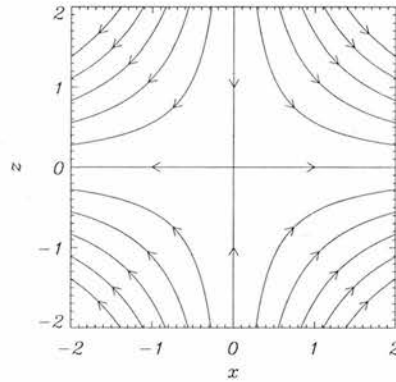


Figure 3.1: Our choice of equilibrium magnetic field.

To study the nature of wave propagation near null points, the linearised MHD equations are used. The derivation of the linearised, non-dimensionalised equations for a $\beta = 0$ plasma can be found in the previous chapter. As mentioned in Section 2.2.3, in this geometry the linearised MHD equations naturally decouple into two equations; one for the fast MHD wave and second for the Alfvén wave. Recall the slow MHD wave is absent under the $\beta = 0$ assumption. The Alfvén wave equations will be discussed in the next chapter. Thus, the equations relevant to studying the nature of the fast MA wave in this chapter are equations (2.10) and (2.11). Substituting the form of the simple 2D null point magnetic configuration (equation 3.1) into these equations, and dropping the star indices (the fact that the equations are now non-dimensionalised is understood) gives:

$$\begin{aligned}
\rho_0 \frac{\partial}{\partial t} v_{\perp} &= v_A^2(x, z) \left(\frac{\partial b_z}{\partial x} - \frac{\partial b_x}{\partial z} \right) \\
\frac{\partial b_x}{\partial t} &= -\frac{\partial}{\partial z} v_{\perp} + \frac{1}{R_m} \left(\frac{\partial^2}{\partial x^2} + \frac{\partial^2}{\partial z^2} \right) b_x, \\
\frac{\partial b_z}{\partial t} &= \frac{\partial}{\partial x} v_{\perp} + \frac{1}{R_m} \left(\frac{\partial^2}{\partial x^2} + \frac{\partial^2}{\partial z^2} \right) b_z,
\end{aligned} \tag{3.2}$$

where the Alfvén speed, $v_A(x, z) = \sqrt{x^2 + z^2}$. $\mathbf{b} = (b_x, 0, b_z)$ and v_{\perp} are perturbed magnetic field and velocity as defined in the previous chapter.

For now, we will neglect the magnetic resistivity (η) in the numerical simulations but will discuss its role in the conclusions. Thus, we take $\eta = 0$ which is equivalent to letting $R_m \rightarrow \infty$. This is called an **ideal** plasma. We also assume the background gas density is uniform (so $\rho_0 = 1$ under our non-dimensionalisation). A spatial variation in ρ_0 can cause phase mixing (Heyvaerts & Priest 1983; De Moortel, Hood & Arber 2000); this idea will be re-visited in Chapter 8.

These equations can now be combined to form a single wave equation:

$$\frac{\partial^2}{\partial t^2} v_{\perp} = (x^2 + z^2) \left(\frac{\partial^2}{\partial x^2} + \frac{\partial^2}{\partial z^2} \right) v_{\perp}, \tag{3.3}$$

This is the wave equation of the form of equation (1.23). This is the primary equation we will be looking at in this chapter (although the form of equations 3.2 is easier to solve numerically). Recall that in its derivation, we have assumed linearised behaviour in an ideal, $\beta = 0$, 2D plasma with uniform density.

3.3 Fast Magnetoacoustic Wave (in cartesian coordinates)

We solve the linearised MHD equations for the fast wave, namely equations (3.2), numerically using a two-step Lax-Wendroff scheme (page 25). The numerical scheme is run in a box with $-4 \leq x \leq 4$ and $-4 \leq z \leq 2$, with attention focussed on the square $-2 \leq x \leq 2$ and $-2 \leq z \leq 2$; this minimises the problems associated with the wave crossing the boundaries of the box (a common problem in numerical simulations). We initially consider a single wave pulse coming in from the top boundary. For the single wave pulse, the boundary conditions were set such that:

$$v_{\perp}(x, 2) = \begin{cases} \sin \omega t & \text{for } 0 \leq t \leq \frac{\pi}{\omega} \\ 0 & \text{otherwise} \end{cases},$$

$$\left. \frac{\partial}{\partial x} v_{\perp} \right|_{x=-4} = 0, \quad \left. \frac{\partial}{\partial x} v_{\perp} \right|_{x=4} = 0, \quad \left. \frac{\partial}{\partial z} v_{\perp} \right|_{z=-4} = 0.$$

Tests show that the central behaviour is largely unaffected by these choices of side and bottom boundary conditions. The other boundary conditions on the perturbed magnetic field follow from the remaining equations and the solenoidal condition, $\nabla \cdot \mathbf{b} = 0$. We also take $\omega = 2\pi$ for our simulations. This choice was made simply because this frequency demonstrates the following effects clearly; a higher frequency would simply show a narrower wave pulse and a lower frequency would show a fatter wave pulse. The numerical simulations were run in a box with 1000×1000 grid points.

3.3.1 Numerical simulation results

We find that the linear, fast magnetoacoustic wave travels towards the neighbourhood of the X-point and bends around it. Since the Alfvén speed, $v_A(x, z)$, is spatially varying, different parts of the wave travel at different speeds, and it travels faster the further it is away from the origin, i.e. the further from the origin, the greater in magnitude $v_A = \sqrt{x^2 + z^2}$ is. So the wave demonstrates *refraction* and this can be seen in Figure (3.2). A similar refraction phenomenon was found by Nakariakov & Roberts (1995). It is this refraction effect that wraps the wave around the null point and it is this that is the key feature of fast wave propagation.

Note also that the length scales (this can be thought of as the distance between the leading and trailing edges of the wave pulse) are decreasing, thus indicating that current will be forming. Also note that after the wave has wrapped around the null, the wave is so thin around the null that the resolution of our simulation is starting to fail to resolve the wave (this is explained more on page 45). However, test runs in a numerical box closer to the origin show that the wave is indeed wrapping around again and again. Finally, we note the wave keeps an approximately constant amplitude as it nears the null (certainly along $x = 0$), although boundary effects do affect the wave amplitude at the edges of the box. This can be seen in Figure 3.3.

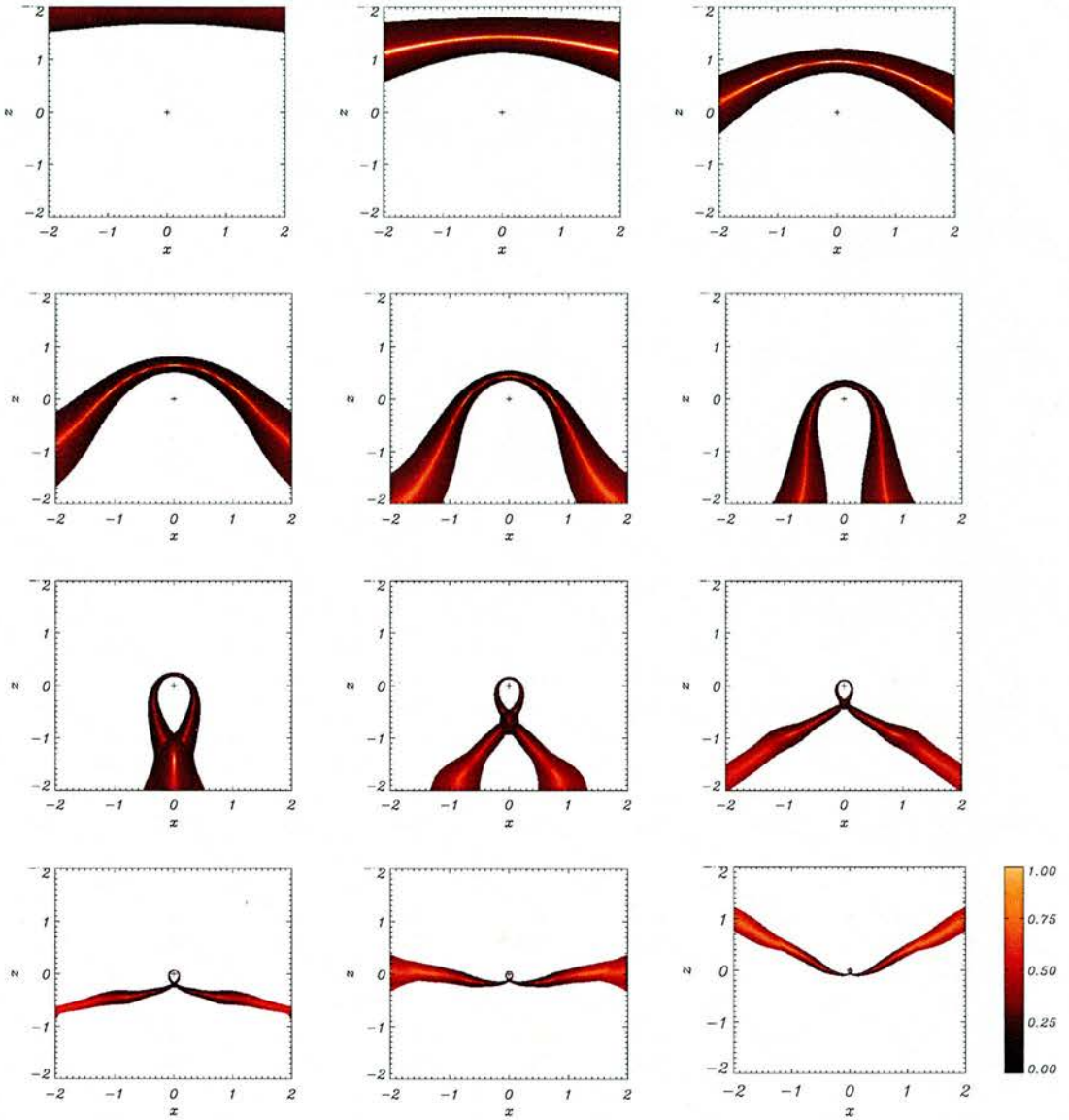


Figure 3.2: Contours of v_{\perp} for numerical simulation for a fast wave sent in from upper boundary for $-4 \leq x \leq 4$, and its resultant propagation at times (a) $t=0.2$, (b) $t=0.6$, (c) $t=1.0$, (d) $t=1.4$, (e) $t=1.8$ and (f) $t=2.2$, (g) $t=2.6$, (h) $t=3.0$, (i) $t=3.4$, (j) $t=3.8$, (k) $t=4.2$ and (l) $t=4.6$, labelling from top left to bottom right. The cross indicates the null point at the origin.

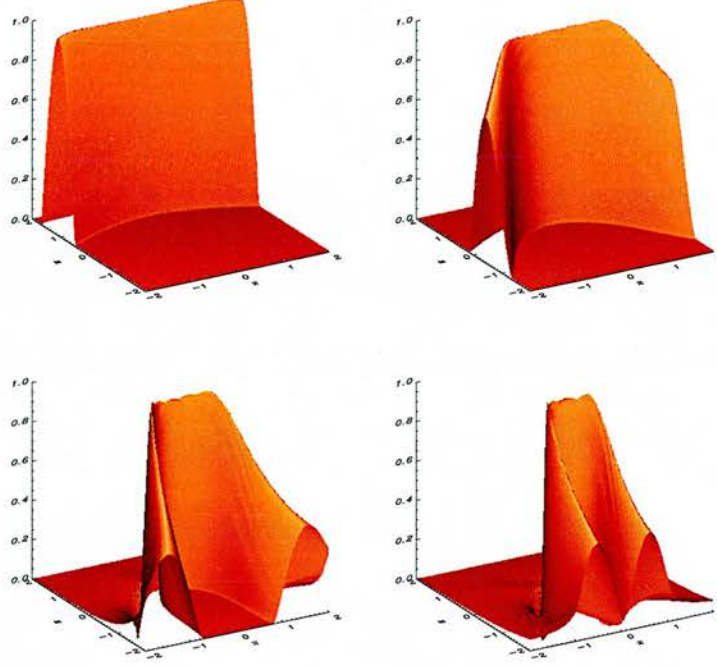


Figure 3.3: Shaded surfaces of v_{\perp} for numerical simulation for a fast wave sent in from upper boundary ($-4 \leq x \leq 4$) and its resultant propagation at times (a) $t=0.625$, (b) $t=1.25$, (c) $t=1.875$ and (d) $t=2.5$, labelling from top left to bottom right. Note that the wave maintains a constant amplitude near the line $x = 0$.

3.3.2 WKB approximation

We can also solve equation (3.3) analytically to gain more insight into the nature of the solution. This will be a common approach in this Thesis: complementing numerical simulations and analytical results to gain a deeper understanding of the solution.

In this Section, we will use the WKB approximation (Section 2.4) to solve equation (3.3). According to the method detailed in Section 2.4.2, substituting $v_{\perp} = e^{i\phi(x,z)} \cdot e^{-i\omega t}$ into (3.3) gives:

$$-\omega^2 v_{\perp} = (x^2 + z^2) \left[-\left(\frac{\partial\phi}{\partial x}\right)^2 - \left(\frac{\partial\phi}{\partial z}\right)^2 - i\left(\frac{\partial^2\phi}{\partial x^2} + \frac{\partial^2\phi}{\partial z^2}\right) \right] \cdot v_{\perp}$$

Now we make the WKB approximation that $\phi \sim \omega \gg 1$ and this leads to a first order PDE of the form:

$$\begin{aligned} \omega^2 &= (x^2 + z^2) (p^2 + q^2) \\ \Rightarrow \mathcal{F}(x, z, \phi, p, q) = 0 &= \frac{1}{2} (x^2 + z^2) (p^2 + q^2) - \frac{1}{2} \omega^2 \end{aligned}$$

where $p = \frac{\partial\phi}{\partial x}$ and $q = \frac{\partial\phi}{\partial z}$ and \mathcal{F} is a non-linear PDE. We include a half in the form of \mathcal{F} to make the equations nicer later. Note all the imaginary terms have disappeared. We now want to apply

Charpit's equations (page 31) so we first work out the quantities:

$$\begin{aligned}\frac{\partial \mathcal{F}}{\partial \phi} &= 0 \\ \frac{\partial \mathcal{F}}{\partial x} &= (p^2 + q^2) x, \quad \frac{\partial \mathcal{F}}{\partial z} = (p^2 + q^2) z, \\ \frac{\partial \mathcal{F}}{\partial p} &= (x^2 + z^2) p, \quad \frac{\partial \mathcal{F}}{\partial q} = (x^2 + z^2) q.\end{aligned}$$

Now we can apply the Charpit's equations (equations 2.24 – 2.28) to generate the following equations:

$$\begin{aligned}\frac{d\phi}{ds} &= \omega^2 \\ \frac{dp}{ds} &= -(p^2 + q^2) x, \quad \frac{dq}{ds} = -(p^2 + q^2) z \\ \frac{dx}{ds} &= (x^2 + z^2) p, \quad \frac{dz}{ds} = (x^2 + z^2) q\end{aligned}\tag{3.4}$$

where ω is the frequency of our wave and s is some parameter along the characteristic.

These five ODEs can be solved in a variety of ways, and often in this Thesis we will solve them numerically using a fourth-order Runge-Kutta method (see page 26). This can be seen (for example) in Chapters 5 and 6. The initial conditions used are:

$$\phi_0 = 0, \quad -3 \leq x_0 \leq 3, \quad z_0 = 2, \quad p_0 = 0, \quad q_0 = -\frac{\omega}{\sqrt{x_0^2 + z_0^2}}$$

However in this simple case, equations (3.4) can also be solved analytically (as opposed to with the Runge-Kutta method which would be a semi-analytical solution). The full derivation is shown in Appendix A. Using this, we generate the analytical solution:

$$\begin{aligned}\phi &= \omega^2 s, \\ x &= \left[x_0 \cos\left(\frac{Ax_0}{z_0} s\right) + z_0 \sin\left(\frac{Ax_0}{z_0} s\right) \right] e^{-As}, \\ z &= \left[z_0 \cos\left(\frac{Ax_0}{z_0} s\right) - x_0 \sin\left(\frac{Ax_0}{z_0} s\right) \right] e^{-As},\end{aligned}\tag{3.5}$$

where again s is some parameter along the characteristic, x_0 is a starting point distinguishing between different characteristic curves, z_0 is a second starting point ($z_0 = 2$ in our simulations), ω is the frequency of our wave and A is a constant such that $A = \frac{z_0 \omega}{\sqrt{x_0^2 + z_0^2}}$.

Contours of constant ϕ can be thought of as defining the positions of the edges of the wave pulse, i.e. with correct choices of s , the WKB solution represents the front, middle and back edges of the wave. The evolution can be seen in Figure (3.4). Also, $s = \omega t$ and so the numerical and analytical work can be directly compared. The agreement between the analytic model and the numerical simulation waves is very good, as seen in an overplot of a numerical simulation (shaded area) and our WKB solution (thick lines) in Figure (3.5). Note the WKB solution is shown for comparison here, but the analytical solution (3.5) gives exactly the same result.

Note that there is a difference between the side and bottom boundary conditions of the simulations and the analytical model. This means that later on in the simulation, say after $t = 3$, the numerical solution differs from the analytical solution when you look at its tails. However, the agreement around the origin is excellent, as seen in Figure (3.6) which shows subfigures (*h*) and (*j*) from Figure (3.5) ($t = 3$ and 3.8), but with rescaled axes to draw attention to the central behaviour. Note also that the numerical simulation has a tendency to spread out and so the wave tails of the numerical simulation always touch the ± 2 boundaries, whereas the spiralling nature of the WKB solution means that the wave tails of the analytical solution eventually all accumulate at the null.

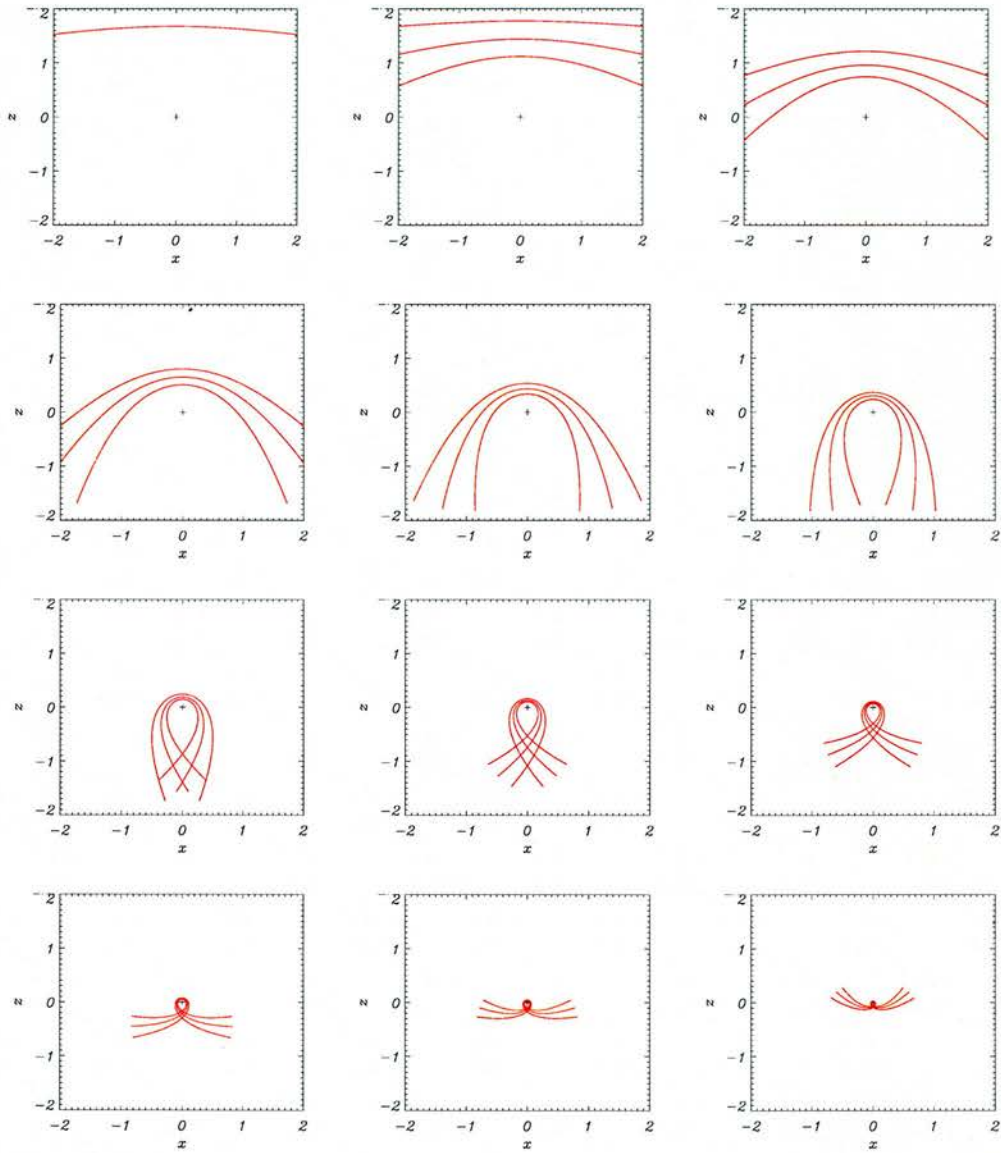


Figure 3.4: Analytical solution v_{\perp} for WKB approximation of a fast wave sent in from upper boundary for $-3 \leq x \leq 3$, and its resultant propagation at times (a) $t=0.2$, (b) $t=0.6$, (c) $t=1.0$, (d) $t=1.4$, (e) $t=1.8$ and (f) $t=2.2$, (g) $t=2.6$, (h) $t=3.0$, (i) $t=3.4$, (j) $t=3.8$, (k) $t=4.2$ and (l) $t=4.6$, labelling from top left to bottom right. The lines represent the front, middle and back edges of the WKB wave solution, where the pulse enters from the top of the box. Again, the cross represents the null point at the origin.

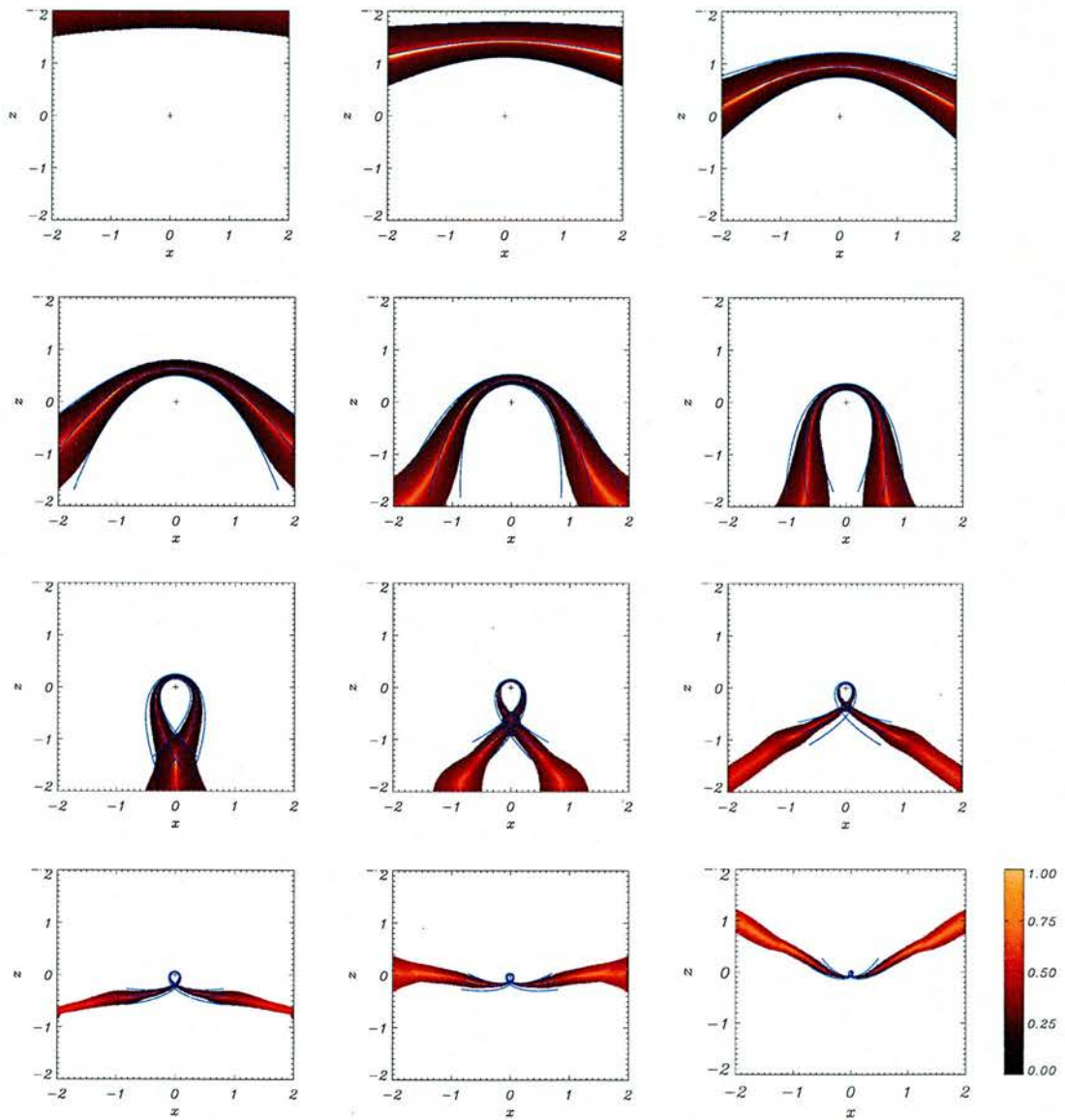


Figure 3.5: Comparison of numerical simulation (shaded area) and analytical solution of v_{\perp} for a fast wave sent in from upper boundary for $-3 \leq x \leq 3$, and its resultant propagation at times (a) $t=0.2$, (b) $t=0.6$, (c) $t=1.0$, (d) $t=1.4$, (e) $t=1.8$ and (f) $t=2.2$, (g) $t=2.6$, (h) $t=3.0$, (i) $t=3.4$, (j) $t=3.8$, (k) $t=4.2$ and (l) $t=4.6$, labelling from top left to bottom right. The lines represent the front, middle and back edges of the WKB wave solution, where the pulse enters from the top of the box.

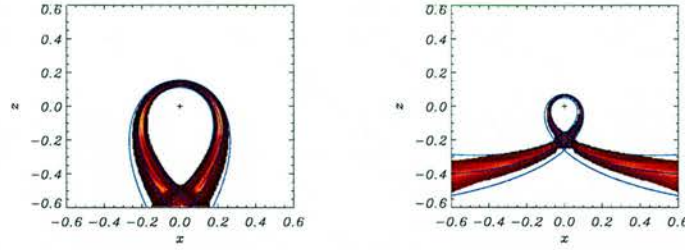


Figure 3.6: Comparison of numerical simulation (shaded area) and analytical solution (blue lines) of v_{\perp} for a fast wave sent in from upper boundary for $-3 \leq x \leq 3$, and its resultant propagation at times $t=3.0$ (left) and $t =3.8$ (right). These are rescaled subfigures of subfigures (h) and (j) from Figure 3.5. The lines represent the front, middle and back edges of the WKB wave solution.

3.3.3 Current accumulation

Since the Alfvén speed drops to zero at the null point the wave never actually reaches there, but the length scales rapidly decrease indicating that the current (and all other gradients) will increase. As a simple illustration, consider the wavefront as it propagates down the z axis at $x = 0$. Here the vertical velocity is $v_z = \frac{dz}{dt} = -z$. Thus, the start of the wave is located at a position $z_s = z_0 e^{-t}$, when the wave is initially at $z = z_0$. If the end of the wave leaves $z = z_0$ at $t = t_0$ then the location of the end of the wave is $z_e = z_0 e^{t_0 - t}$. Thus, the distance between the leading and trailing edge of the wave is $\delta z = z_0 (e^{t_0} - 1) e^{-t}$ and this decreases with time, suggesting that all gradients will increase exponentially.

Since we have a changing perturbed magnetic field whose gradients are increasing in time, we have a build-up of current density. Simulations show that there is a large current accumulation at the neutral point (Figure 3.7) and that this build-up is exponential in time (Figure 3.8), in keeping with our discussion on the thickness of the wave pulse in the above paragraph. Figure 3.8 shows the maximum of the absolute value of the current at each time and a plot of the logarithm of it against time.

This build-up of current is extremely important since it implies that resistive dissipation will eventually become important, regardless of the size of the resistivity, and will convert the wave energy into heat. In fact, the exponential growth of the current means that the time for magnetic diffusion to become important will depend only on $\log \eta$. Thus, refraction of the wave focuses the majority of the wave energy at the null point. This key result will be discussed further in the conclusions. Note that the topology of the current accumulation seems to be approaching that of a current line. The current line comes from the collapse of the width of the fast wave as it approaches the null. Note that while the current grows exponentially in time, the velocity remains finite in magnitude.

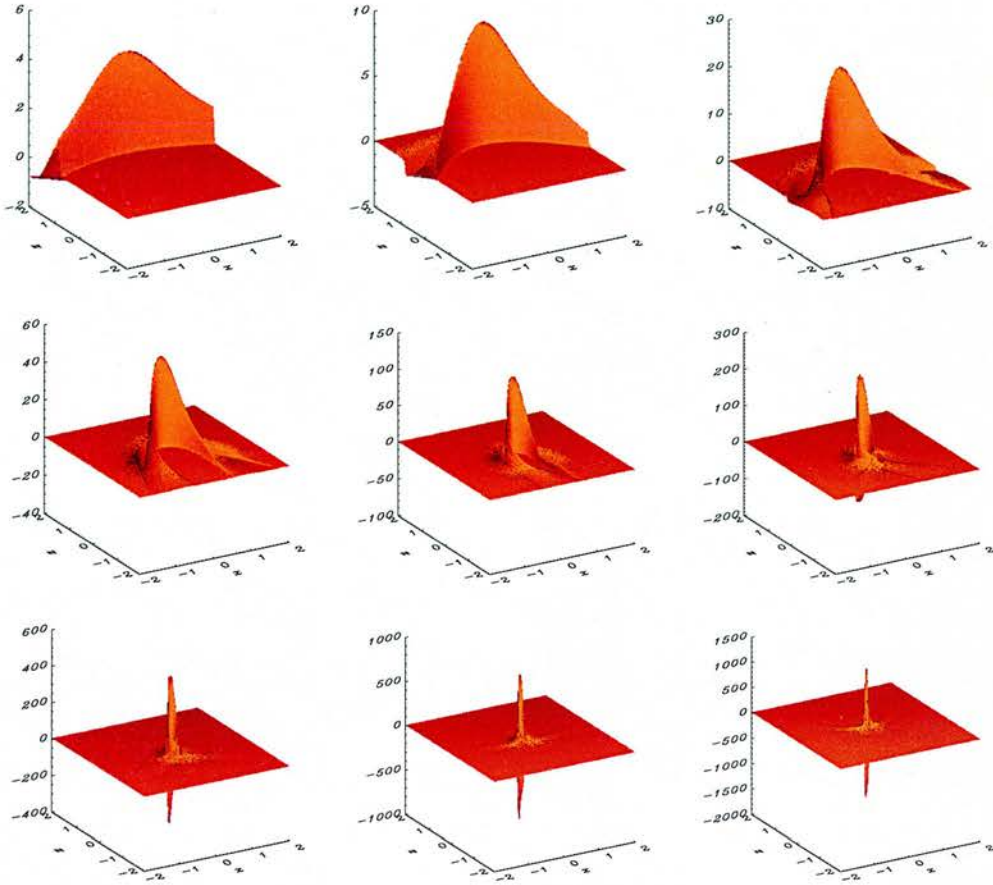


Figure 3.7: Shaded surfaces showing the build up of current at times (a) $t=0.5$, (b) $t=1.0$, (c) $t=1.5$, (d) $t=2.0$, (e) $t=2.5$, (f) $t=3.0$, (g) $t=3.5$, (h) $t=4.0$ and (i) $t=4.5$, labelling from top left to bottom right. Note the change in vertical scale showing the (exponential) increase in current.

As an aside, note that the line in Figure 3.8 (right) starts to deviate from a straight line after (approximately) $t = 3.5$. Recall the discussion above concerning the decrease in width of the pulse, where the distance between the leading and trailing edge of the wave was shown to be $\delta z = 6(e^{t_0} - 1)e^{-t}$. This exponential decrease in length scales means that we will always run out of numerical resolution for the simulation in Figure (3.2); for any topology we want to resolve, for which δz will be of the form $\frac{C}{N}$ (where N is the number of grid points and C is a constant of inverse proportionality), we see that a solution is improperly resolved when $e^t \geq (e^{t_0} - 1)N/C$, i.e. $t \geq \log N + \log(e^{t_0} - 1) - \log C$. Thus, because of this logarithmic dependence on N , we will only be able to resolve the solution up until a certain time and increasing the number of grid points will not substantially improve this. Thus, the line in Figure (3.8) tails off due to a lack of numerical resolution.

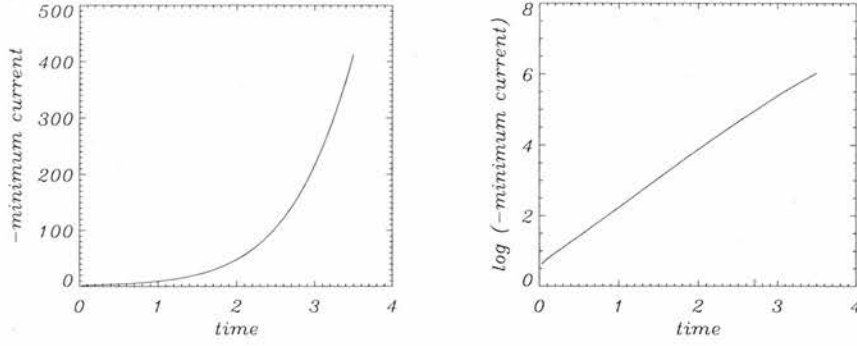


Figure 3.8: (left) (- minimum current) against time elapsed, (right) \log (- minimum current) against time elapsed. The slope of the line between $t = 1$ and $t = 3$ is 1.58.

We can also use our WKB approximation to predict the current density build up. We know:

$$\frac{\partial j}{\partial t} \hat{\mathbf{y}} = \nabla \times \frac{\partial \mathbf{b}}{\partial t} = \nabla \times (\nabla v_{\perp} \times \hat{\mathbf{y}}) = -\nabla^2 v_{\perp} \hat{\mathbf{y}}$$

which from our WKB derivation can be approximated by:

$$\begin{aligned} \nabla^2 v_{\perp} &= -\frac{\omega^2 v_{\perp}}{x^2 + z^2} = -\frac{\omega^2 e^{2As} v_{\perp}}{x_0^2 + z_0^2} = -\left(\frac{A}{z_0}\right)^2 e^{2As} v_{\perp} \\ &= -\left(\frac{A}{z_0}\right)^2 e^{2As} e^{i\phi} e^{-i\omega t} = -\left(\frac{A}{z_0}\right)^2 e^{2As} e^{-i\omega^2 s} e^{-i\omega t} = -\frac{\partial j}{\partial t}. \end{aligned}$$

By considering the modulus of this result, we can see that $|j|$ will grow exponentially with s , i.e. as e^{2As} . To compare with our simulations, we first note that the time in our numerical scheme, t , is related to our parameter s by $t = \omega s$. Now, the exponent $2As$ in the exponential is equal to $2z_0\omega s / \sqrt{x_0^2 + z_0^2}$ and so along $x_0 = 0$ and at $z_0 = 2$ ($x_0 = 0$ is where the maximum current of our numerical simulations occurred) this is simply $2t$. The slope of the numerical experiment in figure (3.8) between $t = 1$ and $t = 3$ is 1.58. This agreement between the analytical and numerical current density build-up is quite good, considering that the WKB solution is only valid for a harmonic wavetrain with $\omega \gg 1$.

3.4 Fast Magnetoacoustic Wave (in polar coordinates)

It is already apparent that the Alfvén speed ($v_A^2 = x^2 + z^2$) plays a vital role in the behaviour described above. Thus, the natural choice here is to switch to polar coordinates. However, as previously mentioned, other authors who have looked at this particular null point always make the change to polar coordinates, whereas using a cartesian system allows for the investigation of more general disturbances. However, now that we have examined the problem in cartesian coordinates, changing to polar coordinates may add to our understanding of the system.

In a circular geometry, the magnetic field described by equation (3.1) (and seen in Figure 3.1) is:

$$\mathbf{B}_0 = -r \cos 2\theta \hat{\mathbf{r}} + r \sin 2\theta \hat{\boldsymbol{\theta}}$$

Thus:

$$\mathbf{B}_0 \cdot \mathbf{B}_0 = r^2 \quad , \quad \nabla \times \mathbf{b} = \frac{1}{r} \left[\frac{\partial}{\partial r} (rb_\theta) - \frac{\partial}{\partial \theta} b_r \right] \hat{\mathbf{y}} \quad , \quad \mathbf{A} = -\frac{1}{2} r^2 \sin 2\theta \hat{\mathbf{y}}$$

Here, the linearised equations for the fast magnetoacoustic wave (i.e. the non-dimensionalised equivalents of equations 3.3) are:

$$\begin{aligned} \frac{\partial v_\perp}{\partial t} &= r^2 \left[\frac{1}{r} \frac{\partial}{\partial \theta} b_r - \frac{1}{r} \frac{\partial}{\partial r} (rb_\theta) \right] \\ \frac{\partial b_r}{\partial t} &= \frac{1}{r} \frac{\partial v_\perp}{\partial \theta} \quad , \quad \frac{\partial b_\theta}{\partial t} = -\frac{\partial v_\perp}{\partial r} \quad , \end{aligned} \quad (3.6)$$

As before, these can be combined to form a single wave equation for the fast wave:

$$\frac{\partial^2 v_\perp}{\partial t^2} = r^2 \left[\frac{1}{r^2} \frac{\partial^2 v_\perp}{\partial \theta^2} + \frac{1}{r} \frac{\partial}{\partial r} \left(r \frac{\partial v_\perp}{\partial r} \right) \right] = r^2 \nabla^2 v_\perp \quad (3.7)$$

where we have used the polar coordinates form of $\nabla^2 = \frac{1}{r} \frac{\partial}{\partial r} \left(r \frac{\partial}{\partial r} \right) + \frac{1}{r^2} \frac{\partial^2}{\partial \theta^2}$. Note that we can change between equations (3.3) and (3.7) using the substitution $x = r \cos \theta$, $z = r \sin \theta$ and $r^2 = x^2 + z^2$.

3.4.1 Numerical simulation

Equations (3.6) can be solved numerically with a number of numerical schemes with the variables defined in polar coordinates. However, polar coordinate systems have a fundamental problem when it comes to crossing the origin; firstly the radial coordinate decreases to zero, then increases from zero. This movement through zero also causes an instantaneous shift of π in the angular coordinate. This can cause a problem in many numerical codes. Secondly, dividing by $r = 0$ is always a problem.

Hence, instead of writing a 2D polar coordinates numerical code to solve equations (3.6) where the wave is driven on the (now circular) boundary, it was decided to re-use the Lax-Wendroff numerical code but now with an *initial pulse condition* as opposed to a driven boundary. The numerical scheme was run in a (square) box with $-6 \leq x \leq 6$ and $-6 \leq z \leq 6$ and an initial pulse was set up around $r = 3$ such that:

$$v_{\perp}(r, \theta, t = 0) = \sqrt{3} \sin [\pi (r - 2.5)] \begin{cases} \text{for } 2.5 \leq r \leq 3.5 \\ \text{for } 0 \leq \theta \leq 2\pi \end{cases} .$$

Of course, this pulse was written into the code in terms of $x = r \cos \theta$ and $z = r \sin \theta$ so what was actually solved was:

$$v_{\perp}(x, z, t = 0) = \sqrt{3} \sin \left[\pi \left(\sqrt{x^2 + z^2} - 2.5 \right) \right] \quad \text{for } 2.5 \leq \sqrt{x^2 + z^2} \leq 3.5 ,$$

$$\left. \frac{\partial v_{\perp}}{\partial x} \right|_{x=-6} = 0, \quad \left. \frac{\partial v_{\perp}}{\partial x} \right|_{x=6} = 0, \quad \left. \frac{\partial v_{\perp}}{\partial z} \right|_{z=-6} = 0, \quad \left. \frac{\partial v_{\perp}}{\partial z} \right|_{z=6} = 0 .$$

This gave a suitable initial pulse. When the numerical experiment began, the initial condition pulse split into two waves; each travelling in different directions. The waves split naturally apart and we then concentrate our attention on the incoming circular wave. The outgoing wave is of no concern to us and the boundary conditions let the wave pass out of the box. This can be seen in Figure 3.9. The top left hand shaded surface shows the initial pulse at $t = 0$. The top right subfigure shows the pulse split into two after $t = 0.5$. The lower left hand side shows the pulse again after $t = 0.5$ but from above. We see that the two waves have disassociated in the sense that we are free to just deal with one (the incoming solution). The bottom right subfigure will be discussed below.

We can also understand the splitting of the initial condition into two wave pulses in terms of D'Alembert's solution. Here our initial condition has the form:

$$\begin{aligned} \sqrt{3} \sin [\pi (r - 2.5)] &= \frac{1}{2} \mathcal{F}(t + \log r) + \frac{1}{2} \mathcal{F}(t - \log r) \\ &= \frac{\sqrt{3}}{2} \sin \left[\pi \left(e^{t + \log r} - 2.5 \right) \right] + \frac{\sqrt{3}}{2} \sin \left[\pi \left(e^{-t + \log r} - 2.5 \right) \right] \end{aligned}$$

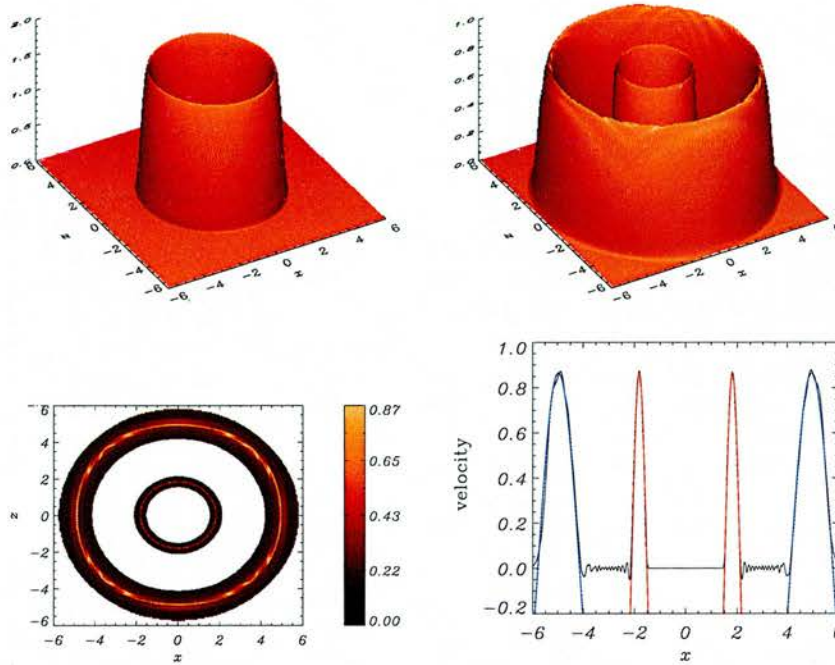


Figure 3.9: The top left hand shaded surface shows the initial pulse at $t = 0$. The top right subfigure shows the pulse split after $t = 0.5$. Lower left hand side shows pulse again after $t = 0.5$ but from above. Bottom right shows a cut along $v_{\perp}(x, z = 0)$ with the black line showing the numerical solution and the coloured lines showing the analytical agreement.

These analytical descriptions match the evolution of the two waves satisfactorily and the agreement can be seen in the bottom right subfigure of Figure 3.9. Note how the numerical solution has some dispersion as the two waves split; this is due to the nature of the Lax-Wendroff scheme (as mentioned on page 25).

The simulation was run with a resolution of 800×800 points. However, since we knew the important behaviour would occur close to the origin, a **stretched grid** was used to focus the majority of the grid points close to the origin¹. This gave better resolution in the areas of interest. The behaviour of the fast wave with a circular geometry can be seen in Figure 3.10. Note how the initial pulse can be seen in the top left subfigure and that it has magnitude $\sqrt{3}$, then, at a later time, the wave has split and has magnitude $\frac{\sqrt{3}}{2}$.

We found that the linear, fast magnetoacoustic wave split into two waves; one approaching the origin the other travelling away from it. The wave travelling towards the origin had the shape of an annulus. We found the annulus contracts, but keeps its original ratios (distance between the front and middle wavefronts compared to middle and trailing wavefronts). Since the Alfvén speed is spatially varying ($\sim r$), a *refraction* effect focusses the wave into the origin. This is the same refraction effect found in Section 3.3.

¹The stretching algorithm smoothly stretched the grid such that 50% of the grid points lay within a radius of 1.5

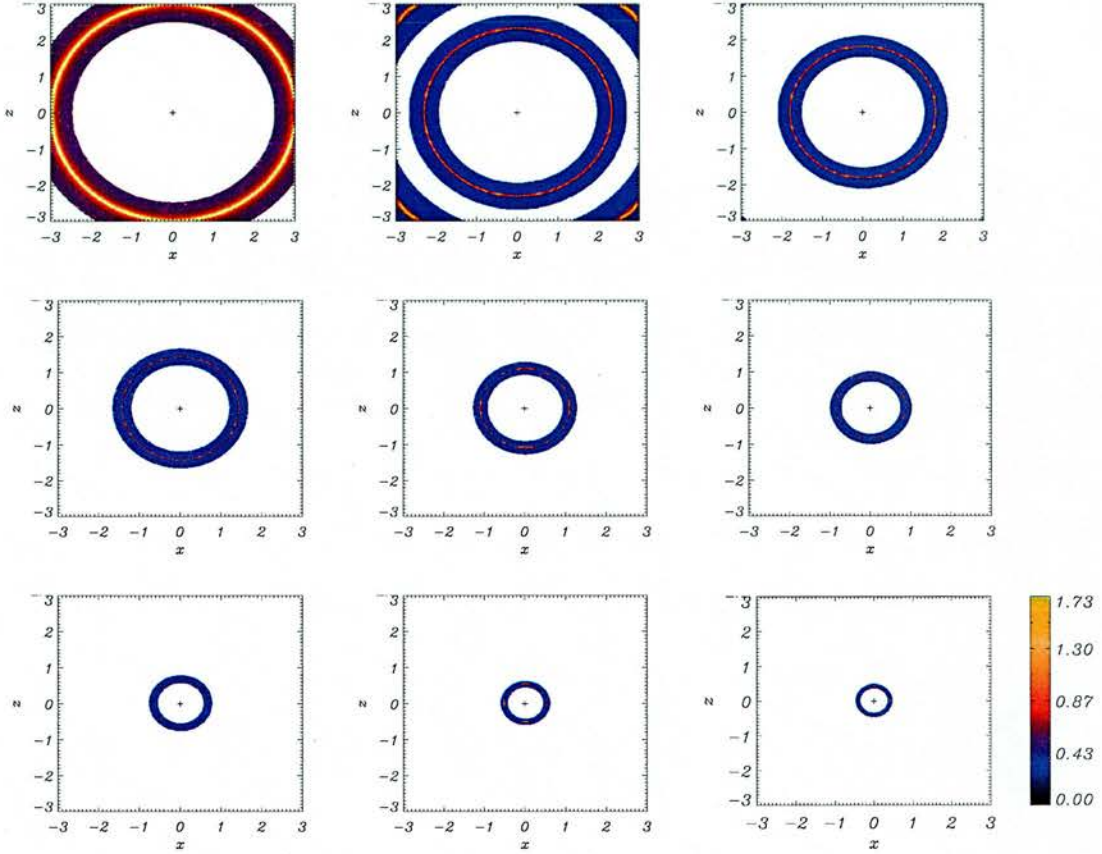


Figure 3.10: Contours of numerical simulation of v_{\perp} for a fast wave pulse initially located about a radius $\sqrt{x^2 + z^2} = 3$, and its resultant propagation at times (a) $t=0$, (b) $t=0.25$, (c) $t=0.5$, (d) $t=0.75$, (e) $t=1.0$ and (f) $t=1.25$, (g) $t=1.5$, (h) $t=1.75$ and (i) $t=2.0$, labelling from top left to bottom right.

3.4.2 Analytical work : Klein-Gordon and Bessel functions

Equation (3.7) is a two dimensional wave equation with a (background) Alfvén speed that varies in space. Since it is a wave equation, we would usually proceed by the usual Fourier component substitution. However, we are unable to do this because we do not have constant coefficients in our equation. Instead we shall have to perform some mathematical manipulation. The right hand side of our equation is $r \frac{\partial}{\partial r} \left(r \frac{\partial v_{\perp}}{\partial r} \right) + \frac{\partial^2 v_{\perp}}{\partial \theta^2}$. We can proceed by considering a change of variable. Let $u = (\ln r - \ln r_0)$ (where $\frac{r}{r_0}$ is a dimensionless quantity). This gives:

$$\frac{\partial^2 v_{\perp}}{\partial t^2} = \frac{\partial}{\partial u} \left(\frac{\partial v_{\perp}}{\partial u} \right) + \frac{\partial^2 v_{\perp}}{\partial \theta^2} = \frac{\partial^2 v_{\perp}}{\partial u^2} + \frac{\partial^2 v_{\perp}}{\partial \theta^2} ,$$

where $\frac{du}{dr} = \frac{1}{r}$ and so $\frac{d}{du} = \frac{dr}{du} \cdot \frac{\partial}{\partial r} = r \frac{\partial}{\partial r}$. Note this substitution works equally well for $u = +\ln \frac{r}{r_0}$ or $u = -\ln \frac{r}{r_0}$, since the signs just cancel out. Here r_0 is an imposed constant and

has the effect of setting $u = 0$ at $r = r_0$, so r_0 can be thought of as a boundary. This is discussed further below.

We now have constant coefficients. Usually we would now try a harmonic solution such that $v_{\perp} = e^{i(\omega t + nu + m\theta)}$ and this would give a dispersion relation (normal mode analysis). However, we have to be careful as n may be complex due to our substitution. In fact, the only separable part we can really justify is that the θ -dependence part satisfies $\sim e^{im\theta}$ (where m is an integer) so that we have periodicity. We now assume we can separate variables such that $v_{\perp}(u, t, \theta) = \Sigma(u, t) \cdot \Theta(\theta)$. So:

$$\begin{aligned} \Theta \frac{\partial^2 \Sigma}{\partial t^2} - \Theta \frac{\partial^2 \Sigma}{\partial u^2} &= \Sigma \frac{\partial^2}{\partial \theta^2} \implies \frac{\Sigma_{tt}}{\Sigma} - \frac{\Sigma_{uu}}{\Sigma} = \frac{\Theta_{\theta\theta}}{\Theta} = \text{constant} = -m^2 \\ \implies \Theta_{\theta\theta} &= -m^2 \Theta \implies \Theta(\theta) = A \cos m\theta + B \sin m\theta . \end{aligned}$$

Where A and B are constants. Thus $\frac{\partial^2}{\partial \theta^2} v_{\perp} = \Theta_{\theta\theta} \Sigma = -m^2 \Theta \Sigma = -m^2 v_{\perp}$, and so our equation simplifies to:

$$\frac{\partial^2 v_{\perp}}{\partial t^2} = \frac{\partial^2 v_{\perp}}{\partial u^2} - m^2 v_{\perp} \implies \frac{\partial^2 \Sigma}{\partial t^2} = \frac{\partial^2 \Sigma}{\partial u^2} - m^2 \Sigma . \quad (3.8)$$

We identify this equation as the **Klein-Gordon** equation.

Klein-Gordon

The Klein-Gordon equation (equation 3.8) is a modified wave equation. It can be solved analytically. Firstly we look at the (simplest) solution where $m = 0$. Setting $m = 0$ reduces the Klein-Gordon equation to the familiar wave equation, $\frac{\partial^2 \Sigma}{\partial t^2} = \frac{\partial^2 \Sigma}{\partial u^2}$. This has the D'Alembert solution and so:

$$\Sigma = \mathcal{F}(u - t) + \mathcal{G}(u + t) , \quad (3.9)$$

where \mathcal{F} and \mathcal{G} are arbitrary functions determined by the initial and boundary conditions. Note the arguments are dimensionless. Using our substitutions $u = \pm \ln \frac{r}{r_0}$ where $r^2 = x^2 + z^2$ and $r_0^2 = x_0^2 + z_0^2$, and recalling that $\Theta = A \cos m\theta + B \sin m\theta$ where $m = 0$ so Θ is a constant that we can absorb into the arbitrary functions, we have:

$$\begin{aligned} v_{\perp}(u, t) &= \mathcal{F} \left[\pm \frac{1}{2} \ln \left(\frac{r^2}{r_0^2} \right) - t \right] + \mathcal{G} \left[\pm \frac{1}{2} \ln \left(\frac{r^2}{r_0^2} \right) + t \right] \\ &= \mathcal{F} \left[\pm \frac{1}{2} \ln \left(\frac{x^2 + z^2}{x_0^2 + z_0^2} \right) - t \right] + \mathcal{G} \left[\pm \frac{1}{2} \ln \left(\frac{x^2 + z^2}{x_0^2 + z_0^2} \right) + t \right] . \end{aligned}$$

We can also solve the Klein-Gordon equation for $m \neq 0$. Starting with the case $m = 1$, our equation becomes $\frac{\partial^2 \Sigma}{\partial t^2} = \frac{\partial^2 \Sigma}{\partial u^2} - \Sigma$. Let $s = \sqrt{t^2 - u^2}$. Now $\frac{\partial}{\partial t} = \frac{t}{s} \frac{d}{ds}$, $\frac{\partial}{\partial u} = -\frac{u}{s} \frac{d}{ds}$ and so our equation becomes:

$$\begin{aligned} \frac{t^2}{s^2} \frac{d^2 \Sigma}{ds^2} + \frac{1}{s} \frac{d\Sigma}{ds} - \frac{t^2}{s^3} \frac{d\Sigma}{ds} &= \frac{u^2}{s^2} \frac{d^2 \Sigma}{ds^2} - \frac{1}{s} \frac{d\Sigma}{ds} - \frac{u^2}{s^3} \frac{d\Sigma}{ds} - \Sigma \\ \implies \frac{d^2 \Sigma}{ds^2} + \frac{1}{s} \frac{d\Sigma}{ds} + \Sigma &= 0. \end{aligned}$$

This is a **Bessel Equation** of the form $\nu = 0$. Thus it has solution:

$$\Sigma = c_1 J_0(s) + c_2 Y_0(s),$$

where

$$\begin{aligned} J_0(s) &= \sum_{m=0}^{\infty} \frac{(-1)^m \cdot s^{2m}}{2^{2m} \cdot (m!)^2}, \\ Y_0(s) &= \frac{2}{\pi} \left[J_0(s) \cdot \left(\ln \frac{s}{2} + \Gamma \right) + \sum_{m=1}^{\infty} \frac{(-1)^{m+1} \cdot h_m \cdot s^{2m}}{2^{2m} \cdot (m!)^2} \right], \end{aligned}$$

where Γ is the Euler-Mascheroni constant, $\Gamma = \lim_{n \rightarrow \infty} (h_n - \ln n)$ and h_m is the harmonic number such that $h_m = \sum_{k=1}^m \frac{1}{k}$.

Our parameter s is valid for $t \geq u$ and so $s = 0$ is allowed, thus we discount our Y_0 solution, due to its logarithmic term. So $\Sigma = c_1 J_0(s)$. Now $v_{\perp} = \Sigma \Theta$ and so our solution is:

$$v_{\perp} = J_0(s) \cdot (A \cos \theta + B \sin \theta),$$

where we have absorbed the constant c_1 . Substituting s back to the original variables gives:

$$v_{\perp} = J_0 \left[\sqrt{t^2 - \left(\ln \frac{r}{r_0} \right)^2} \right] \cdot (A \cos \theta + B \sin \theta). \quad (3.10)$$

This can easily be extended to the case $m \neq 0$ or 1 by rescaling t and u . Thus, our final, general form for v_{\perp} is:

$$v_{\perp} = J_0 \left[m \sqrt{t^2 - \left(\ln \frac{r}{r_0} \right)^2} \right] \cdot (A \cos m\theta + B \sin m\theta). \quad (3.11)$$

Interpretion

Note the solution is only valid for $t \geq \pm \ln \frac{r}{r_0}$ and that the same final result is gained from substituting $s = \sqrt{u^2 - t^2}$ or $s = \sqrt{t^2 - u^2}$, since $J_0(s) = J_0(-s)$.

Considering the boundary of our system to be a shell at radius r_0 , we can interpret the \pm ambiguity on u as a boundary disturbance splitting into two waves; one travelling outwards (r increasing so $r > r_0$, $u = \ln \frac{r}{r_0}$ solution) and one travelling inwards (r decreasing so $r < r_0$, $u = -\ln \frac{r}{r_0}$). Note that the inequality on r here dictates the flow of information; the perturbation starts on the boundary and there is no disturbance in front of the wave, i.e. the inequality that restricts r from taking certain values until time has elapsed is interpreted as regions in the system not yet being affected by the perturbation (as the information has not yet had the time to reach there; the wave-front / information travels at a finite speed). In this Thesis, we are interested in the region inside $r = r_0$ including the origin. Thus, we are interested in the substitution $u = -\ln \frac{r}{r_0}$, with r starting at r_0 and decreasing as t evolves.

In this section, we have solved the Klein-Gordon equation analytically and in doing so found an analytical solution to our (fast) wave equation. However, through making certain substitutions we have actually solved the equation for a particular solution only, i.e. an initial condition of the form $\delta(r - r_0)$. To solve the Klein-Gordon in general, we would need to use numerical techniques. Finally, a great deal of work has been carried out on the Klein-Gordon equation; e.g. Lamb (1909, 1932) worked with this equation whilst looking at the behaviour of sound waves.

3.4.3 WKB approximation

We can also solve equation (3.7) using the WKB approximation. Substituting $v_{\perp} = e^{i\phi(r,\theta)} \cdot e^{-i\omega t}$ into $\frac{\partial^2}{\partial t^2} v_{\perp} = \left[r \frac{\partial}{\partial r} \left(r \frac{\partial}{\partial r} v_{\perp} \right) + \frac{\partial^2}{\partial \theta^2} v_{\perp} \right]$ gives:

$$-\omega^2 = \left[-r^2 \left(\frac{\partial \phi}{\partial r} \right)^2 - \left(\frac{\partial \phi}{\partial \theta} \right)^2 \right] + i \left[r^2 \left(\frac{\partial^2 \phi}{\partial r^2} \right) + r \left(\frac{\partial \phi}{\partial r} \right) + \left(\frac{\partial^2 \phi}{\partial \theta^2} \right) \right]$$

Now we make the WKB approximation that $\phi \sim \omega \gg 1$ and this leads to a first order PDE of the form:

$$\begin{aligned} \omega^2 &= r^2 p^2 + q^2 \\ \Rightarrow \mathcal{F}(r, \theta, \phi, p, q) &= \frac{1}{2} (r^2 p^2 + q^2 - \omega^2) = 0 \end{aligned}$$

where $p = \frac{\partial \phi}{\partial r}$ and $q = \frac{\partial \phi}{\partial \theta}$. Note all the imaginary terms have disappeared. We again include a half in the form of \mathcal{F} to make the equations nicer later.

Applying the method described in Section 2.4.2 gives:

$$\begin{aligned}\frac{\partial \mathcal{F}}{\partial \phi} &= 0, & \frac{\partial \mathcal{F}}{\partial p} &= r^2 p, & \frac{\partial \mathcal{F}}{\partial q} &= q \\ \frac{\partial \mathcal{F}}{\partial r} &= r p^2, & \frac{\partial \mathcal{F}}{\partial \theta} &= 0.\end{aligned}$$

Now we can apply Charpit's relations (equations 2.24 – 2.28) to generate the equations:

$$\begin{aligned}\frac{d\phi}{ds} &= \omega^2, & \frac{dp}{ds} &= -r p^2, & \frac{dq}{ds} &= 0 \\ \frac{dr}{ds} &= p r^2, & \frac{d\theta}{ds} &= q,\end{aligned}\tag{3.12}$$

where ω is the frequency of our wave and s is some parameter along the characteristic. These five ODEs can be solved using a fourth-order Runge-Kutta method, as described on page 26. The initial conditions are:

$$\phi_0 = 0, \quad r(s=0) = r_0, \quad 0 \leq \theta_0 \leq 2\pi, \quad p_0 = -\frac{\omega}{r_0}, \quad q_0 = 0,$$

where r_0 is the radius of the boundary that the disturbance starts from and p_0 is negative so this disturbance propagates towards the origin. We can also see that $q = q_0 = 0$. Finally, $\frac{d}{ds}(pr) = 0 \Rightarrow pr = p_0 r_0 = -\omega$ in agreement with the form of \mathcal{F} .

However, equations (3.12) can also be solved analytically by forming:

$$\begin{aligned}\frac{dp}{ds} / \frac{dr}{ds} &= \frac{dp}{dr} = -\frac{p}{r} \implies \log r = -\log p + \text{constant} \implies rp = -\omega \\ \text{So } \frac{dp}{ds} &= \omega p, \quad \frac{dr}{ds} = -\omega r, \quad p = -\frac{\omega}{r_0} e^{\omega s}, \quad r = r_0 e^{-\omega s},\end{aligned}\tag{3.13}$$

where the initial conditions dictate the constants of integration.

Thus, we can use our WKB solution to plot the evolution of the fast wave from an initial radius $r = 3$, in order to compare to the numerical solution given in subsection 3.4.1. This can be seen in Figure (3.11). The lines represent the front, middle and back edges of the WKB wave solution, where the pulse starts at radii of $r = 2.5, 3$ and 3.5 . The agreement between Figures (3.10) and (3.11) is excellent; the analytical and numerical solutions lie on top of each other. We can also see here how the ratio between the front and middle and between the middle and back of the pulse is preserved. The wave focuses on the origin and contracts around it. From equations (3.13) we see $r = r_0 e^{-\omega s}$, so the wave never actually reaches the origin in a finite time (due to the exponential decay of r).

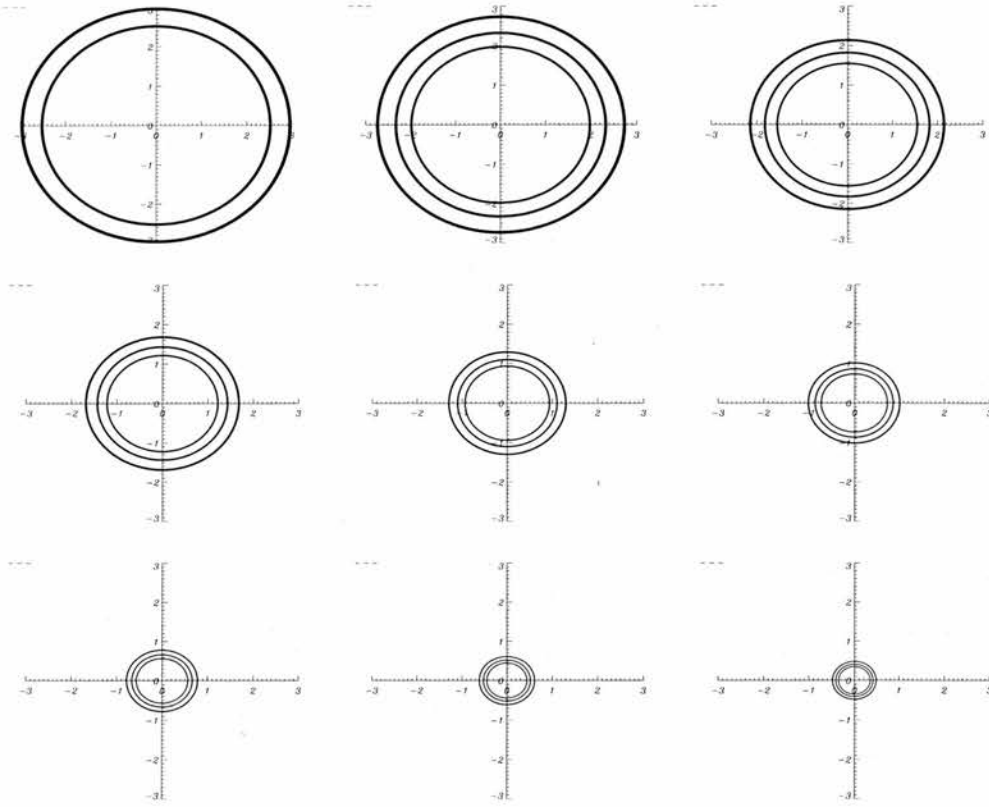


Figure 3.11: Analytical solution of v_{\perp} for WKB approximation of a fast wave sent in from a circular boundary at $r = 2.5, 3$ and 3.5 , and its resultant propagation at times (a) $t=0$, (b) $t=0.25$, (c) $t=0.5$, (d) $t = 0.75$, (e) $t=1.0$ and (f) $t=1.25$, (g) $t=1.5$, (h) $t=1.75$ and (i) $t=2.0$, labelling from top left to bottom right. The lines represent the front, middle and back edges of the WKB wave solution.

3.5 Asymmetric Pulse

As mentioned in the introduction, MHD waves in the neighbourhood of null points have been investigated before in cylindrical coordinates. In this chapter however, we can readily consider asymmetric pulses and how they propagate in the neighbourhood of coronal null points. Hence, to demonstrate the phenomena of wrapping around the null further, we consider the same numerical experiment as above in Section 3.3.1, but with a pulse being driven only on one part of the upper boundary. The pulse studied takes the form;

$$v_{\perp} = \sin(\omega t) \sin\left[\frac{\pi}{2}(x-2)\right] \begin{cases} 0 \leq x \leq 2 \\ 0 \leq t \leq \frac{\pi}{\omega} \end{cases}, z = 2 \quad (3.14)$$

The resulting propagation can be seen in Figure (3.12). Again, it is important to note the majority of the wave energy tends to accumulate at the coronal null point; and this is where wave heating

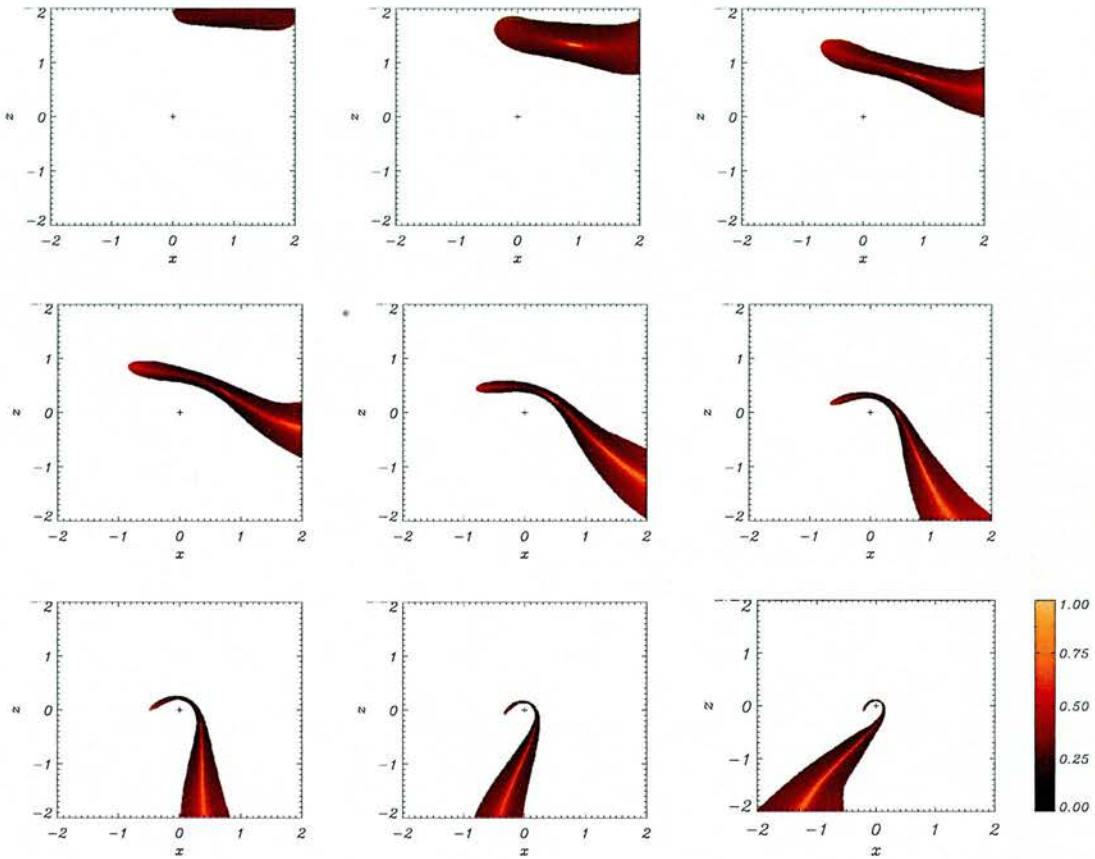


Figure 3.12: Contours of numerical simulation of v_{\perp} for a fast wave sent in from upper boundary for $0 \leq x \leq 2$, $z = 2$ and its resultant propagation at times (a) $t=0.2$, (b) $t=0.6$, (c) $t=1.0$, (d) $t=1.4$, (e) $t=1.8$ and (f) $t=2.2$, (g) $t=2.6$, (h) $t=3.0$, (i) $t=3.4$, labelling from top left to bottom right.

will occur. The growth of the current density occurs in a similar manner to that demonstrated in Figure (3.7). However, it is important to note that the more the pulse is displaced to one side, the more the boundary conditions will influence the subsequent evolution.

3.6 Conclusions

This chapter has described an investigation into the nature of fast MHD waves in the neighbourhood of a simple 2D null point. From the work detailed above, it has been seen that when a fast magnetoacoustic wave propagates near a magnetic X-type neutral point, the wave wraps itself around the null point due to refraction (at least in two dimensions). This behaviour causes a large current density to accumulate at the null and simulations have shown that this build up is exponential in time, although the exponential growth in this linear simulation will be modified by non-linearities. We also note that for the set of disturbances investigated here, there is no evidence of the X-point collapsing; rather, the current density seems to form a spike. However, it is clear that the refraction of the wave focusses the energy of the incident wave towards the null point. As seen from both the numerical work and analytical approximations, the wave continues to wrap around the null point, again and again. The physical significance of this is that any fast magnetoacoustic disturbance in the neighbourhood of a neutral point will be drawn towards the region of zero magnetic field strength and focus all of its energy at this point. Hence, this is where the build-up of current will occur and energy will be dissipated. Therefore, **fast wave heating will naturally occur at coronal null points.**

The numerical experiments and analytical work described above were all conducted using the ideal MHD equations. However, we can make some comments about the addition of resistivity into the model. For the fast magnetoacoustic wave, all the current density accumulates at the null point and appears to form a null line. Hence, no matter how small the value of the resistivity is, if we include the dissipative term, then eventually the $\frac{1}{R_m} \nabla^2 \mathbf{b}$ term in equation (3.2) will become non-negligible and dissipation will become important. In addition, since $\nabla^2 \mathbf{b}$ grows exponentially in time, the diffusion terms become important in a time that depends on $\log \eta$; as found by Craig & Watson (1992) and Craig & McClymont (1993). This means that linear wave dissipation will be very efficient. Thus, we deduce that null points will be the locations of wave energy deposition and preferential heating. This is the key finding of this chapter; null points should effectively trap and dissipate the energy contained in fast MA waves and therefore wave heating will naturally occur at coronal null points.

Chapter 4

Behaviour of Alfvén Wave near a 2D null point

4.1 Basic equations and set-up

In this chapter, we will investigate the behaviour of a linear, Alfvén wave in the neighbourhood of a simple 2D null point. This chapter is based on the second half of the paper by McLaughlin & Hood (2004). A review of previous papers that investigate the behaviour of waves (including Alfvén waves) is found in the introduction of Chapter 3 (Section 3.1).

As in Chapter 3, the basic magnetic field structure considered here is a simple 2D X-type neutral point. As mentioned previously, this simple geometry decouples the fast and Alfvén modes and hence we can investigate their behaviour in depth separately (before moving on to the more complicated coupled scenarios). We again take the magnetic field of equation (3.1), namely:

$$\mathbf{B}_0 = \frac{B_0}{L} (x, 0, -z),$$

where B_0 is a characteristic field strength and L is the length scale for magnetic field variations. Again, this particular choice of magnetic field is only valid in the neighbourhood of the null point located at $x = 0, z = 0$ (since as x and z get very large \mathbf{B}_0 also gets large, which is unphysical)

To study the nature of Alfvén wave propagation near null points, the linearised MHD equations are used. As mentioned in Section 2.2.3, the linearised MHD equations naturally decouple into two equations in this magnetic geometry; one for the fast MHD wave and second for the Alfvén wave. The equations relevant to studying the Alfvén wave are equations (2.12) and (2.13). Substituting the form of the simple 2D null point magnetic configuration (equation 3.1) into these

equations, and dropping the star indices (the fact that the equations are now non-dimensionalised is understood) gives:

$$\begin{aligned} \rho_0 \frac{\partial v_y}{\partial t} &= (\mathbf{B}_0 \cdot \nabla) b_y = \left(x \frac{\partial}{\partial x} - z \frac{\partial}{\partial z} \right) b_y, \\ \frac{\partial b_y}{\partial t} &= (\mathbf{B}_0 \cdot \nabla) v_y + \frac{1}{R_m} \nabla^2 b_y \\ &= \left(x \frac{\partial}{\partial x} - z \frac{\partial}{\partial z} \right) v_y + \frac{1}{R_m} \left(\frac{\partial^2}{\partial x^2} + \frac{\partial^2}{\partial z^2} \right) b_y, \end{aligned} \quad (4.1)$$

where as defined by equation (2.1), v_y is the velocity out of the plane that \mathbf{B}_0 defines. Hence, waves with this velocity will be transverse waves.

For now, we will neglect the magnetic resistivity (η) in the numerical simulations but will discuss its role in the conclusions. Thus, we take $\eta = 0$ which is equivalent to letting $R_m \rightarrow \infty$. This is called an **ideal** plasma. We also assume the background gas density is uniform (so $\rho_0 = 1$ under our non-dimensionalisation). A spatial variation in ρ_0 can cause phase mixing (Heyvaerts & Priest 1983; De Moortel, Hood & Arber 2000); this idea will be re-visited in Chapter 8.

These equations can now be combined to form a single wave equation:

$$\frac{\partial^2}{\partial t^2} v_y = (\mathbf{B}_0 \cdot \nabla)^2 v_y, = \left(x \frac{\partial}{\partial x} - z \frac{\partial}{\partial z} \right)^2 v_y. \quad (4.2)$$

This is the primary equation we will be looking at in this chapter (although the form of equations 4.1 is easier to work with numerically). Recall that in its derivation, we have assumed linearised behaviour in an ideal, 2D plasma with uniform density.

4.2 Numerical simulation

We solve equations (4.1) numerically using the same two-step Lax-Wendroff scheme as described in Section 3.3 (and on page 25). We initially consider a box ($0 \leq x \leq 2, 0 \leq z \leq 2$) with a single wave pulse coming in across half of the top boundary ($0 \leq x \leq 1$). We chose such a pulse because, as shown in Figure 4.1, we found that the Alfvén wave spreads out along the field lines as it propagates and hence this choice of boundary condition illustrated this effect much clearer. The full boundary conditions were:

$$v_y(x, 2) = \begin{cases} \frac{1}{2} \sin \omega t (1 + \cos \pi x) & \text{for } 0 \leq x \leq 1, \quad 0 \leq t \leq \frac{\pi}{\omega} \\ 0 & \text{otherwise} \end{cases}$$

$$\left. \frac{\partial}{\partial x} v_y \right|_{x=2} = 0, \quad \left. \frac{\partial}{\partial x} v_y \right|_{x=0} = 0, \quad \left. \frac{\partial}{\partial z} v_y \right|_{z=0} = 0 .$$

Tests show that the central behaviour is unaffected by these choices of boundary conditions. The other boundary conditions follow from the remaining equations and the solenoidal condition, $\nabla \cdot \mathbf{b} = 0$. Note that we have used a slightly different initial pulse to those in the fast wave investigation. This is because the field lines (see Figure 3.1) leave the box and we know that the Alfvén wave follows the field lines. Hence, we made this choice of initial pulse in case reflections from the side boundaries influenced the subsequent evolution. We have also only modelled the Alfvén wave in the top right quadrant of Figure 3.1. This is because the system is symmetrical and so once we know what is happening for $x \geq 0, z \geq 0$ we also know the behaviour for $x \leq 0, z \geq 0$, and because the wave never actually propagates into the region $z < 0$. Hence, choosing a box $0 \leq x \leq 2, 0 \leq z \leq 2$ allows us to fully utilise our 1000×1000 resolution. We take $\omega = 2\pi$ for our simulations.

We found that the linear Alfvén wave travels down from the top boundary and begins to spread out, following the field lines. As the wave approaches the lower boundary (the separatrix), it thins but keeps its original amplitude. The wave eventually accumulates very near the separatrix; defined by the x axis. This can be seen in Figure 4.1. The Alfvén wave is trapped on the field line it is excited on, and this agrees with the theory of Alfvén waves discussed in Section 1.5.5, i.e. the wave is unable to propagate across the magnetic field.

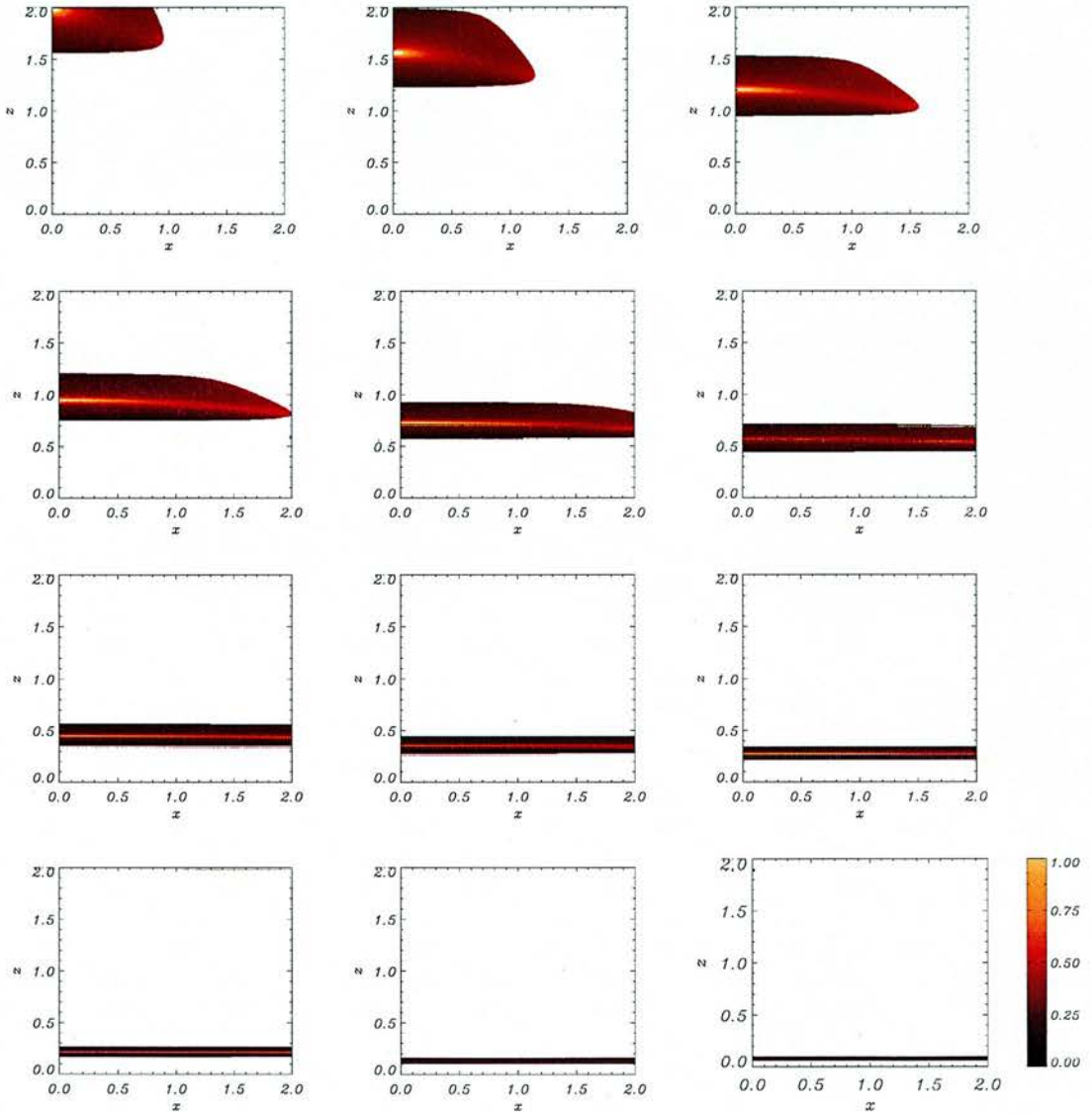


Figure 4.1: Contours of numerical simulation of v_y for an Alfvén wave sent in from upper boundary for $0 \leq x \leq 1$ and its resultant propagation at times (a) $t=0.25$, (b) $t=0.5$, (c) $t=0.75$, (d) $t=1.0$, (e) $t=1.25$, (f) $t=1.5$, (g) $t=1.75$, (h) $t=2.0$, (i) $t=2.25$, (j) $t=2.5$, (k) $t=3.0$, (l) $t=3.5$, labelling from top left to bottom right.

4.3 Analytical work

As mentioned in Section 3.3.2, we can increase our understanding of the numerical simulations presented here by complementing them with analytical models. Here we present two such models: a D'Alembert solution and a WKB approximation.

4.3.1 D'Alembert solution

The Alfvén equation we have to solve takes the form:

$$\frac{\partial^2 v_y}{\partial t^2} = \left(x \frac{\partial}{\partial x} - z \frac{\partial}{\partial z} \right)^2 v_y ,$$

and this can be solved using the method of characteristics. Writing $\frac{\partial}{\partial s} = \left(x \frac{\partial}{\partial x} - z \frac{\partial}{\partial z} \right)$ and comparing the original equation with $\frac{\partial v_y}{\partial s} = \frac{\partial x}{\partial s} \frac{\partial v_y}{\partial x} - \frac{\partial z}{\partial s} \frac{\partial v_y}{\partial z}$ leads to:

$$x = x_0 e^s , \quad z = z_0 e^{-s} , \quad (4.3)$$

where x_0 and z_0 are the starting positions of our characteristics. In our simulation, $z_0 = 2$. Thus, our equation, $\frac{\partial^2 v_y}{\partial t^2} = \frac{\partial^2 v_y}{\partial s^2}$ can be solved with a D'Alembert solution such that:

$$v_y = \mathcal{F}(x_0) \mathcal{G}(t - s) .$$

In order to compare these analytical results with the numerical results above, we substitute the same initial conditions into the D'Alembert solution, i.e. $\mathcal{F}(x_0) = \frac{1}{2} [1 + \cos(\pi x_0)]$ and $\mathcal{G}(t) = \sin(\omega t)$ to get the analytical solution for v_y , namely:

$$v_y(x, z, t) = \begin{cases} \left[1 + \cos\left(\frac{\pi x z}{z_0}\right) \right] \sin \omega \left(t + \log \frac{z}{z_0} \right) & \text{for } \begin{cases} 0 \leq t + \log \frac{z}{z_0} \leq \frac{\pi}{\omega} \\ 0 \leq \frac{\pi x z}{z_0} \leq 1 \end{cases} \\ 0 & \text{elsewhere} \end{cases} \quad (4.4)$$

where $xz = x_0 z_0$ and $s = -\log \frac{z}{z_0}$ from equations (4.3).

Figure 4.2 shows contours of this analytical form of v_y plotted at the same times as in our numerical simulation. The agreement between the analytical and numerical results is excellent (the contours lie on top of each other and $v_{y \text{ analytical}} - v_{y \text{ numerical}}$ is essentially zero), even though the analytical solution does not satisfy the numerical boundary conditions. This comparison can be seen in Figure 4.3, which shows an overplot of a numerical simulation (shaded area) and our analytical solution (blue lines). In the later subfigures, you can also really see the Alfvén wave slowing down, due to its $z = z_0 e^{-s}$ nature.

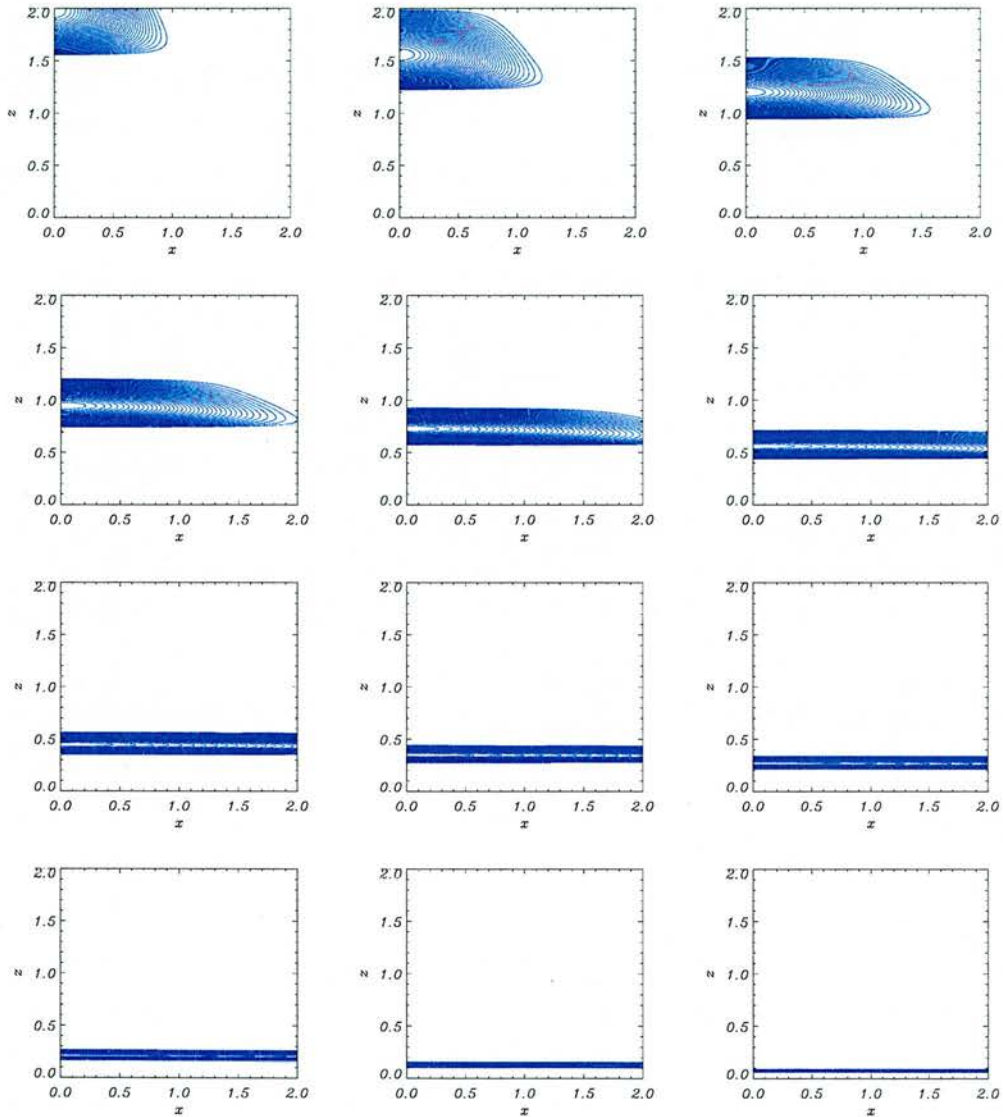


Figure 4.2: Contours of v_y for analytical solution for Alfvén wave sent in from upper boundary for $0 \leq x \leq 1$ and its resultant propagation at times (a) $t=0.25$, (b) $t=0.5$, (c) $t=0.75$, (d) $t = 1.0$, (e) $t=1.25$, (f) $t=1.5$, (g) $t = 1.75$, (h) $t=2.0$, (i) $t=2.25$, (j) $t = 2.5$, (k) $t=3.0$, (l) $t=3.5$, labelling from top left to bottom right.

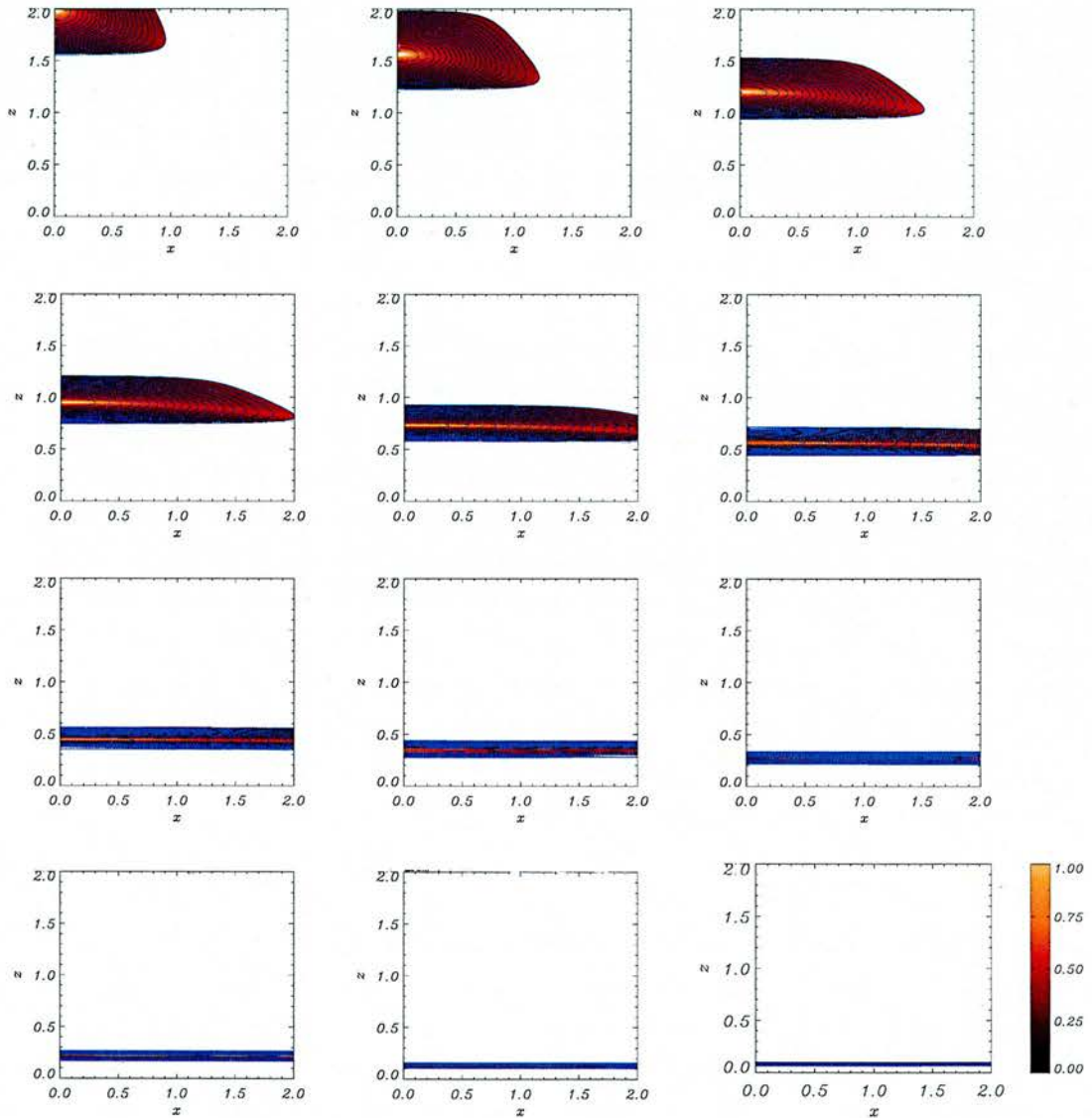


Figure 4.3: Comparison of numerical simulation and analytical solution for Alfvén wave sent in from upper boundary for $0 \leq x \leq 1$ and its resultant propagation at times (a) $t=0.25$, (b) $t=0.5$, (c) $t=0.75$, (d) $t = 1.0$, (e) $t=1.25$, (f) $t=1.5$, (g) $t = 1.75$, (h) $t=2.0$, (i) $t=2.25$, (j) $t = 2.5$, (k) $t=3.0$, (l) $t=3.5$, labelling from top left to bottom right.

4.3.2 WKB approximation

As well as a D'Alembert analytical solution, we can also approximately solve equations (4.2) for the Alfvén wave to gain more insight into the numerical simulations. As in Section 2.4.2, substituting $v_y = e^{i\phi(x,z)} \cdot e^{-i\omega t}$ into $\frac{\partial^2 v_y}{\partial t^2} = (x\frac{\partial}{\partial x} - z\frac{\partial}{\partial z})^2 v_y$ gives:

$$-\omega^2 = \left[-x^2 \left(\frac{\partial \phi}{\partial x} \right)^2 - 2xz \left(\frac{\partial \phi}{\partial x} \right) \left(\frac{\partial \phi}{\partial z} \right) - z^2 \left(\frac{\partial \phi}{\partial z} \right)^2 \right] \\ + i \left[x^2 \left(\frac{\partial^2 \phi}{\partial x^2} \right) + x \left(\frac{\partial \phi}{\partial x} \right) + 2xz \left(\frac{\partial^2 \phi}{\partial x \partial z} \right) + z^2 \left(\frac{\partial^2 \phi}{\partial z^2} \right) + z \left(\frac{\partial \phi}{\partial z} \right) \right]$$

Now we make the WKB approximation that $\phi \sim \omega \gg 1$, leading to a first order PDE of the form:

$$\omega^2 = (xp - zq)^2 \\ \Rightarrow \mathcal{F}(x, z, \phi, p, q) = 0 = \frac{1}{2}(xp - zq)^2 - \frac{1}{2}\omega^2$$

where $p = \frac{\partial \phi}{\partial x}$ and $q = \frac{\partial \phi}{\partial z}$ and \mathcal{F} is a non-linear PDE (we include a half in the form of \mathcal{F} to make the equations nicer later). Note all the imaginary terms have disappeared under the WKB approximation.

We now wish to apply Charpit's method. Thus, we first need to work out the following quantities:

$$\frac{\partial \mathcal{F}}{\partial \phi} = 0, \quad \frac{\partial \mathcal{F}}{\partial p} = x(xp - zq), \quad \frac{\partial \mathcal{F}}{\partial q} = -z(xp - zq) \\ \frac{\partial \mathcal{F}}{\partial x} = p(xp - zq), \quad \frac{\partial \mathcal{F}}{\partial z} = -q(xp - zq)$$

Now we can apply Charpit's equations (equations 2.24 – 2.28). This gives:

$$\frac{d\phi}{ds} = \omega^2, \quad \frac{dp}{ds} = -p\xi, \quad \frac{dq}{ds} = q\xi \\ \frac{dx}{ds} = x\xi, \quad \frac{dz}{ds} = -z\xi \tag{4.5}$$

where ω is the frequency of our wave, s is some parameter along the characteristic. Also $\xi = (xp - zq)$, but note ξ is a constant because:

$$\frac{d\xi}{ds} = \frac{d}{ds}(xp) - \frac{d}{ds}(zq) = 0 \Rightarrow \xi = \text{constant} = x_0 p_0 - z_0 q_0$$

So our equations (4.5) reduce to:

$$\frac{dp}{d\tau} = -p, \quad \frac{dq}{d\tau} = q, \quad \frac{dx}{d\tau} = x, \quad \frac{dz}{d\tau} = -z,$$

where $\tau = \xi s$. These can be easily solved to give:

$$\phi = \omega^2 s, \quad p = p_0 e^{-\tau}, \quad q = q_0 e^{\tau}, \quad x = x_0 e^{\tau}, \quad z = z_0 e^{-\tau} \quad (4.6)$$

We could also have solved equations (4.5) numerically using a fourth-order Runge-Kutta method, as mentioned in Section 3.3.2, although it turned out that the equations were simple enough to be solved by hand in this case. The initial conditions would have been:

$$\phi_0 = 0, \quad 0 \leq x_0 \leq 1, \quad z_0 = 2, \quad p_0 = 0, \quad q_0 = -\frac{\omega}{z_0}$$

From these, we can see that $\xi = \omega$. By using these initial conditions in equations (4.6), we obtain our final forms for our WKB approximations:

$$\phi = \omega^2 s, \quad p = 0, \quad q = -\frac{\omega}{z_0} e^{\tau}, \quad x = x_0 e^{\tau}, \quad z = z_0 e^{-\tau} \quad (4.7)$$

These equations are the same as the forms for x and z we obtained with our D'Alembert solution, namely equations (4.3). Here $\tau = \omega s = t$.

We can also use our WKB solution to plot the particle paths of individual elements from the initial wave. In Figure 4.4, we see the evolution of fluid elements that begin at points $x = 0.1, 0.2, \dots, 1$ along $z = 2$, after a time $t = 1.25$. Notice how the elements simply travel along the fieldlines they start on. They have all also travelled a different distance along their respective fieldlines, but still form a straight line. In accordance with equation (4.7), the front edge of the wave has reached $z = z_0 e^{-t}$, i.e. $z = 2 \times e^{-1.25} = 0.57$.

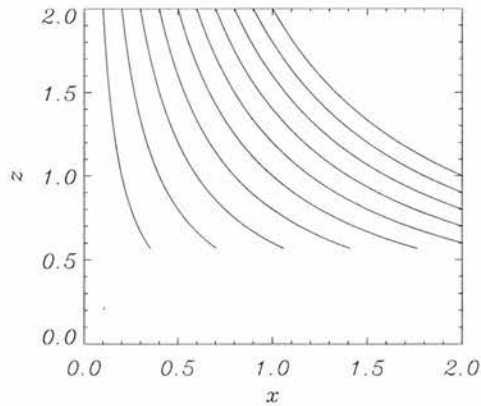


Figure 4.4: Plots of WKB solution for Alfvén wave sent in from the upper boundary and its resultant rays after a time $t = 1.25$ for starting points of $x = 0.1, 0.2, \dots, 1$ along $z = 2$.

4.4 Behaviour of j_x and j_z

As for the fast MA wave investigated in Chapter 3, for the Alfvén wave we have a spatially varying perturbed magnetic field and hence current is forming, given by $\frac{1}{\mu}(\nabla \times \mathbf{b}) = (j_x, 0, j_z)$. In the Alfvén case only $j_x = -\frac{1}{\mu} \frac{\partial b_y}{\partial z}$ and $j_z = \frac{1}{\mu} \frac{\partial b_y}{\partial x}$ are present. We could obtain these quantities by performing further numerical calculations, or alternatively we can use our analytical D'Alembert solution to calculate b_y , j_x and j_z :

$$b_y = - \left[1 + \cos \left(\frac{\pi x z}{z_0} \right) \right] \sin \omega \left(t + \log \frac{z}{z_0} \right), \quad (4.8)$$

$$j_x = \frac{\omega}{z} \left[1 + \cos \left(\frac{\pi x z}{z_0} \right) \right] \cos \omega \left(t + \log \frac{z}{z_0} \right) - \frac{\pi x}{z_0} \sin \left(\frac{\pi x z}{z_0} \right) \sin \omega \left(t + \log \frac{z}{z_0} \right) \quad (4.9)$$

$$j_z = \frac{\pi z}{z_0} \sin \left(\frac{\pi x z}{z_0} \right) \sin \omega \left(t + \log \frac{z}{z_0} \right) \quad (4.10)$$

$$\text{all for } \begin{cases} 0 \leq t + \log \frac{z}{z_0} \leq \frac{\pi}{\omega} \\ 0 \leq \frac{\pi x z}{z_0} \leq 1 \end{cases}.$$

The evolution of the current can be seen in Figures 4.5 and 4.7.

From Figure 4.5, we see that j_x spreads out along the field lines, accumulating along the separatrix ($z = 0$). j_x also takes a discontinuous form; this is due to our choice of initial conditions and this is confirmed by the analytical solution. j_x also increases in time. From equation (4.9), we see that j_x grows like $\frac{1}{z}$ and thus, in accordance with equation (4.3), this means j_x grows like e^s , i.e. grows as e^t (since $s = t + \text{constant}$ in the D'Alembert solution). The behaviour of the maximum of j_x with time can be seen in Figure 4.6; the slope of the line is +1 in agreement with our analytical solution.

The behaviour of j_z can be seen in Figure 4.7. j_z takes the spatial form of the initial pulse and, in the same way as v_y , spreads out along the fieldlines. It decays in amplitude as it approaches the separatrix. The analytical solution (equation 4.10) shows that it behaves like z (and z is going to zero). Thus, in accordance with equation (4.3) j_z decays as e^{-t} . The behaviour of the maximum of j_z with time can be seen in Figure 4.8. In this case, the slope of the line is -1 in agreement (again) with our analytical solution.

Hence, the Alfvén wave causes current density to build up along the separatrix (through the j_x component).

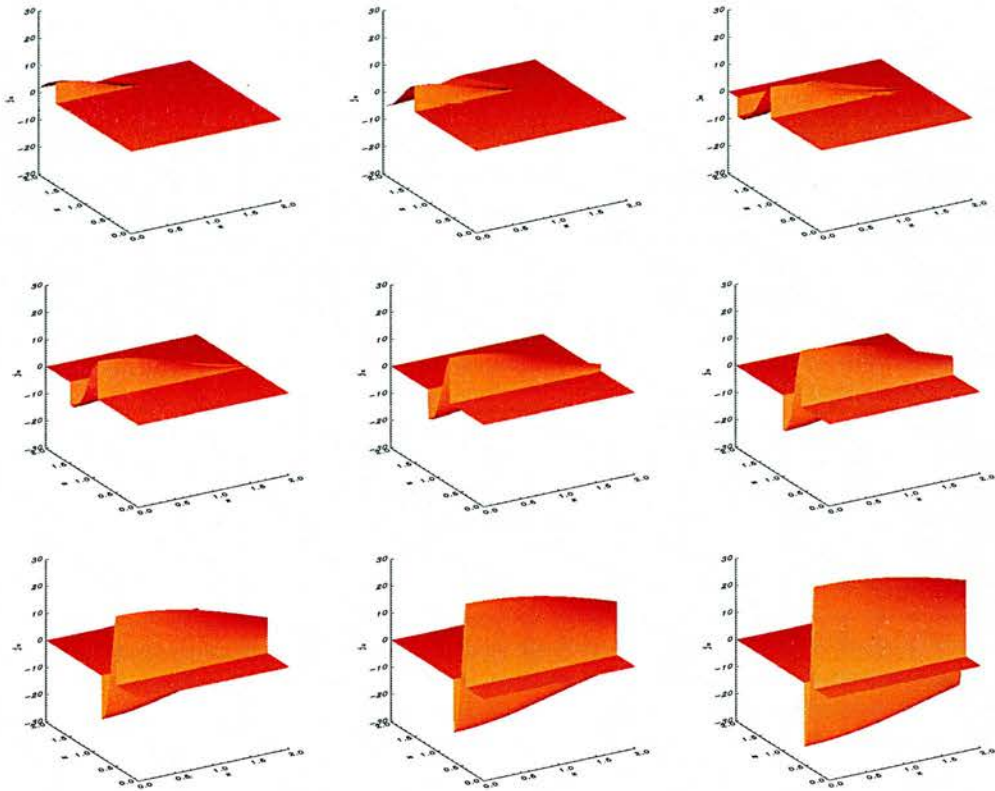


Figure 4.5: Shaded surfaces showing the build up of j_x at times (a) $t=0.2$, (b) $t=0.4$, (c) $t=0.6$, (d) $t=0.8$, (e) $t=1.0$, (f) $t=1.2$, (g) $t=1.4$, (h) $t=1.6$ and (i) $t=1.8$, labelling from top left to bottom right. The x -axis represents the separatrix.

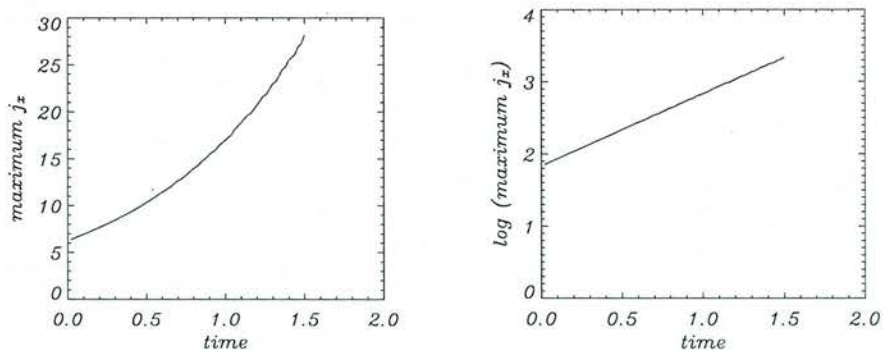


Figure 4.6: Maximum j_x against time elapsed (left), $\log(\text{maximum } j_x)$ against time elapsed (right). The slope of the line is +1.

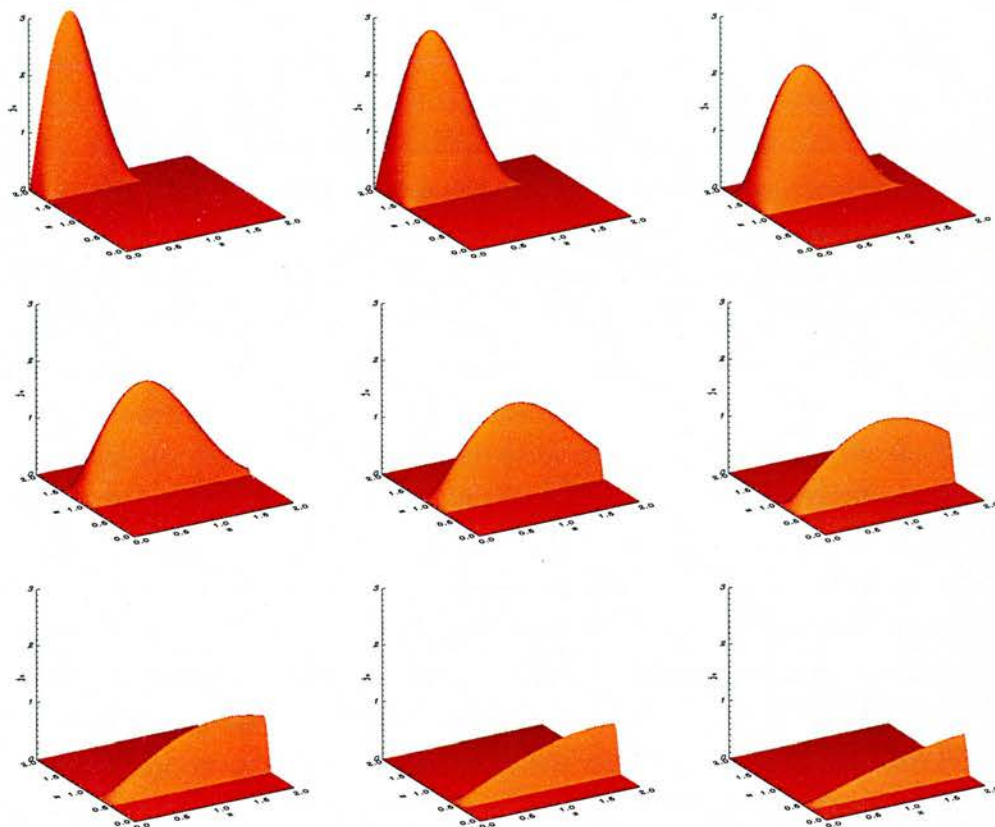


Figure 4.7: Shaded surfaces showing the build up of j_z at times (a) $t=0.2$, (b) $t=0.4$, (c) $t=0.6$, (d) $t=0.8$, (e) $t=1.0$, (f) $t=1.2$, (g) $t=1.4$, (h) $t=1.6$ and (i) $t=1.8$, labelling from top left to bottom right.

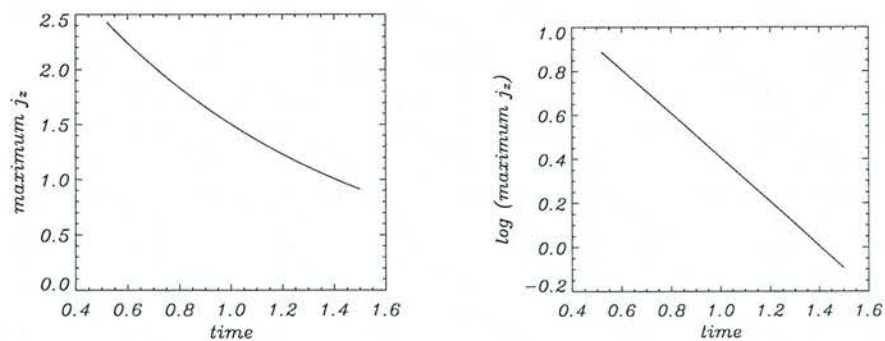


Figure 4.8: Maximum j_z against time elapsed (left), $\log(\text{maximum } j_z)$ against time elapsed (right). The slope of the line is -1 .

4.5 Conclusions

This chapter has described an investigation into the nature of linear Alfvén waves in the neighbourhood of a simple 2D null point. The results show that the Alfvén wave propagates along the field lines, accumulating on the separatrix and hence, due to symmetry, along the separatrices. The wave also thins and stretches along the separatrices. The wave thins but keeps its original amplitude. The current j_x increases and accumulates along the separatrix, whilst j_z decays away. This is seen in both the analytical and numerical work.

The work carried out so far in this chapter was in an **ideal** plasma, and we now consider the effect of including resistivity. Recall equation (4.1) for the Alfvén wave:

$$\begin{aligned}\frac{\partial b_y}{\partial t} &= \left(x \frac{\partial}{\partial x} - z \frac{\partial}{\partial z}\right) v_y + \frac{1}{R_m} \left(\frac{\partial^2}{\partial x^2} + \frac{\partial^2}{\partial z^2}\right) b_y \\ &= \left(x \frac{\partial}{\partial x} - z \frac{\partial}{\partial z}\right) v_y + \frac{1}{R_m} \frac{\partial}{\partial x} j_z - \frac{1}{R_m} \frac{\partial}{\partial z} j_x\end{aligned}$$

In order for the resistive terms to become important (terms involving η or $\frac{1}{R_m}$), they have to become comparable to the convective term; $(x \frac{\partial}{\partial x} - z \frac{\partial}{\partial z}) v_y$. So we have to calculate the behaviour of $\frac{\partial}{\partial x} j_z$ and the behaviour of $\frac{\partial}{\partial z} j_x$ over time. From Figure 4.9, we see that the maximum of $\frac{\partial}{\partial x} j_z$ decays exponentially over time, and from Figure 4.10, we see that the maximum of $-\frac{\partial}{\partial z} j_x$ increase exponentially over time.

Now consider $\nabla^2 \mathbf{b} = \frac{\partial}{\partial x} \frac{\partial b_y}{\partial x} + \frac{\partial}{\partial z} \frac{\partial b_y}{\partial z} = \frac{\partial j_z}{\partial x} + \frac{\partial j_x}{\partial z}$. As shown above, $\frac{\partial j_z}{\partial x}$ decays away (exponentially) but $\frac{\partial j_x}{\partial z}$ increases (exponentially). We have also seen that the current accumulates along the separatrices. Hence, eventually (due to its exponential increase), the resistive term, $\eta \frac{\partial^2 b_y}{\partial z^2} = \eta \frac{\partial j_x}{\partial z}$, will become important, no matter how small the value of η , whereas the resistive terms involving $\frac{\partial}{\partial x} j_z$ will become negligible. However, with realistic coronal values of the resistivity (page 6), this will only occur very close to the separatrix (and by symmetry the separatrices). Hence, **all the Alfvén wave energy will be dissipated along the separatrices**. This is a different behaviour to that of the fast wave in the sense that the two wave types deposit all their wave energy at different areas (along the separatrices as opposed to the null point), although the phenomenon of depositing wave energy in a specific area is common to both.

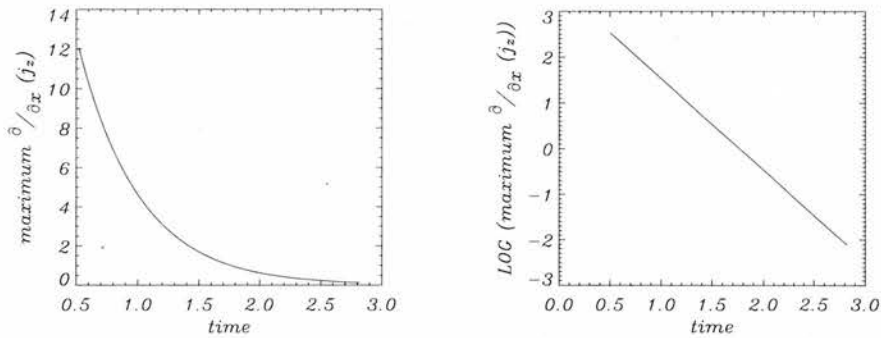


Figure 4.9: Plot of maximum $\frac{\partial}{\partial x} j_z$ against time (left), plot of log maximum $\frac{\partial}{\partial x} j_z$ against time (right). The slope of the line is -2 .

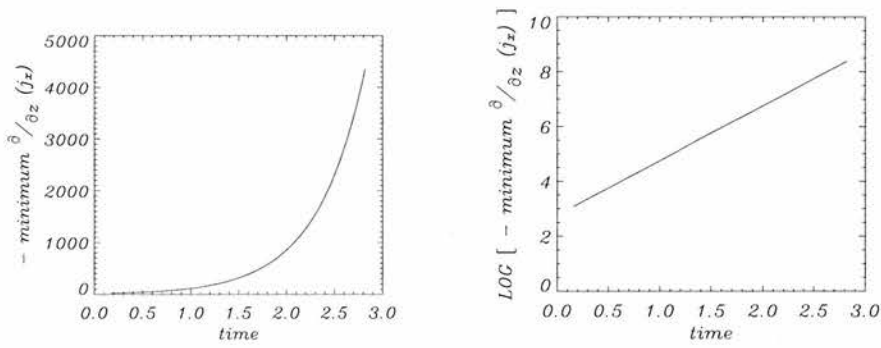


Figure 4.10: Plot of - minimum $\frac{\partial}{\partial z} j_x$ against time (left), plot of $-\log$ minimum $\frac{\partial}{\partial z} j_x$ against time (right). The slope of the line is $+2$.

Finally, the model was run again numerically but this time with resistivity included (with $R_m = 10^3$). As predicted, the Alfvén wave showed the same behaviour as before; it followed the field lines and accumulated close to the separatrix. However, once the wave had reached this area, its magnitude started to slowly decrease (due to the dissipation). Since dissipation spreads out a wave, there was an idea that the wave may be able to cross the (previously uncrossable) separatrix if the dissipation spread the wave out enough. However, we did not find any evidence for this crossing. There was also still current build-up (via j_x) along the separatrix. Thus, the x -axis remained the area where preferential heating occurred in this model.

Chapter 5

MHD wave propagation in the neighbourhood of two null points

5.1 Introduction

Chapters 3 and 4 detailed the propagation of the fast MHD wave and the Alfvén wave in the neighbourhood of a single 2D null point¹. The two investigations threw up some very interesting results; the fast wave was found to focus all its wave energy at the null resulting in (exponential) current build-up there. Also, the Alfvén wave was found to follow the field lines and dissipate all of its wave energy along the separatrix (and by symmetry; the separatrices). Thus, though both wave modes cause preferential heating in different topological areas, the phenomenon of dissipating the majority of the wave energy at a specific place is a feature of both wave types. It also highlights the importance the topology of the magnetic field plays in the nature of the system.

However, we now have to question whether or not these findings are unique to the simple 2D magnetic configuration, or if the ideas carry through to more complicated configurations. The specific question asked by this chapter is *do the findings carry through to a configuration of more than one null point?* Thus, the nature of fast magnetoacoustic and Alfvén waves is investigated in a $\beta = 0$ plasma in the neighbourhood of a pair of two-dimensional null points. This gives an indication of wave propagation in the low β solar corona, for a more complicated magnetic configuration than that looked at by McLaughlin & Hood (2004). It can be argued that null points appear in pairs, (e.g. by a local bifurcation) which makes it relevant to investigate multiple null point topologies. A double null point may arise as a bifurcation of a single 2D null point (Galsgaard *et al.* 1996; Brown & Priest 1998)

¹These two investigations were carried out in a $\beta = 0$ plasma; so the slow wave was absent.

Multiple null point topologies have also been investigated by various authors. Galsgaard *et al.* (1996) looked at the dynamic reconnection properties of a 3D double null. They investigated responses of the magnetic field to specific perturbations on the boundaries of a 3D box; they tilted the spine axis to form a pure $m = 1$ mode. They found that for a perturbation parallel or orthogonal to the separator (between the two nulls), current accumulation occurred in the separator plane perpendicular to the direction in which the spine was moved. For any other orientation, the current was focussed along the separator line. In the model, the boundary motions move the field lines but do not return them to their original positions. Thus, the Poynting flux induced by the imposed motion (and then fixing the field after the motion is complete) accumulates at the resulting current sheet and provides the energy released in the reconnection. However, if the boundary motions are simply due to the passing of incoming waves through the boundary, then it is not clear that the current sheet will form. If this is the case, will the energy in the wave, again due to the Poynting flux through the boundary, dissipate or simply pass through one of the other boundaries?

Galsgaard & Nordlund (1997) found that when magnetic structures containing many null points are perturbed, current accumulates along separator lines. The perturbations used were random shear motions on two opposite boundaries. Again, the field lines were not returned to their original position. Galsgaard *et al.* (1997a) looked at shearing a 3D potential null point pair, with continuous (opposite) shear on two opposite boundaries (parallel to the separator). This generated a wave pulse that travelled towards the interior of the domain from both directions, and resulted in current accumulation along the separator line with maximum value at the null points. From these experiments (which share a lot with Galsgaard *et al.* 1996) it was concluded that to drive current along the full length of the separator line, the perturbation wavelength had to be longer than the length of the separator line. Galsgaard *et al.* (1997b) looked at perturbations in 3D magnetic configurations containing a double null point pair connected by a separator. The boundary motions used were very similar to those described above (i.e. shear the boundary and fix). Their experiments showed that the nulls can either accumulate current individually or act together to produce a singular current collapse along the separator. However, in all these previous works the boundary conditions used have tried to mimic the effect of photospheric footpoint motions by moving the boundary and holding it fixed. This chapter will look at the 2D null point pair and investigate the propagation and transient behaviour of an individual wave pulse entering the magnetic structure.

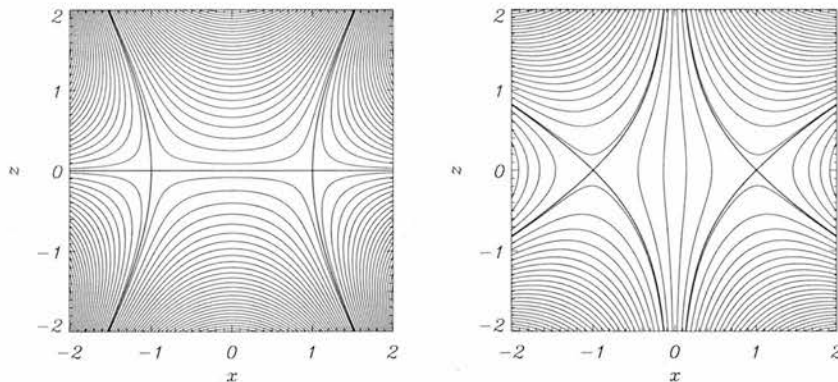


Figure 5.1: *Left* Magnetic field configuration containing two nulls joined by a separator. *Right* Magnetic field configuration containing two nulls not joined by a separator.

5.2 Basic Equations and set-up

In this chapter, we will investigate the behaviour of the linear fast MA wave and Alfvén wave in the neighbourhood of a simple 2D two null points configuration. This chapter is based on the paper by McLaughlin & Hood (2005).

The basic magnetic structure is taken as a simple 2D two null points configuration. However, there are two such configurations to consider; one containing a **separator** and one that does not (as defined on page 10). The aim of studying waves in a 2D configuration is one of simplicity; the individual effects are much easier to identify when there is no coupling between the fast and Alfvén modes (as reasoned in Chapters 3 and 4). The magnetic field with a separator is taken as:

$$\mathbf{B}_0 = \frac{B_0}{L^2} (x^2 - z^2 - L^2, 0, -2xz), \quad (5.1)$$

where B_0 is a characteristic field strength and L is the length scale for magnetic field variations. This configuration can be seen on the left hand side of Figure 5.1. The other magnetic configuration considered takes the form:

$$\mathbf{B}_0 = \frac{B_0}{L^2} (2xz, 0, x^2 - z^2 - L^2), \quad (5.2)$$

and can be seen on the right hand side of Figure (5.1). Obviously, these magnetic configurations are no longer valid far away from the null points, as the field strength tends to infinity. Chapter 6 looks at a magnetic configuration that falls off as x and z get very large.

As in Chapters 3 and 4, to study the nature of wave propagation near null points, the linearised MHD equations are used. The derivation of the linearised, non-dimensionalised equations for a $\beta = 0$ plasma can be found in Chapter 2. As mention is Section 2.2.3, the linearised MHD equations naturally decouple into two equations; one for the fast MHD wave and second for the

Alfvén wave. The equations relevant to studying the nature of the fast MA wave in this chapter are equations (2.10) and (2.11). Thus, defining the background field as $\mathbf{B}_0 = (B_x, 0, B_z)$ and the perturbation as $\mathbf{b} = (b_x, 0, b_z)$, we obtain:

$$\begin{aligned} \rho_0 \frac{\partial}{\partial t} v_{\perp} &= v_A^2(x, z) \left(\frac{\partial b_z}{\partial x} - \frac{\partial b_x}{\partial z} \right) \\ \frac{\partial b_x}{\partial t} &= -\frac{\partial}{\partial z} v_{\perp} + \frac{1}{R_m} \left(\frac{\partial^2}{\partial x^2} + \frac{\partial^2}{\partial z^2} \right) b_x, \\ \frac{\partial b_z}{\partial t} &= \frac{\partial}{\partial x} v_{\perp} + \frac{1}{R_m} \left(\frac{\partial^2}{\partial x^2} + \frac{\partial^2}{\partial z^2} \right) b_z, \end{aligned} \quad (5.3)$$

where the Alfvén speed, $v_A(x, z) = \sqrt{B_x^2 + B_z^2}$ and v_{\perp} is velocity as defined in the Chapter 2 (page 20). Note that these are the same equations as (3.2), but with a more general form for the (background) Alfvén speed (v_A). We will again neglect the magnetic resistivity (η) in our investigations, but will discuss its role in the conclusions. Thus, we consider an ideal plasma ($\eta = 0$ or $R_m \rightarrow \infty$). Again, we also assume the background gas density is uniform (so $\rho_0 = 1$ under our non-dimensionalisation). These simplifications allow us to combine the above equations into a single wave equation:

$$\frac{\partial^2}{\partial t^2} v_{\perp} = (B_x^2 + B_z^2) \left(\frac{\partial^2}{\partial x^2} + \frac{\partial^2}{\partial z^2} \right) v_{\perp}. \quad (5.4)$$

This is the wave equation of the form of equation (1.23). This is the primary equation for the fast MA wave we will be looking at in this chapter (although the form of equations (5.3) is easier to solve numerically). Recall that in its derivation, we have assumed linearised behaviour in an ideal, $\beta = 0$, 2D plasma with uniform density.

The equations relevant to studying the Alfvén wave are equations (2.12) and (2.13). Again defining $\mathbf{B}_0 = (B_x, 0, B_z)$ and $\mathbf{b} = (0, b_y, 0)$ yields:

$$\begin{aligned} \rho_0 \frac{\partial v_y}{\partial t} &= (\mathbf{B}_0 \cdot \nabla) b_y = \left(B_x \frac{\partial}{\partial x} + B_z \frac{\partial}{\partial z} \right) b_y, \\ \frac{\partial b_y}{\partial t} &= (\mathbf{B}_0 \cdot \nabla) v_y + \frac{1}{R_m} \nabla^2 b_y \\ &= \left(B_x \frac{\partial}{\partial x} + B_z \frac{\partial}{\partial z} \right) v_y + \frac{1}{R_m} \left(\frac{\partial^2}{\partial x^2} + \frac{\partial^2}{\partial z^2} \right) b_y, \end{aligned} \quad (5.5)$$

where as defined by equation (2.1), v_y is the velocity out of the plane that \mathbf{B}_0 defines. Hence, waves with this velocity will be transverse waves.

As above, we will neglect the dissipation terms and consider a uniform background density ($R_m \rightarrow \infty$, $\rho_0 = 1$). Hence, these equations can also be combined to form a single wave equation:

$$\frac{\partial^2}{\partial t^2} v_y = (\mathbf{B}_0 \cdot \nabla)^2 v_y, = \left(B_x \frac{\partial}{\partial x} + B_z \frac{\partial}{\partial z} \right)^2 v_y. \quad (5.6)$$

This is the primary equation we will be looking at for the Alfvén wave in this chapter. In its derivation, we have assumed linearised behaviour in an ideal, $\beta = 0$, 2D plasma with uniform density.

Thus, equations (5.4) and (5.6) will allow us to study the behaviour of the fast and Alfvén waves. Note that these are general equations, whereby taking $B_x = x$ and $B_z = -z$, i.e. the magnetic configuration considered in Chapters 3 and 4, returns us to equations (3.3) and (4.2) that we have studied previously. We will also call upon the general forms of equations (5.4) and (5.6) in Chapter 6.

5.3 Fast Waves in the neighbourhood of two null points

We consider the effect of sending a fast magnetoacoustic wave into these two magnetic configurations from the top and side boundaries. Unlike in Chapter 3, we also consider the effect of sending in a wave pulse from a side boundary because the magnetic configuration does not possess rotational symmetry. Also, since the fast MA wave can cross field lines, it behaves identically across both magnetic configurations (Figure 5.1) and so we only have two cases to investigate, i.e. equation (5.4) is true for both magnetic configurations because the Alfvén speed, $v_A(x, z)$, is equal to $\sqrt{B_x^2 + B_z^2} = \left[(x^2 + z^2)^2 - 2(x^2 - z^2) + 1 \right]^{\frac{1}{2}}$ for both configurations (for both equations 5.1 and 5.2). However, equation (5.6) for the Alfvén wave does depend upon the magnetic configuration and so that section will involve more experiments.

5.3.1 Upper Boundary

We solve the linearised MHD equations (5.3) for the fast wave numerically using our two-step Lax-Wendroff scheme (page 25). The numerical scheme is run in a box with $-3 \leq x \leq 3$ and $-4 \leq z \leq 2$, with our attention focused on $-2 \leq x \leq 2$ and $-2 \leq z \leq 2$ (to minimise the effects of the boundaries). For a single wave pulse coming in from the top boundary, the boundary conditions are taken as:

$$v_{\perp}(x, 2) = \begin{cases} \sin \omega t & \text{for } 0 \leq t \leq \frac{\pi}{\omega} \\ 0 & \text{otherwise} \end{cases},$$

$$\left. \frac{\partial}{\partial x} v_{\perp} \right|_{x=-3} = 0, \quad \left. \frac{\partial}{\partial x} v_{\perp} \right|_{x=3} = 0, \quad \left. \frac{\partial}{\partial z} v_{\perp} \right|_{z=-4} = 0.$$

Tests show that the central behaviour is largely unaffected by these choices of side and bottom boundary conditions. The other boundary conditions on the perturbed magnetic field follow from the remaining equations and the solenoidal condition, $\nabla \cdot \mathbf{b} = 0$. We take $\omega = 2\pi$ for our simulations.

We find that the linear, fast magnetoacoustic wave travels towards the neighbourhood of the two null points and begins to wrap around them. Since the Alfvén speed, $v_A(x, z)$, is spatially varying, different parts of the wave travel at different speeds, and it travels faster the further it is away from the null points ($v_A(x, z) = 0$ at the null points). This is a similar effect to that described in the case of a single null point in Chapter 3. However, in this case there is a non-zero Alfvén speed between the two null points, i.e. for $-1 < x < 1$, $z = 0$. The fast wave slows down greatly when it approaches this area, but manages to cross this line (the separator if we were considering a setup such as that of the left hand side of Figure 5.1. Hence the wave bends between the two null points and passes through the area between them. This part of the wave is then again susceptible to the refraction effect, and so continues to wrap around the null points, breaking into two waves along the line $x = 0$ (due to symmetry). Each part of the wave then continues to wrap around its closest null point, repeatedly, eventually accumulating at the null points ($x = -1$ and $x = +1$, along $z = 0$). This can be seen in the shaded contours of Figure 5.2.

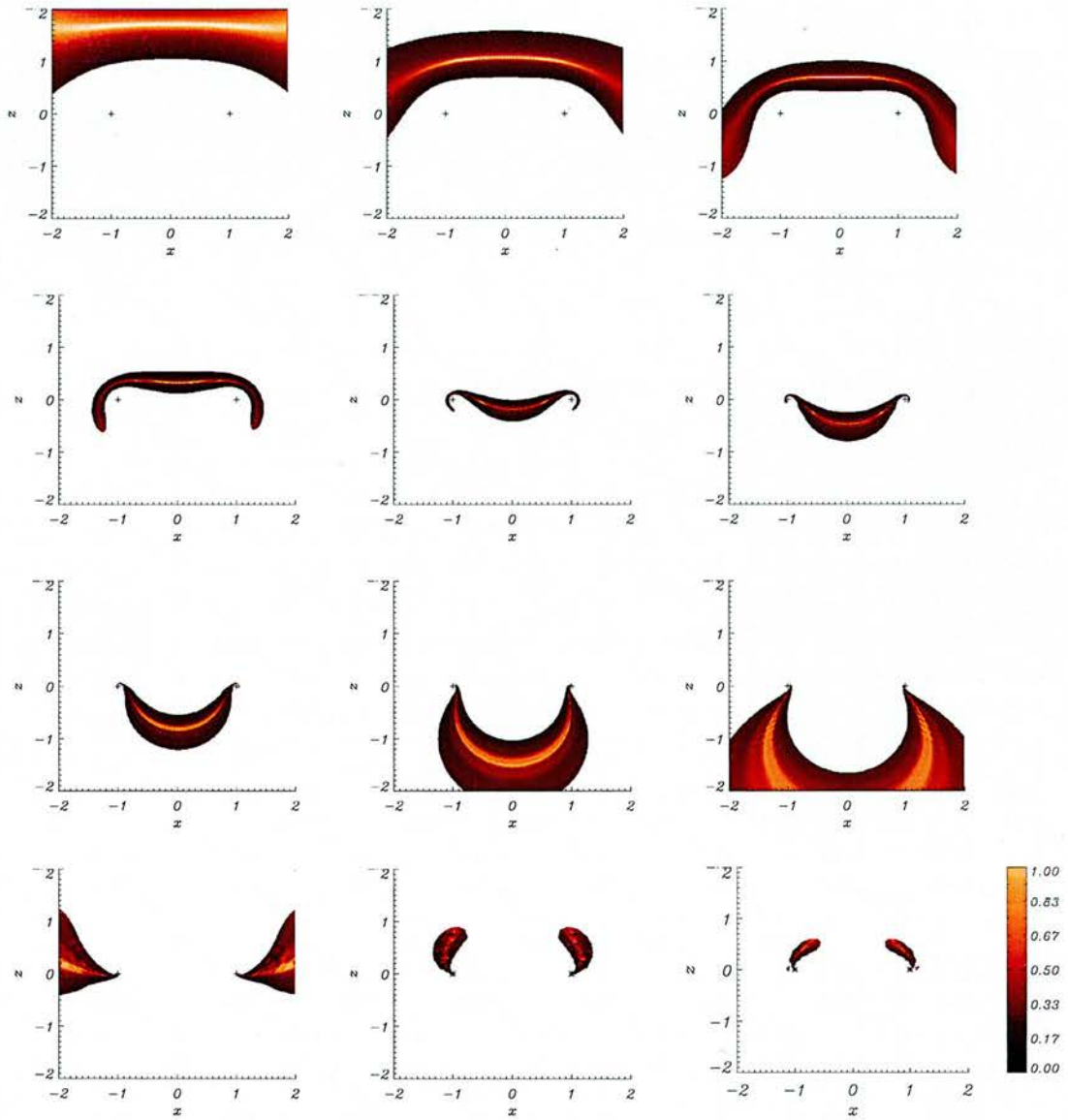


Figure 5.2: Contours of numerical simulation of v_{\perp} for a fast wave sent in from upper boundary for $-3 \leq x \leq 3$, and its resultant propagation at times (a) $t=0.25$, (b) $t=0.5$, (c) $t=0.75$, (d) $t=1.0$, (e) $t=1.5$ and (f) $t=1.75$, (g) $t=2.0$, (h) $t=2.25$, (i) $t=2.5$, (j) $t=3.0$, (k) $t=3.5$ and (l) $t=3.75$, labelling from top left to bottom right.

5.3.2 Analytical Results : WKB approximation

As we did in Section 3.3.2, we can also solve equation (5.4) analytically to gain more insight into the behaviour of the solution. As before, we substitute $v_{\perp} = e^{i\phi(x,z)} \cdot e^{-i\omega t}$ into (5.4) to give:

$$-\omega^2 v_{\perp} = \left[(x^2 + z^2)^2 - 2(x^2 - z^2) + 1 \right] \left[- \left(\frac{\partial \phi}{\partial x} \right)^2 - \left(\frac{\partial \phi}{\partial z} \right)^2 - i \left(\frac{\partial^2 \phi}{\partial x^2} + \frac{\partial^2 \phi}{\partial z^2} \right) \right] \cdot v_{\perp}$$

Now we make the WKB approximation such that $\phi \sim \omega \gg 1$ (as detailed in Section 2.4.2). This leads to a first order PDE of the form:

$$\begin{aligned} \omega^2 &= \left[(x^2 + z^2)^2 - 2(x^2 - z^2) + 1 \right] (p^2 + q^2) \\ \Rightarrow \mathcal{F}(x, z, \phi, p, q) = 0 &= \frac{1}{2} \left[(x^2 + z^2)^2 - 2(x^2 - z^2) + 1 \right] (p^2 + q^2) - \frac{1}{2} \omega^2 \end{aligned}$$

where $p = \frac{\partial \phi}{\partial x}$ and $q = \frac{\partial \phi}{\partial z}$. We then work out the quantities required in Charpit's method:

$$\begin{aligned} \frac{\partial \mathcal{F}}{\partial \phi} &= 0 \\ \frac{\partial \mathcal{F}}{\partial p} &= p \left[(x^2 + z^2)^2 - 2(x^2 - z^2) + 1 \right] \\ \frac{\partial \mathcal{F}}{\partial q} &= q \left[(x^2 + z^2)^2 - 2(x^2 - z^2) + 1 \right] \\ \frac{\partial \mathcal{F}}{\partial x} &= 2x (x^2 + z^2 - 1) (p^2 + q^2) \\ \frac{\partial \mathcal{F}}{\partial z} &= 2z (x^2 + z^2 + 1) (p^2 + q^2) \end{aligned}$$

Now we can apply Charpit's method (equations 2.24 – 2.28):

$$\begin{aligned} \frac{d\phi}{ds} &= \omega^2 \\ \frac{dp}{ds} &= -2x (x^2 + z^2 - 1) (p^2 + q^2) \\ \frac{dq}{ds} &= -2z (x^2 + z^2 + 1) (p^2 + q^2) \\ \frac{dx}{ds} &= p \left[(x^2 + z^2)^2 - 2(x^2 - z^2) + 1 \right] \\ \frac{dz}{ds} &= q \left[(x^2 + z^2)^2 - 2(x^2 - z^2) + 1 \right] \end{aligned}$$

where ω is the frequency of our wave and s is some parameter along the characteristic.

These five ODEs were solved numerically using a fourth-order Runge-Kutta method (unlike in Sections 3.3.2 and 4.3.2, these equations are too complicated to find conserved quantities and

hence solve analytically, so we must proceed *semi*-analytically). The initial conditions used were:

$$\phi_0 = 0, \quad -3 \leq x_0 \leq 3, \quad z_0 = 2, \quad p_0 = 0, \quad q_0 = -\frac{\omega}{\sqrt{[(x_0^2 + z_0^2)^2 - 2(x_0^2 - z_0^2) + 1]}}$$

where we take $\omega = 2\pi$ as in our numerical simulations.

Contours of constant ϕ can be thought of as defining the positions of the edges of the wave pulse, i.e. with correct choices of s , the WKB solution represents the front, middle and back edges of the wave. The evolution can be seen in Figure 5.3. Also, $s = \omega t$ and so the numerical and analytical work can be directly compared. The agreement between the analytic model and the leading edge of the wavefront is very good, as seen in an overplot of a numerical simulation (shaded area) and our WKB solution (thick lines) in Figure 5.4.

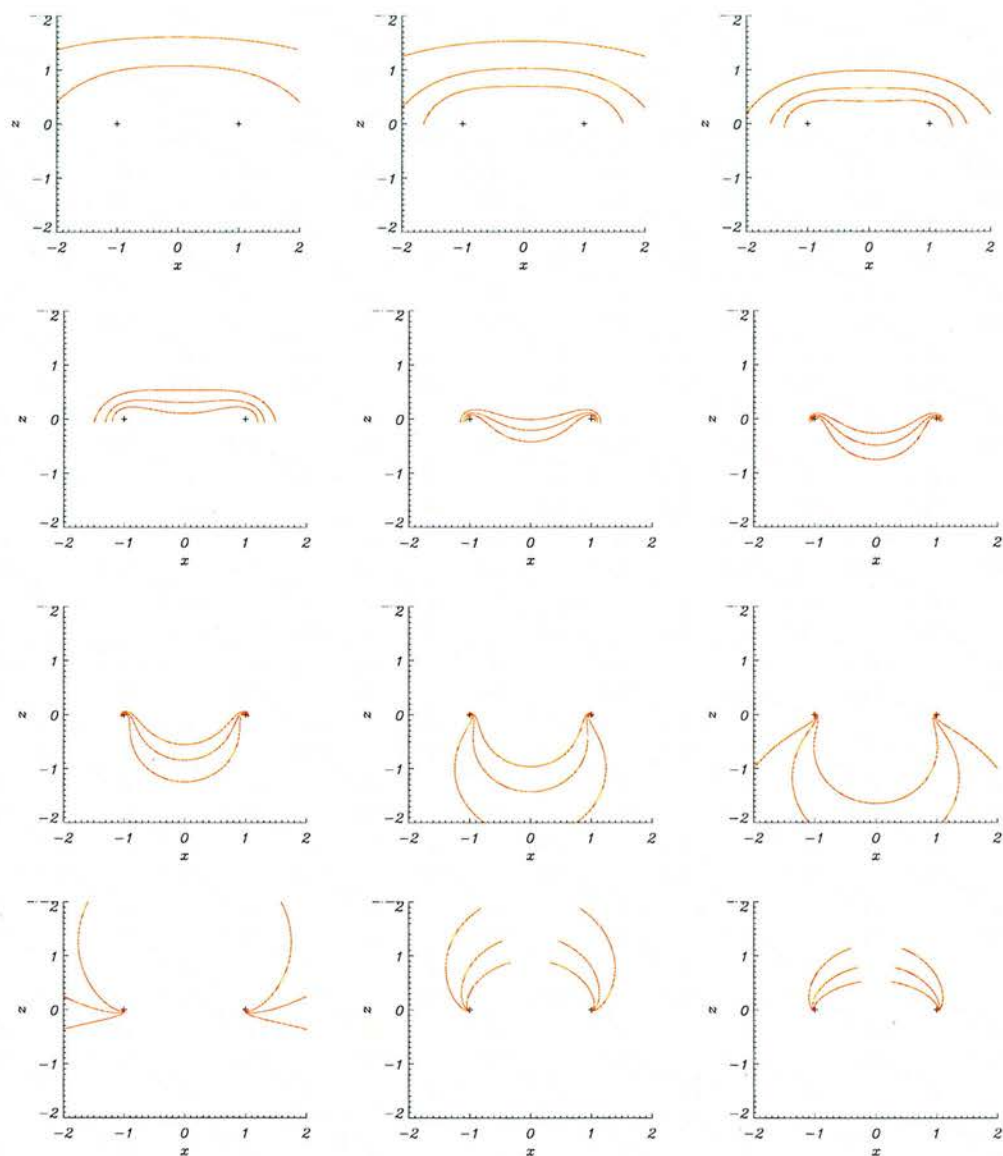


Figure 5.3: Analytical solution of v_{\perp} for WKB approximation of a fast wave sent in from upper boundary for $-3 \leq x \leq 3$, and its resultant propagation at times (a) $t=0.25$, (b) $t=0.5$, (c) $t=0.75$, (d) $t=1.0$, (e) $t=1.5$ and (f) $t=1.75$, (g) $t=2.0$, (h) $t=2.25$, (i) $t=2.5$, (j) $t=3.0$, (k) $t=3.5$ and (l) $t=3.75$, labelling from top left to bottom right. The lines represent the front, middle and back edges of the WKB wave solution, where the pulse enters from the top of the box.

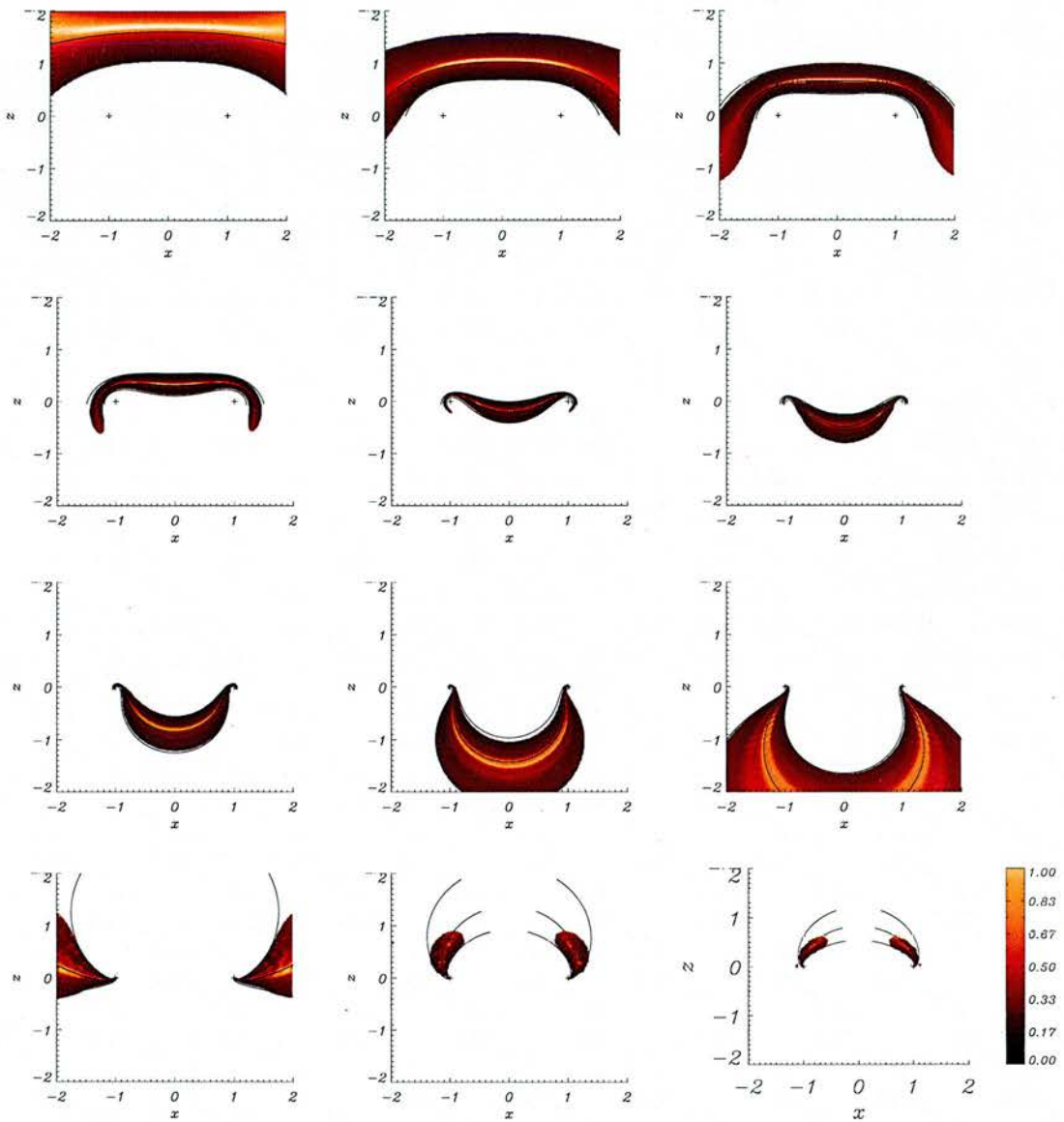


Figure 5.4: Comparison of numerical simulation (shaded area) and analytical solution for v_{\perp} for a fast-wave sent in from upper boundary for $-3 \leq x \leq 3$, and its resultant propagation at times (a) $t=0.25$, (b) $t=0.5$, (c) $t=0.75$, (d) $t=1.0$, (e) $t=1.5$ and (f) $t=1.75$, (g) $t=2.0$, (h) $t=2.25$, (i) $t=2.5$, (j) $t=3.0$, (k) $t=3.5$ and (l) $t=3.75$, labelling from top left to bottom right. The lines represent the front, middle and back edges of the WKB wave solution, where the pulse enters from the top of the box.

We can also use our WKB solution to plot the rays of individual elements from the initial wave. In Figure 5.5, we see the spiral evolution of elements that begin at points $x = -2, -1.5, -1, 0, 0.3$ and 0.5 along $z = 2$. Note that an element that begins at $x = 0, z = 2$ is not affected by the null points and passes between the two and off to $-\infty$. In effect, the two null points cancel out the effect of each other at this point, although any perturbation to an element travelling along this path would send the element spiralling towards one of the nulls. The behaviour of such a particle can be shown:

$$v_A(0, z) = \sqrt{B_x^2 + B_z^2} \Big|_{x=0} = -(z^2 + 1) = \frac{\partial z}{\partial t}$$

Hence, solving for z , we find $z = \tan(A - t)$, where $A = \arctan z_0$ and z_0 is some starting position (which is $z_0 = 2$ in our simulations).

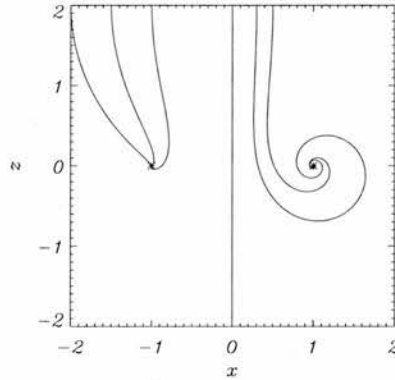


Figure 5.5: Plots of WKB solution for a fast wave sent in from the upper boundary and its resultant rays for starting points of $x = -2, -1.5, -1, 0, 0.3$ and 0.5 along $z = 2$.

5.3.3 Side Boundary

We also investigate the effect of solving the linearised MHD equations for a fast wave coming in from the side boundary, along $x = -2$. Again, the two-step Lax-Wendroff numerical scheme was run in a box with $-2 \leq x \leq 4$ and $-3 \leq z \leq 3$, with our attention focused on $-2 \leq x \leq 2$ and $-2 \leq z \leq 2$. For a single wave pulse from the side boundary, the boundary conditions were:

$$v_{\perp}(-2, z) = \begin{cases} \sin \omega t & \text{for } 0 \leq t \leq \frac{\pi}{\omega} \\ 0 & \text{otherwise} \end{cases},$$

$$\left. \frac{\partial v_{\perp}}{\partial x} \right|_{x=4} = 0, \quad \left. \frac{\partial v_{\perp}}{\partial z} \right|_{z=-3} = 0, \quad \left. \frac{\partial v_{\perp}}{\partial z} \right|_{z=3} = 0.$$

Again, tests show that the central behaviour is largely unaffected by these choices of the remaining boundary conditions.

We find that the linear, fast wave travels in from the left hand side of the box and begins to feel the effect of the left hand side null point (at $x = -1, z = 0$). The wave thins and begins to wrap around this null point. As the ends of the wave wrap around behind the left null point, they then become influenced by the second, right hand side null point (at $x = +1, z = 0$). These arms of the wave then proceed to wrap around the right null point, flattening the wave. Furthermore, the two parts of the wave now travelling through the area between the null points have non-zero Alfvén speed, and so pop through (the wave in the lower half plan now travels up, crossing the line $-1 < x < 1$ and $z = 0$, and vice versa for the wave in the upper half plan). These parts of the wave break along $x = 0$ and then proceed to wrap around the null point closest to them. Eventually, the wave accumulates at both null points. This can be seen in Figure 5.6.

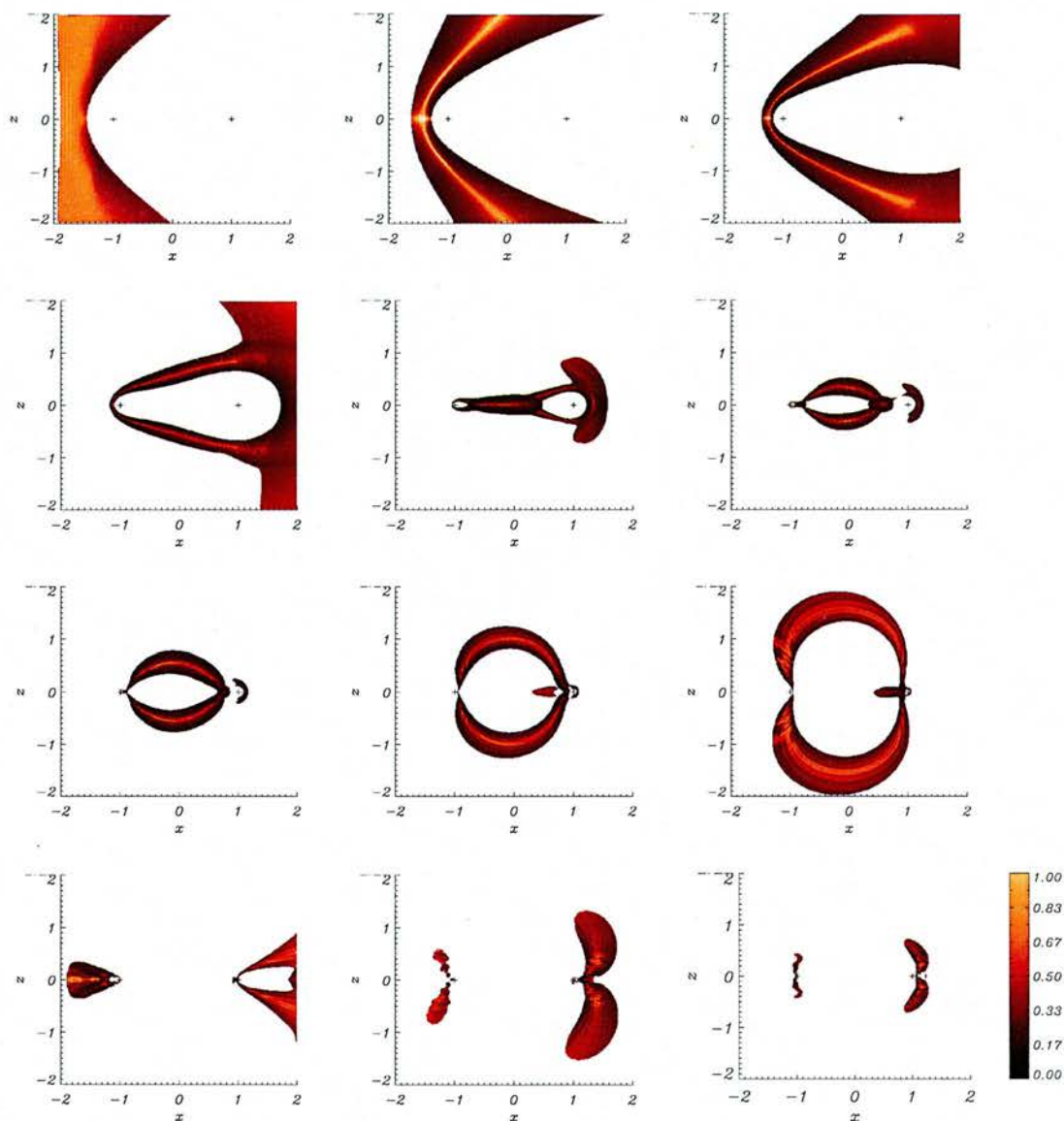


Figure 5.6: Contours of numerical simulation of v_{\perp} for a fast wave sent in from the side boundary for $-3 \leq x \leq 3$, and its resultant propagation at times (a) $t=0.25$, (b) $t=0.5$, (c) $t=0.75$, (d) $t=1.0$, (e) $t=1.5$ and (f) $t=1.75$, (g) $t=2.0$, (h) $t=2.25$, (i) $t=2.5$, (j) $t=3.0$, (k) $t=3.5$ and (l) $t=3.75$, labelling from top left to bottom right.

5.3.4 Analytical Results

As described in Section 5.3.2, equation (5.4) was again solved numerically using a fourth-order Runge-Kutta method but this time using different initial conditions. The initial conditions used in this case were:

$$\phi_0 = 0, \quad x_0 = -2, \quad -3 \leq z_0 \leq 3, \quad p_0 = \frac{2\pi}{\left[(x_0^2 + z_0^2)^2 - 2(x_0^2 - z_0^2) + 1 \right]}, \quad q_0 = 0$$

The thick black lines in Figure 5.7 shows constant ϕ at different values of the parameter s . (where as stated before, constant ϕ can be thought of as defining the position of parts of the wave pulse). As before, the agreement between the analytic model and the wavefront is very good and can be seen in an overplot of a numerical simulation and our WKB solution in Figure 5.8.

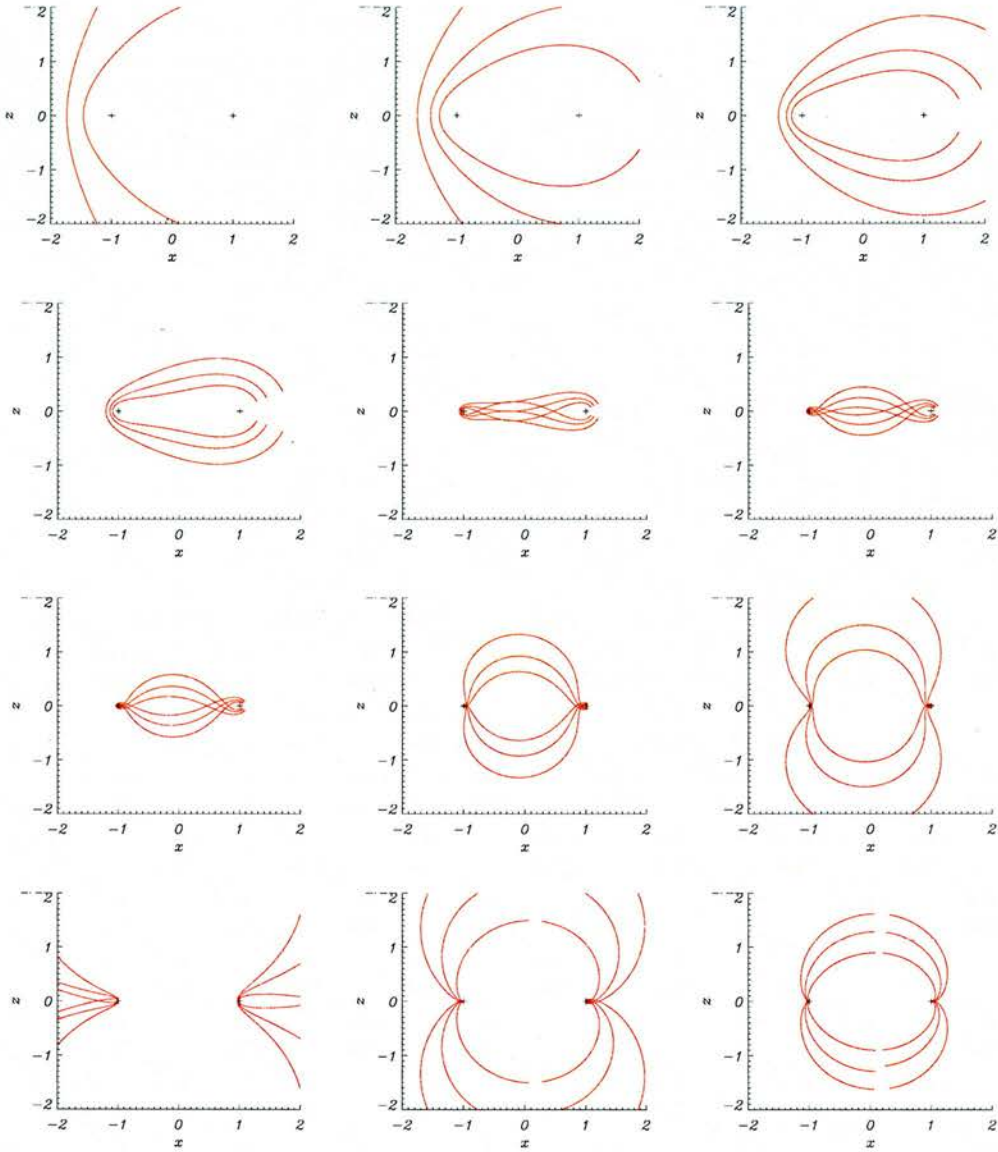


Figure 5.7: Analytical solution of v_{\perp} for WKB approximation of a fast wave sent in from side boundary for $-3 \leq x \leq 3$, and its resultant propagation at times (a) $t=0.25$, (b) $t=0.5$, (c) $t=0.75$, (d) $t=1.0$, (e) $t=1.5$ and (f) $t=1.75$, (g) $t=2.0$, (h) $t=2.25$, (i) $t=2.5$, (j) $t=3.0$, (k) $t=3.5$ and (l) $t=3.75$, labelling from top left to bottom right. The lines represent the front, middle and back edges of the WKB wave solution, where the pulse enters from the side of the box.

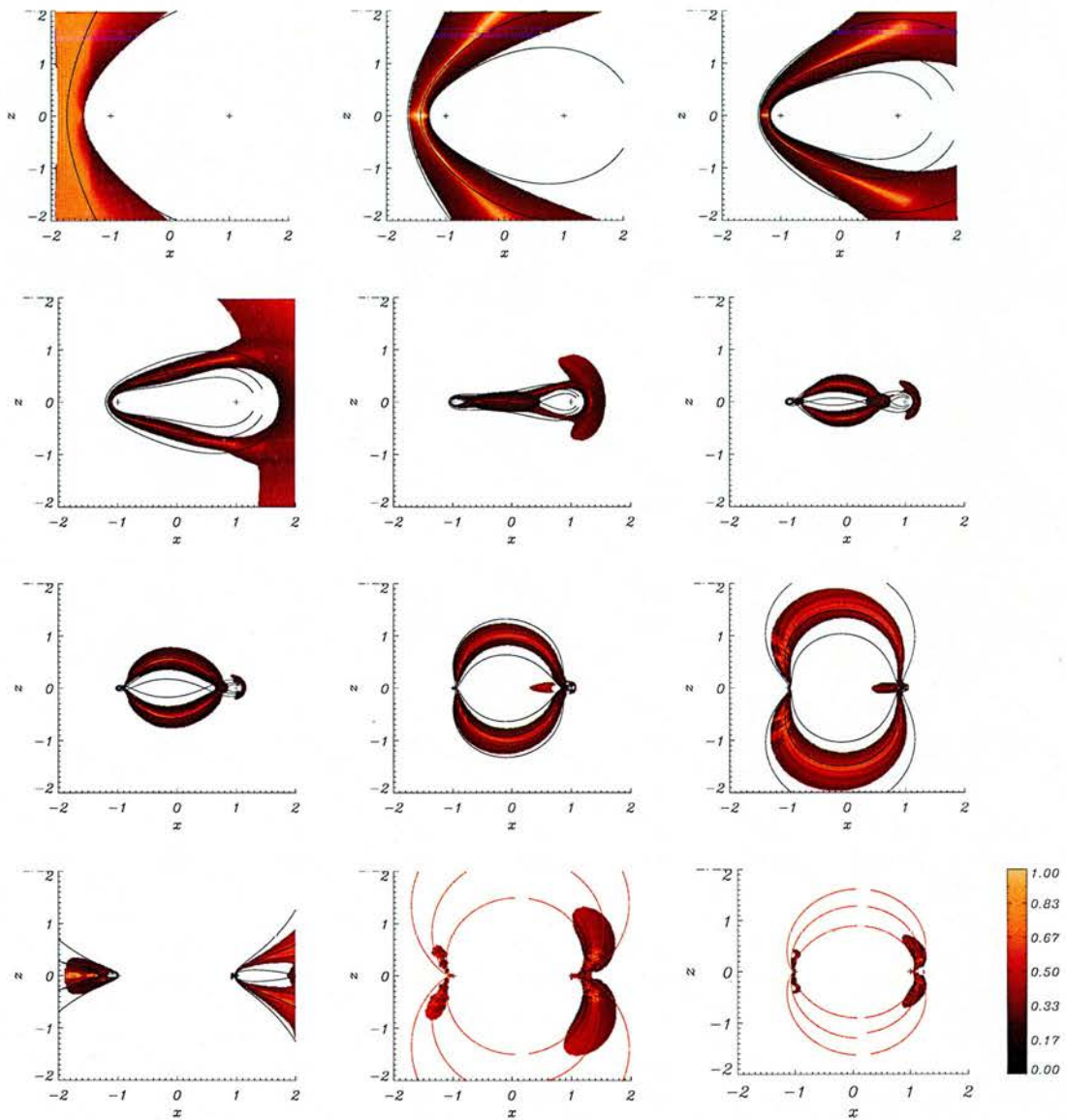


Figure 5.8: Comparison of numerical simulation (shaded area) and analytical solution of v_{\perp} for a fast wave sent in from side boundary for $-3 \leq x \leq 3$, and its resultant propagation at times (a) $t=0.25$, (b) $t=0.5$, (c) $t=0.75$, (d) $t=1.0$, (e) $t=1.5$ and (f) $t=1.75$, (g) $t=2.0$, (h) $t=2.25$, (i) $t=2.5$, (j) $t=3.0$, (k) $t=3.5$ and (l) $t=3.75$, labelling from top left to bottom right. The lines represent the front, middle and back edges of the WKB wave solution, where the pulse enters from the top of the box.

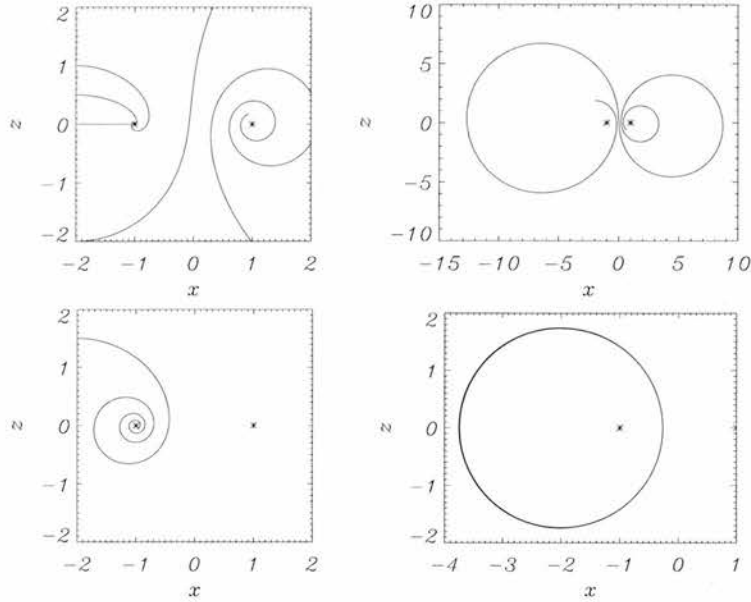


Figure 5.9: Plots of WKB solution for a fast wave sent in from the side boundary and its resultant rays. *Top left* displays starting points of $z = -2, 0, 0.5$ and $+1$ along $x = -2$. *Bottom left* displays a starting point of $z = +1.5$. The *top right* subfigure shows a starting point of $z = 1.86 > \sqrt{3}$, and the *bottom right* shows $z = \sqrt{3}$. Note the change of scale in the two right hand subfigures.

We can also use our WKB solution to plot the rays of individual elements from the initial wave. In Figure 5.9, we see the spiral evolution of elements that begin at points $z = -2, 0, 0.5, 1, 1.5$ and 1.86 along $x = -2$. Note that for a wavefront extending between $-2 \leq z \leq +2$, there is a critical distance where some elements of the wave are sucked into the nearest (left hand) null point, and others spiral round it at such a great distance that they feel the influence of the second (right hand) null point and begin spiralling towards it ($x = +1, z = 0$). Note that for a starting position of $z = \sqrt{3}$, the wave element orbits in a circle (radius $\sqrt{3}$). This is the critical starting distance; a starting distance, say z_0 , less than this will spiral into the left hand null point, whereas the wave particle will spiral into the right hand null point if $z_0 > \sqrt{3}$. This can be seen in the bottom right subfigure of Figure 5.9. Simulations show that this critical distance is $\sqrt{L^2 - 1}$, where L is the distance between the origin and the side boundary (here $L = |x_0| = 2$). When $x_0 = -2$ and $z_0 = \sqrt{3}$ (i.e. critical starting distance), the equations are satisfied by:

$$\begin{aligned}
 x &= \frac{-1}{(2 + \sqrt{3} \sin \theta)}, & p &= -\frac{\pi}{\sqrt{3}} \cos \theta, \\
 z &= \frac{\sqrt{3} \cos \theta}{(2 + \sqrt{3} \sin \theta)}, & q &= \pi + \frac{2\pi}{\sqrt{3}} \sin \theta,
 \end{aligned}$$

where $\theta = 4\pi s - \pi/3$, and confirm the periodic circular orbit, i.e. $(x + 2)^2 + z^2 = 3$.

5.4 Alfvén Waves in the neighbourhood of two null points

Now we turn our attention to the behaviour of the Alfvén Wave around two null points. Equations (5.5) were solved numerically using the two-step Lax-Wendroff scheme. In Section 4.2, it was shown that in the neighbourhood of a single X-point, the linear Alfvén wave spreads out along the field lines, eventually accumulating along the separatrices. Hence, for our two null points, we have *four* cases to consider; an Alfvén wave pulse coming in from the top boundary and coming in from the side boundary for both magnetic configurations shown in Figure 5.1.

5.4.1 Two null points connected by a separator

We first consider the two null point magnetic configuration containing a separator, as shown on the left hand side of Figure 5.1.

5.4.2 Case 1 : Upper Boundary

We initially consider a box ($-2 \leq x \leq 2$, $-2 \leq z \leq 2$) with a single wave pulse coming in across part of the top boundary ($1 \leq x \leq 2$, $z = 2$). We choose such a pulse because, as Section 4.2 showed, the Alfvén wave spreads out along the field lines as it propagates and we found that this choice of boundary condition illustrated this effect much clearer. In fact, the wave never crosses the separator ($z = 0$) and so the final, high resolution run was performed in a box ($-2.5 \leq x \leq 2.5$, $-0.5 \leq z \leq 2$). The full boundary conditions were;

$$v_y(x, 2) = (\sin \omega t) (\sin \pi x / 2) \quad \text{for} \quad \begin{cases} 1 \leq x \leq 2 \\ 0 \leq t \leq \frac{\pi}{\omega} \end{cases},$$

$$\frac{\partial v_y}{\partial z} \Big|_{z=2} = 0 \quad \text{otherwise}$$

$$\frac{\partial v_y}{\partial x} \Big|_{x=2.5} = 0, \quad \frac{\partial v_y}{\partial x} \Big|_{x=-2.5} = 0, \quad \frac{\partial v_y}{\partial z} \Big|_{z=-0.5} = 0.$$

Tests show that the central behaviour is unaffected by these choices. The other boundary conditions follow from the remaining equations.

We found that the linear Alfvén wave travels down from the top boundary and begins to spread out, following the field lines. As the wave approaches the separator along $z = 0$ and the separatrix that passes through $x = -1$, the wave thins but keeps its original amplitude. The wave eventually accumulates very near the separator and separatrix, specifically because it cannot cross the field lines (and thus is confined to its original domain of connectivity). This can be seen in Figure 5.10.

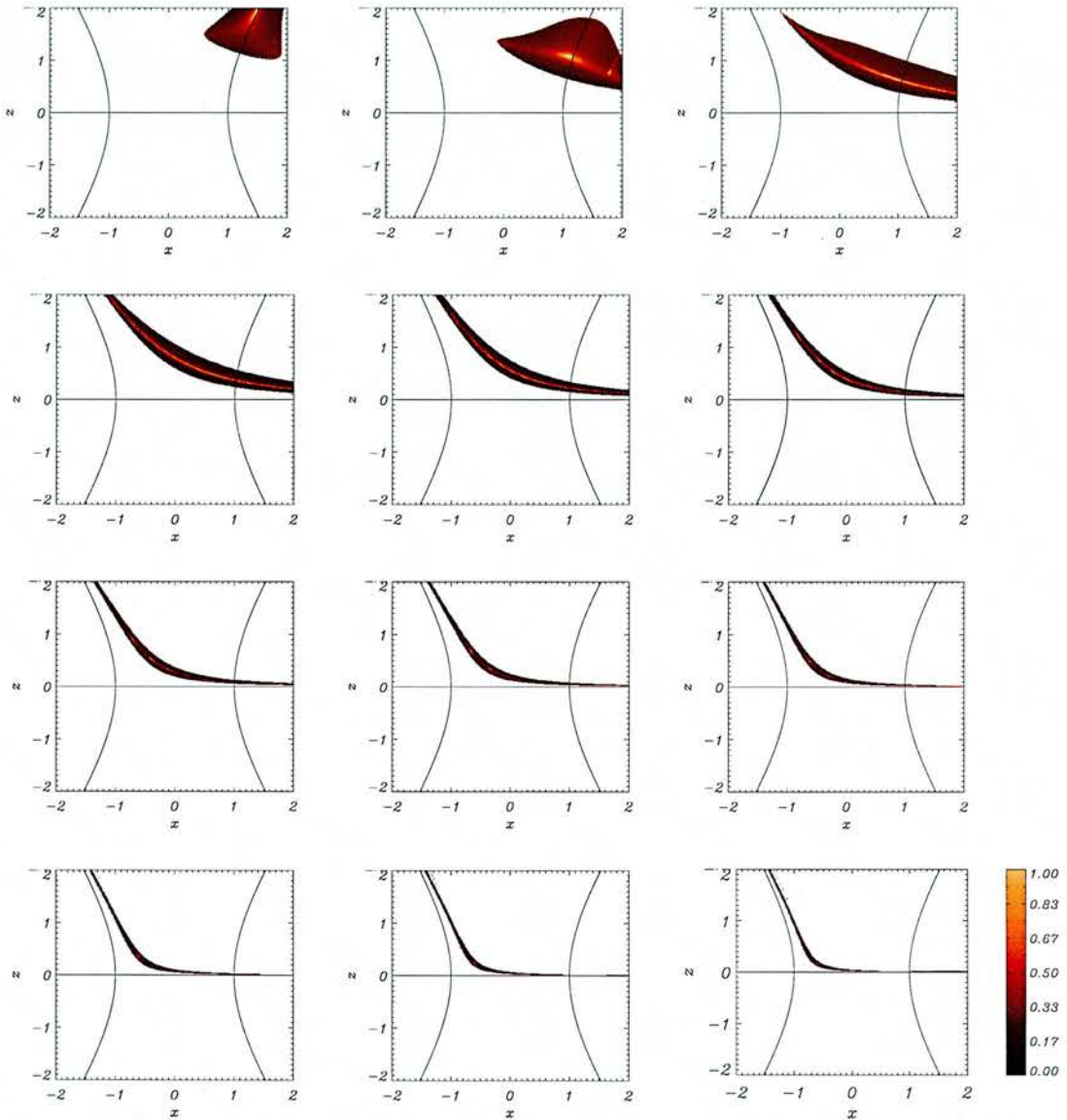


Figure 5.10: Contours of numerical simulation for Alfvén wave entering box at $1 \leq x \leq 2$, $z = 2$, at times (a) $t=0.25$, (b) $t=0.5$, (c) $t=0.75$, (d) $t=1.0$, (e) $t=1.25$, (f) $t=1.5$, (g) $t=1.75$, (h) $t=2.0$, (i) $t=2.25$, (j) $t=2.5$, (k) $t=2.75$ and (l) $t=3.0$, labelling from top left to bottom right.

Analytical Results

As above and in previous chapters, we can solve our equations for the Alfvén wave analytically to gain a better understanding of the numerical results. As in all four cases we will study for the Alfvén wave, the equation we have to solve is:

$$\frac{\partial^2 v_y}{\partial t^2} = \left(B_x \frac{\partial}{\partial x} + B_z \frac{\partial}{\partial z} \right)^2 v_y, \quad (5.7)$$

In this experiment, $B_x = x^2 - z^2 - 1$, $B_z = -2xz$ (this is the magnetic configuration shown on the left hand side of Figure 5.1). We will again use the WKB approximation to gain insight into the numerical simulations. As in Section 5.3.2, substituting $v_y = e^{i\phi(x,z)} \cdot e^{-i\omega t}$ into equation (5.7) gives:

$$\begin{aligned} -\omega^2 = & \left[-(x^2 - z^2 - 1)^2 \left(\frac{\partial \phi}{\partial x} \right)^2 + 4xz(x^2 - z^2 - 1) \frac{\partial \phi}{\partial x} \frac{\partial \phi}{\partial z} - 4x^2 z^2 \left(\frac{\partial \phi}{\partial z} \right)^2 \right] \\ + i & \left[(x^2 - z^2 - 1)^2 \frac{\partial^2 \phi}{\partial x^2} - 4xz(x^2 - z^2 - 1) \frac{\partial^2 \phi}{\partial x \partial z} + 4x^2 z^2 \frac{\partial^2 \phi}{\partial z^2} \right. \\ & \left. + 4x^2 z \frac{\partial \phi}{\partial x} + 2z(x^2 - z^2 - 1) \frac{\partial \phi}{\partial x} + 4xz^2 \frac{\partial \phi}{\partial z} - 2x(x^2 - z^2 - 1) \frac{\partial \phi}{\partial z} \right] \end{aligned}$$

Now we make the WKB approximation that $\phi \sim \omega \gg 1$ and this leads to a first order PDE of the form:

$$\begin{aligned} -\omega^2 &= -(x^2 - z^2 - 1)^2 p^2 + 4xz(x^2 - z^2 - 1) pq - 4x^2 z^2 q^2 \\ \Rightarrow \mathcal{F}(x, z, \phi, p, q) &= \frac{1}{2} [(x^2 - z^2 - 1)p - 2xzq]^2 - \frac{1}{2} \omega^2 = 0 \end{aligned}$$

where again $p = \frac{\partial \phi}{\partial x}$ and $q = \frac{\partial \phi}{\partial z}$ and \mathcal{F} is a non-linear PDE (we include a half in the form of \mathcal{F} to make the equations nicer later). Note all the imaginary terms have disappeared under the WKB approximation.

We require the following quantities to invoke Charpit's method:

$$\begin{aligned} \frac{\partial \mathcal{F}}{\partial \phi} &= 0 \\ \frac{\partial \mathcal{F}}{\partial p} &= (x^2 - z^2 - 1) [(x^2 - z^2 - 1)p - 2xzq] \\ \frac{\partial \mathcal{F}}{\partial q} &= -2xz [(x^2 - z^2 - 1)p - 2xzq] \\ \frac{\partial \mathcal{F}}{\partial x} &= (2xp - 2zq) [(x^2 - z^2 - 1)p - 2xzq] \\ \frac{\partial \mathcal{F}}{\partial z} &= -(2zp + 2xq) [(x^2 - z^2 - 1)p - 2xzq] \end{aligned}$$

Now we can apply Charpit's equations (equations 2.24 – 2.28) to obtain:

$$\begin{aligned}
 \frac{d\phi}{ds} &= \omega^2 \\
 \frac{dp}{ds} &= (2zq - 2xp) \xi \\
 \frac{dq}{ds} &= (2zp + 2xq) \xi \\
 \frac{dx}{ds} &= (x^2 - z^2 - 1) \xi \\
 \frac{dz}{ds} &= (-2xz) \xi
 \end{aligned} \tag{5.8}$$

where $\xi = [(x^2 - z^2 - 1)p - 2xzq]$, ω is the frequency of our wave and s is some parameter along the characteristic.

These five ODEs were solved numerically using a fourth-order Runge-Kutta method. The initial conditions used were:

$$\phi_0 = 0, \quad 1 \leq x_0 \leq 2, \quad z_0 = 2, \quad p_0 = 0, \quad q_0 = -\frac{\omega}{2x_0z_0}$$

Constant ϕ can be thought of as defining the position of the edge of the wave pulse. Figure 5.11 shows constant ϕ at different values of the parameter s . With correct choices of s the WKB solution can be directly compared to our numerical solution. This can be seen in Figure 5.12 and it can be seen that the agreement is very good.

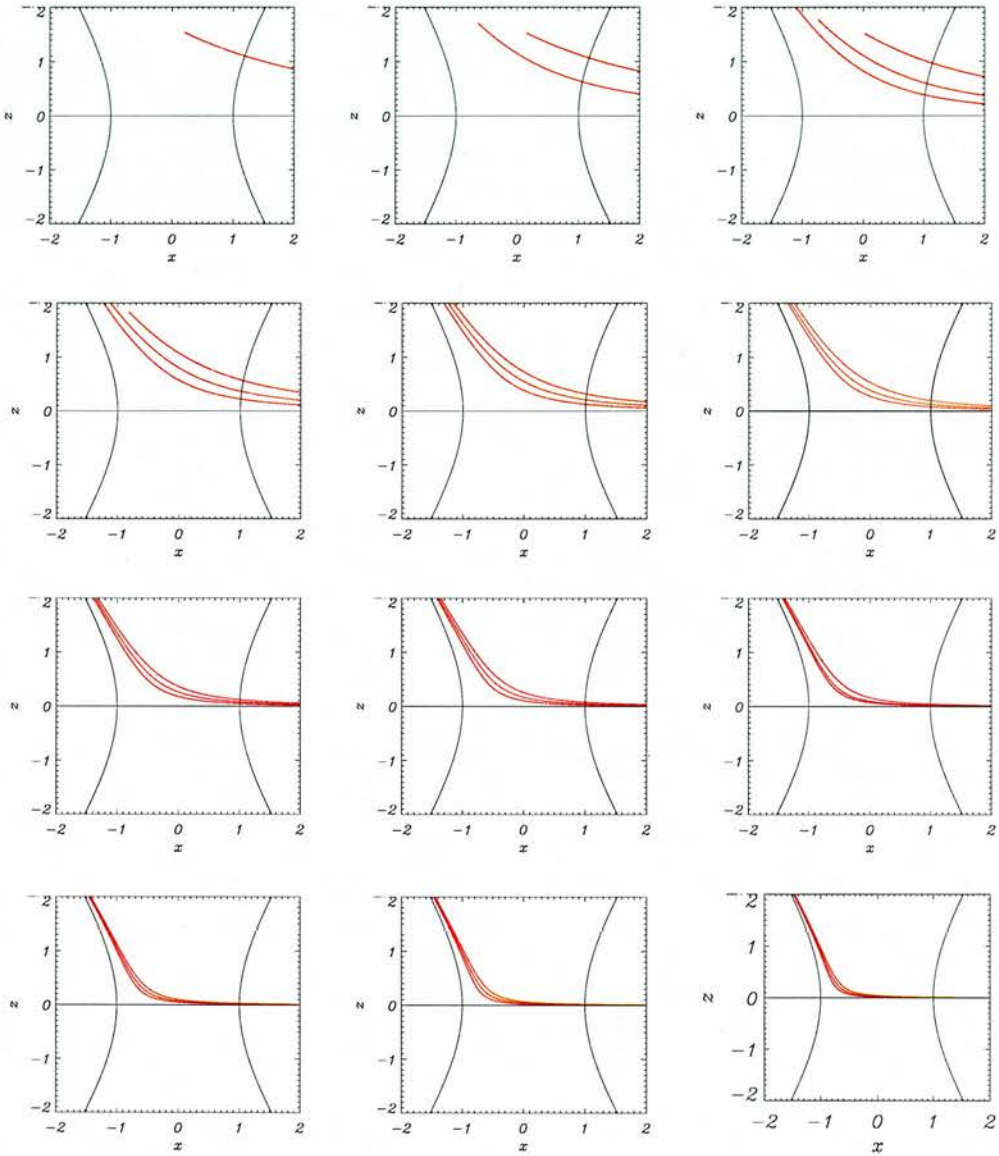


Figure 5.11: Analytical solution for WKB approximation of an Alfvén wave sent in from upper boundary for $1 \leq x \leq 2$, and its resultant propagation at times (a) $t=0.25$, (b) $t=0.5$, (c) $t=0.75$, (d) $t=1.0$, (e) $t=1.25$, (f) $t=1.5$, (g) $t=1.75$, (h) $t=2.0$, (i) $t=2.25$, (j) $t=2.5$, (k) $t=2.75$ and (l) $t=3.0$, labelling from top left to bottom right. The lines represent the front, middle and back edges of the WKB wave solution.

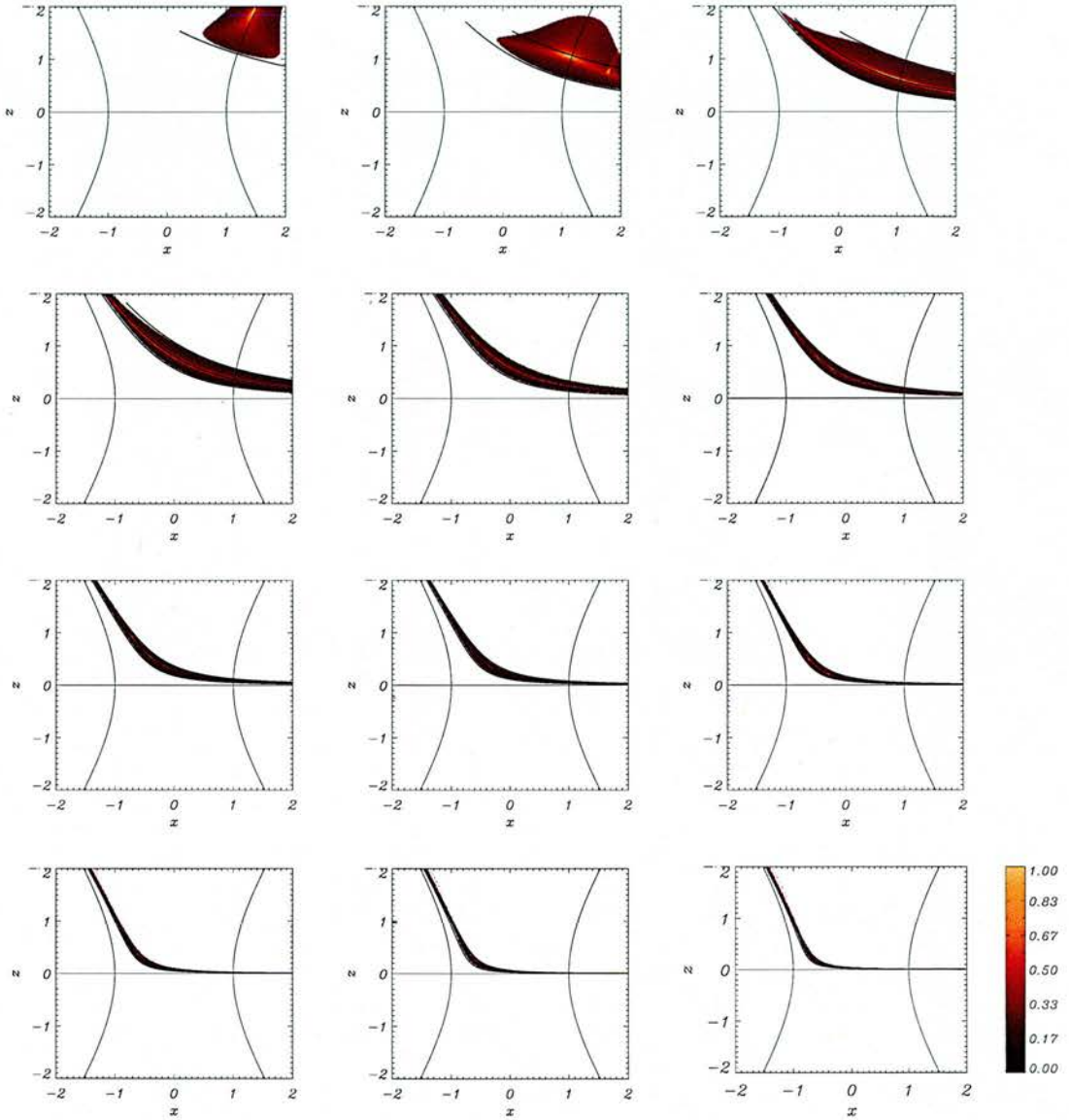


Figure 5.12: Comparison of numerical simulation (shaded area) and analytical solution for Alfvén wave sent in from top boundary for $1 \leq x \leq 2$, and its resultant propagation at times (a) $t=0.25$, (b) $t=0.5$, (c) $t=0.75$, (d) $t=1.0$, (e) $t=1.25$, (f) $t=1.5$, (g) $t=1.75$, (h) $t=2.0$, (i) $t=2.25$, (j) $t=2.5$, (k) $t=2.75$ and (l) $t=3.0$, labelling from top left to bottom right. The lines represent the front, middle and back edges of the WKB wave solution, where the pulse enters from the top of the box.

We can also use our WKB solution to plot the rays of individual elements from the initial wave. In Figure 5.13, starting points of $x=1, 1.25, 1.5, \sqrt{7/3}$ (*separatrix*) and 1.75 are plotted.

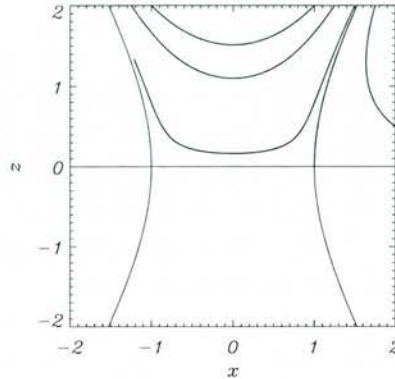


Figure 5.13: Plots of WKB solution for an Alfvén wave sent in from the upper boundary and its resultant rays (thick lines). Starting points of $x=1, 1.25, 1.5, \sqrt{7/3}$ and 1.75 are plotted.

5.4.3 Case 2 : Side Boundary

We now consider a box ($-2 \leq x \leq 2, -2 \leq z \leq 2$) with a single wave pulse coming in across part of the side boundary ($x = -2, -1 \leq z \leq 1$), but with the same magnetic configuration as Case 1 (i.e. two null point field containing separator). This will highlight the importance of the magnetic topology. In fact, the Alfvén wave never passes the (left) separatrix and so the final, high resolution run was performed in a box ($-2 \leq x \leq 0.5, -2.5 \leq z \leq 2.5$). The full boundary conditions were;

$$v_y(-2, z) = \begin{cases} (\sin \omega t) \left[\sin \frac{\pi}{2}(1+z) \right] & \text{for } \begin{cases} -1 \leq z \leq 1 \\ 0 \leq t \leq \frac{\pi}{\omega} \end{cases} \\ 0 & \text{otherwise} \end{cases} ,$$

$$\left. \frac{\partial v_y}{\partial x} \right|_{x=0.5} = 0, \quad \left. \frac{\partial v_y}{\partial z} \right|_{z=-2.5} = 0, \quad \left. \frac{\partial v_y}{\partial z} \right|_{z=2.5} = 0 .$$

Tests show that the central behaviour is unaffected by these choices. The other boundary conditions follow from the remaining equations and the solenoidal condition.

In this experiment, we found that the linear Alfvén wave travels in from the side boundary and begins to spread out, following the field lines. As the wave approaches the (left) separatrix (that passes through $x = -1$), the wave thins (but keeps its original amplitude). Because the wave is following the field lines, it cannot cross the separatrix and so the wave eventually accumulates very near this special field line. This can be seen in Figure 5.14.

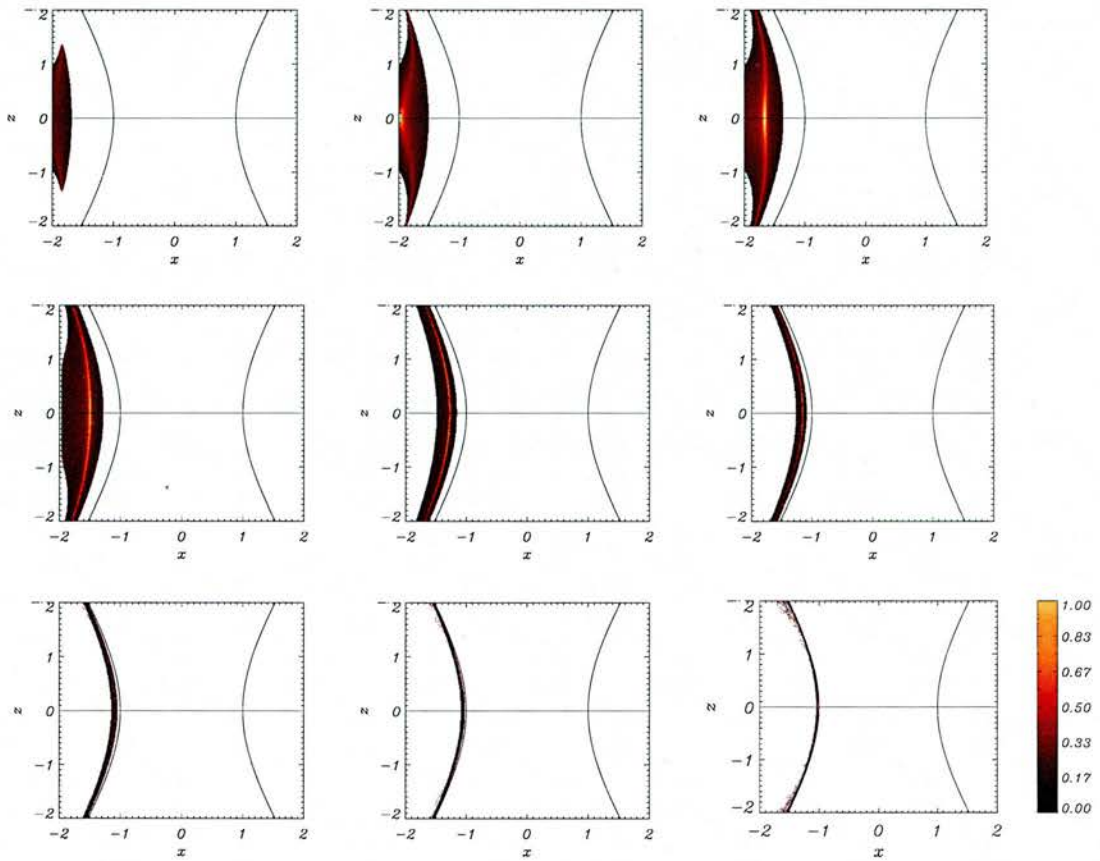


Figure 5.14: Contours of numerical simulation for Alfvén wave entering box at $x = -2$, $-1 \leq z \leq 1$, at times (a) $t=0.167$, (b) $t=0.33$, (c) $t=0.5$, (d) $t=0.67$, (e) $t=0.833$, (f) $t=1.0$, (g) $t=1.167$, (h) $t=1.33$, (i) $t=1.5$, labelling from top left to bottom right.

Analytical Results

By solving the same characteristic equations as in subsection 5.4.2 (equations 5.8) but with different choices of initial condition (i.e. modelling the wave coming in from the side), we can obtain an analytical result to match our numerical simulation. Again, we use the fourth-order Runge-Kutta method. The initial conditions used were:

$$\phi_0 = 0, \quad x_0 = -2 \quad -1 \leq z_0 \leq 1, \quad p_0 = \frac{\omega}{x_0^2 + z_0^2 + 1}, \quad q_0 = 0$$

The WKB solution can be seen in Figure 5.15 at various times. The comparison of the numerical simulation and analytical solution can be seen in Figure 5.16.

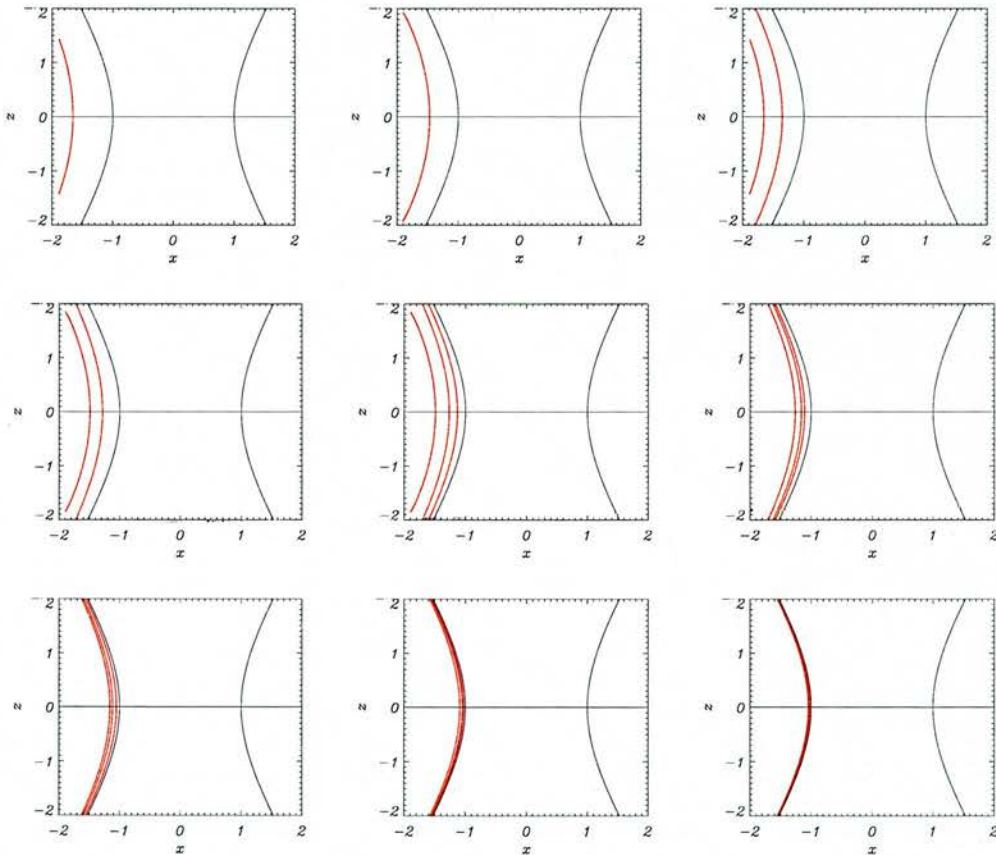


Figure 5.15: Contours of the WKB approximation of an Alfvén wave entering box at $x = -2$, $-1 \leq z \leq 1$, at times (a) $t=0.167$, (b) $t=0.33$, (c) $t=0.5$, (d) $t=0.67$, (e) $t=0.833$, (f) $t=1.0$, (g) $t=1.167$, (h) $t=1.33$, (i) $t=1.5$, labelling from top left to bottom right. The lines represent the front, middle and back edges of the WKB wave solution.

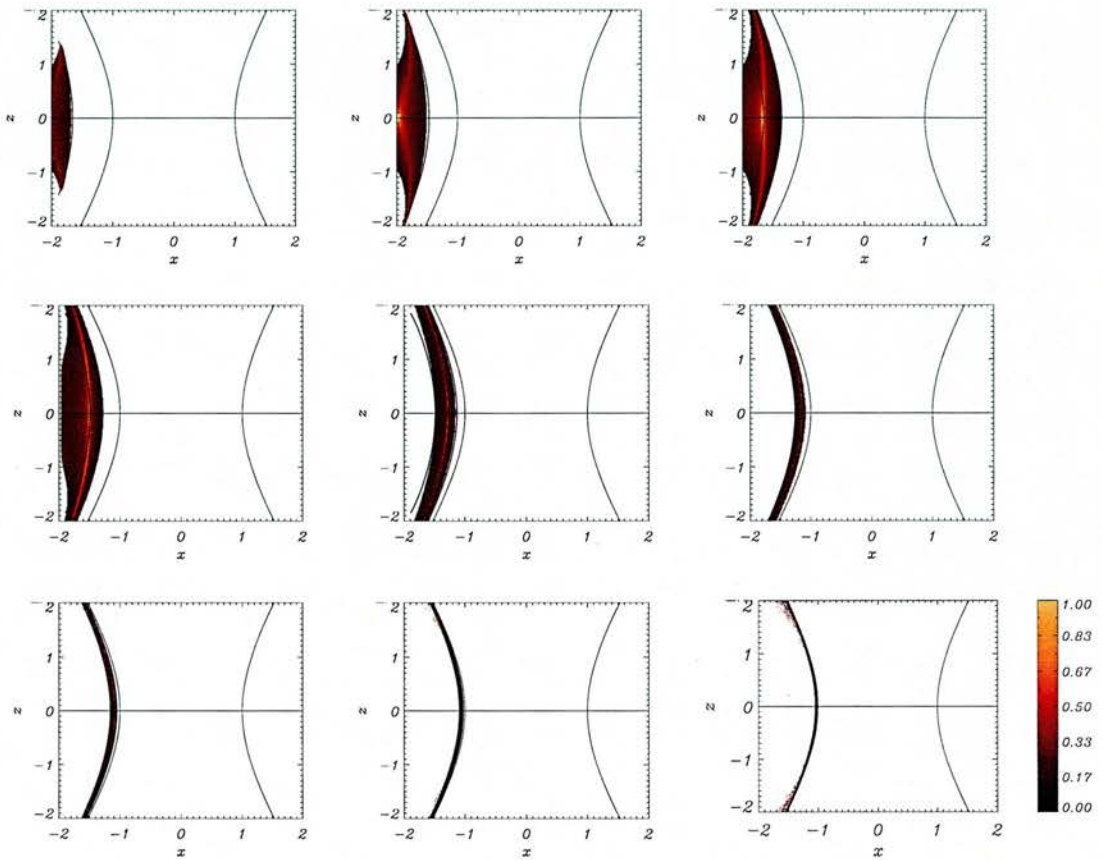


Figure 5.16: Comparison of numerical simulation (shaded area) and analytical solution for Alfvén wave entering box at $x = -2$, $-1 \leq z \leq 1$, at times (a) $t=0.167$, (b) $t=0.33$, (c) $t = 0.5$, (d) $t=0.67$, (e) $t=0.833$, (f) $t=1.0$, (g) $t=1.167$, (h) $t=1.33$, (i) $t=1.5$, labelling from top left to bottom right. The lines represent the front, middle and back edges of the WKB wave solution, where the pulse enters from the left hand side of the box.

5.4.4 Two null points not connected by a separator

We now consider the two null point magnetic configuration that does not contain a separator, as shown on the right hand side of Figure 5.1.

5.4.5 Case 3 : Upper Boundary

We consider a box ($-2 \leq x \leq 2$, $-2 \leq z \leq 2$) with a single wave pulse coming in across part of the top boundary ($-1 \leq x \leq 1$, $z = 2$), i.e. crossing the separatrices. After viewing the preliminary results, the final (high resolution) run was performed in a box ($-2.5 \leq x \leq 2.5$, $-3 \leq z \leq 2$). The full boundary conditions were;

$$v_y(x, 2) = \begin{cases} \sin \omega t \left[\sin \frac{\pi}{2} (1 + x) \right] & \text{for } \begin{cases} -1 \leq x \leq 1 \\ 0 \leq t \leq \frac{\pi}{\omega} \end{cases} , \\ 0 & \text{otherwise} \end{cases} ,$$

$$\left. \frac{\partial v_y}{\partial x} \right|_{x=2.5} = 0 , \quad \left. \frac{\partial v_y}{\partial x} \right|_{x=-2.5} = 0 , \quad \left. \frac{\partial v_y}{\partial z} \right|_{z=-3} = 0 .$$

The other boundary conditions were chosen in the same way as before.

We found that the linear Alfvén wave travels down from the top boundary and begins to spread out, following the field lines. The wave thins as it descends, but keeps its original amplitude. The wave takes the shape of the separatrices that pass through $x = \pm 2$, $z = +\sqrt{2/3}$. The wave accumulates along these separatrices for $z > 0$. The rest of the wave (the part between $-1 < x < +1$) continues descending and eventually accumulates along the separatrices in the lower half of the box. This can be seen in Figure 5.17. The part of wave in the small region about $x = 0$ descends indefinitely, since the separatrices converge along $x = 0$ at infinity. This can be shown:

$$\frac{\partial^2 v_y}{\partial t^2} = \left(B_x \frac{\partial}{\partial x} + B_z \frac{\partial}{\partial z} \right)^2 v_y = \left(B_z \frac{\partial}{\partial z} \right)^2 v_y \Big|_{x=0} .$$

Let $\frac{\partial}{\partial s} = \left(B_z \frac{\partial}{\partial z} \right)$ and comparing the original equation with $\frac{\partial v_y}{\partial s} = \frac{\partial x}{\partial s} \frac{\partial v_y}{\partial x} + \frac{\partial z}{\partial s} \frac{\partial v_y}{\partial z}$ leads to:

$$z = \tan(A - t) \Big|_{x=0} ,$$

where $A = \arctan z_0$ and z_0 is the starting position of our characteristic. Thus z starts at $x = 0$, $z = 2$ and descends, following the line $x = 0$ but becoming closer to zero. The particle passes through $z = 0$ at $t = \arctan 2$ and becomes more and more negative (i.e. continues to descend) thereafter.

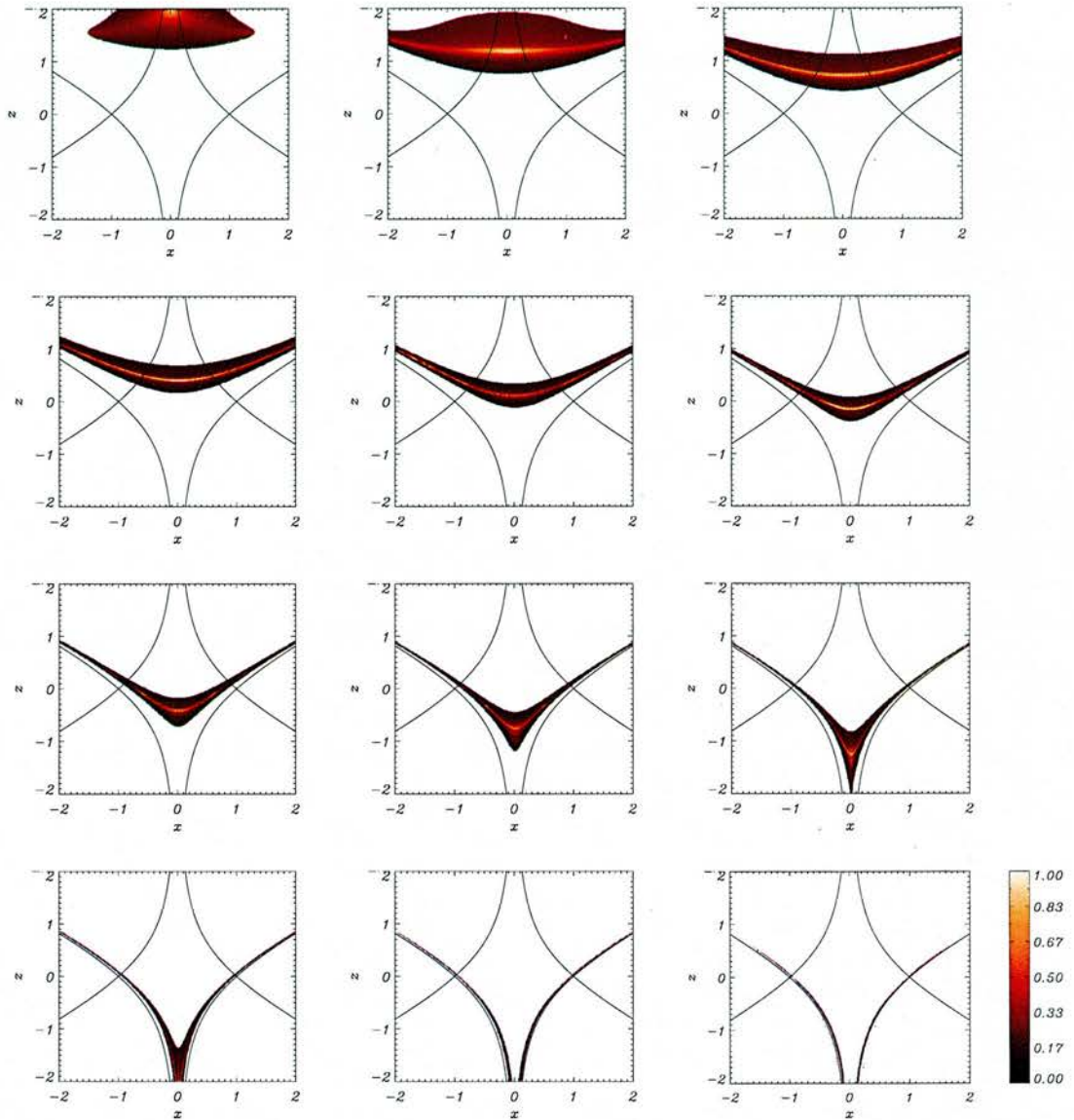


Figure 5.17: Contours of numerical simulation for Alfvén wave entering box at $1 \leq x \leq 2, z = 2$, at times (a) $t=0.25$, (b) $t=0.5$, (c) $t=0.75$, (d) $t=1.0$, (e) $t=1.25$, (f) $t=1.5$, (g) $t=1.75$, (h) $t=2.0$, (i) $t=2.25$, (j) $t=2.5$, (k) $t=2.75$ and (l) $t=2.0$, labelling from top left to bottom right.

Analytical Results

Again, we can solve equations (5.7) to gain an analytical solution for our Alfvén wave. In this experiment, our magnetic field takes the form $B_x = 2xz$ and $B_z = x^2 - z^2 - 1$. As we have done several times now, we substitute $v_y = e^{i\phi(x,z)} \cdot e^{-i\omega t}$ into (5.7) in accordance with Section 2.4.2. This gives:

$$\begin{aligned}
 -\omega^2 = & \left[-4x^2z^2 \left(\frac{\partial\phi}{\partial x} \right)^2 - 4xz(x^2 - z^2 - 1) \frac{\partial\phi}{\partial x} \frac{\partial\phi}{\partial z} - (x^2 - z^2 - 1)^2 \left(\frac{\partial\phi}{\partial z} \right)^2 \right] \\
 + i & \left[4x^2z^2 \frac{\partial^2\phi}{\partial x^2} + 4xz(x^2 - z^2 - 1) \frac{\partial^2\phi}{\partial xz} + (x^2 - z^2 - 1)^2 \frac{\partial^2\phi}{\partial z^2} \right. \\
 & \left. + 4xz^2 \frac{\partial\phi}{\partial x} + 2x(x^2 - z^2 - 1) \frac{\partial\phi}{\partial z} + 4x^2z \frac{\partial\phi}{\partial z} - 2z(x^2 - z^2 - 1) \frac{\partial\phi}{\partial z} \right]
 \end{aligned}$$

Now we make the WKB approximation that $\phi \sim \omega \gg 1$ and this leads to a first order PDE of the form:

$$\begin{aligned}
 -\omega^2 = & -4x^2z^2p^2 - 4xz(x^2 - z^2 - 1)pq - (x^2 - z^2 - 1)^2q^2 \\
 \Rightarrow \mathcal{F}(x, z, \phi, p, q) = & \frac{1}{2} [2xzp + (x^2 - z^2 - 1)q]^2 - \frac{1}{2}\omega^2 = 0
 \end{aligned}$$

where again $p = \frac{\partial\phi}{\partial x}$ and $q = \frac{\partial\phi}{\partial z}$. Note all the imaginary terms have disappeared. We include a half in the form of \mathcal{F} to make the equations nicer later.

Working out the quantities required to use Charpit's method:

$$\begin{aligned}
 \frac{\partial\mathcal{F}}{\partial\phi} &= 0 \\
 \frac{\partial\mathcal{F}}{\partial p} &= 2xz [2xzp + (x^2 - z^2 - 1)q] \\
 \frac{\partial\mathcal{F}}{\partial q} &= (x^2 - z^2 - 1) [2xzp + (x^2 - z^2 - 1)q] \\
 \frac{\partial\mathcal{F}}{\partial x} &= (2zp + 2xp) [2xzp + (x^2 - z^2 - 1)q] \\
 \frac{\partial\mathcal{F}}{\partial z} &= (2xp - 2zq) [2xzp + (x^2 - z^2 - 1)q]
 \end{aligned}$$

Now we can apply Charpit's method (page 31) to generate the equations:

$$\begin{aligned}
 \frac{d\phi}{ds} &= \omega^2 \\
 \frac{dp}{ds} &= -(2zp + 2xq)\zeta \\
 \frac{dq}{ds} &= -(2xp - 2zq)\zeta \\
 \frac{dx}{ds} &= (2xz)\zeta \\
 \frac{dz}{ds} &= (x^2 - z^2 - 1)\zeta
 \end{aligned} \tag{5.9}$$

where $\zeta = [2xzp + (x^2 - z^2 - 1)q]$, ω is the frequency of our wave and s is some parameter along the characteristic.

These five ODEs were solved numerically using a fourth-order Runge-Kutta method. The initial conditions used were:

$$\phi_0 = 0, \quad -1 \leq x_0 \leq 1, \quad z_0 = 2, \quad p_0 = 0, \quad q_0 = -\frac{\omega}{x_0^2 - z_0^2 - 1}$$

As mentioned before, constant ϕ can be thought of as defining the position of the edge of the wave pulse. Figure 5.18 shows constant ϕ at different values of the parameter s . With correct choices of s the WKB solution can be directly compared to our numerical solution and this can be seen in Figure 5.19. The agreement is very good.

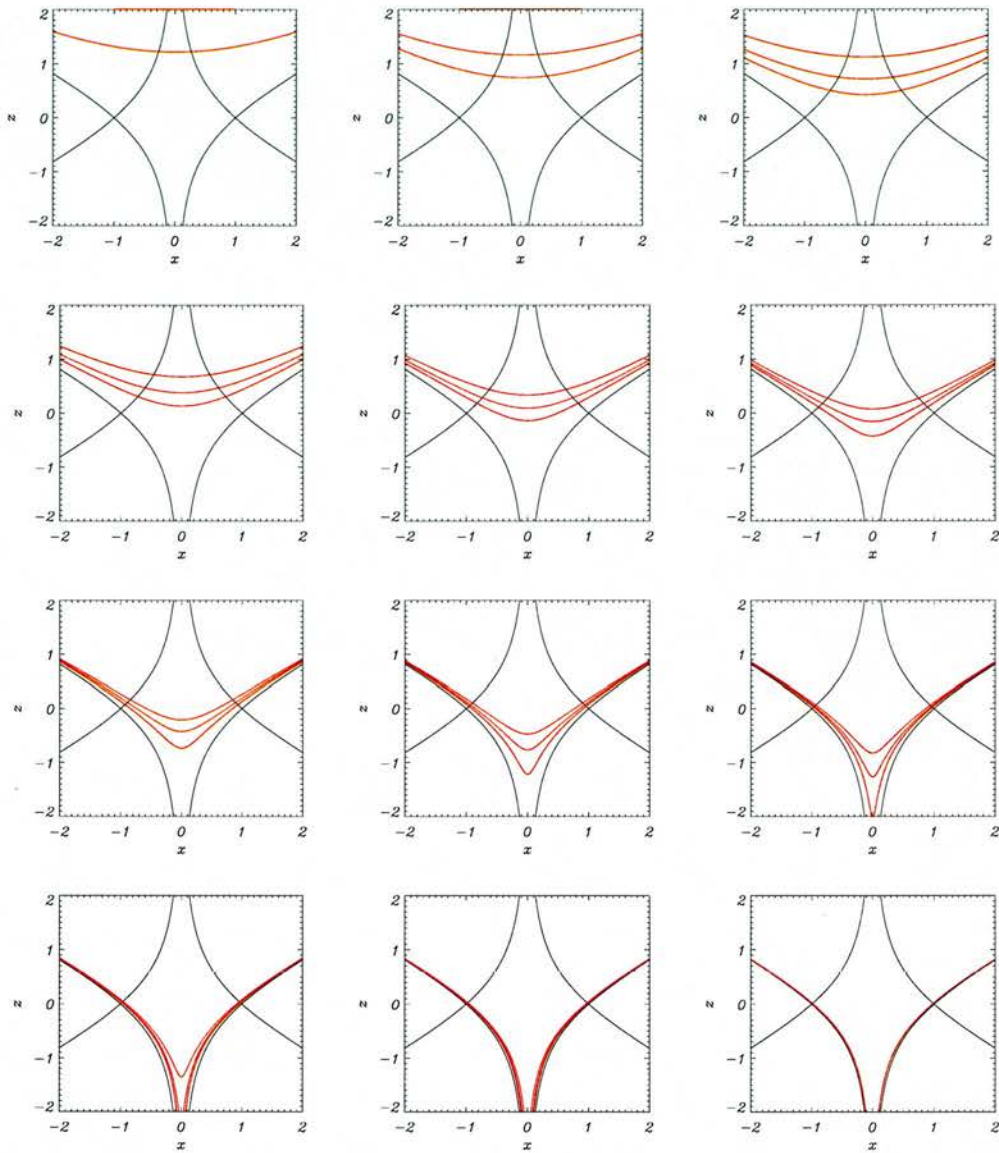


Figure 5.18: Analytical solution for WKB approximation of an Alfvén wave sent in from upper boundary for $-1 \leq x \leq 1, z = 2$ and its resultant propagation at times (a) $t=0.25$, (b) $t=0.5$, (c) $t=0.75$, (d) $t=1.0$, (e) $t=1.25$, (f) $t=1.5$, (g) $t=1.75$, (h) $t=2.0$, (i) $t=2.25$, (j) $t=2.5$, (k) $t=2.75$ and (l) $t=2.0$, labelling from top left to bottom right. The lines represent the front, middle and back edges of the WKB wave solution.

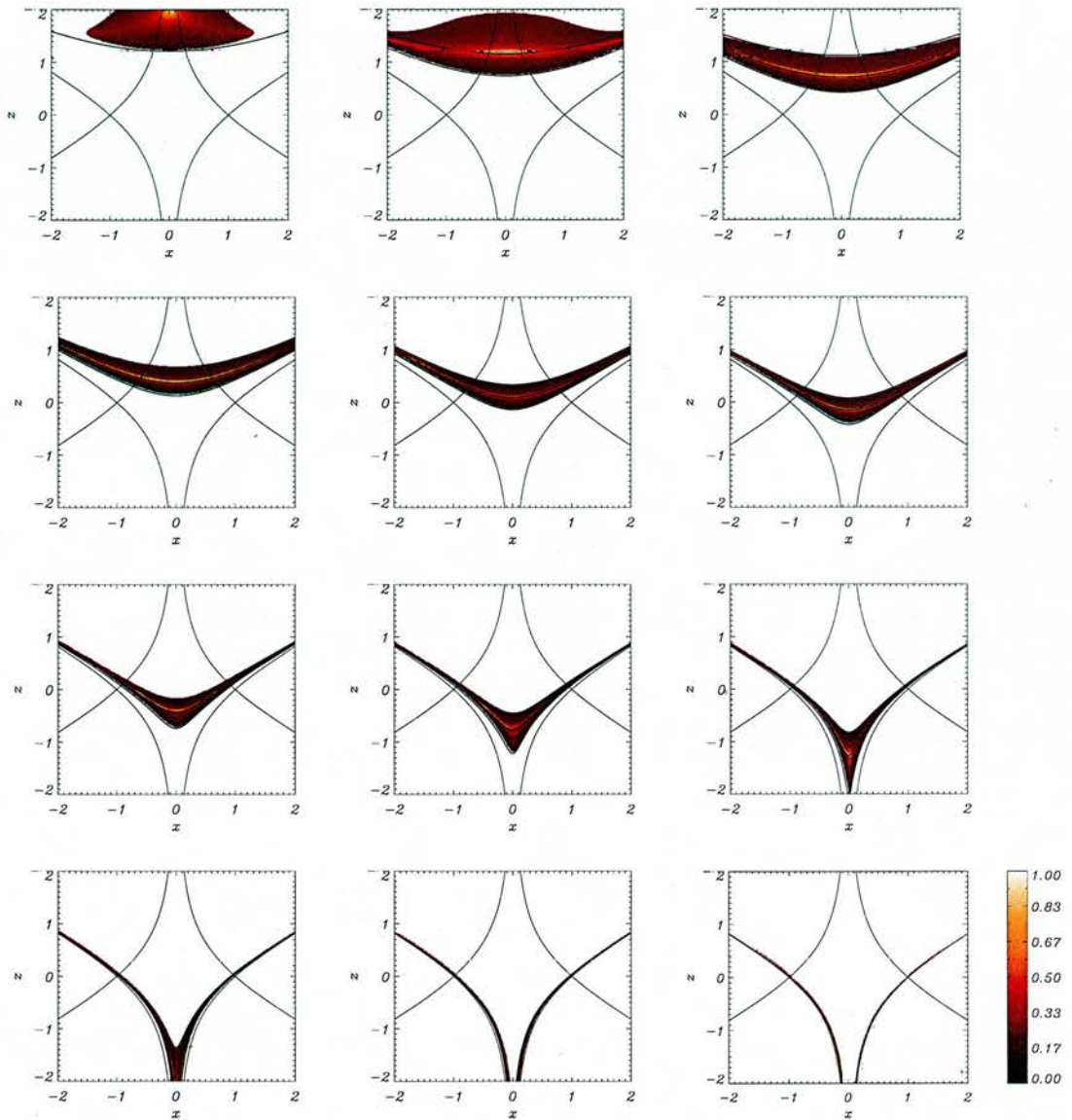


Figure 5.19: Comparison of numerical simulation (shaded area) and analytical solution for Alfvén wave sent in from top boundary for $-1 \leq x \leq 1, z = 2$ and its resultant propagation at times (a) $t=0.25$, (b) $t=0.5$, (c) $t=0.75$, (d) $t=1.0$, (e) $t=1.25$, (f) $t=1.5$, (g) $t=1.75$, (h) $t=2.0$, (i) $t=2.25$, (j) $t=2.5$, (k) $t=2.75$ and (l) $t=3.0$, labelling from top left to bottom right. The lines represent the front, middle and back edges of the WKB wave solution, where the pulse enters from the top of the box.

5.4.6 Case 4 : Side Boundary

For our final experiment on the behaviour of the Alfvén wave near two null points, we now consider a box ($-2 \leq x \leq 2$, $-2 \leq z \leq 2$) with a single wave pulse coming in across the side boundary ($x = -2$, $0 \leq z \leq 1$). The final high resolution run was performed in a box ($-2 \leq x \leq 0.5$, $-2.5 \leq z \leq 2.5$). The full boundary conditions were;

$$v_y(-2, z) = \begin{cases} \sin \omega t \sin \frac{\pi}{2} (z + 1) & \text{for } \begin{cases} 0 \leq z \leq 1 \\ 0 \leq t \leq \frac{\pi}{\omega} \end{cases} \\ 0 & \text{otherwise} \end{cases} ,$$

$$\left. \frac{\partial v_y}{\partial x} \right|_{x=0.5} = 0 , \quad \left. \frac{\partial v_y}{\partial z} \right|_{z=-2.5} = 0 , \quad \left. \frac{\partial v_y}{\partial z} \right|_{z=2.5} = 0 .$$

We found that the linear Alfvén wave travels in from the side boundary and begins to spread out, following the field lines. As the wave approaches the separatrix (that passes through $x = -1$, $z = \sqrt{2/3}$), the wave thins (but keeps its original amplitude). The wave eventually accumulates very near this separatrix. This can be seen in Figure 5.20.

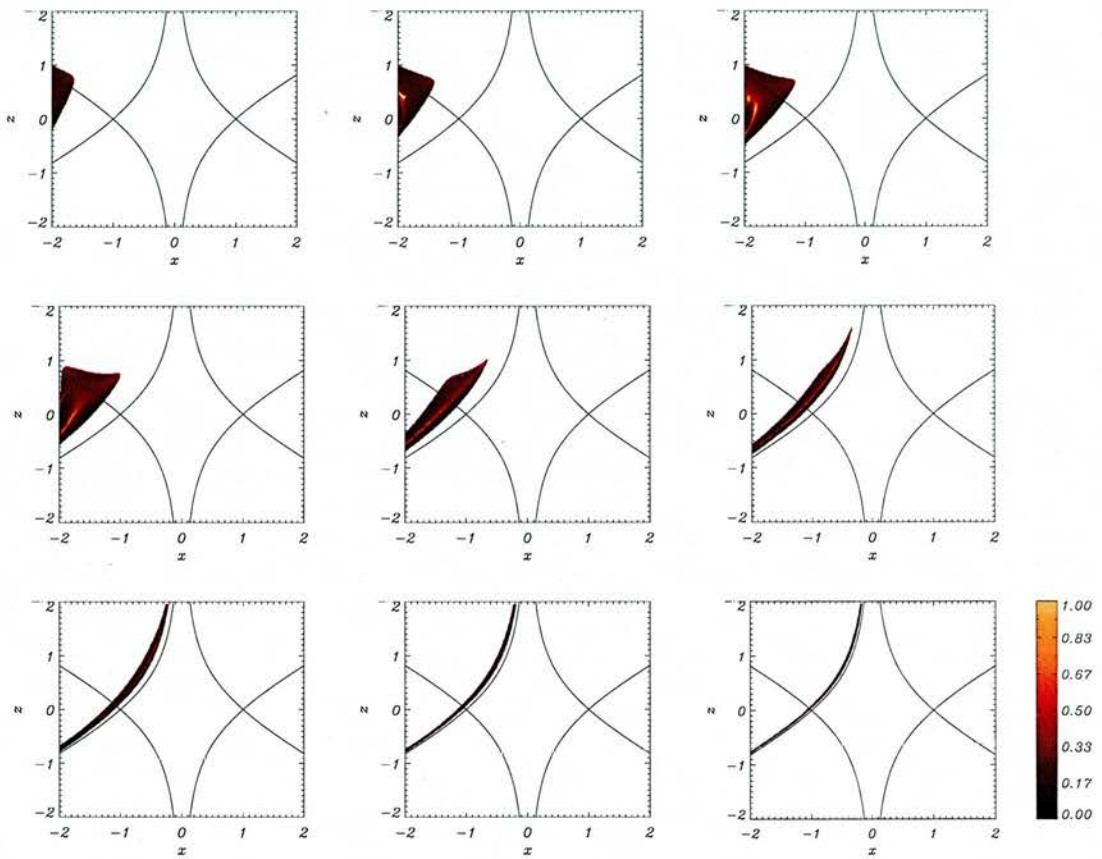


Figure 5.20: Contours of numerical simulation for Alfvén wave entering box at $x = -2$, $0 \leq z \leq 1$, at times (a) $t=0.167$, (b) $t=0.33$, (c) $t = 0.5$, (d) $t=0.67$, (e) $t=0.833$, (f) $t=1.0$, (g) $t=1.167$, (h) $t=1.33$, (i) $t=1.5$, labelling from top left to bottom right.

Analytical Results

By solving the same characteristic equations as in Section 5.4.5 (equations 5.9) but with different choices of initial condition (i.e. modelling the wave coming in from side boundary), we can obtain an analytical result to match our numerical simulation. Again, we use our fourth-order Runge-Kutta method. The initial conditions used were:

$$\phi_0 = 0, \quad x_0 = -2 \quad 0 \leq z_0 \leq 1, \quad p_0 = \frac{\omega}{2x_0z_0}, \quad q_0 = 0$$

The WKB solution can be seen in Figure 5.21 at various times. The comparison of the numerical simulation and analytical solution can be seen in Figure 5.22. If you look at the path of the wave, you can really see it bending to follow the field lines and taking on the shape of the separatrices.

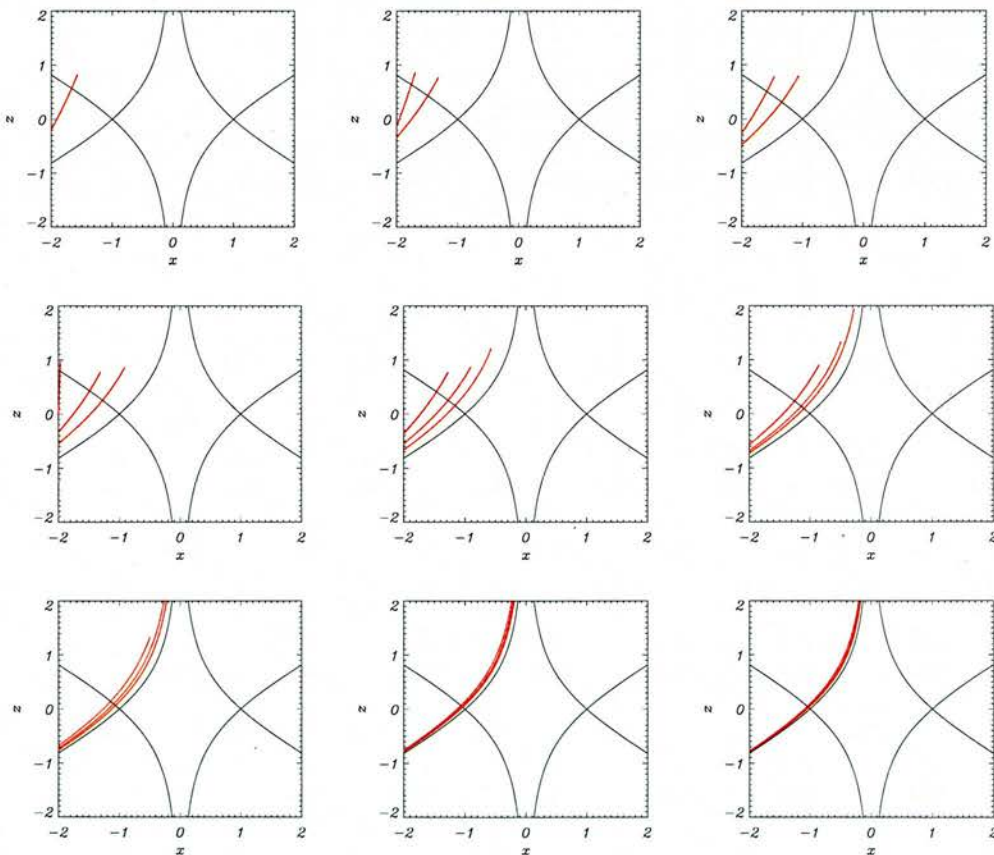


Figure 5.21: Contours of the WKB approximation of an Alfvén wave entering box at $x = -2$, $0 \leq z \leq 1$, at times (a) $t=0.167$, (b) $t=0.33$, (c) $t=0.5$, (d) $t=0.67$, (e) $t=0.833$, (f) $t=1.0$, (g) $t=1.167$, (h) $t=1.33$, (i) $t=1.5$, labelling from top left to bottom right. The lines represent the front, middle and back edges of the WKB wave solution.

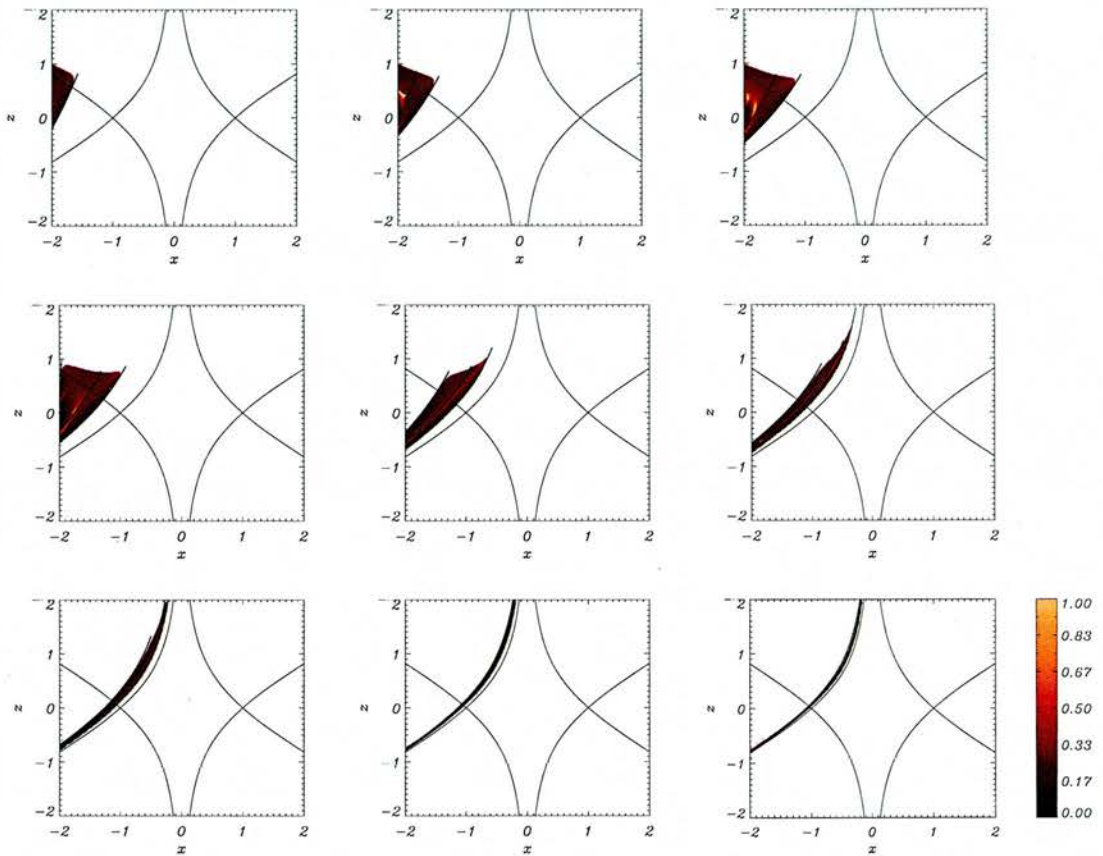


Figure 5.22: Comparison of numerical simulation (shaded area) and analytical solution for Alfvén wave entering box at $x = -2$, $0 \leq z \leq 1$, at times (a) $t=0.167$, (b) $t=0.33$, (c) $t=0.5$, (d) $t=0.67$, (e) $t=0.833$, (f) $t=1.0$, (g) $t=1.167$, (h) $t=1.33$, (i) $t=1.5$, labelling from top left to bottom right. The lines represent the front, middle and back edges of the WKB wave solution, where the pulse enters from the left hand side of the box.

5.5 Conclusions

This chapter describes an investigation into the nature of MHD waves in the neighbourhood of two null points. From the work explained above, it has been seen that when a fast magnetoacoustic wave propagates near the two null point configuration, the wave bends due to refraction and begins to wrap itself around the null points. The wave *splits* and part of it travels (and wraps) around one of the null points and the rest wraps around the other null point. In the case of the fast wave approaching the two null points from above, the wave travels down towards the null points and begins to wrap around them. In addition, since the Alfvén speed is non-zero between the null points, the wave can travel through this area (into the lower half plane). This part of the wave is also affected by the refraction effect and the wave continues to wrap around its closest null point. The wave splits into two along the line $x = 0$ (due to symmetry), with each half of the wave going to its closest null point. Each part of the wave then continues to wrap around its respective null point repeatedly, eventually accumulating at that point.

In the case of the fast wave pulse travelling in from the side boundary, we see a similar effect (i.e. a refraction effect, wave splitting and accumulation at the nulls), but in this case the wave is *not* equally shared between the null points. For a fast wave travelling in from the left boundary, initially the pulse thins and begins to feel the effect of the left hand-side null point. The wave begins to wrap around this null point (due to refraction). As the ends of the wave wrap around behind the left null point, they then become influenced by the second, right hand side null point. These arms of the wave then proceed to wrap around the right null point, flattening the wave. Furthermore, the two parts of the wave now travelling through the area between the null points have non-zero Alfvén speed, and so pop through. These parts of the wave break along $x = 0$ and then proceed to wrap around the null point closest to them. The angle that the fast wave approaches the null points from will determine what proportion of wave ends up at each null point (when the wave splits).

Furthermore, since we have a changing perturbed magnetic field with increasing gradients, we will have a build up of current density. All the wave is accumulating at the null points. This means that the perturbed magnetic field will have large gradients at those points and that is where current will accumulate. It is clear the refraction effect focusses all the energy of the incident wave towards the null points. The physical significance of this is that any fast magnetoacoustic disturbance in the neighbourhood of a null point pair will be drawn towards the regions of zero magnetic field strength and focus all of its energy at that point. With a large current accumulation at the nulls, this is where energy will be dissipated. Therefore, **wave heating will naturally occur at these null points**. This is the same phenomenon as observed in Chapter 3. This gives us confidence that the key result (**fast waves cause heating at null points**) is a general key result to 2D $\beta = 0$ magnetic configurations (rather than being specific to certain magnetic fields).

In the cases of the Alfvén wave, the results show that the wave propagates along the field lines and eventually accumulates very near to the separatrices. The wave thins but keeps its original amplitude and in fact is confined to the field lines. This is again in agreement with work carried out for a single null in Chapter 4. As hypothesised above, since we have wave accumulation along the separatrices, the gradients of the perturbed magnetic field (j_x and j_z) will build up along these as well. Hence we will have current build up along the separatrices. Therefore, if all the current is accumulating along the separatrices, then **this is where Alfvén wave heating will naturally occur due to dissipation.**

In view of the fact that the waves eventually dissipate due to resistive damping (for example), it would be useful to have an estimate of the nature of the wave damping. Dissipation enters our model through the addition of a $\eta \nabla^2 \mathbf{b}$ term to equation (5.6) and the WKB model can be extended to include the effects of resistivity. For the model describing the Alfvén wave pulse entering the top boundary (Section 5.4.2), it was found that along the separatrices the diffusion term become important in a time that depends on $\log \eta$ (see Section 5.6 below) as found by Craig & McClymont (1991; 1993) and Hassam (1992). This means that the linear wave dissipation will be very efficient. This method can also be applied to the other cases investigated in this chapter.

Démoulin *et al.* (1994b) investigated the magnetic field topology of a flare event. They found that the high intensity regions of H_α were located on or close to the separator lines. Their findings show a link to ours and support the possibility of transferring our results to 3D. We can also easily extend the model to 2.5D with the addition of a third spatial coordinate, by taking into account an extra Fourier component of the form e^{imy} , where m is the azimuthal mode number. This would lead to coupling of all the wave modes, and probably result in energy accumulating at *both* the separatrices and the null points.

Note that all the experiments conducted here that send in an Alfvén wave pulse from the boundary do so *across* a separatrix. If the initial wave pulse does not cross a separatrix, it will follow the field lines and leave the box (there will be no wave accumulation at any separatrices).

5.6 Including the effects of resistivity

We can learn something about the nature of the wave damping by considering an extension to our WKB expansion for the Alfvén wave investigated in Section 5.4.2. Firstly, we consider solutions of the form $e^{i(\omega\bar{\phi}-\omega t)}$, where $\omega \gg 1$ and $\bar{\phi}$ is of order unity. We now use the variable $\bar{\phi}$, where $\omega\bar{\phi} = \phi$ and where ϕ has the same definition as in our previous WKB approximations (as in Section 5.4.2). We introduce this new variable so we only have one large variable (i.e. ω) in our equations, since we want to consider an expansion with this (single) large parameter.

We also assume a specific scaling for the resistivity, such that $\eta = \eta_0/\omega^2$, where η_0 is of order unity. This specific form is for illustration only; alternative forms are possible and they modify the series expansion for $\bar{\phi}$.

Using the same method with which we reached equation (5.6), the linearised equations for the Alfvén wave including resistivity can be combined to form a single wave equation for b_y :

$$\frac{\partial^2 b_y}{\partial t^2} = (\mathbf{B}_0 \cdot \nabla)^2 b_y + \frac{\eta_0}{\omega^2} \frac{\partial}{\partial t} \nabla^2 b_y.$$

Substituting in $b_y = e^{i(\omega\bar{\phi}-\omega t)}$ gives:

$$-\omega^2 b_y = -\omega^2 (\mathbf{B}_0 \cdot \nabla \bar{\phi})^2 b_y + i\omega b_y (\mathbf{B}_0 \cdot \nabla)^2 \bar{\phi} + \eta_0 \left(i\omega |\nabla \bar{\phi}|^2 b_y + b_y \nabla^2 \bar{\phi} \right).$$

Now usually we would expand $\bar{\phi}$ in terms of $\frac{1}{\omega}$, such that $\bar{\phi} = \phi_0 + \frac{1}{\omega}\phi_1 + \frac{1}{\omega^2}\phi_2 + \dots$. However, here we shall instead consider the simpler expansion $\bar{\phi} = \phi_0 + i\frac{\eta_0}{\omega}\phi_1$, where we have taken a factor of $i\frac{\eta_0}{\omega}$ out of ϕ_1 for simplification (ϕ_1 is real). We have cut the expansion off above $\mathcal{O}(\frac{1}{\omega})$ simply to illustrate the point here and higher order expansions are of course possible.

Making this substitution gives:

$$\begin{aligned} -\omega^2 &= -\omega^2 (\mathbf{B}_0 \cdot \nabla \phi_0)^2 - 2i\omega\eta_0 (\mathbf{B}_0 \cdot \nabla \phi_0) (\mathbf{B}_0 \cdot \nabla \phi_1) + \eta_0^2 (\mathbf{B}_0 \cdot \nabla \phi_1)^2 \\ &+ i\omega (\mathbf{B}_0 \cdot \nabla)^2 \phi_0 - \eta_0 (\mathbf{B}_0 \cdot \nabla)^2 \phi_1 + i\eta_0\omega |\nabla \phi_0|^2 + [\text{other terms}]. \end{aligned}$$

Comparing terms of order of ω^2 and ω :

$$\begin{aligned} (\mathbf{B}_0 \cdot \nabla \phi_0)^2 &= 1 & \Rightarrow (\mathbf{B}_0 \cdot \nabla \phi_0) &= 1, \\ -2\eta_0 (\mathbf{B}_0 \cdot \nabla \phi_0) (\mathbf{B}_0 \cdot \nabla \phi_1) + (\mathbf{B}_0 \cdot \nabla)^2 \phi_0 + \eta_0 |\nabla \phi_0|^2 &= 0 & \Rightarrow (\mathbf{B}_0 \cdot \nabla) \phi_1 &= \frac{1}{2} |\nabla \phi_0|^2. \end{aligned}$$

Now:

$$\nabla \phi_0 = \left(\frac{\partial \phi_0}{\partial x}, 0, \frac{\partial \phi_0}{\partial z} \right) \quad \Rightarrow \quad |\nabla \phi_0|^2 = \left(\frac{\partial \phi_0}{\partial x} \right)^2 + \left(\frac{\partial \phi_0}{\partial z} \right)^2 = p^2 + q^2,$$

where $p = \frac{\partial\phi_0}{\partial x}$ and $q = \frac{\partial\phi_0}{\partial z}$ as in Section 5.4.2. Hence:

$$\begin{aligned} \left(B_x \frac{\partial\phi_1}{\partial x} + B_z \frac{\partial\phi_1}{\partial z} \right) &= \frac{1}{2} (p^2 + q^2) , \\ \Rightarrow \frac{d\phi_1}{ds} = \frac{dx}{ds} \frac{\partial\phi_1}{\partial x} + \frac{dz}{ds} \frac{\partial\phi_1}{\partial z} &= \frac{1}{2} \xi (p^2 + q^2) , \end{aligned} \quad (5.10)$$

where $\xi = [(x^2 - z^2 - 1)p - 2xzq]$ and we have used Charpit's equations from Section 5.4.2, i.e. $\frac{dx}{ds} = \xi B_x$ and $\frac{dz}{ds} = \xi B_z$.

Hence, we can solve for ϕ_1 by adding equation (5.10) to (5.8) and utilising the same Runge-Kutta method to solve them all. The behaviour of ϕ_1 can be seen in Figure 5.23, where $\log \phi_1$ along the separatrix is plotted against s . The behaviour is described by $\phi_1 = \frac{1}{2} e^{4\omega s}$, where $\omega = 2\pi$.

We can now substitute our new form for ϕ_1 into our $e^{i(\omega\bar{\phi} - \omega t)}$, where $\bar{\phi} = \phi_0 + i\frac{\eta_0}{\omega}\phi_1 = \phi_0 + i\omega\eta\phi_1$. Hence:

$$\begin{aligned} b_y &= \exp [i (\omega\phi_0 - \omega t)] \exp (-\omega^2\eta\phi_1) , \\ &= \exp [i (\omega\phi_0 - \omega t)] \exp \left\{ -\frac{1}{2}\omega^2\eta [\exp (4\omega s)] \right\} . \end{aligned} \quad (5.11)$$

Therefore, the diffusive term will become important when $\frac{1}{2}\omega^2\eta e^{4\omega s}$ becomes of order unity, i.e. on a timescale of $s \approx -\frac{1}{4\omega} \log \eta$, under the above assumptions.

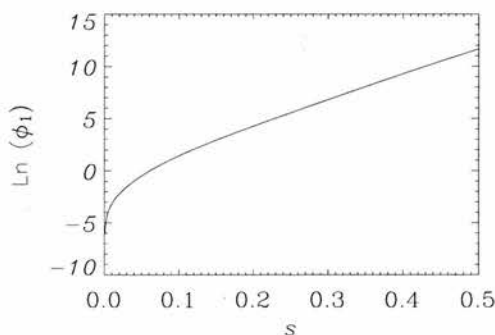


Figure 5.23: Behaviour of $\log (\phi_1)$ against time elapsed. The slope of the line between $s = 0.1$ and $s = 0.5$ is 4ω .

Chapter 6

Behaviour of MHD waves in the neighbourhood of two dipoles

6.1 Introduction

Chapter 5 showed that the key results from Chapters 3 and 4 carried over from the simple 2D single magnetic null point to a more complicated magnetic configuration. There is however another aspect of the models of Chapters 3 and 4 we must now address. Recall the form of the magnetic fields used in the previous chapters (equations 3.1, 5.1 and 5.2). These choices of magnetic field are only valid in the neighbourhood of the null point(s), because as x and z get very large, \mathbf{B}_0 also gets large, which is unphysical. Thus, we now want to investigate the behaviour of MHD waves near a more realistic magnetic configuration (and one that still involves a magnetic null). We want to again ask: *do the findings of Chapters 3 and 4 carry through to a more realistic configuration?* One such choice is a magnetic field created by two dipoles, of the form:

$$\mathbf{B}_0 = B_0 L^2 (B_x, 0, B_z) \quad \text{where} \quad B_x = \frac{-(x+a)^2 + z^2}{[(x+a)^2 + z^2]^2} + \frac{-(x-a)^2 + z^2}{[(x-a)^2 + z^2]^2},$$
$$B_z = -\frac{2(x+a)z}{[(x+a)^2 + z^2]^2} - \frac{2(x-a)z}{[(x-a)^2 + z^2]^2} \quad (6.1)$$

where B_0 is a characteristic field strength, L is the length scale for magnetic field variations and $2a$ is the separation of the dipoles. We choose $a = 0.5$ for our simulations. This magnetic field can be seen in Figure 6.1. It comprises of four separatrices and an X-point located at $(x, z) = (0, a)$. Note that as x or z gets very large, the field strength becomes small; this is a more physical field than those previously investigated in this Thesis.

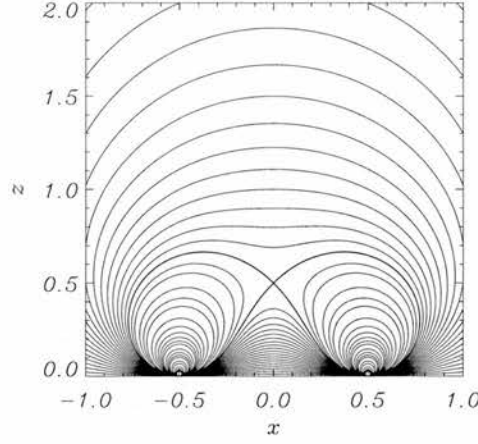


Figure 6.1: Our choice of equilibrium magnetic field.

6.2 Basic Equations and set-up

In this chapter, we will investigate the behaviour of the linear fast MA wave and Alfvén wave in the neighbourhood of a two dipoles configuration.

As in Chapters 3 and 4, the linearised MHD equations are used to study the nature of wave propagation near the dipoles. The derivation of the linearised, non-dimensionalised equations for a $\beta = 0$ plasma can be found in Chapter 2. As mention is Section 2.2.3, the linearised MHD equations naturally decouple into two equations: one for the fast MHD wave and the second for the Alfvén wave. The equations relevant to studying the nature of the fast MA wave in this chapter are equations (2.10) and (2.11). Thus, defining $\mathbf{B}_0 = (B_x, 0, B_z)$ and $\mathbf{b} = (b_x, 0, b_z)$ we obtain:

$$\begin{aligned}
 \rho_0 \frac{\partial}{\partial t} v_{\perp} &= v_A^2(x, z) \left(\frac{\partial b_z}{\partial x} - \frac{\partial b_x}{\partial z} \right) \\
 \frac{\partial b_x}{\partial t} &= -\frac{\partial}{\partial z} v_{\perp} + \frac{1}{R_m} \left(\frac{\partial^2}{\partial x^2} + \frac{\partial^2}{\partial z^2} \right) b_x, \\
 \frac{\partial b_z}{\partial t} &= \frac{\partial}{\partial x} v_{\perp} + \frac{1}{R_m} \left(\frac{\partial^2}{\partial x^2} + \frac{\partial^2}{\partial z^2} \right) b_z,
 \end{aligned} \tag{6.2}$$

where the Alfvén speed, $v_A(x, z) = \sqrt{B_x^2 + B_z^2}$ and v_{\perp} is perturbed magnetic field and velocity as defined in Chapter 2 (page 20). Note that these are the same equations as (3.2) and (5.3), but with a different form for the (background) Alfvén speed (v_A).

We will again neglect the magnetic resistivity (η) in our investigations, but will discuss its role in the conclusions. Thus, we consider an ideal plasma ($\eta = 0$ or $R_m \rightarrow \infty$). We also again assume the background gas density is uniform (so $\rho_0 = 1$ under our non-dimensionalisation).

These simplifications allow us to combine the above equations into a single wave equation:

$$\frac{\partial^2}{\partial t^2} v_{\perp} = (B_x^2 + B_z^2) \left(\frac{\partial^2}{\partial x^2} + \frac{\partial^2}{\partial z^2} \right) v_{\perp}. \quad (6.3)$$

This is the wave equation of the form of equation (1.23). This is the primary equation for the fast MA wave we will be looking at in this chapter (although the form of equations (6.2) is easier to solve numerically). Recall that in its derivation, we have assumed linearised behaviour in an ideal, $\beta = 0$, 2D plasma with uniform density.

The equations relevant to studying the Alfvén wave are equations (2.12) and (2.13). Again defining $\mathbf{B}_0 = (B_x, 0, B_z)$ and $\mathbf{b} = (0, b_y, 0)$ yields:

$$\begin{aligned} \rho_0 \frac{\partial v_y}{\partial t} &= (\mathbf{B}_0 \cdot \nabla) b_y = \left(B_x \frac{\partial}{\partial x} + B_z \frac{\partial}{\partial z} \right) b_y, \\ \frac{\partial b_y}{\partial t} &= (\mathbf{B}_0 \cdot \nabla) v_y + \frac{1}{R_m} \nabla^2 b_y \\ &= \left(B_x \frac{\partial}{\partial x} + B_z \frac{\partial}{\partial z} \right) v_y + \frac{1}{R_m} \left(\frac{\partial^2}{\partial x^2} + \frac{\partial^2}{\partial z^2} \right) b_y, \end{aligned} \quad (6.4)$$

where as defined by equation (2.1), v_y is the velocity out of the plane that \mathbf{B}_0 defines. Hence, waves with this velocity will be transverse waves (energy flow perpendicular to the wavevector).

As above, we will neglect the dissipation terms and consider a uniform background density ($R_m \rightarrow \infty$, $\rho_0 = 1$). Hence, these equations can also be combined to form a single wave equation:

$$\frac{\partial^2}{\partial t^2} v_y = (\mathbf{B}_0 \cdot \nabla)^2 v_y = \left(B_x \frac{\partial}{\partial x} + B_z \frac{\partial}{\partial z} \right)^2 v_y. \quad (6.5)$$

This is the primary equation we will be looking at for the Alfvén wave in this chapter. In its derivation, we have assumed linearised behaviour in an ideal, $\beta = 0$, 2D plasma with uniform density.

Thus, equations (6.3) and (6.5) will allow us to study the behaviour of the fast and Alfvén waves. Note that as in Section 5.2, these are general equations to which we will be applying this chapter's particular choice of \mathbf{B}_0 (equation 6.1). Thus, substituting in the \mathbf{B}_0 of equation (3.1) would recover the equations used in Chapters 3 and 4, and substituting the \mathbf{B}_0 of equation (5.1) or (5.2) would recover the equations used in Chapter 5.

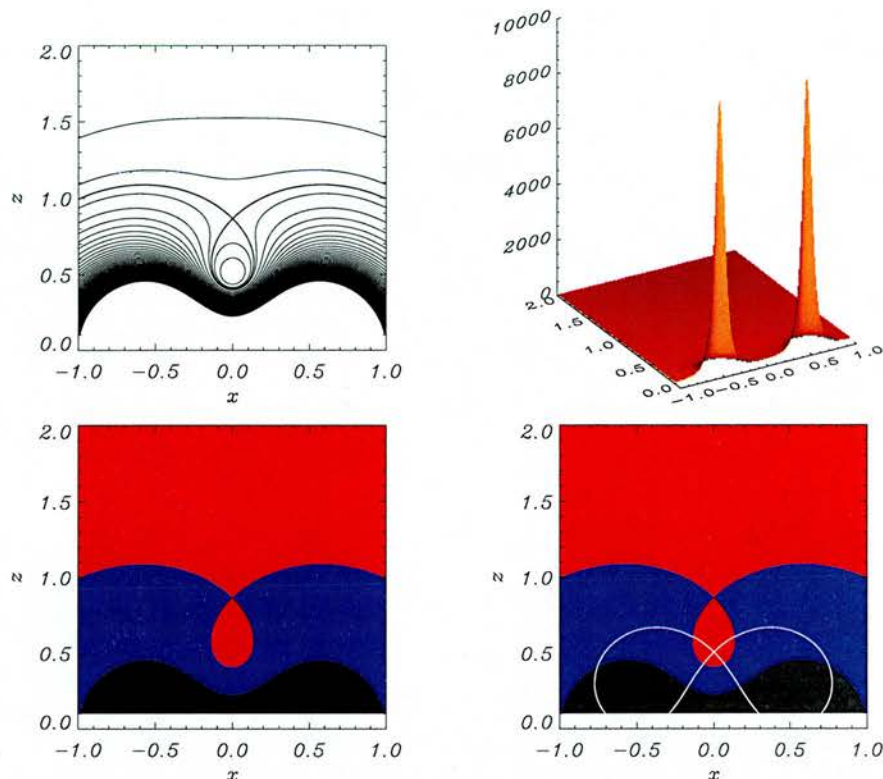


Figure 6.2: **Representations of v_A^2 .** *Top left* shows a contour plot of v_A^2 , with cut-off value above $v_A^2 = 20$ (cut-off at $z = z_0 = 0.1$). *Top right* shows a shaded surface of v_A^2 . *Bottom left* subfigure shows the same contour plot as the top left subfigure, but is now colour coded; red represents values $0 \leq v_A^2 \leq 1$, blue represents $1 \leq v_A^2 \leq 20$ and black represents $v_A^2 \geq 20$. Thus we can see that around the X-point there is an area of small v_A^2 . *Bottom right* subfigure shows the same colour contour as bottom left, but with the skeleton of the magnetic field superimposed on top.

6.2.1 Alfvén speed profile

Equation (6.3) contains a term v_A^2 for a variable Alfvén speed. The magnetic configuration described by equation (6.1) gives this speed as $v_A^2(x, z) = B_x^2(x, z) + B_z^2(x, z)$. A line contour and colour contour graphical representation of v_A^2 is shown in Figure 6.2. The top left figure shows a contour plot of v_A^2 . Note how there is a massive rise in v_A^2 as we approach the loci of the dipoles (at $(x, z) = (\pm a, 0)$ where $a = 0.5$ in our simulations). In fact, this contour has been cut-off for values of $v_A^2 \geq 20$ in the subfigure, otherwise the contour lines get too close together near $(x, z) = (\pm a, 0)$. The reason for this can be seen in the top right subfigure; this shaded surface of v_A^2 shows clearly that the velocity profile changes massively across the magnetic region, and reaches a maximum at the loci. The bottom left subfigure shows the same contour plot as the top left subfigure, but is now colour coded; red represents values $0 \leq v_A^2 \leq 1$, blue represents $1 \leq v_A^2 \leq 20$ and black represents $v_A^2 \geq 20$. Thus we can see that around the X-point there is a small island of low Alfvén speed. The bottom right subfigure shows the same colour contour as

the left, but with the skeleton of the magnetic field superimposed on top.

Due to our choice of equilibrium magnetic field, there are two singularities at $(x, z) = (\pm a, 0)$ and hence $v_A^2 \rightarrow \infty$ as these points. If we were to generate a wave along $z = 0$, our Lax-Wendroff scheme would be unable to deal with this extreme speed differential. Thus, in this chapter we will generate our waves not along $z = 0$ but along $z = z_0$, where z_0 is small (and so close to the $z = 0$ line). This choice still starts the waves in a region of varying Alfvén speed, but reduces the massive differential to something easier to work with numerically. Thus, starting the waves at $z = z_0$ results in very little loss of information about the system. In addition, the CFL condition (Section 2.3.2) dictates that our timestep has to be very small (because our speed is so large in some places). Thus, to reduce the computing time and with very little loss of understanding, $z_0 = 0.1$ was set in the experiments (recall $a = 0.5$).

6.3 Fast Waves

We now look at the behaviour of fast MHD waves in the neighbourhood of two dipoles. In this more realistic magnetic configuration, there are three scenarios which we shall visit in order to fully understand the system. Firstly, the two dipoles create a natural X-point (Figure 6.1) and we want to know if the fast wave wraps around this null point in a similar way to that described in Chapter 3. Thus, Simulation One describes a localised, linear fast wave approaching this X-point. There is also a second, new feature to this magnetic configuration; it contains regions of very high (background) Alfvén speed. Thus, Simulation Two describes a linear fast wave generated in this area, but localised to one side of the (symmetric) system. Simulation Three describes a scenario similar to Simulation Two, but now with a pulse generated along the entire lower boundary. Simulations One and Two will build towards an understanding of the complete system of Simulation Three.

All three simulations generate a linear fast wave pulse on the lower boundary, a pulse that then continues to travel up into the magnetic configuration. The lower boundary was set at z_0 in all three experiments, where $z_0 = 0.1$ and $a = 0.5$.

6.4 Simulation One

We solve the linearised MHD equations for the fast wave, namely equations (6.2), numerically using our two-step Lax-Wendroff scheme. The numerical scheme is run in a box with $-1 \leq x \leq 1$ and $z_0 \leq z \leq 2$, using the magnetic field shown in Figure 6.1. We initially consider a single wave pulse coming in from the bottom boundary, localised along $-0.2 \leq x \leq 0.2$, $z = z_0 = 0.1$. For the single wave pulse, the boundary conditions were set such that:

$$v_{\perp}(x, z_0) = \begin{cases} \sin \omega t \sin \left[\frac{5\pi}{2} (x + 1) \right] & \text{for } -0.2 \leq x \leq 0.2, \quad 0 \leq t \leq \frac{\pi}{\omega} \\ 0 & \text{otherwise} \end{cases}$$

$$\left. \frac{\partial}{\partial x} v_{\perp} \right|_{x=x_{min}} = 0, \quad \left. \frac{\partial}{\partial x} v_{\perp} \right|_{x=x_{max}} = 0, \quad \left. \frac{\partial}{\partial z} v_{\perp} \right|_{z=z_{max}} = 0.$$

In the final run shown here, the simulation was carried out in a box $-0.6 \leq x \leq 0.6$ and $z_0 \leq z \leq 1$, so as to maximise the usefulness of our 1000×1000 grid.

We find that the linear, fast magnetoacoustic wave travels up from the lower boundary (from z_0) and begins to spread out. The propagation can be seen in Figure 6.3. In the early subfigures of Figure 6.3, we can see that the pulse travels faster at the ends (wings) than in its centre, due to the variation in Alfvén speed. The wave then continues to *refract* around the null point, and wraps itself around it. The (background) Alfvén speed is zero at $(x, z) = (0, 0.5)$ (the X-point) and so the fast wave cannot cross this point. Consequently, the null acts as an immovable barrier to the propagation of the wave and thus is a focus for the wrapping around effect. The wave continues to wrap around the null and becomes thinner. The wave (eventually) accumulates very close to the X-point.

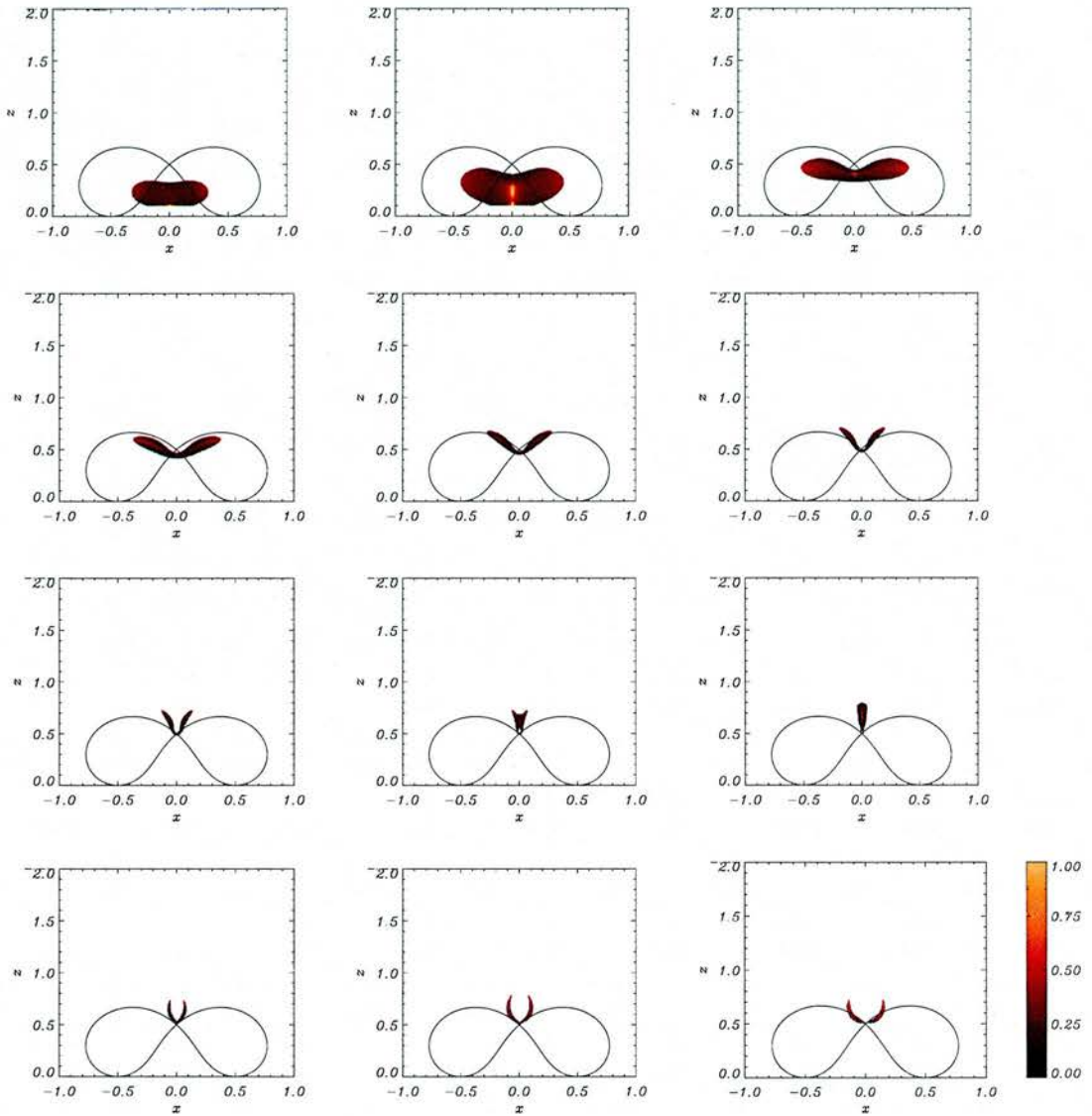


Figure 6.3: Contours of numerical simulation v_{\perp} for a fast wave sent in from lower boundary for $-0.2 \leq x \leq 0.2$, $z = 0.1$ and its resultant propagation at times (a) $t=0.05$, (b) $t=0.1$, (c) $t=0.15$, (d) $t=0.2$, (e) $t=0.25$ and (f) $t=0.3$, (g) $t=0.35$, (h) $t=0.4$, (i) $t=0.45$, (j) $t=0.5$, (k) $t=0.55$ and (l) $t=0.6$, labelling from top left to bottom right.

6.5 Simulation Two

6.5.1 Numerical simulation

In this simulation, we again solve the linearised MHD equations for the fast wave numerically (using the two-step Lax-Wendroff scheme). We now consider a single wave pulse coming in from the bottom boundary, localised along $-1 \leq x \leq 0$, $z = z_0 = 0.1$. This allows us to explore a different topological area than that of Simulation One. Here, the boundary conditions were set such that:

$$v_{\perp}(x, z_0) = \begin{cases} \sin \omega t \sin [\pi (x + 1)] & \text{for } -1 \leq x \leq 0, \quad 0 \leq t \leq \frac{\pi}{\omega} \\ 0 & \text{otherwise} \end{cases}$$

$$\left. \frac{\partial}{\partial x} v_{\perp} \right|_{x=x_{min}} = 0, \quad \left. \frac{\partial}{\partial x} v_{\perp} \right|_{x=x_{max}} = 0, \quad \left. \frac{\partial}{\partial z} v_{\perp} \right|_{z=z_{max}} = 0.$$

In the final run shown here, the simulation was carried out in a box $-1.4 \leq x \leq 1.4$ and $z_0 \leq z \leq 1.7$, so again as to maximise the use of our 1000×1000 grid.

The results can be seen in Figures 6.5 and 6.6. We find that the localised pulse starting between $-1 \leq x \leq 0$ rises, but not all parts rise at the same speed. The central part of the pulse rises much faster, with the maximum occurring over $x = -0.5$. This is due to the high (background) Alfvén speed localised in that area (as seen in Section 6.2.1). This pulls the wave pulse out of its original shape. This area of high velocity is a new effect not seen in previous chapters.

Part of the wave pulse also approaches the null (extreme right of the generated wave), and this part appears to get caught around the X-point. As in Simulation One, the wave cannot cross the null and refracts around it. This also occurs here; part of the wave gets caught and wraps around the null (again and again). However, since the wave is being stretched out and thinned as it encircles the null, our resolution runs out at after some point (as discussed on page 45). Thus, we cannot clearly see the wave wrapping around the null in Figures 6.5 and 6.6. However, in Figure 6.4 we can see a blow-up of the region around the X-point and thus can see that the effect proceeds in a similar way to the asymmetric pulse described in Section 3.5. We have plotted $(x, z) \rightarrow (-x, -z)$ to help the comparison (i.e. reflected the image in the line $y = -x$). Thus, this part of the fast wave pulse accumulates at the X-point. The resolution in Figure 6.4 is coarse since it is a blow-up from the resolution of the simulation.

The rest of the wave, meanwhile, continues to rise and spread out. This part proceeds at a slower speed than before, again due to the Alfvén speed profile (Section 6.2.1). Once above the magnetic skeleton, the wave appears to simply continue to rise and spread out. The wave no longer heavily influenced by the magnetic null point.

However, since part of the wave is wrapping around the null, and a second part is rising away from the magnetic region, there must come a point where the wave splits. This can be seen in Figure 6.6. Turning our attention to the behaviour on the right of the null, we see that the wave continues to spread out; part of it appears to be travelling to the top right corner and part of it is hooked around the null. In the second row of subfigures, we see the wave stretched between these two goals. The wave then splits, with part of it ultimately wrapping around the null and continuing much in the same way as the asymmetric wave pulse in Section 3.5. The other part of the wave then continues to spread out and travel away from the magnetic region. This can be seen in the bottom rows of subfigures. The actual wave splitting itself occurs when the wave enters the right hand region of high velocity (large v_A^2 around $(\pm 0.5, 0)$) this thins the wave massively and forces the two parts to split.

Thus, a wave pulse starting between $-1 \leq x \leq 0$ travels into the magnetic region (unevenly due to the change in speed profile). Part of the wave experiences a slight refraction effect due to the Alfvén speed profile, but ultimately spreads out and propagates away. However, part of the wave is caught by the null and refracted into the X-point. This part of the wave accumulates at the X-point.

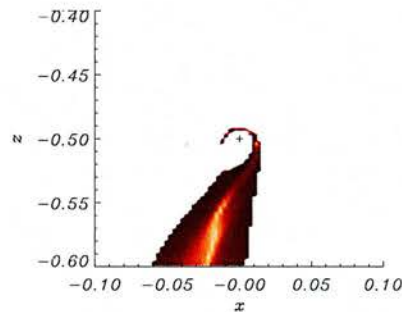


Figure 6.4: Contour of the numerical simulation of v_{\perp} for a fast wave sent in from lower boundary for $-1 \leq x \leq 0$ after time $t = 0.44$. Figure shows blow-up of region around the null point. The image has been reflected in the line $y = -x$.

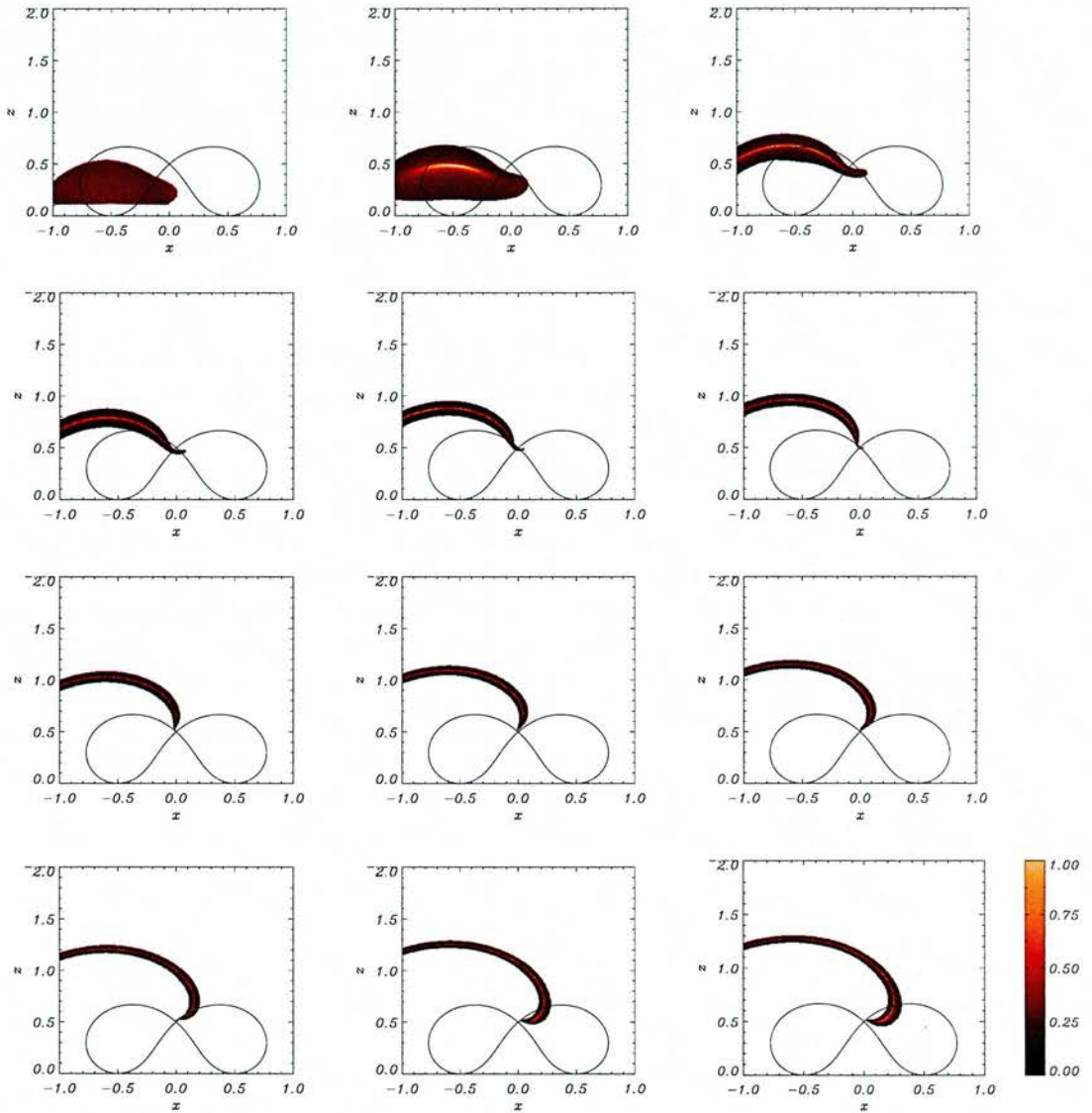


Figure 6.5: Contours of numerical simulation v_{\perp} for a fast wave sent in from lower boundary for $-1 \leq x \leq 0$, $z = 0.1$ and its resultant propagation at times (a) $t=0.055$, (b) $t=0.11$, (c) $t=0.165$, (d) $t = 0.22$, (e) $t=0.275$ and (f) $t=0.33$, (g) $t=0.385$, (h) $t=0.44$, (i) $t=0.495$, (j) $t = 0.55$, (k) $t=0.605$ and (l) $t=0.66$, labelling from top left to bottom right.

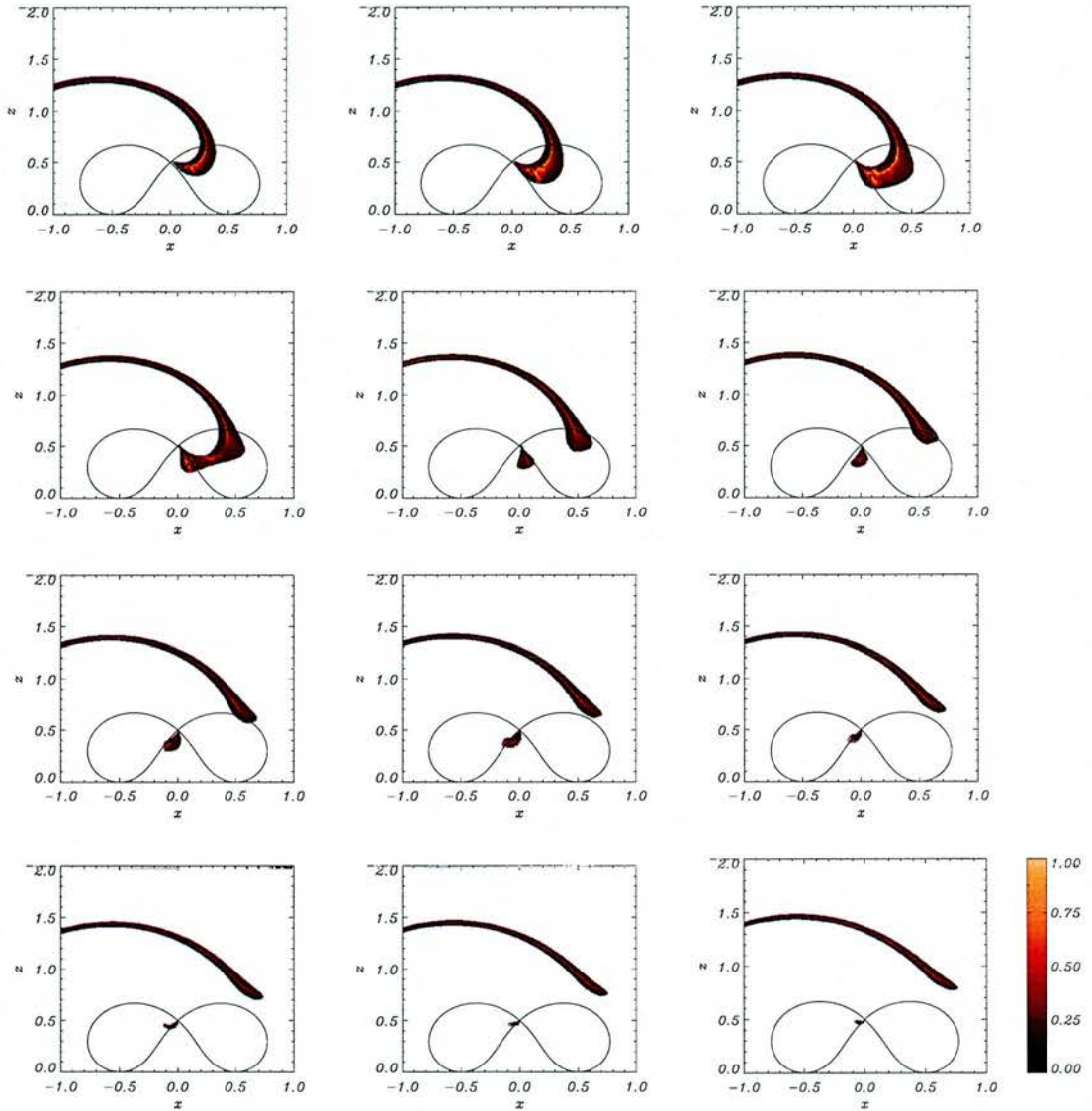


Figure 6.6: Contours of numerical simulation of v_{\perp} for a fast wave sent in from lower boundary for $-1 \leq x \leq 0$, $z = 0.1$ and its resultant propagation at times (a) $t=0.72$, (b) $t=0.74$, (c) $t=0.76$, (d) $t=0.78$, (e) $t=0.8$ and (f) $t=0.82$, (g) $t=0.84$, (h) $t=0.86$, (i) $t=0.88$, (j) $t=0.9$, (k) $t=0.92$ and (l) $t=0.94$, labelling from top left to bottom right.

6.5.2 WKB approximation

It is clear from Section 6.5.1 that quite a complicated splitting effect is in operation here. We can, however, use a WKB solution to gain extra insight into the numerical simulation, as we done so in previous chapters. Substituting $v_{\perp} = e^{i\phi(x,z)} \cdot e^{-i\omega t}$ into equation (6.3) gives:

$$-\omega^2 v_{\perp} = (B_x^2 + B_z^2) \left[-\left(\frac{\partial\phi}{\partial x}\right)^2 - \left(\frac{\partial\phi}{\partial z}\right)^2 - i\left(\frac{\partial^2\phi}{\partial x^2} + \frac{\partial^2\phi}{\partial z^2}\right) \right] v_{\perp}$$

Now we make the WKB approximation that $\phi \sim \omega \gg 1$ and this leads to a first order PDE of the form:

$$\begin{aligned} \omega^2 &= (B_x^2 + B_z^2) (p^2 + q^2) \\ \Rightarrow \mathcal{F}(x, z, \phi, p, q) = 0 &= \frac{1}{2} (B_x^2 + B_z^2) (p^2 + q^2) - \frac{1}{2} \omega^2 \end{aligned}$$

where $p = \frac{\partial\phi}{\partial x}$ and $q = \frac{\partial\phi}{\partial z}$ and we include a half in the form of \mathcal{F} (a non-linear PDE) to make the equations nicer later. Note all the imaginary terms have disappeared under our WKB approximation.

Applying the method described on page 31 requires us to calculate the following quantities:

$$\begin{aligned} \frac{\partial\mathcal{F}}{\partial\phi} &= 0 \\ \frac{\partial\mathcal{F}}{\partial p} &= (B_x^2 + B_z^2) p \\ \frac{\partial\mathcal{F}}{\partial q} &= (B_x^2 + B_z^2) q \\ \frac{\partial\mathcal{F}}{\partial x} &= \left(B_x \frac{\partial}{\partial x} B_x + B_z \frac{\partial}{\partial x} B_z \right) (p^2 + q^2) \\ \frac{\partial\mathcal{F}}{\partial z} &= \left(B_x \frac{\partial}{\partial z} B_x + B_z \frac{\partial}{\partial z} B_z \right) (p^2 + q^2) \end{aligned}$$

Now we can apply Charpit's relations (equations 2.24 – 2.28) to obtain:

$$\begin{aligned} \frac{d\phi}{ds} &= \omega^2 \\ \frac{dp}{ds} &= -\left(B_x \frac{\partial}{\partial x} B_x + B_z \frac{\partial}{\partial x} B_z \right) (p^2 + q^2) \\ \frac{dq}{ds} &= -\left(B_x \frac{\partial}{\partial z} B_x + B_z \frac{\partial}{\partial z} B_z \right) (p^2 + q^2) \\ \frac{dx}{ds} &= (B_x^2 + B_z^2) p \\ \frac{dz}{ds} &= (B_x^2 + B_z^2) q \end{aligned} \tag{6.6}$$

where ω is the frequency of our wave and s is some parameter along the characteristic. Note that these equations for the fast wave have been derived generally (i.e. we haven't substituted for \mathbf{B}_0).

These five ODEs can be solved numerically using a fourth-order Runge-Kutta method (as in earlier chapters). The initial conditions used were:

$$\phi_0 = 0, \quad -1 \leq x_0 \leq 1, \quad z_0 = 0.1, \quad p_0 = 0, \quad q_0 = \frac{\omega}{\sqrt{B_x(x_0, z_0)^2 + B_z(x_0, z_0)^2}} \quad (6.7)$$

where \mathbf{B}_0 is given by equation (6.1). Thus, by only plotting the fieldlines coming from $-1 \leq x_0 \leq 0$, we can make a direct comparison with the numerical work of Simulation Two. This can be seen in Figures 6.7 and 6.8. The agreement is very good. Following the splitting of the fast wave in Figure 6.8 is particularly interesting to follow. In the figure, each wavefront is drawn using IDL's symbol command (*psym*); hence, each line is made up of many tiny crosses. The author believes this allows us to see the wave stretching and splitting more clearly.

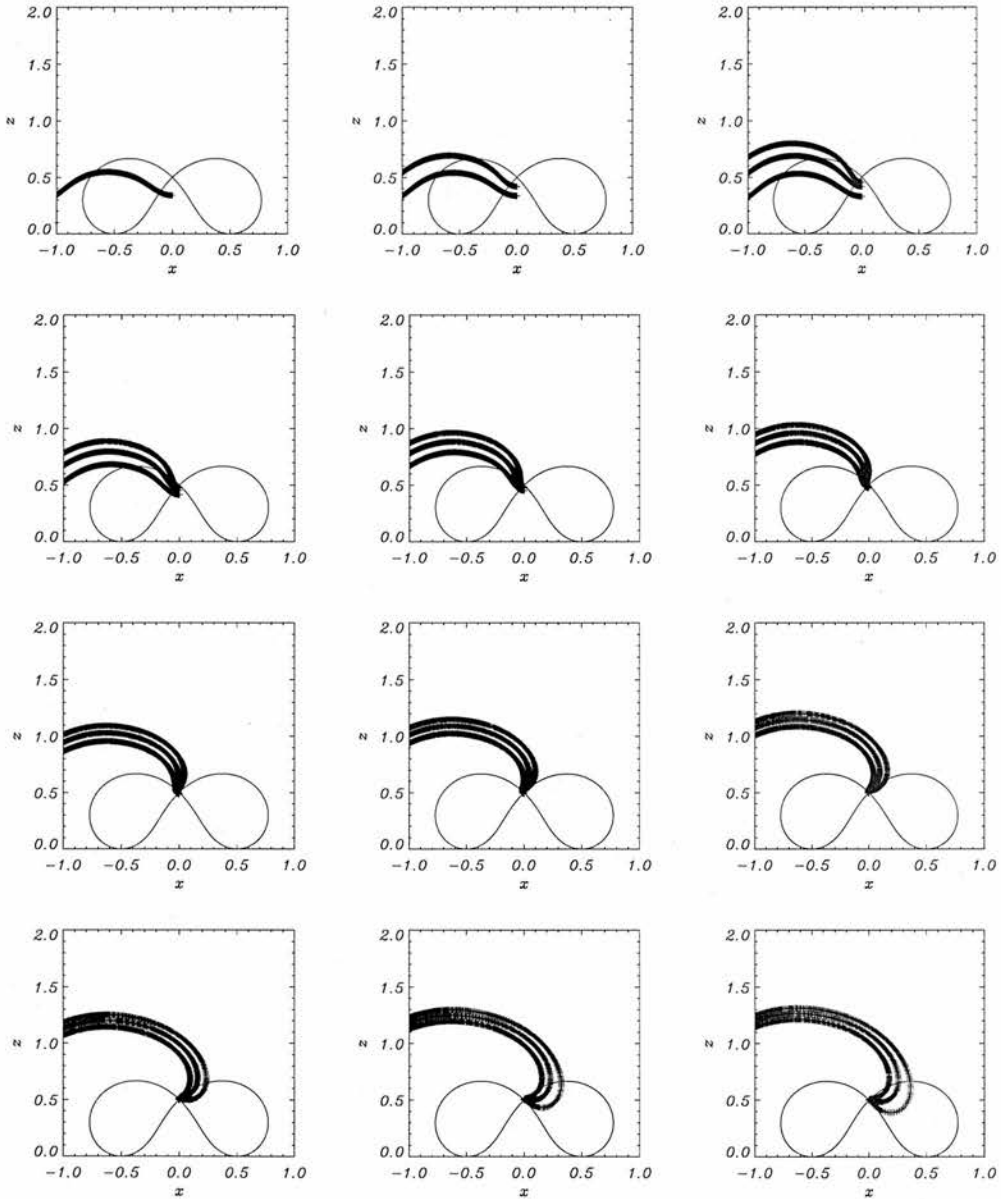


Figure 6.7: Analytical solution of v_{\perp} for WKB approximation of a fast wave sent in from lower boundary for $-1 \leq x \leq 0$, $z = 0.1$ and its resultant propagation at times (a) $t=0.055$, (b) $t=0.11$, (c) $t=0.165$, (d) $t=0.22$, (e) $t=0.275$ and (f) $t=0.33$, (g) $t=0.385$, (h) $t=0.44$, (i) $t=0.495$, (j) $t=0.55$, (k) $t=0.605$ and (l) $t=0.66$, labelling from top left to bottom right. The curves consisting of the crosses represent the front, middle and back edges of the WKB wave solution, where the pulse enters from the top of the box.

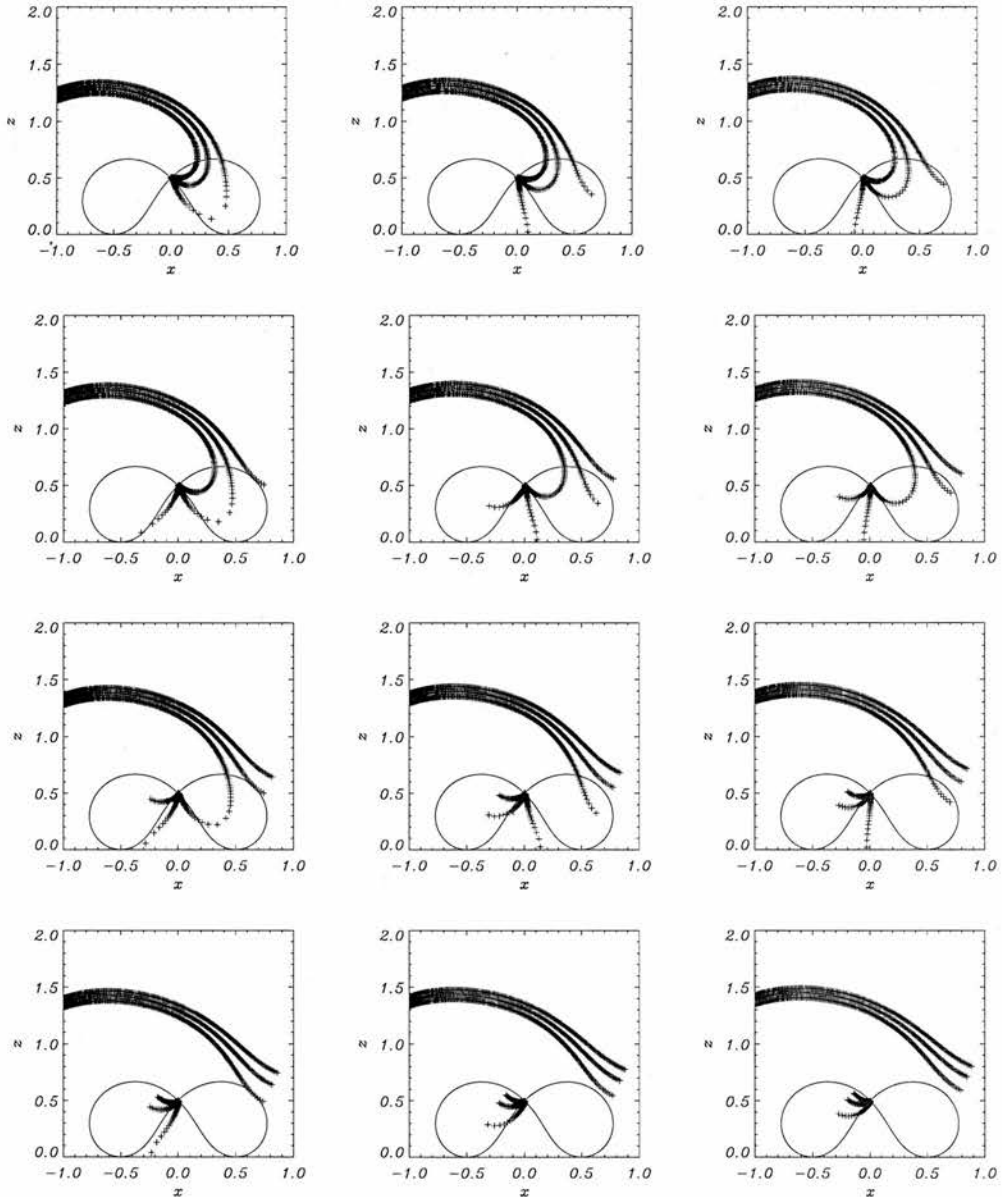


Figure 6.8: Analytical solution of v_{\perp} for WKB approximation of a fast wave sent in from lower boundary for $-1 \leq x \leq 0$, $z = 0.1$ and its resultant propagation at times (a) $t=0.72$, (b) $t=0.74$, (c) $t=0.76$, (d) $t=0.78$, (e) $t=0.8$ and (f) $t=0.82$, (g) $t=0.84$, (h) $t=0.86$, (i) $t=0.88$, (j) $t=0.9$, (k) $t=0.92$ and (l) $t=0.94$, labelling from top left to bottom right. The curves consisting of the crosses represent the front, middle and back edges of the WKB wave solution, where the pulse enters from the bottom of the box.

We can also use our WKB solution to map out the rays of the wavefront. This can be seen in Figure 6.9. In the left subfigure, we see the rays for starting points of $-1 \leq x_0 \leq 0$ set at intervals of 0.01. The line $x_0 = -0.4$ has been removed (this starting point leads to a spiralling particle path that would confuse the plot). We see that the lines for $x_0 \leq -0.5$ do not appear to be influenced by the null and simply propagate at varying angles. The rays for starting points of $x_0 \geq -0.5$ and (approximately) $x_0 \leq -0.4$ are influenced by the null, but only in so much as to deflect the ray. However, for starting points greater than (approximately) $x_0 = -0.4$, the rays spiral in towards the X-point and are trapped. Thus, **there is a critical starting point that divides these two types of behaviour**. The central figure shows the rays for $x_0 = -0.403$ (red) and $x_0 = -0.402$ (blue). We can see that the critical starting point is thus somewhere in the middle of these two. Increasing the resolution shows the critical starting point to be $x_0 = -0.40236$ to five decimal places. Finally, the right hand figure shows the particle path for a starting point of $x_0 = -0.4$. This clearly demonstrates the particle spiralling into the null.

By varying the z_0 of our WKB approximation, we tried to work out a formula giving $x_{0 \text{ critical}} = f(z_0)$, but this was more complicated than originally thought. The solution appears to be of the form $x_{0 \text{ critical}} = 0.78z_0 - 0.46$, though this only gives a crude approximation. Most likely it involves a more complicated equation (since the magnetic field follows quite a complicated equation).

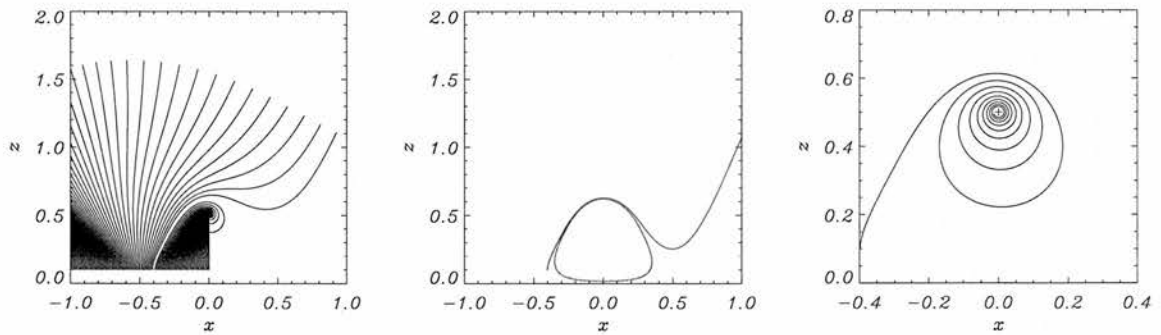


Figure 6.9: *Left* rays for starting points of $-1 \leq x_0 \leq 0$ except $x_0 = -0.4$ set at intervals of 0.01. *Centre* rays for $x_0 = -0.403$ (red) and $x_0 = -0.402$ (blue). *Right* rays for starting point of $x_0 = -0.4$.

6.6 Simulation Three

6.6.1 Numerical simulation

Our final simulation again solves equations (6.2) using our two-step Lax-Wendroff scheme, but this time for a wave pulse coming in from the entire lower boundary. Using the magnetic field in Figure 6.1, the boundary conditions were set such that:

$$v_{\perp}(x, z_0) = \begin{cases} \sin \omega t \sin \left[\frac{\pi}{2} (x + 1) \right] & \text{for } -1 \leq x \leq 1, \quad 0 \leq t \leq \frac{\pi}{\omega} \\ 0 & \text{otherwise} \end{cases}$$

$$\left. \frac{\partial}{\partial x} v_{\perp} \right|_{x=x_{\min}} = 0, \quad \left. \frac{\partial}{\partial x} v_{\perp} \right|_{x=x_{\max}} = 0, \quad \left. \frac{\partial}{\partial z} v_{\perp} \right|_{z=z_{\max}} = 0.$$

In the final run shown here, the experiment was carried out in a box $-1.4 \leq x \leq 1.4$ and $z_0 \leq z \leq 1.7$, so as to maximise the use of our 1000×1000 grid.

We find that the linear, fast MHD wave travels up from the lower boundary and is influenced by the magnetic configuration. The results can be seen in Figures 6.10 and 6.11. The resultant propagation is identical to the behaviour described in Section 6.5 (Simulation Two), since the magnetic region is symmetrical about $x = 0$. Initially, we see wave distort due to the two regions of enhanced Alfvén speed. Then, the central part of the wave slows down and refracts around the null point (located at $(x, z) = (0, 0.5)$). The rest of the wave (the *wings*) continue to propagate upwards, and because the wave is spreading out (as seen most clearly in the rays of Figure 6.9), the wave gives the impression of pivoting about the null. As this pivoting continues, the two wings eventually cross each other. However, due to the linear nature of the model, both wings pass each other and do not affect each other.

The two wings continue to pivot and near to the null, part of the wave wraps tightly around it. This can be seen clearly in Figure 6.12. This shows a blow-up of the wave accumulation around the null. Even though the resolution is coarse in this area, it is clear that this is the same behaviour seen in Section 3.3.1 for the fast wave wrapping around the simple X-point (compare Figures 6.12 and 3.2). In Figure 6.12 we have let $(x, z) \rightarrow (-x, -z)$ to help the comparison (i.e. again reflected the image in the line $y = -x$).

In Figure 6.11, the propagation continues. Eventually the wave is stretched so much in the region $-0.6 \leq x \leq 0.6, 0.2 \leq z \leq 0.5$ that it splits; part of the wave remains close to the X-point (and ultimately accumulates there) and part of the wave is repelled by the regions of high Alfvén speed and is ejected away from the magnetic skeleton. These parts then continue to propagate upwards and outwards, forming a distinctive cross shape.

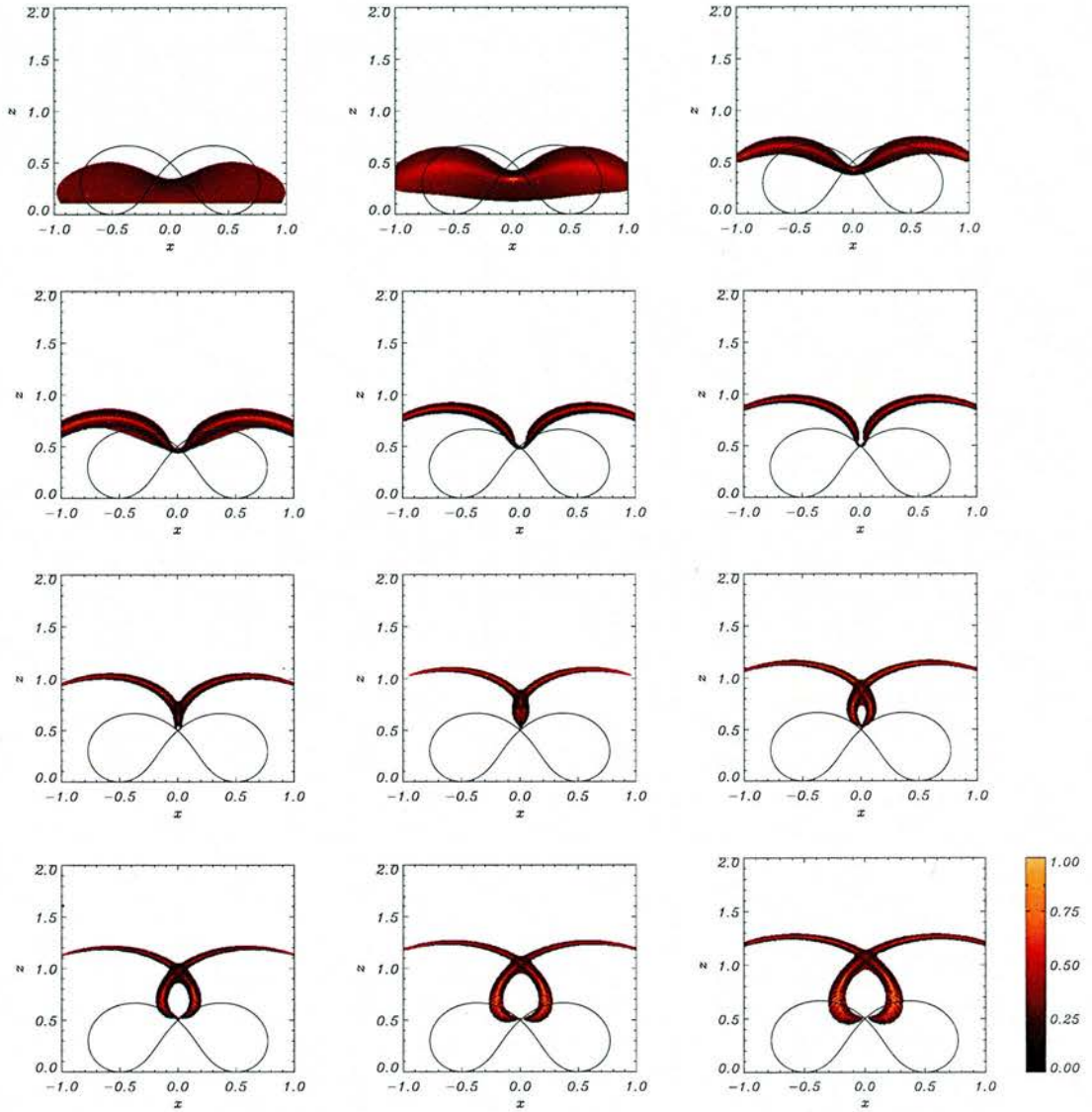


Figure 6.10: Contours of numerical simulation v_{\perp} for a fast wave sent in from lower boundary for $-1 \leq x \leq 1$, $z = 0.1$ and its resultant propagation at times (a) $t=0.055$, (b) $t=0.11$, (c) $t=0.165$, (d) $t = 0.22$, (e) $t=0.275$ and (f) $t=0.33$, (g) $t=0.385$, (h) $t=0.44$, (i) $t=0.495$, (j) $t = 0.55$, (k) $t=0.605$ and (l) $t=0.66$, labelling from top left to bottom right.

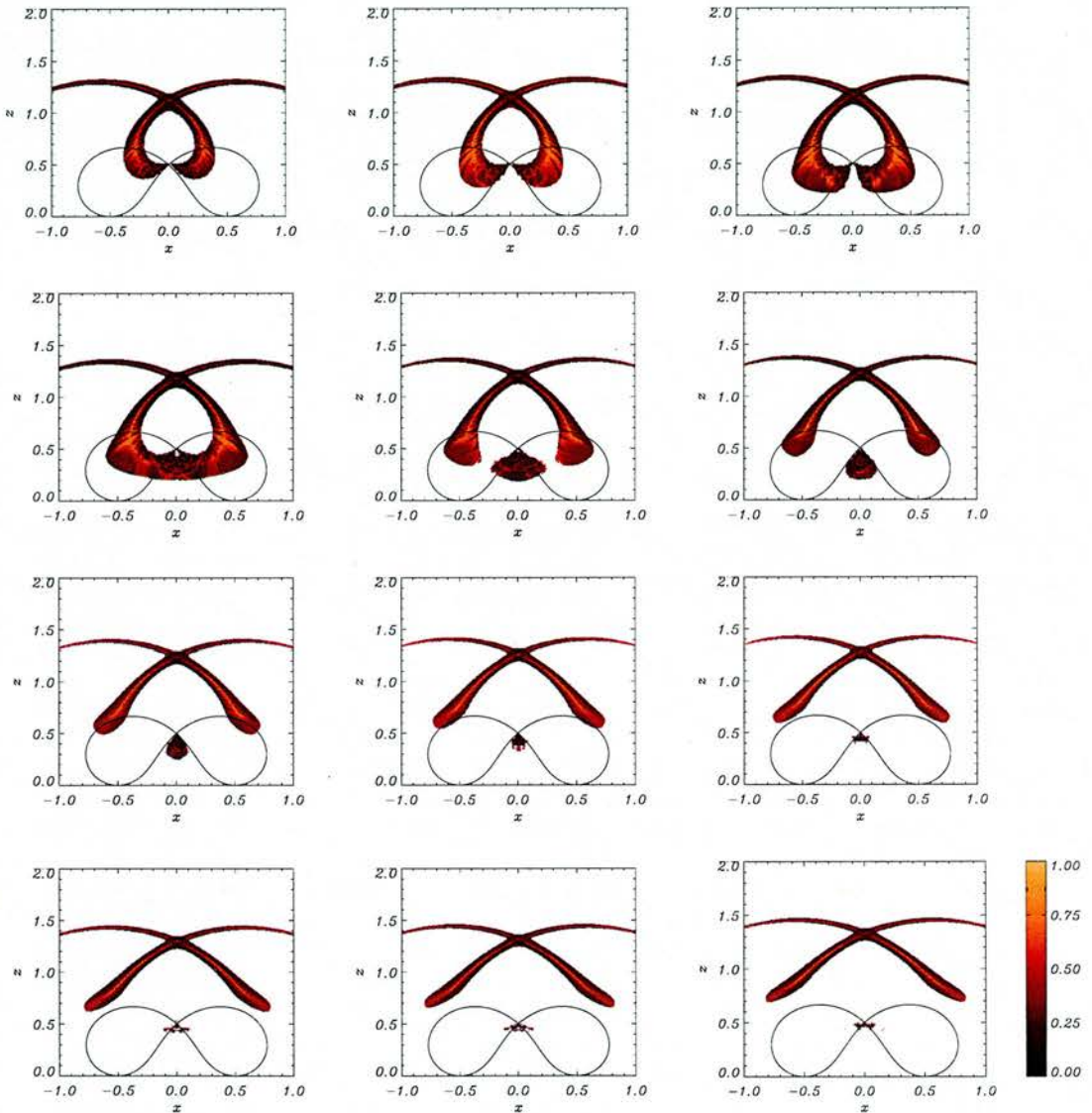


Figure 6.11: Contours of numerical simulation v_{\perp} for a fast wave sent in from lower boundary for $-1 \leq x \leq 1$, $z = 0.1$ and its resultant propagation at times (a) $t=0.72$, (b) $t=0.74$, (c) $t=0.76$, (d) $t=0.78$, (e) $t=0.8$ and (f) $t=0.82$, (g) $t=0.84$, (h) $t=0.86$, (i) $t=0.88$, (j) $t=0.9$, (k) $t=0.92$ and (l) $t=0.94$, labelling from top left to bottom right.

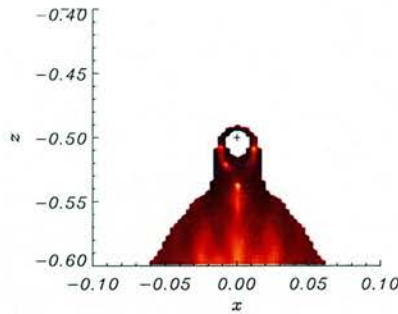


Figure 6.12: Contour of the numerical simulation of v_{\perp} for a fast wave sent in from lower boundary for $-1 \leq x \leq 1$ after time $t = 0.44$. Figure shows blow-up of region around the null point. The image has been reflected in the line $y = -x$.

6.6.2 WKB approximation

We can again use the WKB approximation, as detailed in Section 2.4, to find a semi-analytical solution, and thus compare it to Simulation Three. In Section 6.5.2, we found a WKB approximation for our fast wave equation (equations 6.6) using the initial conditions of equations (6.7). Thus, by plotting the fieldlines coming from $-1 \leq x_0 \leq 1$, we can make a direct comparison with Simulation Three. This can be seen in Figures 6.14 and 6.15, which are plotted at the same times as Figures 6.10 and 6.11. The agreement is very good. Again, each wavefront drawn here is made using IDL's symbol command. Hence, each line is made up of many tiny crosses and so we can see the wave stretching and splitting more clearly.

Note that in the numerical simulation, the fast wave diffuses slightly and resolution runs out, hence some parts of the wave are unresolved fully. This is not the case in the WKB approximation, where the wavefronts are crisp. Thus, the numerical and WKB results show the same behaviour, but have small differences close to the leading and trailing wavefronts. However, the comparison with the middle WKB wavefront is excellent.

We can also use our WKB solution to map out the rays of the wavefront. This can be seen in Figure 6.13. Here, we can see rays for starting points of $-1 \leq x_0 \leq 1$ set at intervals of 0.01. The blue lines shows starting points $-0.4 < x < 0.4$, green lines show starting points of $x_0 = \pm 0.4$, and all other starting points ($x_0 < -0.4, x_0 > 0.4$) are in red. We can clearly see that the critical points (where the wave splits to head to the null or away from the magnetic skeleton) are around $x_0 = \pm 0.4$.

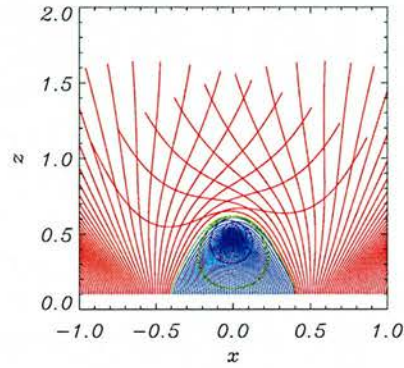


Figure 6.13: rays for starting points of $-1 \leq x_0 \leq 1$ set at intervals of 0.01. Blue lines shows starting points $-0.4 < x < 0.4$. Green lines show starting points of $x_0 = \pm 0.4$. All other starting points ($x_0 < -0.4, x_0 > 0.4$) are in red.

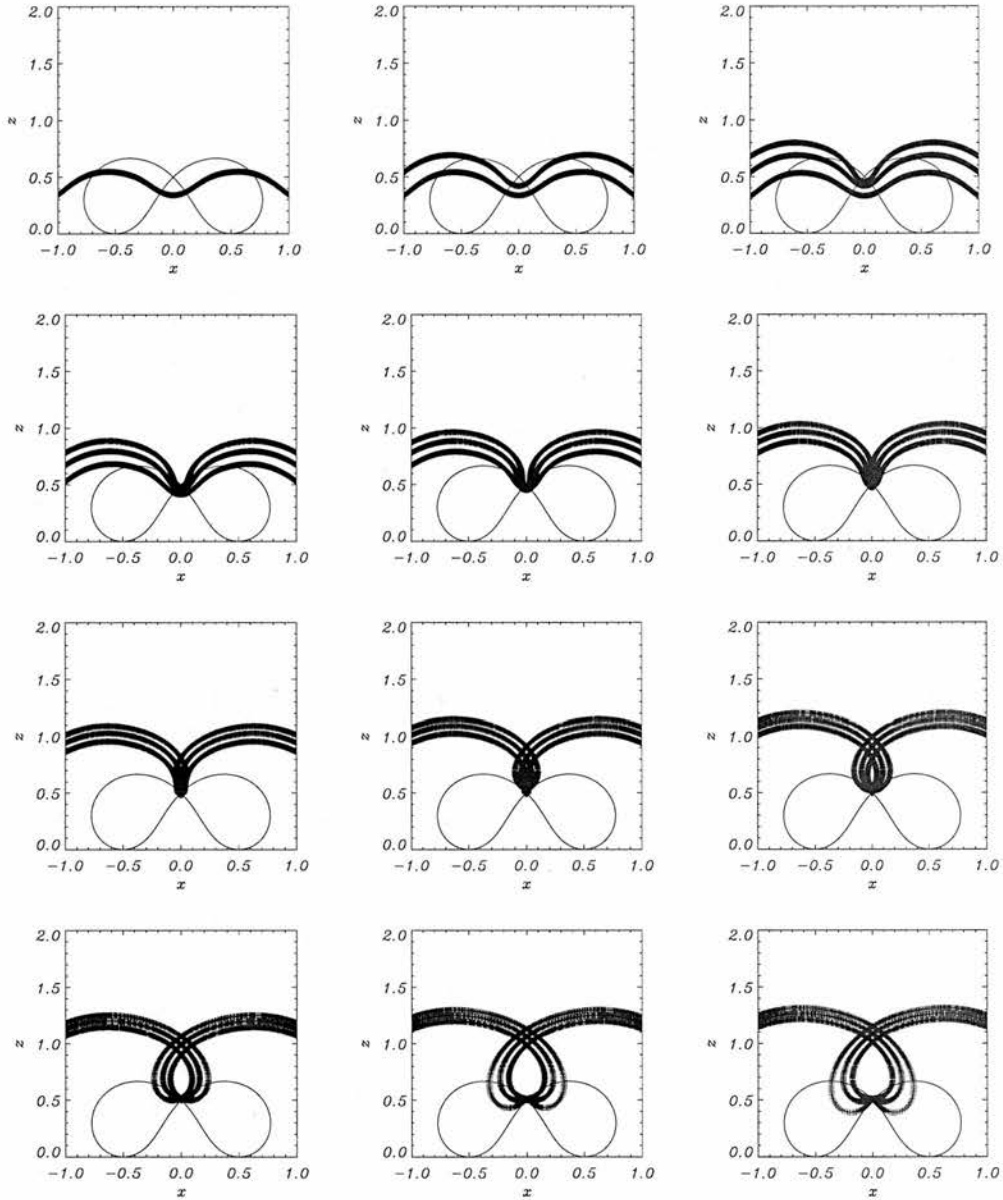


Figure 6.14: Analytical solution of v_{\perp} for WKB approximation of a fast wave sent in from lower boundary for $-1 \leq x \leq 1$, $z = 0.1$ and its resultant propagation at times (a) $t=0.055$, (b) $t=0.11$, (c) $t=0.165$, (d) $t=0.22$, (e) $t=0.275$ and (f) $t=0.33$, (g) $t=0.385$, (h) $t=0.44$, (i) $t=0.495$, (j) $t=0.55$, (k) $t=0.605$ and (l) $t=0.66$, labelling from top left to bottom right. The lines represent the front, middle and back edges of the WKB wave solution, where the pulse enters from the bottom of the box.

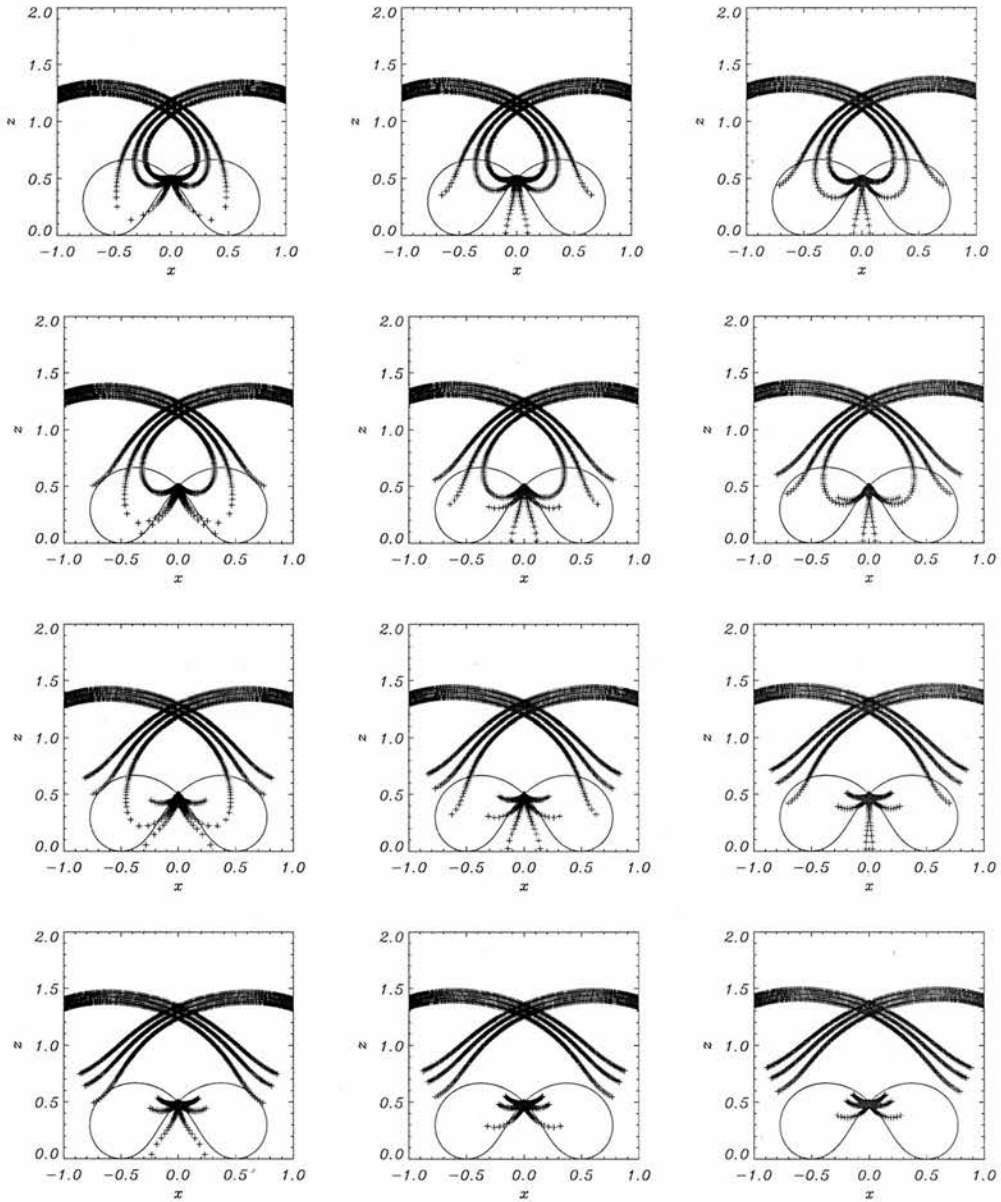


Figure 6.15: Analytical solution of v_{\perp} for WKB approximation of a fast wave sent in from lower boundary for $-1 \leq x \leq 1$, $z = 0.1$ and its resultant propagation at times (a) $t=0.72$, (b) $t=0.74$, (c) $t=0.76$, (d) $t=0.78$, (e) $t=0.8$ and (f) $t=0.82$, (g) $t=0.84$, (h) $t=0.86$, (i) $t=0.88$, (j) $t=0.9$, (k) $t=0.92$ and (l) $t=0.94$, labelling from top left to bottom right. The lines represent the front, middle and back edges of the WKB wave solution, where the pulse enters from the bottom of the box.

6.7 Alfvén Waves

We now turn our attention to studying the behaviour of the Alfvén wave in the neighbourhood of two dipoles. Again, we will be launching a wave into the system from the lower boundary ($z = z_0$). However, from our findings in Chapters 4 and 5, we already have a good idea of how the wave will behave. In all previous $\beta = 0$ ideal, uniform density plasma experiments in this Thesis, we found that the linear Alfvén wave was confined to travel along the field lines. Thus, an initially localised wave follows the field lines and spreads out if the field lines are spreading out.

Hence, we will not carry out three similar simulations (as we did above for the fast wave). Instead, we will look at one case for the Alfvén wave and find that the behaviour is of the same nature as found previously in Chapters 4 and 5. Thus, no further cases are shown here since any other experiments would just show the same type of predictable behaviour.

6.7.1 Numerical simulation

The equations describing the behaviour of the Alfvén wave, equations (6.4), were solved numerically using our two-step Lax-Wendroff scheme. We initially consider a box ($-1 \leq x \leq 1$, $z_0 \leq z \leq 2$) using the magnetic field shown in Figure 6.1. We initially consider a single wave pulse coming in from the bottom boundary, localised along $-1 \leq x \leq -0.7$, $z = z_0$, where the pulse was chosen so it crosses a separatrix. For the single wave pulse, the boundary conditions were set such that:

$$v_y(x, z_0) = \sin \omega t \sin \left[\frac{10\pi}{3} (x + 1) \right] \quad \text{for } \begin{cases} -1 \leq x \leq -0.7 \\ 0 \leq t \leq \frac{\pi}{\omega} \end{cases},$$

$$v_y = 0 \quad \text{otherwise}$$

$$\left. \frac{\partial}{\partial x} v_y \right|_{x=x_{min}} = 0, \quad \left. \frac{\partial}{\partial x} v_y \right|_{x=x_{max}} = 0, \quad \left. \frac{\partial}{\partial z} v_y \right|_{z=z_{max}} = 0.$$

In the final run shown here, the simulation was carried out in a box $-1.4 \leq x \leq 1$ and $z_0 \leq z \leq 1.6$, so as to maximise the usefulness of our 1000×1000 grid. Also, $z_0 = 0.2$ was chosen (as opposed to $z_0 = 0.1$) as it demonstrates the nature more clearly ($z_0 = 0.1$ gets a bit messy close to $(x, z) = (-0.5, 0)$).

We found that the linear Alfvén wave travels up from the $z = z_0$ boundary and begins to spread out, following the field lines. This can be seen in Figure 6.16. As it follows the field lines, part of the wave accumulates along the separatrix and appears to stick to the separatrices (depositing parts of itself as it goes). This behaviour stretches the wave thinly along the separatrices.

Part of the wave also appears to be propagating away from the magnetic skeleton (though it is actually just following the field lines and spreading out, see Section 6.7.2). These two goals for different parts of the wave result in a sharp wave front being formed. Note that as the wavefront gets very sharp (as seen in the bottom row of subfigures), the resolution of the simulation is unable to fully resolve the wave behaviour / accumulation. However, it is clear that part of the wave is propagating away from the magnetic skeleton and the other part of the wave has accumulated along the separatrices (thus displaying the same nature seen previously in Chapters 4 and 5).

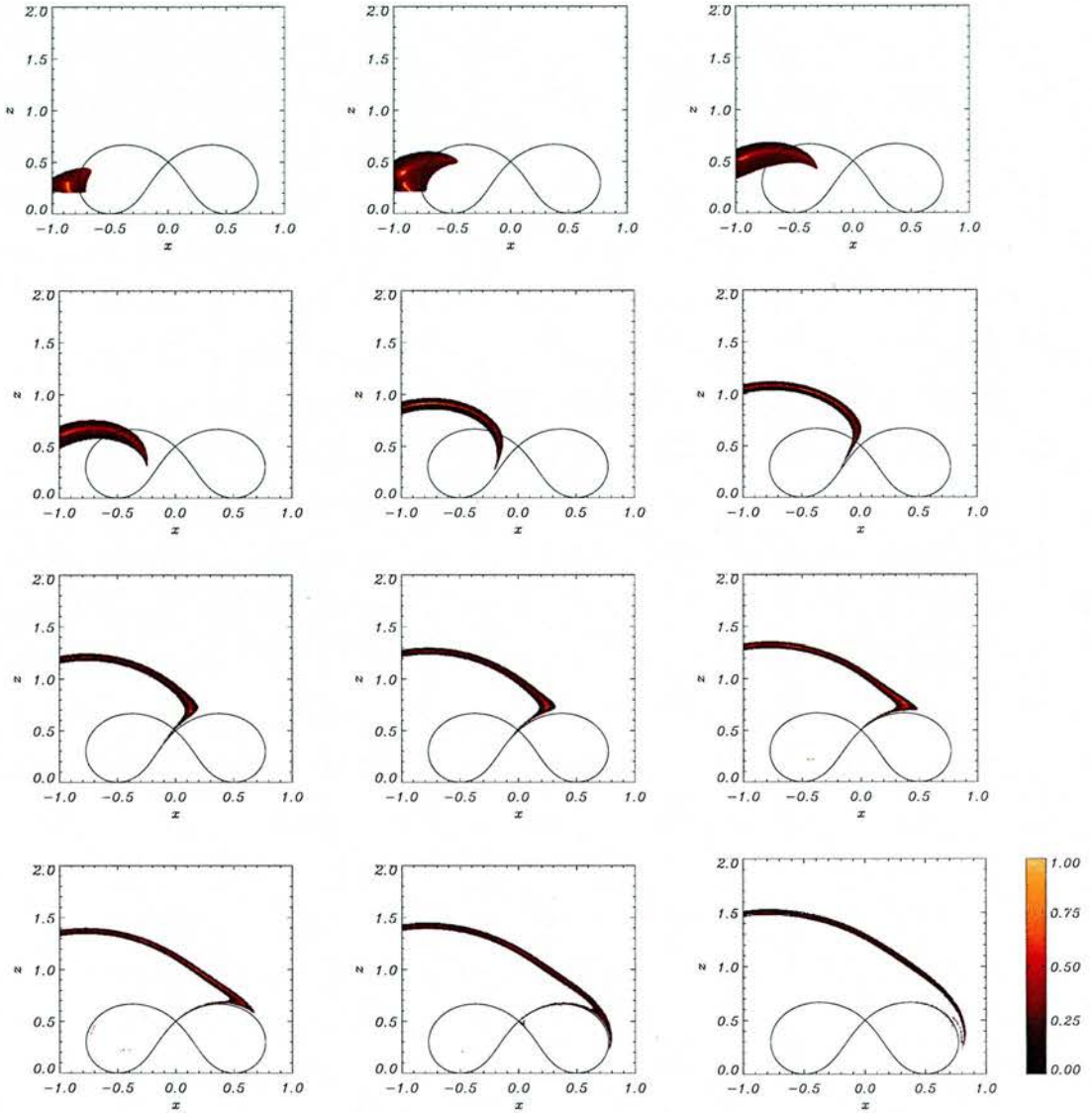


Figure 6.16: Contours of v_y for an Alfvén wave sent in from lower boundary for $-1 \leq x \leq -0.7$ and its resultant propagation at times (a) $t=0.05$, (b) $t=0.1$, (c) $t=0.15$, (d) $t=0.2$, (e) $t=0.4$, (f) $t=0.6$, (g) $t=0.8$, (h) $t=0.9$, (i) $t=1.0$, (j) $t=1.1$, (k) $t=1.2$, (l) $t=1.4$, labelling from top left to bottom right.

6.7.2 WKB approximation

Again, we can use our WKB approximation to gain insight into the numerical simulation. The Alfvén equations we have to solve are:

$$\frac{\partial^2 v_y}{\partial t^2} = \left(B_x \frac{\partial}{\partial x} + B_z \frac{\partial}{\partial z} \right)^2 v_y, \quad (6.8)$$

as mentioned in Section 5.2.

Using the magnetic field for the two dipoles (equation 6.1) and substituting $v_y = e^{i\phi(x,z)} \cdot e^{-i\omega t}$ into equation (6.8) gives:

$$\begin{aligned} -\omega^2 &= \left[-B_x^2 \left(\frac{\partial \phi}{\partial x} \right)^2 - 2B_x B_z \frac{\partial \phi}{\partial x} \frac{\partial \phi}{\partial z} - B_z^2 \left(\frac{\partial \phi}{\partial z} \right)^2 \right] \\ &+ i \left[B_x^2 \frac{\partial^2 \phi}{\partial x^2} + 2B_x B_z \frac{\partial^2 \phi}{\partial x \partial z} + B_z^2 \frac{\partial^2 \phi}{\partial z^2} \right] \\ &+ B_z \left(\frac{\partial B_x}{\partial x} \right) \frac{\partial \phi}{\partial x} - B_x \left(\frac{\partial B_z}{\partial z} \right) \frac{\partial \phi}{\partial z} + B_z \left(\frac{\partial B_z}{\partial x} \right) \frac{\partial \phi}{\partial z} + B_x \left(\frac{\partial B_x}{\partial z} \right) \frac{\partial \phi}{\partial x} \end{aligned}$$

Now we make the WKB approximation such that $\phi \sim \omega \gg 1$ and this leads to a first order PDE of the form:

$$\begin{aligned} -\omega^2 &= -B_x^2 p^2 + 2B_x B_z pq - B_z q^2 \\ \Rightarrow \mathcal{F}(x, z, \phi, p, q) &= \frac{1}{2} (B_x p + B_z q)^2 - \frac{1}{2} \omega^2 = 0 \end{aligned}$$

where again $p = \frac{\partial \phi}{\partial x}$ and $q = \frac{\partial \phi}{\partial z}$. Note all the imaginary terms have disappeared under the WKB approximation.

In order to apply Charpit's relations, we must work out the following quantities:

$$\begin{aligned}\frac{\partial \mathcal{F}}{\partial \phi} &= 0 \\ \frac{\partial \mathcal{F}}{\partial p} &= B_x (B_x p + B_z q) \\ \frac{\partial \mathcal{F}}{\partial q} &= B_z (B_x p + B_z q) \\ \frac{\partial \mathcal{F}}{\partial x} &= (B_x p + B_z q) \frac{\partial}{\partial x} (B_x p + B_z q) \\ \frac{\partial \mathcal{F}}{\partial z} &= (B_x p + B_z q) \frac{\partial}{\partial z} (B_x p + B_z q) .\end{aligned}$$

Now we can work out Charpit's equations (equations 2.24 – 2.28) to give:

$$\begin{aligned}\frac{d\phi}{ds} &= \omega^2 , \\ \frac{dp}{ds} &= - \left(p \frac{\partial B_x}{\partial x} + q \frac{\partial B_z}{\partial x} \right) \xi , \\ \frac{dq}{ds} &= - \left(p \frac{\partial B_x}{\partial z} + q \frac{\partial B_z}{\partial z} \right) \xi , \\ \frac{dx}{ds} &= B_x \xi , \\ \frac{dz}{ds} &= B_z \xi\end{aligned}\tag{6.9}$$

where ω is the frequency of our wave and s is some parameter along the characteristic. Also $\xi = (B_x p + B_z q)$

These five ODEs can be solved numerically using our fourth-order Runge-Kutta method, as in previous chapters (such as in Section 5.3.2). The initial conditions are:

$$\phi_0 = 0 , \quad -1 \leq x_0 \leq -0.7 , \quad z_0 = 0.2 , \quad p_0 = 0 , \quad q_0 = \frac{\omega}{B_z(x_0, z_0)}$$

By plotting positions of constant ϕ we can visualise the wavefront. This can be seen in Figure 6.17. Here, we have plotted the wave fronts at the same times as in the numerical simulation to allow a direct comparison. The agreement is very good. The plots have been made using IDL's symbol command and hence each wavefront is made up of many tiny crosses. Not only can we see part of the wave accumulating along the separatrices more clearly now, but we can also see how stretched the wave gets across the skeleton.

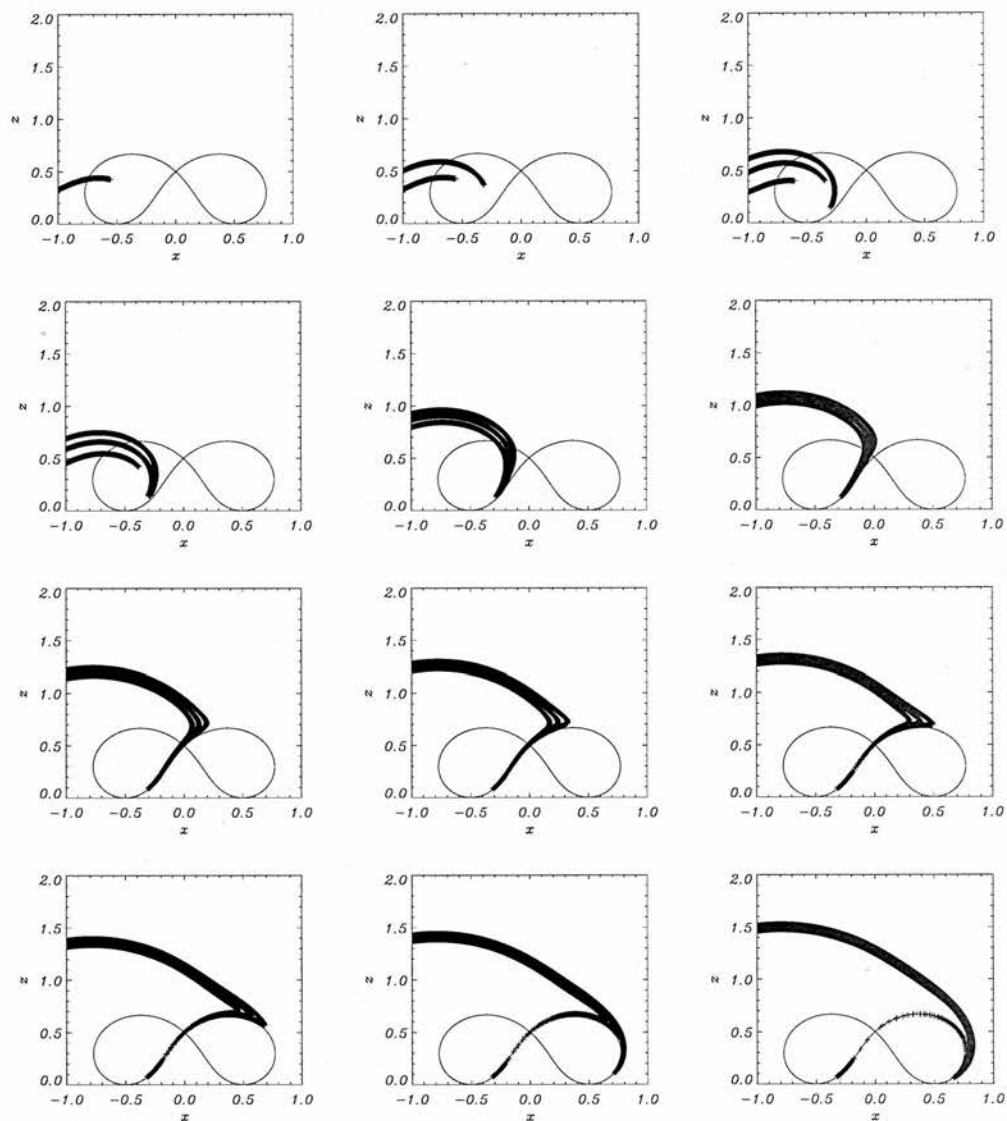


Figure 6.17: Analytical solution for WKB approximation of an Alfvén wave sent in from lower boundary for $-1 \leq x \leq -0.7$, and its resultant propagation at times (a) $t=0.05$, (b) $t=0.1$, (c) $t=0.15$, (d) $t=0.2$, (e) $t=0.4$, (f) $t=0.6$, (g) $t=0.8$, (h) $t=0.9$, (i) $t=1.0$, (j) $t=1.1$, (k) $t=1.2$, (l) $t=1.4$, labelling from top left to bottom right. The lines represent the front, middle and back edges of the WKB wave solution.

We can also use our WKB solution to plot the rays of individual elements from the initial wave. These can be seen in Figure 6.18.

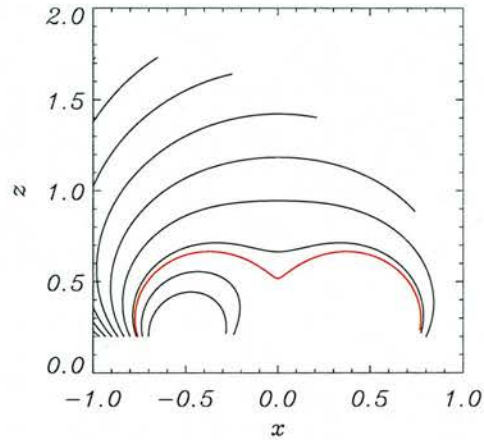


Figure 6.18: Plots of WKB solution for an Alfvén wave sent in from the lower boundary and its resultant rays (thick lines). Starting points of $-1 \leq x_0 \leq -0.7$ at intervals of $\frac{1}{30}$ are plotted. Also shown in red is starting point $x_0 = -0.758$

6.8 Conclusions

This chapter describes an investigation into the nature of MHD waves in the neighbourhood of two magnetic dipoles. From the work above, it has been seen that when a fast wave is generated on the lower boundary it propagates upwards and is influenced by the magnetic configuration. Firstly, it is influenced by the two regions of high Alfvén speed; this distorts the initially straight wave to form two peaks (with maximums located over the loci of the magnetic field). These localised areas of high speed is a new effect not seen in previous chapters. The wave continues to propagate upwards but travels slower and slower as it approaches the null (located at $(x, z) = (0, 0.5)$). The linear fast wave cannot cross the null. Meanwhile, the rest of the wave (the *wings*) continue to propagate upwards and spread out (as the fast wave tends to do). Thus, this gives the visual impression that the wave is pivoting about the null point (which is acting as a fulcrum). As this pivoting continues, the two wings eventually cross each other. However, due to the linear nature of the model, both wings pass each other and do not affect each other.

The two wings continue to pivot about their fulcrum but, near to the null, part of the wave is wrapping tightly around it. Near the null, a *refraction* effect spirals the wave into the X-point, wrapping it around again and again. The other part of the wave (above the magnetic skeleton) appears to simply continue to rise and spread out. However, since part of the wave is wrapping around the null, and a second part is rising away from the magnetic region, there must come a

point where the wave splits. The wave is stretched between its two goals and ultimately splits near the regions of high Alfvén speed (the localised high speed thins the wave and forces the split). Part of the (now split) wave spirals into the null and the other part propagates away from the magnetic skeleton; no longer heavily influenced by the magnetic null point. These parts form a distinctive cross shape.

Thus, this answers a question raised by Chapter 3; does the key effect (fast wave preferential heating occurs at null points) persist in this more complicated magnetic configuration. The answer is yes, but only if the wave is close enough to the null point. In fact, this makes sense; if the fast wave is too far away from the magnetic null, it will not feel its effect until it is much closer. This also answers a second query; because there were no length scales in the experiments of Chapter 3, it seemed to suggest that a very long, very large fast wave could be deflected by a tiny single point (the null). This seemed unphysical, akin to a tiny pebble modifying the flow of a large river! Thus, from the work in this chapter we can see that this is not the case; it is more that (only) a localised area around the null point behaves like the system of Chapter 3, and the rest of the wave is much more like the behaviour of the fast wave in a uni-directional magnetic field (Section 1.5.4), i.e. the fast wave propagates (almost) isotropically. In our analogy, it is like a small region around the pebble affects the flow of the river, but the rest of the river is unaffected (to a certain extent).

We also looked at the behaviour of the Alfvén wave near two dipoles. We saw that when a linear Alfvén wave was launched from the lower boundary into the magnetic region, it is confined to the path of the field lines (the Alfvén wave cannot cross them). Thus, part of the wave accumulates along the separatrix and appears to stick to the separatrices (depositing parts of itself as it goes). This behaviour stretches the wave thinly along the separatrices. The other part of the wave appears to be propagating away from the magnetic skeleton (though it is actually just following the field lines that are spreading out). This was apparent in the numerical simulation but more clearly seen in the WKB approximation. These two goals for different parts of the wave result in a sharp wavefront being formed. All the behaviour of the Alfvén wave agrees with what we learnt from Chapter 4 and 5; that the Alfvén wave follows the field lines and each fluid element is trapped on the field line it starts on. The (WKB) rays also shows this.

Furthermore, since we have the Alfvén wave accumulating and stretched along the separatrices, we will have a build-up of current density at these locations. Therefore, since current is accumulating along the separatrices, this will be the location where ohmic dissipation will extract the energy in the wave. Thus, **Alfvén wave heating will naturally occur along the separatrices** due to dissipation. The rest of the Alfvén wave (the part travelling away from the magnetic skeleton) does not create large gradients and thus does not generate large currents. This part of the wave simply travels out of our system.

Chapter 7

Magnetoacoustic mode coupling in the neighbourhood of a null point

7.1 Introduction

In this chapter we look at the behaviour of the fast MA wave in the neighbourhood of a simple 2D X-point, as we did in Chapter 3. However, we now consider a $\beta \neq 0$ plasma (i.e. lift the cold plasma restriction). This extends the model of Chapter 3 to include pressure gradients and the most obvious effect of this is the introduction of *slow magnetoacoustic waves* to the system.

Lifting the $\beta = 0$ restriction introduces plasma pressure to our model and hence there will now be an interplay between this and the magnetic pressure. This is understood through the plasma β parameter (as defined on page 7). There will now also be coupling between the two MA waves (and perhaps even wave transition) near where the sound speed and Alfvén speed become comparable in magnitude (i.e. at the areas where the plasma $\beta \approx 1$). Also, since the sound speed is now non-zero (most importantly, it is non-zero at the null point), the fast wave may now be able to pass through the null point and thus perhaps take energy away from that area. However, the exact behaviour is unknown and will be looked at here. We will not consider the Alfvén wave here. Recall that for Alfvén waves that are decoupled from fast waves, the value of the plasma β is unimportant (the plasma pressure plays no role in its propagation) and so its description in Chapter 4 remains valid in this linear, 2D regime.

A very detailed and comprehensive set of 2D numerical simulations of wave propagation in a stratified magneto-atmosphere were conducted by Rosenthal *et al.* (2002) and Bogdan *et al.* (2003). In these simulations, an oscillating piston generated both fast and slow MHD waves on a lower boundary and sent these waves up into the stratified, magnetised plasma. Their calculations

showed that there was coupling between the fast and slow waves, and that this coupling was confined to a thin layer where the sound speed and the Alfvén velocity are comparable in magnitude, i.e. where the plasma $\beta \approx 1$. Away from this conversion zone, the waves were decoupled as either the magnetic pressure or plasma pressure dominated. One of the aims of these papers was to see how the topology affected the propagation of waves, with the ratio of the sound speed to the Alfvén speed varying along every magnetic line of force. In this, their papers and the work done in this chapter have the same ultimately goal; a fully 3D understanding of MHD wave propagation in the solar corona.

Other authors have also looked at MHD mode coupling. Cally & Bogdan (1997) describes 2D simulations in which both f -modes and p -modes are (partially) converted to slow magnetoacoustic gravity waves, due to strong gravitational stratification. De Moortel *et al.* (2004) investigated driving slow waves on the boundary of a 2D geometry with a horizontal density variation. They found coupling between slow and fast waves and phase mixing of the slow waves. The coupling of different wave modes has also been investigated by Ferraro & Plumpton (1958), Zhugzhda & Dzhalilov (1982) (with Meijer G-functions) and Cally (2001) (with hypergeometric ${}_2F_3$ functions). All these works considered mode coupling through a gravitational stratification (vertical density inhomogeneity). Finally, the coupling of fast waves and Alfvén waves has been investigated by Parker (1991) (linear with a density gradient) and by Nakariakov *et al.* (1997) (nonlinear excitation).

7.2 Basic equations and set-up

In this chapter, we will look at the nature of fast and slow magnetoacoustic waves in a finite β plasma in the neighbourhood of a two-dimensional null point.

As in Chapter 3, the basic magnetic field structure is taken as a simple 2D X-type neutral point (equation 3.1), hence:

$$\mathbf{B}_0 = \frac{B_0}{L} (x, 0, -z),$$

where B_0 is a characteristic field strength and L is the length scale for magnetic field variations. This magnetic field can be seen in Figure 7.1.

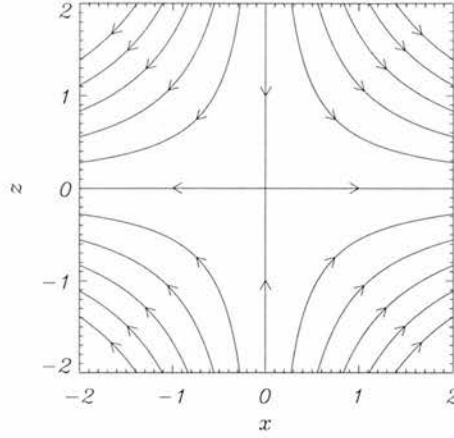


Figure 7.1: Our choice of equilibrium magnetic field.

To study the behaviour of the fast and slow MA waves near the X-point, we will use the linearised MHD equations (as derived in Chapter 2). The relevant equations are (taken from Section 2.2.2):

$$\begin{aligned}
 \rho_0 \frac{\partial}{\partial t} v_{\perp} &= -(\mathbf{B}_0 \cdot \mathbf{B}_0) (\nabla \times \mathbf{b}) + \frac{\beta_0}{2} \nabla A_0 \cdot \nabla p_1 \\
 \rho_0 \frac{\partial}{\partial t} v_{\parallel} &= -\frac{\beta_0}{2} (\mathbf{B}_0 \cdot \nabla) p_1 \\
 \frac{\partial}{\partial t} b_x &= -\frac{\partial}{\partial z} v_{\perp} + \frac{1}{R_m} \nabla^2 b_x \\
 \frac{\partial}{\partial t} b_z &= \frac{\partial}{\partial x} v_{\perp} + \frac{1}{R_m} \nabla^2 b_z \\
 \frac{\partial}{\partial t} p_1 &= -\gamma \left[\nabla \cdot \left(\frac{\mathbf{B}_0 v_{\parallel}}{\mathbf{B}_0 \cdot \mathbf{B}_0} \right) - \nabla \cdot \left(\frac{v_{\perp} \nabla A_0}{\mathbf{B}_0 \cdot \mathbf{B}_0} \right) \right]
 \end{aligned} \tag{7.1}$$

where we have split the velocity into parallel and perpendicular components, where $v_{\perp} = \sqrt{\mathbf{B}_0 \cdot \mathbf{B}_0} \mathcal{V}_{\perp}$ and $v_{\parallel} = \sqrt{\mathbf{B}_0 \cdot \mathbf{B}_0} \mathcal{V}_{\parallel}$ and where \mathcal{V}_{\perp} and \mathcal{V}_{\parallel} are defined by equation (2.1), i.e.:

$$\mathbf{v}_1 = \mathcal{V}_{\parallel} \left(\frac{\mathbf{B}_0}{\sqrt{\mathbf{B}_0 \cdot \mathbf{B}_0}} \right) - \mathcal{V}_{\perp} \left(\frac{\nabla A_0}{\sqrt{\mathbf{B}_0 \cdot \mathbf{B}_0}} \right) + v_y \hat{\mathbf{y}}$$

Here, we take $v_y \hat{\mathbf{y}} = 0$ (there is no Alfvén wave). By splitting the velocity into components like this, we hope to make our MHD mode detection and interpretation easier later (e.g. since the slow wave is primarily field aligned, etc.). However, it does give us a complicated form for the time derivative of p_1 (recall the simplicity of equation (1.21); $\frac{\partial}{\partial t} p_1 = -\gamma p_0 (\nabla \cdot \mathbf{v}_1)$). We have also set $\beta_0 = \frac{2\mu p_0}{B_0^2}$, where β_0 is the plasma beta at a distance of unity from the null point. This dimensionless parameter governs the strength of the coupling between v_{\perp} and v_{\parallel} and is discussed further in Section 7.3.

We also assume that the background gas density is uniform (and so $\rho_0 = 1$ in our non-dimensionalised units). We substitute in the form of our equilibrium magnetic field (equation 3.1) where $\mathbf{B}_0 = (x, 0, -z)$ and $A_0 = -xz$. This gives our linearised, non-dimensionalised, perturbation equations with pressure and resistivity included:

$$\begin{aligned}
 \frac{\partial}{\partial t} v_{\perp} &= v_A^2(x, z) \left(\frac{\partial b_z}{\partial x} - \frac{\partial b_x}{\partial z} \right) - \frac{\beta_0}{2} \left(z \frac{\partial p_1}{\partial x} + x \frac{\partial p_1}{\partial z} \right) \\
 \frac{\partial}{\partial t} v_{\parallel} &= -\frac{\beta_0}{2} \left(x \frac{\partial p_1}{\partial x} - z \frac{\partial p_1}{\partial z} \right) \\
 \frac{\partial b_x}{\partial t} &= -\frac{\partial}{\partial z} v_{\perp} + \frac{1}{R_m} \left(\frac{\partial^2 b_x}{\partial x^2} + \frac{\partial^2 b_x}{\partial z^2} \right) \\
 \frac{\partial b_z}{\partial t} &= \frac{\partial}{\partial x} v_{\perp} + \frac{1}{R_m} \left(\frac{\partial^2 b_z}{\partial x^2} + \frac{\partial^2 b_z}{\partial z^2} \right) \\
 \frac{\partial p_1}{\partial t} &= \frac{-\gamma}{x^2 + z^2} \left[\left(x \frac{\partial v_{\parallel}}{\partial x} - z \frac{\partial v_{\parallel}}{\partial z} \right) - 2 \frac{x^2 - z^2}{x^2 + z^2} v_{\parallel} \right. \\
 &\quad \left. + \left(z \frac{\partial v_{\perp}}{\partial x} + x \frac{\partial v_{\perp}}{\partial z} \right) - \frac{4xz}{x^2 + z^2} v_{\perp} \right] \tag{7.2}
 \end{aligned}$$

where the Alfvén speed, $v_A(x, z)$, is equal to $\sqrt{x^2 + z^2}$. These are the equations we will be solving in this chapter.

Note that by taking $\beta_0 = 0$ and ignoring resistivity ($R_m \rightarrow \infty$), we recover the equations discussed in Chapter 3.

7.3 Plasma β

The parameter of key importance in equations (7.2) is β_0 . The plasma β parameter is defined as the ratio of the thermal plasma pressure to the magnetic pressure (recall equation 1.12). In most parts of the corona, the plasma β is much less than unity, and hence the pressure gradients in the plasma can be neglected. However, near null points the magnetic field is diminishing (and is zero at the null) and so the plasma β can become very large. There is also coupling between the perpendicular and parallel velocity components (through β_0) and this coupling is most effective where the sound speed and the Alfvén velocity are comparable in magnitude. Bogdan *et al.* (2003) call this zone the magnetic canopy or the $\beta \approx 1$ layer. Note that in this Thesis, we use β for the (true) plasma beta and β_0 for the value of the plasma beta at a radius of unity ($r = 1$).

The true plasma β varies through the whole region, since magnetic field is varying everywhere throughout our model. In our system, $\beta \propto \frac{1}{x^2 + z^2}$ and thus will reach infinity at the origin. From

equilibrium quantities;

$$\beta = \frac{2\mu p_0}{\mathbf{B}_0 \cdot \mathbf{B}_0} = \frac{2\mu p_0}{B_0^2} \frac{1}{x^2 + z^2} \quad \text{and} \quad \beta_0 = \frac{2\mu p_0}{B_0^2}, \Rightarrow \beta = \frac{\beta_0}{x^2 + z^2} = \frac{\beta_0}{r^2}, \quad (7.3)$$

where $r^2 = x^2 + z^2$ and so we can think of the $\beta = 1$ layer as occurring at radius $r = \sqrt{\beta_0}$. This is the radius at which the thermal plasma pressure is equal to the magnetic pressure.

However, we believe that it is not the $\beta = 1$ layer that is most important in understanding this system, but that it is the layer where the sound speed is equal to the Alfvén speed, i.e. the layer where $c_s^2 = v_A^2$. Recall our definition of the sound speed, $c_s = \sqrt{\frac{\gamma p_0}{\rho_0}}$, and Alfvén speed, $v_A = \frac{B_0}{\sqrt{\mu \rho_0}} \sqrt{x^{*2} + z^{*2}}$, where $*$ denotes a dimensionless quantity and γ, p_0, ρ_0, B_0 and μ are constants as detailed in Section 2.2.2. Thus, the $c_s^2 = v_A^2$ layer occurs at:

$$\begin{aligned} c_s^2 = v_A^2 &\Rightarrow \frac{\gamma p_0}{\rho_0} = \frac{B_0^2}{\mu \rho_0} (x^2 + z^2) \Rightarrow \frac{\gamma \mu p_0}{B_0^2} = x^2 + z^2 \Rightarrow \frac{\gamma}{2} \beta_0 = x^2 + z^2 \\ &\Rightarrow \frac{\gamma}{2} \beta = 1 \quad \text{or alternatively} \quad r = \sqrt{\frac{\gamma}{2} \beta_0} \end{aligned}$$

where we have dropped the star indices on x and z (the fact that they are non-dimensionalised is understood). Thus, the $c_s^2 = v_A^2$ layer (or alternatively the $\beta = \frac{2}{\gamma}$ layer) occurs at a radius $r = \sqrt{\frac{\gamma}{2} \beta_0}$. We believe it is *this* layer that is of critical importance to the system. This is the radius at which the Alfvén speed and sound speed are comparable, and it is through this that the mixing or coupling arises.

Of course, the difference between the $\beta = 1$ layer at $r = \sqrt{\beta_0}$ and the $c_s^2 = v_A^2$ layer at $r = \sqrt{\frac{\gamma}{2} \beta_0}$ is very small, and hence can be grouped together as the $\beta \approx 1$ layer. Thus, Bogdan *et al.* (2003) are justified in considering the $\beta \approx 1$ layer to be the critical layer. However in this chapter, we consider the $c_s^2 = v_A^2$ layer to be of greatest importance.

In this chapter, we will investigate two cases;

- $\beta_0 = 0.25$ (referred to as the low β case) where the $\beta = 1$ layer occurs at a radius $r = \sqrt{0.25} = 0.5$ and correspondingly the $c_s^2 = v_A^2$ layer occurs at a radius of $r = \sqrt{\frac{5}{24}} = 0.456$,
- $\beta_0 = 2.25$ (referred to as the high β case) where $\beta = 1$ layer occurs at $r = \sqrt{2.25} = 1.5$ and so the $c_s^2 = v_A^2$ layer occurs at a radius of $r = \sqrt{\frac{15}{8}} = 1.37$.

We shall show that the location of the $c_s^2 = v_A^2$ layer from the null point drastically changes the nature of the system.

7.4 Polar coordinates ($\beta_0 = 0.25$ system)

We begin by looking at radial case for the $\beta \neq 0$ system. Recall the $\beta = 0$ system was considered in polar coordinates back in Section 3.4, where the (background) Alfvén speed ($v_A^2 = x^2 + z^2$) encourages the switch to polar coordinates. Again, in a circular geometry, our particular choice of magnetic field has the form:

$$\mathbf{B}_0 = -r \cos 2\theta \hat{\mathbf{r}} + r \sin 2\theta \hat{\boldsymbol{\theta}}$$

where $\mathbf{B}_0 \cdot \mathbf{B}_0 = r^2$, $\nabla \times \mathbf{b} = \frac{1}{r} \left[\frac{\partial}{\partial r} (rb_\theta) - \frac{\partial}{\partial \theta} b_r \right] \hat{\boldsymbol{\phi}}$, $\mathbf{A} = -\frac{1}{2} r^2 \sin 2\theta \hat{\boldsymbol{\phi}}$

This section proceeds as follows: 7.4.1 describes the behaviour of v_\perp , 7.4.2 describes the behaviour of v_\parallel and 7.4.4 details a small β_0 expansion of the system.

7.4.1 Numerical Simulation : v_\perp

In Chapter 3, we studied the cartesian form of our system before studying the polar form. Here, it is hoped that the circular geometry will give us critical insight into the system which can then be used to understand the cartesian system. We will only look at the low β case in polar coordinates ($\beta = 0.25$), since the $\beta = 2.25$ gives similar results (because our system doesn't have any obvious length scales). We will look at both the low and high β systems in cartesian coordinates.

As in Section 3.4.1, we now solve our equations (7.2) numerically using our 2D cartesian Lax-Wendroff numerical code (instead of writing a polar coordinates version of the code). Thus, we use the cartesian code but with an *initial pulse condition* as opposed to a driven boundary. This will give us a simulation of the $\beta \neq 0$ plasma behaviour. The numerical scheme was run in a (square) box with $-6 \leq x \leq 6$ and $-6 \leq z \leq 6$ and an initial pulse was set up around $r = 3$ such that:

$$v_\perp(r, \theta, t = 0) = \sqrt{3} \sin[\pi(r - 2.5)] \begin{cases} \text{for } 2.5 \leq r \leq 3.5 \\ \text{for } 0 \leq \theta \leq 2\pi \end{cases}$$

Of course, this pulse was written into the code in terms of $x = r \cos \theta$ and $z = r \sin \theta$ so what was actually solved was:

$$\begin{aligned}
 v_{\perp}(x, z, t = 0) &= \sqrt{3} \sin \left[\pi \left(\sqrt{x^2 + z^2} - 2.5 \right) \right] \quad \text{for } 2.5 \leq \sqrt{x^2 + z^2} \leq 3.5, \\
 \frac{\partial}{\partial x} v_{\perp} \Big|_{x=-6} &= 0, \quad \frac{\partial}{\partial x} v_{\perp} \Big|_{x=6} = 0, \quad \frac{\partial}{\partial z} v_{\perp} \Big|_{z=-6} = 0, \quad \frac{\partial}{\partial z} v_{\perp} \Big|_{z=6} = 0, \\
 v_{\parallel}(x, z, t = 0) &= 0, \\
 \frac{\partial}{\partial x} v_{\parallel} \Big|_{x=-6} &= 0, \quad \frac{\partial}{\partial x} v_{\parallel} \Big|_{x=6} = 0, \quad \frac{\partial}{\partial z} v_{\parallel} \Big|_{z=-6} = 0, \quad \frac{\partial}{\partial z} v_{\parallel} \Big|_{z=6} = 0. \quad (7.4)
 \end{aligned}$$

This gave a suitable initial pulse. When the numerical experiment began, the initial condition pulse split into two waves; each travelling in different directions. The waves split naturally apart and we can then concentrate our attention on the incoming circular wave. The outgoing wave is of no concern to us and the boundary conditions let the wave pass out of the box (this concept is similar to that of Section 3.4.1). The simulation was run with a resolution of 800×800 points. However, since we knew the important behaviour would occur close to the origin, a **stretched grid** was used to focus the majority of the grid points close to the null point¹. This gave better resolution in the areas of interest. We took $\beta_0 = 0.25$ and $R_m = 10^3$.

The evolution of the $\beta \neq 0$, linear fast wave can be seen in Figure 7.2. We found that the fast wave split into two waves; one approaching the origin and the other travelling away from it (as expected). The wave travelling towards the origin initially had the shape of an annulus. We found that the annulus contracts (as in Section 3.4.1 and Figure 7.2) and that, at least initially, this contraction appeared to preserve the original ratios (distance between the front and middle wavefronts compared to middle and trailing wavefronts). However, as the wave continues to propagate, it is distorted from its original shape; there is a decrease in Alfvén speed along the axes (separatrices) and so the annulus starts to take on a quasi-diamond shape (with the corners located along the separatrices). This can be seen in the second and third row of subfigures. Eventually, the wave crosses the $c_s^2 = v_A^2$ layer (indicated by a black circle in the figure). Now it begins a more complicated evolution (unlike anything seen in the equivalent $\beta = 0$ case in Figure 7.2).

¹The stretching algorithm smoothly stretched the grid such that 50% of the grid points lay within a radius of 1.5.

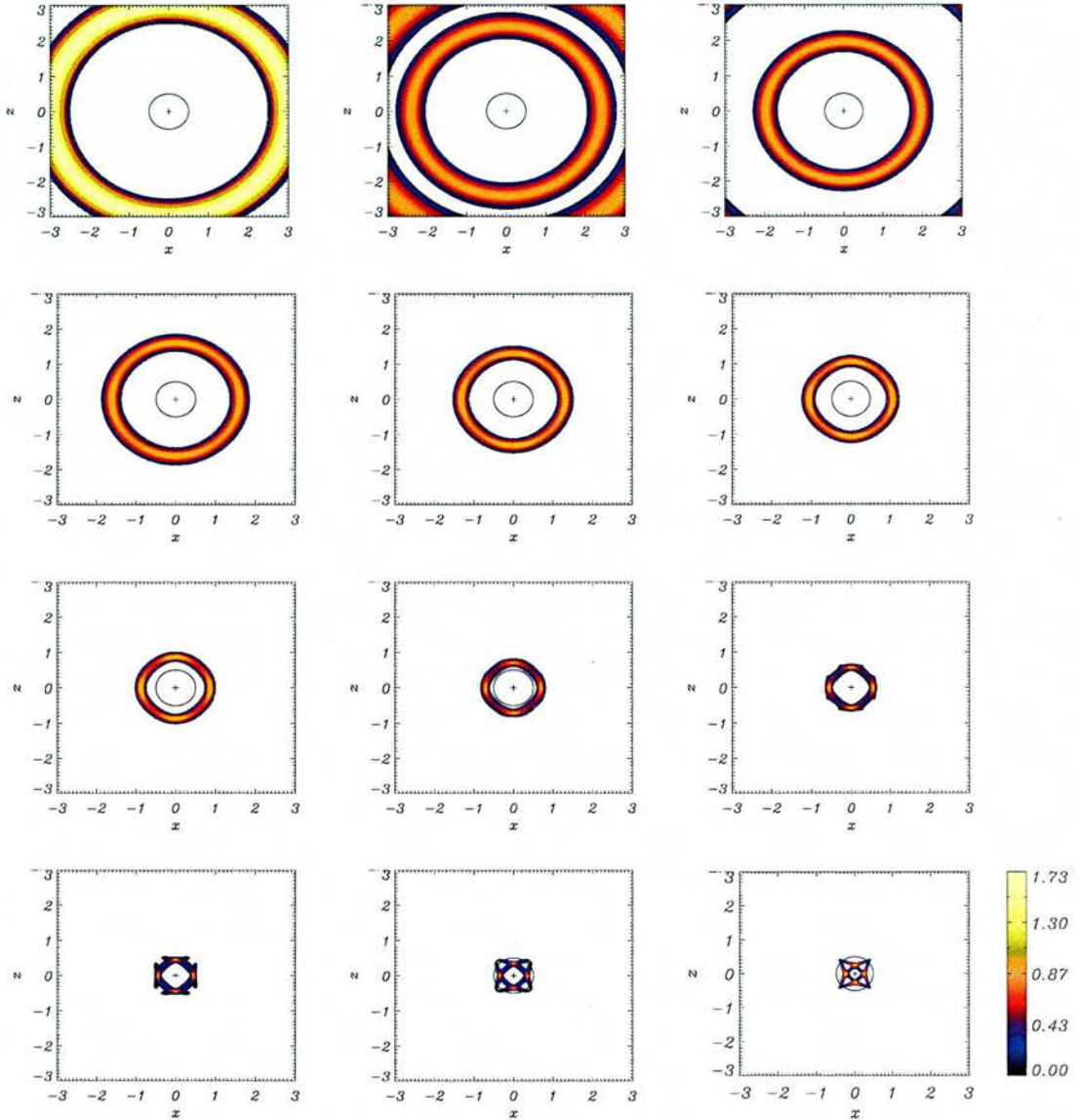


Figure 7.2: Contours of numerical simulation of v_{\perp} for a fast wave pulse initially located about a radius $\sqrt{x^2 + z^2} = 3$, and its resultant propagation at times (a) $t=0$, (b) $t=0.2$, (c) $t=0.4$, (d) $t=0.6$, (e) $t=0.8$, (f) $t=1.0$, (g) $t=1.2$, (h) $t=1.4$, (i) $t=1.6$, (j) $t=1.8$, (k) $t=2.0$ and (l) $t=2.2$, labelling from top left to bottom right. The black circle indicates the position of the $c_s^2 = v_A^2$ layer, which occurs at $\sqrt{x^2 + z^2} = \sqrt{\frac{\gamma\beta_0}{2}}$. The cross denotes the null point in the magnetic configuration.

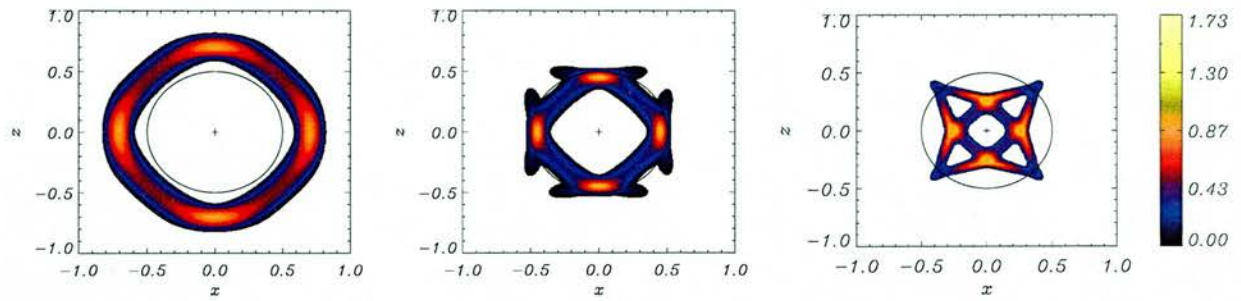


Figure 7.3: Blow-up subfigures of v_{\perp} from Figure 7.2 at times (a) $t=1.4$, (b) $t=1.8$ and (c) $t=2.2$, labelling left to right.

Some of the subfigures are shown as blown up versions in Figure 7.3, specifically showing the wave evolution just before, during and just after crossing the $c_s^2 = v_A^2$ layer. We will not explain the evolution any further, since this is best left to the cartesian case (see below); following the evolution of this (initially circular) fast wave until it reaches (and possibly crosses) the origin will not really give us any deep understanding of the system until we have looked at the cartesian case.

Thus, in this section we have learnt that initially the fast wave evolved in a similar manner to its $\beta = 0$ equivalent. By looking at the equations (equations 7.2), we see this makes sense; at large radii, the pressure terms are negligible and so the Alfvén speed is essentially spatially varying like r , and so the *refraction* effect dominates the evolution.

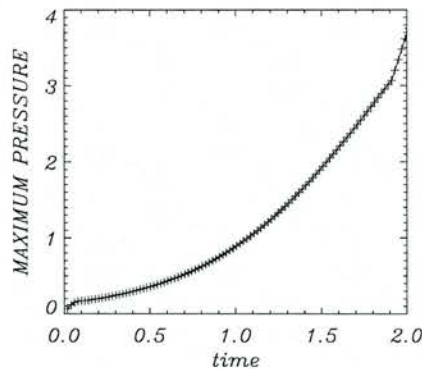


Figure 7.4: Increase in pressure as fast wave approaches and crosses the $c_s^2 = v_A^2$ layer. The wave crosses the $c_s^2 = v_A^2$ layer at approximately $t = 1.5$.

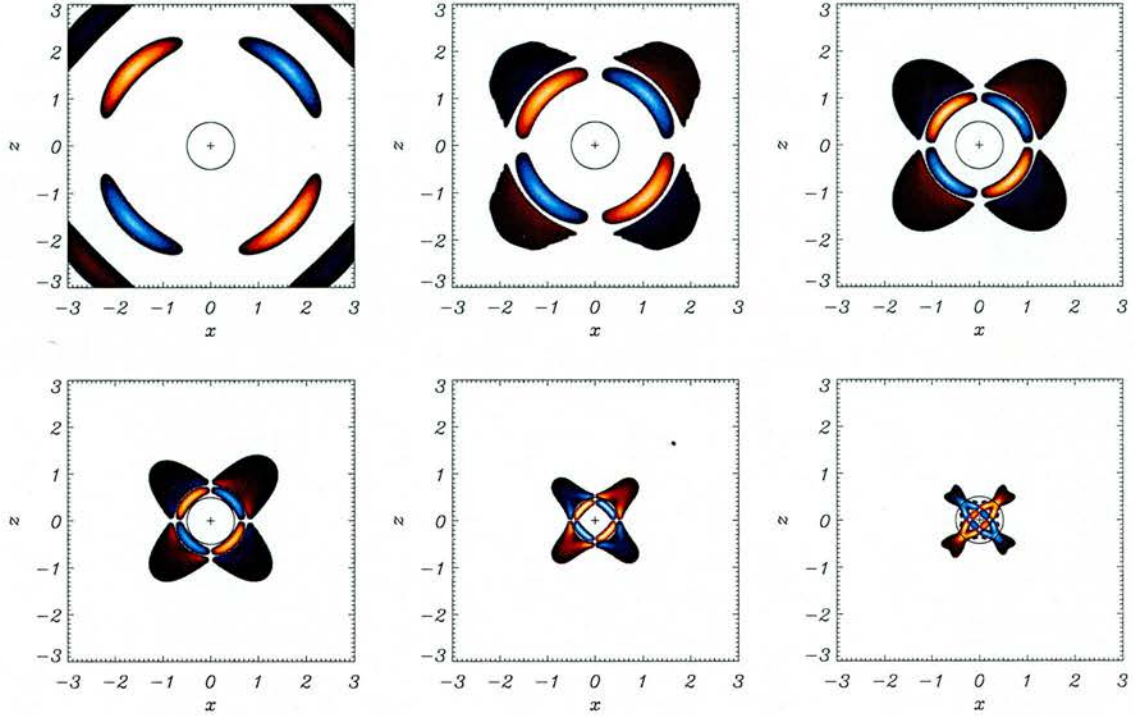


Figure 7.5: Contours of numerical simulation of p_1 for a fast wave pulse initially located about a radius $\sqrt{x^2 + z^2} = 3$, and its resultant propagation at times (a) $t=0.2$, (b) $t=0.6$, (c) $t=1.0$, (d) $t=1.4$, (e) $t=1.8$, (f) $t=2.2$, labelling from top left to bottom right. The black circle indicates the position of the $c_s^2 = v_A^2$ layer and the cross denotes the null point in the magnetic configuration. p_1 has an alternating form, where orange represents $p_1 > 0$ and blue represents $p_1 < 0$. The pressure appears to follow a $\sin 2\theta$ pattern.

We can see the behaviour of the perturbed pressure (p_1) in Figure 7.5 (above). p_1 propagates towards the origin like the fast wave and is zero along the axes. Hence, because of the alternating nature of the pressure, the maximum gradients in pressure (i.e. the maximum pressure force) will occur along these points (i.e. *along the separatrices*). This pressure force acts against the magnetic force in the momentum equation and thus reduces the acceleration of the fast wave along the separatrices, as mentioned above and seen in Figure 7.2 (i.e. $\frac{\partial}{\partial t} v_{\perp}$ is smaller along the axes). Note also that the pressure is increasing all the time and this can be seen in Figure 7.4 (previous page). Note this graph includes the time where the wave crosses the $c_s^2 = v_A^2$ layer (from the graph, we see this crossing does not affect the build-up in pressure) but does not show the behaviour of p_1 at the time when the wave crosses the origin (since this is outside the scope of this section).

7.4.2 Numerical Simulation : v_{\parallel}

We can also look at the behaviour of v_{\parallel} (the parallel component of our wave). This has a much more complicated behaviour than our perpendicular component and can be seen in Figure 7.6. Firstly, we notice that we have positive and negative parts to the wave, unlike the perpendicular component which was always positive. We see that the wave has an alternating structure in the θ direction. Secondly, we set an initial condition in v_{\perp} only (equations 7.4), there was no initial condition on the parallel wave; $v_{\parallel}(x, z, 0) = 0$. Hence, this v_{\parallel} wave has been generated from our v_{\perp} initial condition. By looking at equations (7.2) and our initial conditions, we see that v_{\perp} acts as a driver for v_{\parallel} (and p_1).

Thus, we are trying to solve a second order differential equation with a driver term, which is an inhomogeneous equation. The general solution to such equations consists of two parts; a *complementary function* and a *particular integral*. The complementary function is a solution to the corresponding homogeneous differential equation whereas the particular integral is a solution to the inhomogeneous differential equation.

Thus, returning our attention to Figure 7.6, we see that there should be two parts to the v_{\parallel} wave. We do see a part which has the same speed and frequency as the perpendicular component wave and, using the definition above, this wave can be thought of as the particular integral to the equations. There will also be a complementary function part to the wave, though it is very difficult to see in the figure (it will be easier to see in the cartesian case).

It is interesting to note that the waves in Figure 7.6 have a smaller amplitude than those in Figure 7.2. The v_{\perp} waves in Figure 7.2 have an amplitude of $\mathcal{O}\left(\frac{\sqrt{3}}{2}\right)$ compared to the v_{\parallel} waves in Figure 7.6 which have an amplitude of $\mathcal{O}\left(\beta_0 \frac{\sqrt{3}}{2}\right)$ (recall the initial condition was a wave of amplitude $\sqrt{3}$ that split equally into two).

The next section will explain how we choose to interpret the waves seen in the perpendicular and parallel velocities.

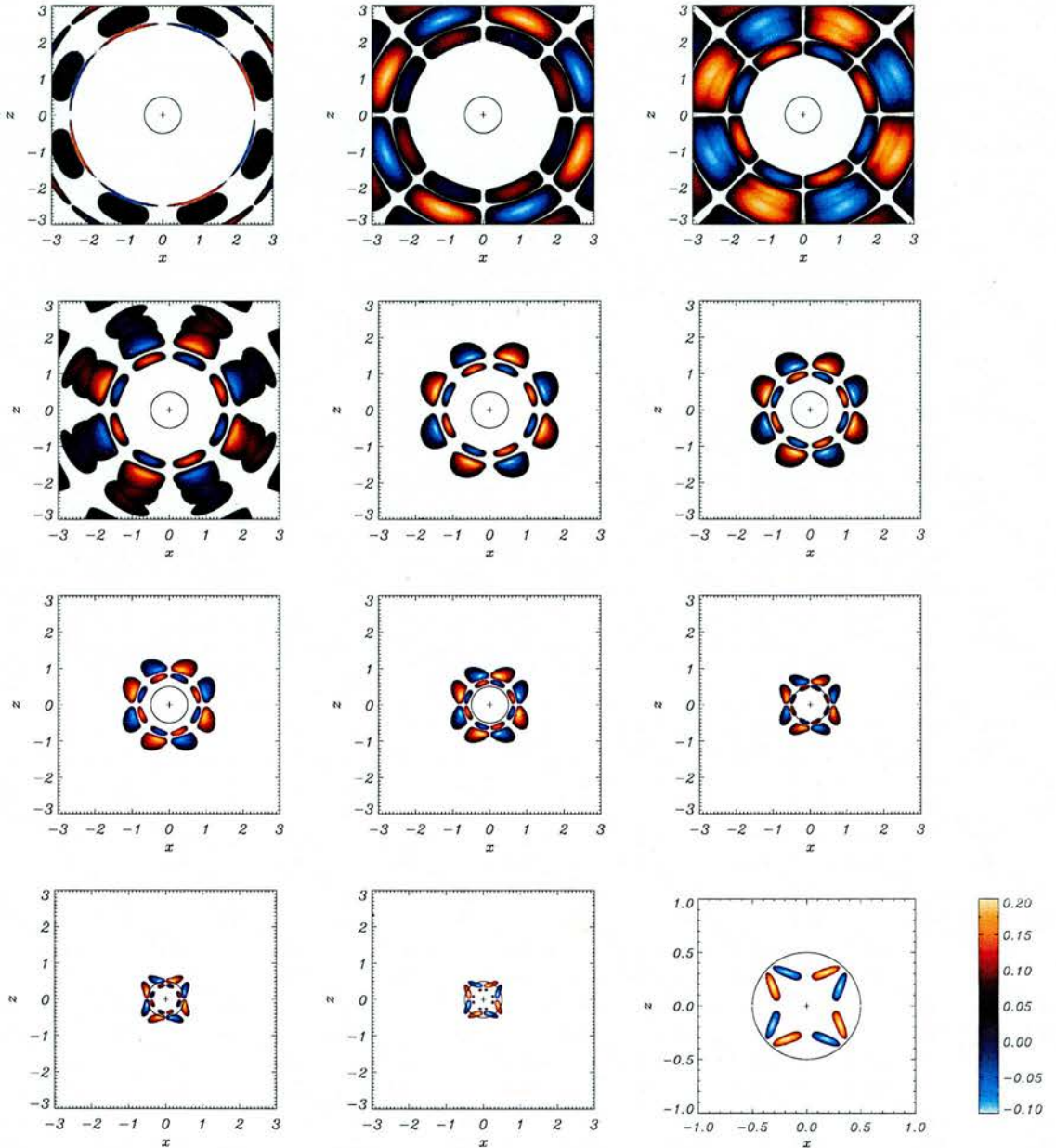


Figure 7.6: Contours of numerical simulation of v_{\parallel} for a fast wave pulse initially located about a radius $\sqrt{x^2 + z^2} = 3$, and its resultant propagation at times (a) $t=0.02$, (b) $t=0.2$, (c) $t=0.4$, (d) $t=0.6$, (e) $t=0.8$, (f) $t=1.0$, (g) $t=1.2$, (h) $t=1.4$, (i) $t=1.6$, (j) $t=1.8$, (k) $t=2.0$ and (l) $t=2.2$, labelling from top left to bottom right. The black circle indicates the position of the $c_s^2 = v_A^2$ layer. The cross denotes the null point in the magnetic configuration. The last subfigure shows a blow-up of the central region (axes have changed).

7.4.3 Interpretating the waves we see in \mathbf{v}_\perp and \mathbf{v}_\parallel

Recall from Section 1.5.6 that $\mathbf{v}_{\text{Alfvén}}$, \mathbf{v}_{slow} and \mathbf{v}_{fast} are all orthogonal. Thus, we may consider them as an **orthogonal basis** of vectors for our system. In this chapter, we do not consider the Alfvén wave ($\mathbf{v}_{\text{Alfvén}} = v_y \hat{\mathbf{y}}$) and so our 2D vectors may be described in terms of the vectors \mathbf{v}_{fast} and \mathbf{v}_{slow} . Due to our choice of coordinate system (Section 2.2.1), we choose to work in the directions perpendicular and parallel to the magnetic field. Thus, we may represent these two vectors in terms of \mathbf{v}_{fast} and \mathbf{v}_{slow} , i.e.

$$\mathbf{v}_\perp = A\mathbf{v}_{\text{fast}} + B\mathbf{v}_{\text{slow}} \quad , \quad \mathbf{v}_\parallel = C\mathbf{v}_{\text{fast}} + D\mathbf{v}_{\text{slow}}$$

Alternatively, we may express our two magnetoacoustic velocities in terms of \mathbf{v}_\perp and \mathbf{v}_\parallel , i.e.

$$\mathbf{v}_{\text{fast}} = E\mathbf{v}_\perp + F\mathbf{v}_\parallel \quad , \quad \mathbf{v}_{\text{slow}} = G\mathbf{v}_\perp + H\mathbf{v}_\parallel$$

where A, B, C, D, E, F, G and H are unknown functions that depend upon the magnetic geometry (and possibly the plasma β). This representation is only possible because both \mathbf{v}_{fast} & \mathbf{v}_{slow} and \mathbf{v}_\perp & \mathbf{v}_\parallel form orthogonal bases.

However, we must be careful. The concepts of fast and slow waves (Section 1.5.4) were derived for a unidirectional magnetic field and so these ideas may not carry over to more complicated geometries quite as simply as claimed here. However, we shall continue to use terms such as fast and slow wave in our interpretation of the waves in this chapter (i.e use the terminology and intuition gained from the unidirectional magnetic field model). Thus, **we choose to interpret the waves seen in our parallel and perpendicular velocities with the terminology of fast and slow waves**. In previous chapters, where we saw wave behaviour in the perpendicular component, we interpreted it as fast wave behaviour; we do the same thing here for both MA wave types.

We do not know the forms of the functions A, B, C, D, E, F, G and H . However, we are driving waves in the perpendicular velocity component in a low β region (see Section 7.5) and so we interpret this as predominantly fast wave. From initial experiments, it is believed that a good way of interpreting the waves we see in our magnetic configuration is as follows:

$$\begin{aligned} \text{fast wave} &= (\text{large perpendicular component}) + (\text{parallel component}) \\ &= (\text{large component in } \mathbf{v}_\perp) + (\text{component in } \mathbf{v}_\parallel) \quad , \\ \text{slow wave} &= (\text{small perpendicular component}) + (\text{parallel component}) \\ &= (\text{small component in } \mathbf{v}_\perp) + (\text{component in } \mathbf{v}_\parallel) \quad . \end{aligned} \tag{7.5}$$

This method of interpretation will be used to identify the MHD modes in the cartesian coordinate sections below.

7.4.4 Small β_0 expansion

We can try to gain insight into our numerical simulations using a small β expansion of the ideal equations. Recall our equations are:

$$\begin{aligned}\frac{\partial}{\partial t} v_{\perp} &= -(\mathbf{B}_0 \cdot \mathbf{B}_0)(\nabla \times \mathbf{b}) + \frac{\beta_0}{2} \nabla A_0 \cdot \nabla p_1, \\ \frac{\partial}{\partial t} v_{\parallel} &= -\frac{\beta_0}{2} (\mathbf{B}_0 \cdot \nabla) p_1, \\ \frac{\partial}{\partial t} \mathbf{b} &= (\nabla v_{\perp}) \times \hat{\mathbf{y}}, \\ \frac{\partial}{\partial t} p_1 &= -\gamma \left[\nabla \cdot \left(\frac{\mathbf{B}_0}{\mathbf{B}_0 \cdot \mathbf{B}_0} v_{\parallel} - \frac{\nabla A}{\mathbf{B}_0 \cdot \mathbf{B}_0} v_{\perp} \right) \right],\end{aligned}\tag{7.6}$$

and that in polar coordinates our magnetic quantities are:

$$\begin{aligned}\mathbf{B}_0 &= -r \cos 2\theta \hat{\mathbf{r}} + r \sin 2\theta \hat{\theta}, \quad \mathbf{B}_0 \cdot \mathbf{B}_0 = r^2, \\ \nabla \times \mathbf{b} &= \frac{1}{r} \left[\frac{\partial}{\partial r} (r b_{\theta}) - \frac{\partial}{\partial \theta} b_r \right] \hat{\mathbf{y}}, \quad \mathbf{A} = -\frac{1}{2} r^2 \sin 2\theta \hat{\mathbf{y}}\end{aligned}$$

We now assume forms for v_{\perp} and v_{\parallel} such that:

$$v_{\perp} = v_{\perp 1}(r, t) + \beta_0^2 v_{\perp 2}(r, \theta, t), \quad v_{\parallel} = \beta_0 v_{\parallel 1}(r, \theta, t).$$

Substituting these forms into the above equations gives:

$$\begin{aligned}\frac{\partial^2}{\partial t^2} v_{\perp 1} &= r \frac{\partial}{\partial r} \left(r \frac{\partial}{\partial r} v_{\perp 1} \right) + \mathcal{O}(\beta_0), \\ \frac{\partial}{\partial t} v_{\parallel 1} &= -\frac{1}{2} (\mathbf{B}_0 \cdot \nabla) p_1 + \mathcal{O}(\beta_0), \\ \frac{\partial}{\partial t} p_1 &= -\gamma \nabla \cdot \left[\left(\frac{\sin 2\theta}{r} v_{\perp 1} \right) \hat{\mathbf{r}} + \left(\frac{\cos 2\theta}{r} v_{\perp 1} \right) \hat{\theta} \right] + \mathcal{O}(\beta_0) \\ &= \gamma \sin 2\theta r \frac{\partial}{\partial r} \left(\frac{v_{\perp 1}}{r^2} \right) + \mathcal{O}(\beta_0)\end{aligned}$$

Note that we previously saw a $\sin 2\theta$ behaviour for p_1 in Figure 7.5. This gives us confidence that our small β_0 expansion could be applicable. We have also cancelled a factor of β_0 from the equation for $\frac{\partial}{\partial t} v_{\parallel 1}$.

Substituting the equation for $\frac{\partial}{\partial t} p_1$ into the equation for $\frac{\partial}{\partial t} v_{\parallel 1}$ and ignoring terms of order β_0 (make the small β_0 expansion) gives:

$$\begin{aligned}\frac{\partial^2}{\partial t^2} v_{\parallel 1} &= \frac{\gamma}{2} \left\{ -r \cos 2\theta \sin 2\theta \frac{\partial}{\partial r} r \left[\frac{\partial}{\partial r} \left(\frac{v_{\perp 1}}{r^2} \right) \right] + r \sin 2\theta \cos 2\theta \left(\frac{v_{\perp 1}}{r^2} \right) \right\} \\ &= \frac{\gamma}{4} \sin 4\theta r^3 \frac{\partial}{\partial r} \frac{1}{r} \left[\frac{\partial}{\partial r} \left(\frac{v_{\perp 1}}{r^2} \right) \right] = \frac{\gamma}{4} \sin 4\theta \mathcal{F}(r, t)\end{aligned}$$

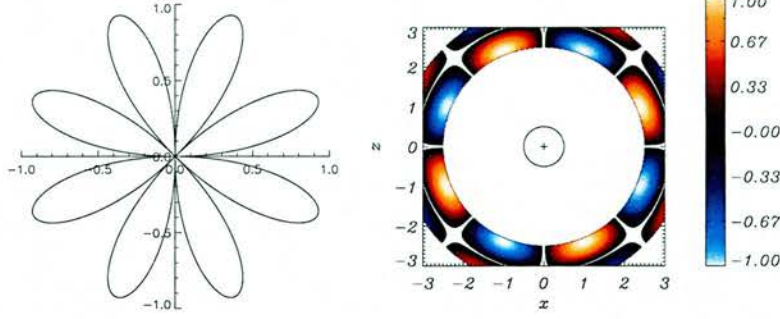


Figure 7.7: (Left) Plot of $r = \sin 4\theta$. (Right) Contour of $\frac{\gamma}{4} \sin 4\theta \frac{\sqrt{3}}{r^2} [(8 - \pi^2 r^2) \sin \pi(r - 2.5) - 5\pi r \cos \pi(r - 2.5)]$ for $2.5 \leq r \leq 3.5$.

where $\mathcal{F}(r, t)$ is a known function that depends only on r and t . This function is determined by the behaviour of $v_{\perp 1}$. Thus, we can see that with our choice of magnetic null point (equation 3.1) and by driving v_{\perp} , then the form of v_{\parallel} naturally develops a $\sin 4\theta$ dependence. The left hand side of Figure 7.7 shows a plot of $r = \sin 4\theta$.

If we assume our initial condition for v_{\perp} takes the same form as its $\beta = 0$ equivalent, i.e.:

$$\begin{aligned} v_{\perp 1} &= \sqrt{3} \sin [\pi(r - 2.5)] = \frac{1}{2} \mathcal{F}(t + \log r) + \frac{1}{2} \mathcal{F}(t - \log r) \\ &= \frac{\sqrt{3}}{2} \sin [\pi(re^t - 2.5)] + \frac{\sqrt{3}}{2} \sin [\pi(re^{-t} - 2.5)] \end{aligned}$$

then it can be shown that;

$$\begin{aligned} \frac{\partial^2}{\partial t^2} v_{\parallel 1} &= \frac{\gamma}{4} \sin 4\theta r^3 \frac{\partial}{\partial r} \frac{1}{r} \left[\frac{\partial}{\partial r} \left(\frac{v_{\perp 1}}{r^2} \right) \right] \\ &= \frac{\gamma}{8} \sin 4\theta \frac{\sqrt{3}}{r^2} [(8 - \pi^2 e^{2t} r^2) \sin \pi(re^t - 2.5) - 5\pi e^t r \cos \pi(re^t - 2.5) \\ &\quad + (8 - \pi^2 e^{-2t} r^2) \sin \pi(re^{-t} - 2.5) - 5\pi e^{-t} r \cos \pi(re^{-t} - 2.5)] \end{aligned} \quad (7.7)$$

However, this cannot be integrated in time. By choosing a different form for the initial condition (one where it is possible to integrate $r^3 \frac{\partial}{\partial r} \frac{1}{r} \left[\frac{\partial}{\partial r} \left(\frac{1}{r^2} \mathcal{F} \right) \right]$ twice in time), then we could directly compare numerical and analytical results. The right hand side of Figure 7.7 shows a contour of $\frac{\gamma}{4} \sin 4\theta \frac{\sqrt{3}}{r^2} [(8 - \pi^2 r^2) \sin \pi(r - 2.5) - 5\pi r \cos \pi(r - 2.5)]$ for $2.5 \leq r \leq 3.5$. Though this is not the true integral of equation (7.7), it bears a resemblance to the top row of Figure 7.6, although the scales are different. This figure is included here to show that our small β_0 approximation appears to be on the right track (even though we could not fully solve it). Thus, we still have confidence that the $\sin 4\theta$ dependence does indeed arise naturally in the parallel component of our system. This will be of use in the next section, where we consider the magnetoacoustic waves in a cartesian coordinate system.

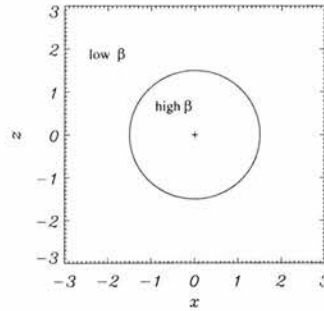


Figure 7.8: Regions of high and low β in our equilibrium magnetic field, where $\beta = \frac{\beta_0}{x^2+z^2}$ and β_0 is a constant. The black circle indicates the position of the $c_s^2 = v_A^2$ layer

7.5 Mode conversion across the $c_s^2 = v_A^2$ layer

As mentioned above, the $c_s^2 = v_A^2$ layer is of critical importance to our system. Recall that the fast and slow MA waves are related to the interplay of the magnetic and plasma pressure (Section 1.5.6). Thus, when the Alfvén speed and sound speed are dissimilar, there is no coupling between the fast and slow MA waves. However, near the $c_s^2 = v_A^2$ layer, the magnetic and plasma pressures can interact; this is how the mixing or coupling arises.

Our system consists of a region of low β plasma far outside the $c_s^2 = v_A^2$ layer (since this is related to the $\beta = 1$ layer) and a region of high β plasma within (see Figure 7.8). This is understood from our definition of the plasma β for this magnetic field; $\beta = \frac{\beta_0}{x^2+z^2}$ (where β_0 is a constant). Recall from Section 1.5.6 that slow and fast waves have differing properties depending on if they are in a high or low β environment. To summarise:

	Fast Wave	Slow Wave
High β	Behaves like sound wave (speed c_s)	Guided along \mathbf{B}_0 Transverse wave travelling at v_A
Low β	Propagates roughly isotropically (speed v_A)	Guided along \mathbf{B}_0 Longitudinal wave travelling at speed c_T

In our investigations, we are sending a wave pulse into our system from the top boundary, i.e. in the low β region. At some point this wave will cross the $c_s^2 = v_A^2$ layer and enter the high β environment. Thus, we have a low β wave approaching the layer, coupling and mixing inside the layer and emerging as a mixture of high β fast and slow waves.

At this time there does not exist a robust set of rules connecting low and high β waves across the $c_s^2 = v_A^2$ layer or across the $\beta = 1$ layer (Carlsson & Stein 1999). It is hoped the work here will contribute to such a set of rules, specifically in what happens when a low β fast wave crosses the $c_s^2 = v_A^2$ layer and becomes part high β fast wave and part high β slow wave (or alternately what happens when it crosses the $\beta = 1$ layer a little time earlier).

7.6 Cartesian coordinates ($\beta_0 = 0.25$ system)

We now look at the wave behaviour in a cartesian system. As mentioned above, we will investigate two cases in this chapter

- $\beta_0 = 0.25$ (referred to as the low β case) where the $\beta = 1$ layer occurs at a radius $r = \sqrt{0.25} = 0.5$ and correspondingly the $c_s^2 = v_A^2$ layer occurs at a radius of $r = \sqrt{\frac{5}{24}} = 0.456$,
- $\beta_0 = 2.25$ (referred to as the high β case) where $\beta = 1$ layer occurs at $r = \sqrt{2.25} = 1.5$ and so the $c_s^2 = v_A^2$ layer occurs at a radius of $r = \sqrt{\frac{15}{8}} = 1.37$.

This section considers the low β case of $\beta_0 = 0.25$.

7.6.1 Numerical Simulation : v_{\perp} ($\beta_0 = 0.25$)

We now solve linearised MHD equations, namely equations (7.1), numerically using our two-step Lax-Wendroff scheme (page 2.3.1). The numerical scheme is run in a box with $-4 \leq x \leq 4$ and $-4 \leq z \leq 4$ and we initially consider a single wave pulse coming in from the top boundary. For the single wave pulse, the boundary conditions were set such that:

$$\begin{aligned}
 v_{\perp}(x, 4) &= \begin{cases} \sin \omega t & \text{for } 0 \leq t \leq \frac{\pi}{\omega} \\ 0 & \text{otherwise} \end{cases}, \\
 \frac{\partial v_{\perp}}{\partial x} \Big|_{x=-4} &= 0, \quad \frac{\partial v_{\perp}}{\partial x} \Big|_{x=4} = 0, \quad \frac{\partial v_{\perp}}{\partial z} \Big|_{z=-4} = 0, \\
 v_{\parallel}(x, 4) &= 0, \quad \frac{\partial v_{\parallel}}{\partial x} \Big|_{x=-4} = 0, \quad \frac{\partial v_{\parallel}}{\partial x} \Big|_{x=4} = 0, \quad \frac{\partial v_{\parallel}}{\partial z} \Big|_{z=-4} = 0.
 \end{aligned} \tag{7.8}$$

Tests show that the central behaviour is largely unaffected by the choices of side and bottom boundary conditions. The other boundary conditions on the perturbed magnetic field follow from the remaining equations and the solenoidal condition. We set $\beta_0 = 0.25$ and $R_m = 10^3$ (an effective resistivity of 10^{-3}). The results can be seen in Figures 7.9, 7.13 and 7.16.

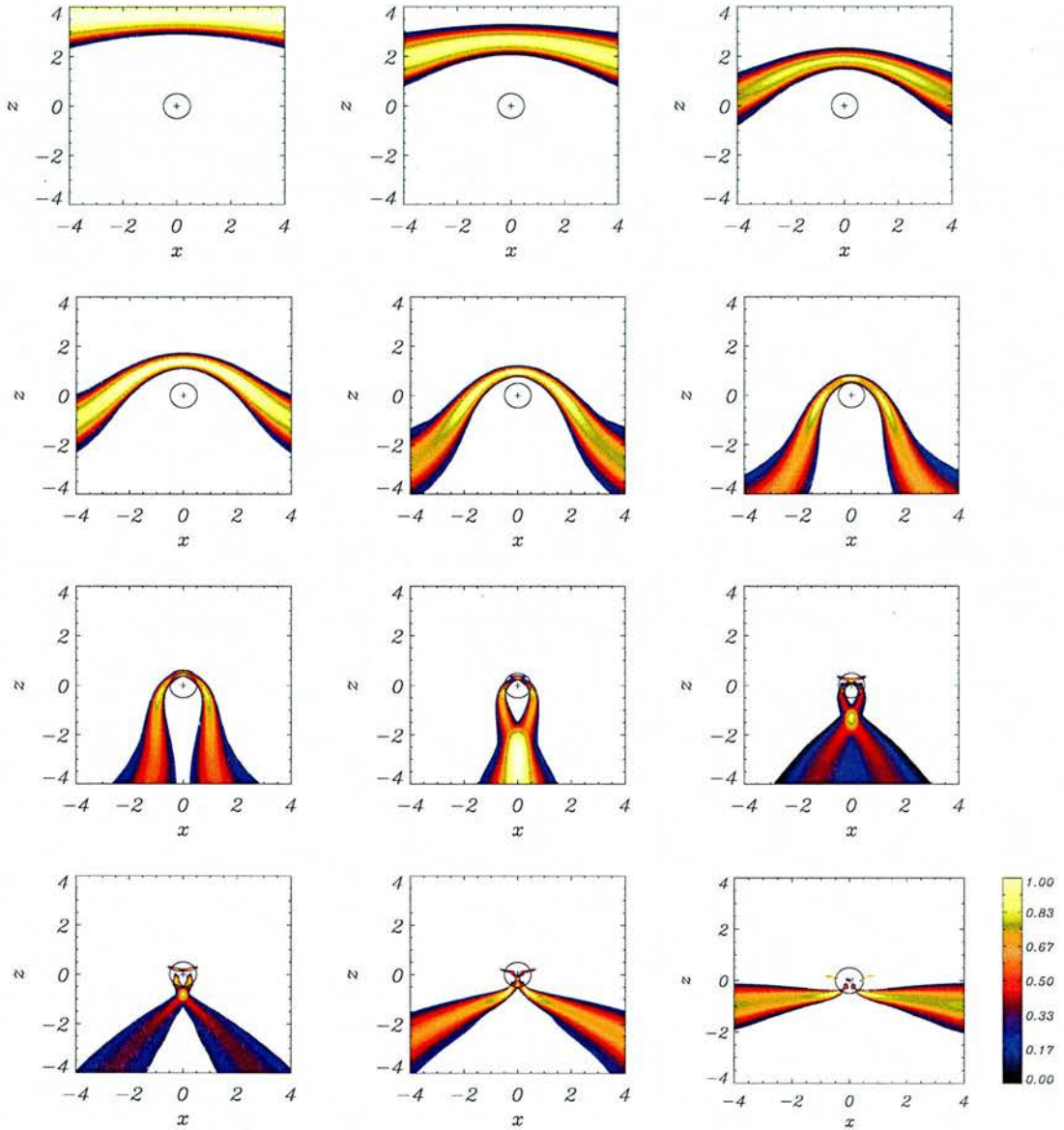


Figure 7.9: Contours of v_{\perp} for numerical simulation for a fast wave sent in from upper boundary for $-4 \leq x \leq 4$ and $\beta_0 = 0.25$ and its resultant propagation at times (a) $t=0.33$, (b) $t=0.67$, (c) $t=1.0$, (d) $t=1.33$, (e) $t=1.67$ and (f) $t=2.0$, (g) $t=2.33$, (h) $t=2.67$, (i) $t=3.0$, (j) $t=3.33$, (k) $t=3.67$ and (l) $t=4.0$, labelling from top left to bottom right. The black circle indicates the position of the $c_s^2 = v_A^2$ layer. The cross denotes the null point in the magnetic configuration.

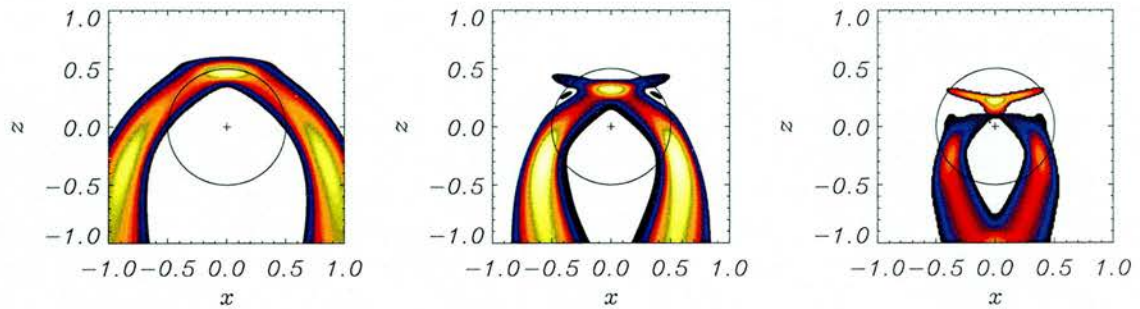


Figure 7.10: Blow-up subfigures of v_{\perp} from Figure 7.9 at times (a) $t=2.33$, (b) $t=2.67$ and (c) $t=3.0$, labelling left to right.

We can see the behaviour of v_{\perp} in Figure 7.9. We find that the wave travels towards the neighbourhood of the null point and begins to wrap around it. Through the MHD mode interpretation given on page 157, we identify this wave as a low β fast wave. This fast wave demonstrates *refraction*, as was seen in Chapter 3.

However, there are new effects to be seen in this $\beta \neq 0$ system. Once the fast wave reaches the $c_s^2 = v_A^2$ layer (denoted by the black circle around the null) the wave nature changes. Part of the wave now appears to be spreading out along field lines. Remembering that in this geometry the slow wave could have a component in v_{\perp} and referring to the table on page 160, we believe this is a high β slow wave. The wave can particularly be seen in subfigures (g) to (i).

The rest of the wave in the high β region appears to continue to wrap around the null. The wings of the fast wave (outside in the low β region) continue to wrap around the null. This wrapping effect continues again and again, but each time part of the (low β) fast wave is converted to (high β) slow wave as it crosses the $c_s^2 = v_A^2$ layer. Note that this wave conversion was also seen in Figure 7.2. Figure 7.10 shows a blow-up of subfigures (g) to (i). In this figure we can see the wave behaviour as it nears and crosses the $c_s^2 = v_A^2$ layer. This figure can also be compared to Figure 7.3; we can convince ourselves a similar wave conversion was occurring in the radial geometry.

Figure 7.11 shows shaded surfaces of v_{\perp} at various times. This figure can be directly compared to its $\beta = 0$ equivalent; Figure 3.3. Note that in this $\beta \neq 0$ case, the wave does not maintain a constant amplitude near the line $x = 0$. Instead, some of the wave amplitude decays away (boundary effects also affect the wave amplitude at the edges of the box, as before).

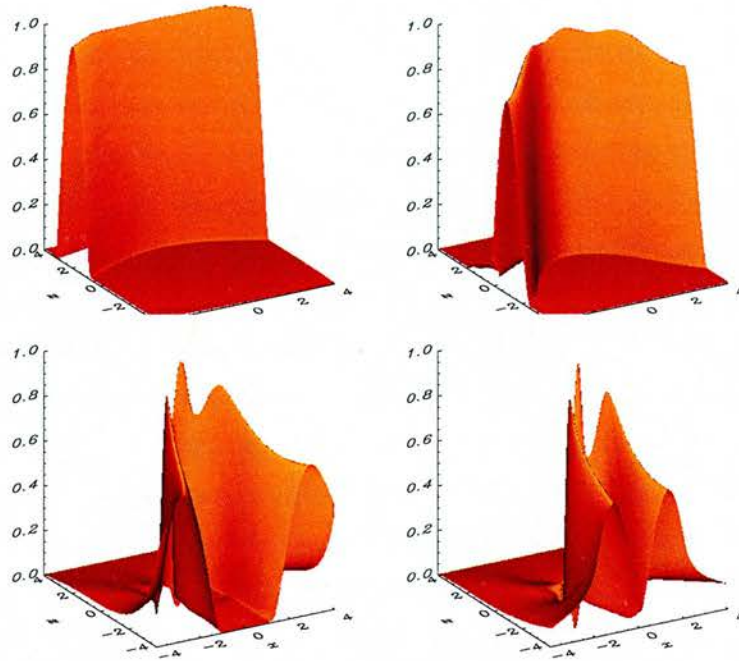


Figure 7.11: Shaded surfaces of v_{\perp} for numerical simulation for a fast wave sent in from upper boundary ($-4 \leq x \leq 4$) with $\beta_0 = 0.25$ and its resultant propagation at times (a) $t=0.625$, (b) $t=1.25$, (c) $t=1.875$ and (d) $t=2.5$, labelling from top left to bottom right.

Figure 7.12 shows shaded surfaces of v_{\perp} at times $t=3.0$ and $t=3.67$. These correspond to subfigures (i) and (k) in Figure 7.9. Here we see shaded surfaces of v_{\perp} but with the z -axis inverted ($z \rightarrow -z$). This allows us to see the build-up of what we have called the high β slow wave, which is located behind the main part of the wave in the figure. We can see that it has amplitude of less than half that of the main wave. However, we have been unable to precisely plot the development of its amplitude.

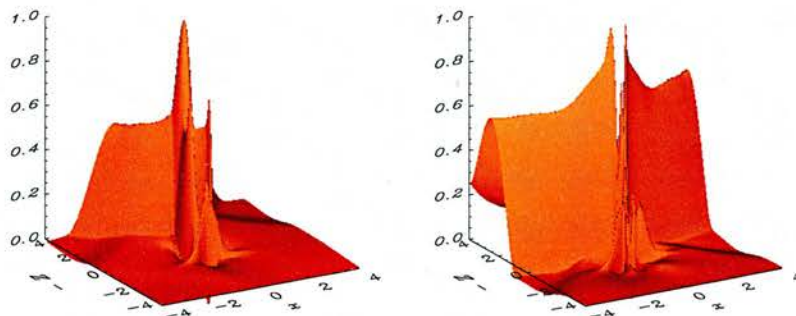


Figure 7.12: Shaded surfaces of v_{\perp} for numerical simulation for a fast wave sent in from upper boundary ($-4 \leq x \leq 4$) with $\beta_0 = 0.25$ and its resultant propagation at times (Left) $t=3.0$ and (Right) $t=3.67$. Note the y -axis has been inverted ($z \rightarrow -z$).

7.6.2 Numerical Simulation : v_{\parallel} ($\beta_0 = 0.25$)

Figure 7.13 shows the numerical simulation of the parallel component for the wave. We see that an antisymmetric wave (compared to the symmetric perpendicular wave) focussing in towards the null. This is the fast wave component showing up in the parallel velocity component. This aspect travels at the same speed and frequency as the perpendicular component wave. As mentioned previously, v_{\perp} drives v_{\parallel} . Thus, mathematically this can be thought of as the particular solution to the inhomogenous equations.

There are also several other noteworthy aspects to this figure. Firstly, it is obviously complicated compared to the (relatively) simple perpendicular velocity (Figure 7.9); but then again this was also the case for our circular geometry (compare Figures 7.2 and 7.6). Also, the driven perpendicular velocity was symmetric along and across its pulse. This leads to an antisymmetry along and across the parallel velocity.

After the wave enters inside the $c_s^2 = v_A^2$ layer, it spreads out along the field lines. This supports our interpretation in Figure 7.9 of the creation of a high β slow wave at the $c_s^2 = v_A^2$ layer; obviously the slow wave will show up in the parallel velocity (since it is field guided). It is also interesting to note that all the waves in Figure 7.13 have a very small amplitude compared to those in Figure 7.9. Waves in the perpendicular component have an amplitude of order unity whereas waves in the parallel component are of order β_0 . The size of β_0 used will affect the magnitude of the coupling and determine how much pressure and parallel velocity feedback on the system.

Finally, recall that in Figure 7.6 the symmetric, circular perpendicular wave drove the alternating, antisymmetric parallel wave, and that the magnetic configuration naturally lead to a $\sin 4\theta$ dependence. This explains the complicated, lobe-like structuring in Figure 7.13, i.e. the lobes come from the magnetic configuration (but the wave is no longer circular so the $\sin 4\theta$ is less apparent).

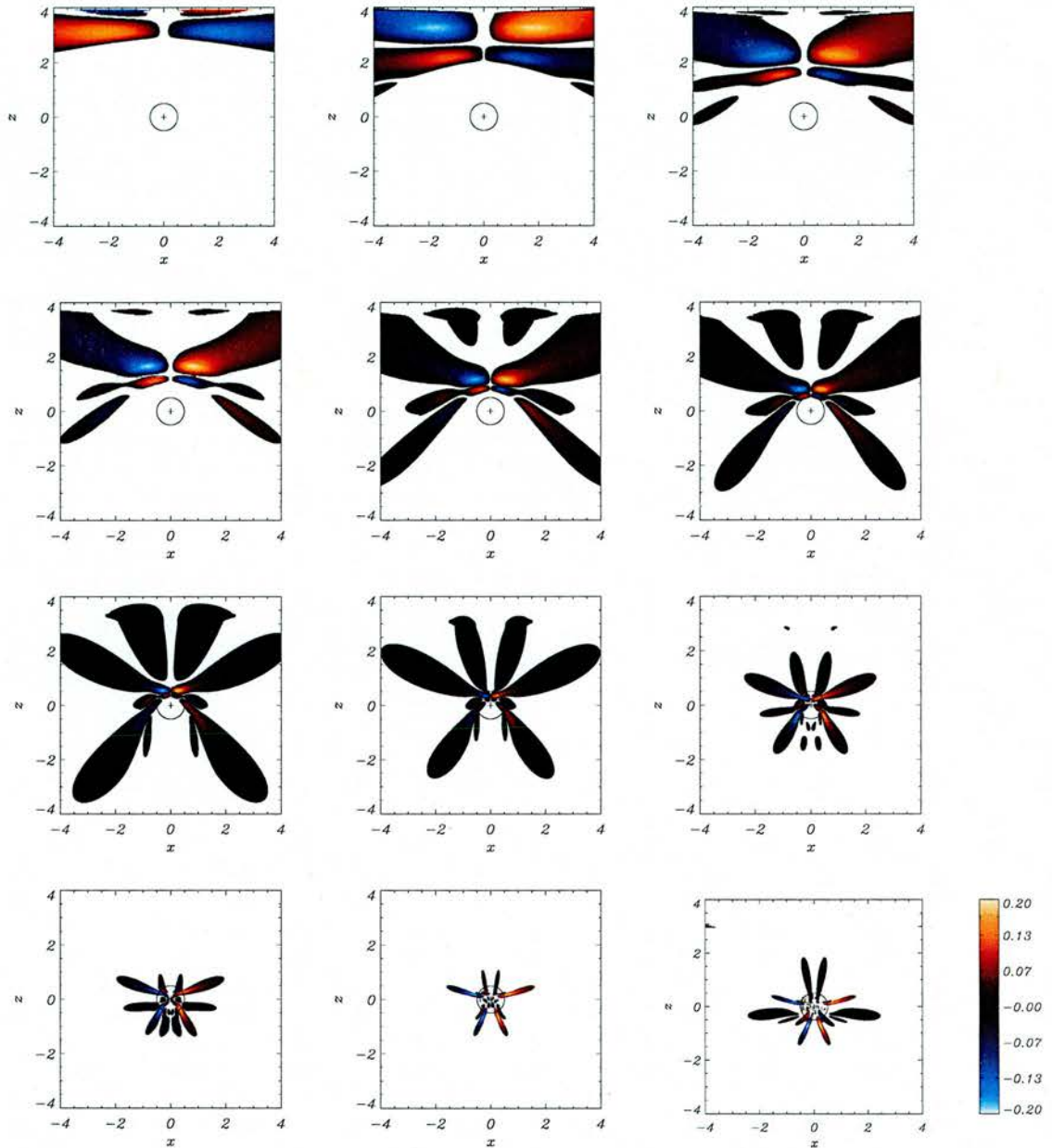


Figure 7.13: Contours of v_{\parallel} for numerical simulation for a fast wave sent in from upper boundary for $-4 \leq x \leq 4$ and $\beta_0 = 0.25$ and its resultant propagation at times (a) $t=0.33$, (b) $t=0.67$, (c) $t=1.0$, (d) $t=1.33$, (e) $t=1.67$ and (f) $t=2.0$, (g) $t=2.33$, (h) $t=2.67$, (i) $t=3.0$, (j) $t=3.33$, (k) $t=3.67$ and (l) $t=4.0$, labelling from top left to bottom right. The black circle indicates the position of the $c_s^2 = v_A^2$ layer. The cross denotes the null point in the magnetic configuration.

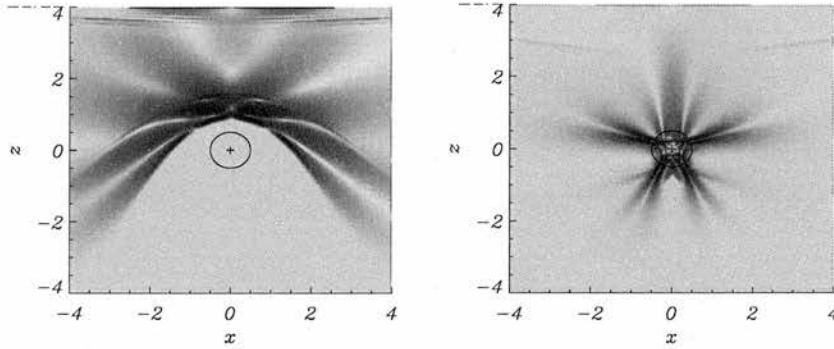


Figure 7.14: Shaded surface (from above) of v_{\parallel} for numerical simulation for a fast wave (pulse) sent in from upper boundary for $-4 \leq x \leq 4$ and $\beta_0 = 0.25$ at time $t = 1.5$ (left) and $t = 3.5$ (right).

There is another aspect to the parallel velocity component, one which is not easily seen in the contour plots of Figure 7.13. There is a second part to the parallel wave, one that lags behind the first. This is the low β slow wave part of the parallel velocity. Figure 7.14 shows a shaded surface of the parallel velocity; the slow wave can be seen at the top of the subfigures. This part of the parallel wave has an amplitude of order $\beta_0^{1.6}$ (see Figure 7.15) and has a discontinuous form, and is thus difficult to pick up in the contours of Figure 7.13. However, it is definitely there and can be thought of as the complementary function to the equations (as defined in Section 7.4.2). Some of the properties of this low β slow wave can be seen in Figure 7.15. We can see that the slow wave travels with a speed proportional to $\sqrt{\beta_0}$ as would be expected (as $c_s^2 \sim \beta_0$).

Finally, we have been unable to determine where the power for the amplitude of the complementary function comes from (i.e. the amplitude goes like $\beta_0^{1.6}$). We suspect that the power is probably 1.5 rather than 1.6 (i.e. a deviation due to numerical error). We also suspect that the wave has the form $v_{\parallel} = \beta_0 (v_{CF} + v_{PI})$ and at some point the particular integral is multiplied by $\sqrt{\beta_0}$ to give it an amplitude of order $\beta_0^{1.5}$.

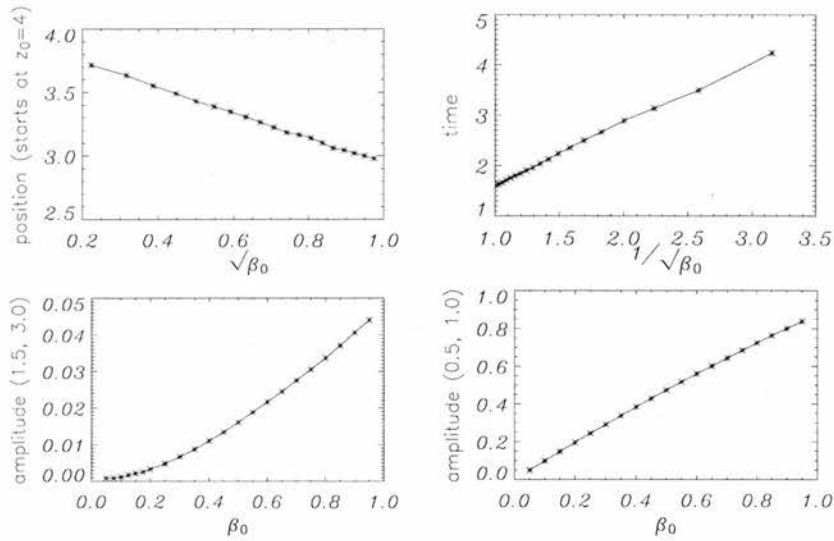


Figure 7.15: Graphs showing various aspects of the parallel velocity component. *Top left* shows position reached by (homogeneous solution) slow wave after $t = 1.5$ along $x = 1.5$ (gradient -0.99). *Top right* shows time taken for the slow wave to reach $z = 3$ along $x = 1.5$ (gradient 1.22). Both top graphs can be explained if $c_{\text{slow}} \sim \sqrt{\beta_0}$. *Bottom left* panel shows amplitude of slow wave at $(x, z) = (1.5, 3)$. Amplitude $\sim \beta_0^{1.6}$. *Bottom right* panel shows that amplitude of inhomogeneous wave at $(x = 0.5, z = 1.0)$ increases linearly with β_0 (gradient 0.87). It is also spatially independent of β_0 .

7.6.3 Current ($\beta_0 = 0.25$)

Since we have a changing perturbed magnetic field whose gradients are increasing in time, we have a build up of current density. Figure 7.16 shows the buildup of current density as time increases. We see that the refraction of the waves focuses the majority of the wave energy at the null point. However, close to the null point, current also builds up along the separatrices. Inside the $c_s^2 = v_A^2$ layer, these two aspects of the current build up come from the two aspects of the perpendicular velocity; the high β fast wave leads to current accumulation near the null and the high β slow wave leads to accumulation along the separatrices.

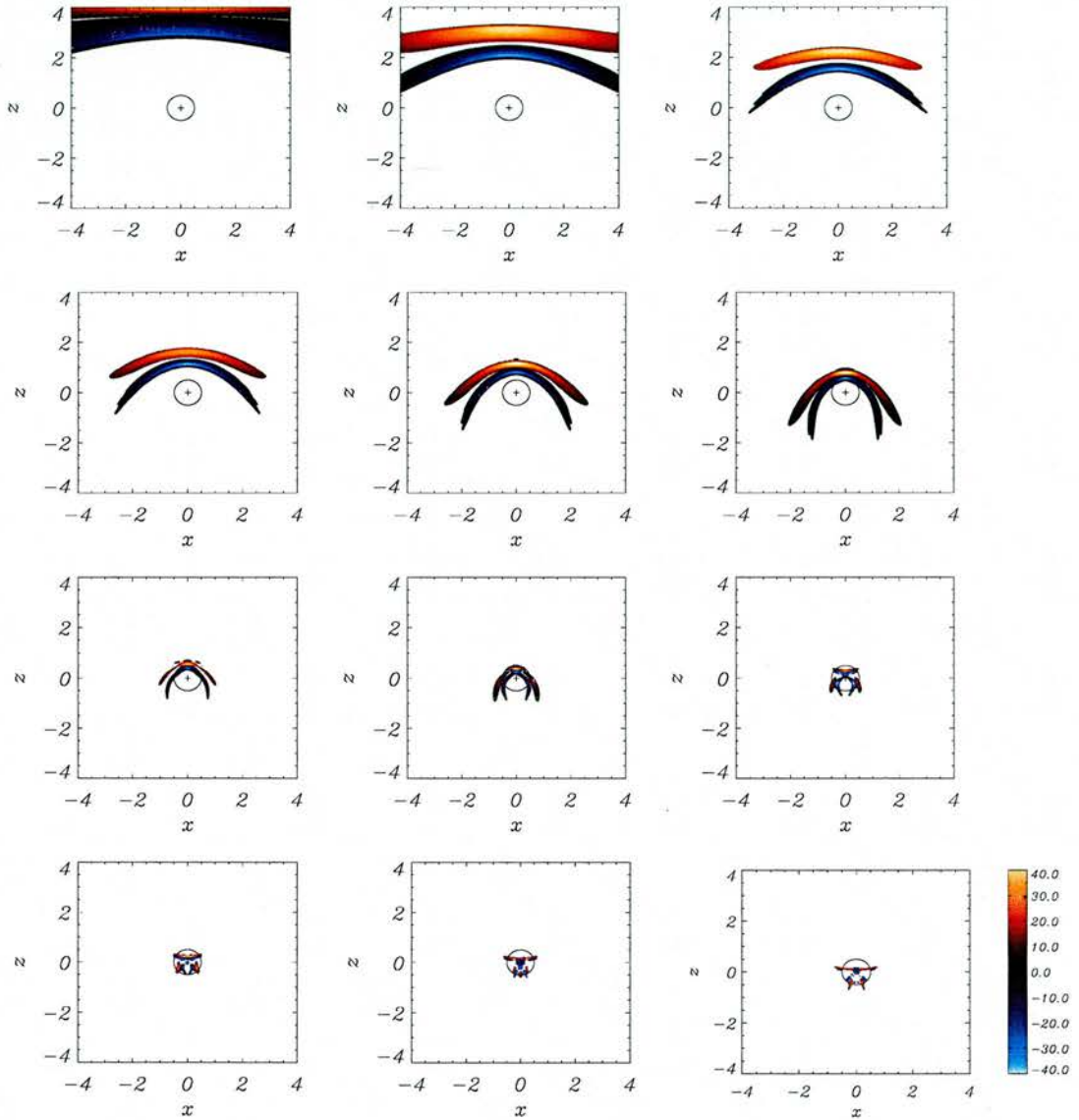


Figure 7.16: Numerical simulation of current for a wave sent in from top boundary for $\beta_0 = 0.25$ and its resultant propagation at times (a) $t=0.33$, (b) $t=0.67$, (c) $t=1.0$, (d) $t=1.33$, (e) $t=1.67$ and (f) $t=2.0$, (g) $t=2.33$, (h) $t=2.67$, (i) $t=3.0$, (j) $t=3.33$, (k) $t=3.67$ and (l) $t=4.0$, labelling from top left to bottom right. As before, the black circle indicates the position of the $c_s^2 = v_A^2$ layer and the cross denotes the null point in the magnetic configuration.

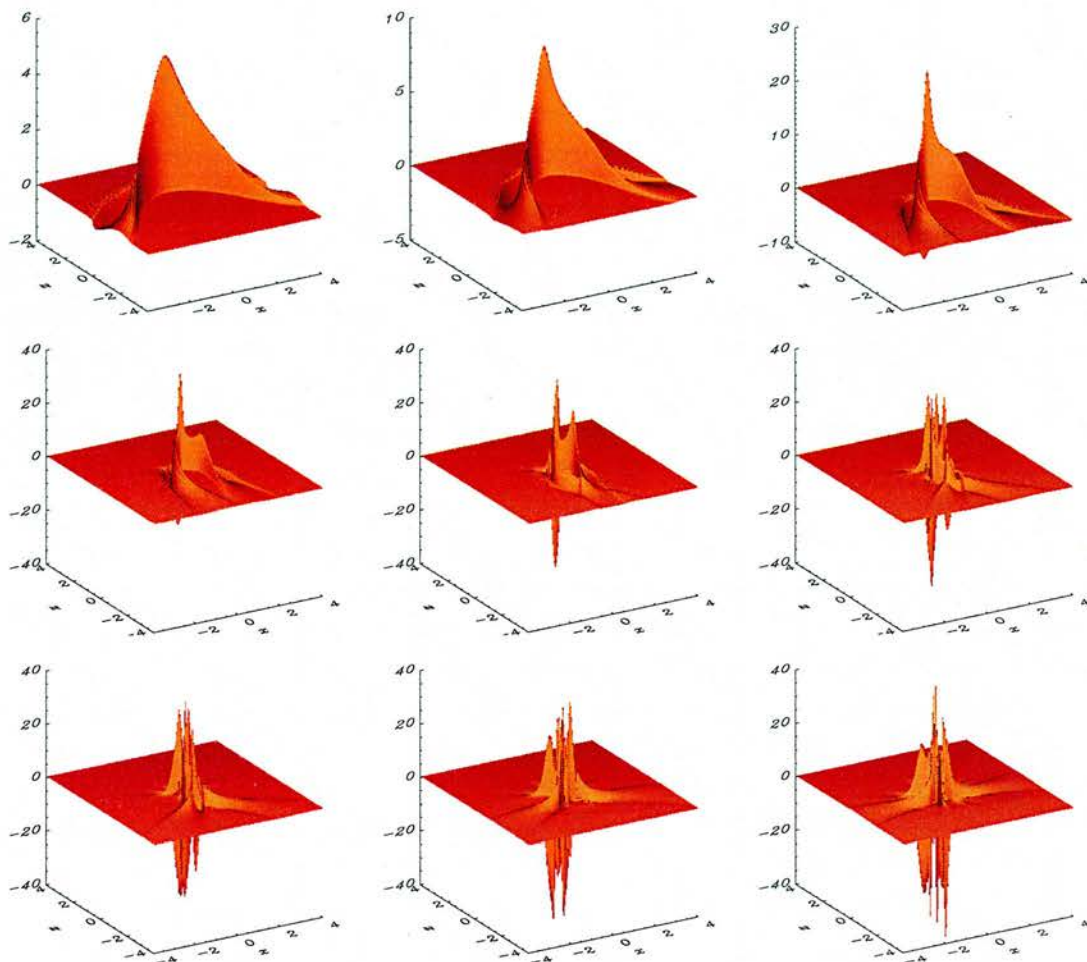


Figure 7.17: Shaded surfaces of $-$ current for a wave sent in from top boundary for $\beta_0 = 0.25$ and its resultant propagation at times (a) $t = 1.33$, (b) $t = 1.67$ and (c) $t = 2.0$, (d) $t = 2.33$, (e) $t = 2.67$, (f) $t = 3.0$, (g) $t = 3.33$, (h) $t = 3.67$ and (i) $t = 4.0$, labelling from top left to bottom right.

Figure 7.17 shows shaded surfaces of the build-up of current at times equal to those of subfigures (d) \dots (l) in Figure 7.16. This Figure can be directly compared to the $\beta = 0$ case (Figure 3.7). We can clearly see there is a different type of current build-up in the $\beta \neq 0$ case, most notably that the exponential build-up seen previously is now gone (at least in the times we are considering).

7.7 Cartesian coordinates ($\beta_0 = 2.25$ system)

In this second set of simulations, we set $\beta_0 = 2.25$. This puts the $c_s^2 = v_A^2$ layer at a larger radius than before (at a radius of $r = \sqrt{\frac{\gamma\beta_0}{2}} = 1.37$ as opposed to $r = 0.456$). All other boundary and initial conditions remain the same (described in equations 7.8). The results can be seen in Figures 7.18, 7.20 and 7.21.

7.7.1 Numerical Simulation : v_\perp ($\beta_0 = 2.25$)

The behaviour of the perpendicular component of the magnetoacoustic wave can be seen in Figure 7.18. We find that the linear, magnetoacoustic wave travels towards the neighbourhood of the null point and begins to wrap around it. We identify this as the low β fast wave (and this propagation has been seen before). However, when the wave passes through the $c_s^2 = v_A^2$ layer, a secondary wave becomes apparent; the high β slow wave. The propagation now proceeds in three ways: Firstly, the generated high β slow wave spreads out along the field lines and accumulates along the separatrices. Secondly, the high β fast wave continues to refract and some of the fast wave (located very close to the null point) *passes through the null*. This is a new effect, not seen in the cold plasma model of Chapter 3! The fast wave can now pass through the null because, although $v_A(x, z) = 0$ at the null, there is now a non-zero sound speed there (and $c_{\text{fast}}^2 = v_A^2 + c_{\text{sound}}^2$). Thus, the high β fast wave has passed (slowly) through the null. This passing causes a large current accumulation near the null. The high β fast wave thus continues downwards and leaves the $c_s^2 = v_A^2$ layer, converting to a low β fast wave and spreading out (since the low β fast wave propagates roughly isotropically).

Since the wave passing through the null is a new effect, it is worth looking more closely. Figure 7.19 shows the perpendicular component of the velocity from when it enters the $c_s^2 = v_A^2$ layer to a little time later. We can see that in this high β region, the low β fast wave splits into two high β waves (a fast wave and a slow wave). By looking at the subfigures, we can following the split in detail.

Thirdly, the rest of the fast wave located away from the null (low β fast wave) is not affected by the non-zero sound speed (as $v_A^2 \gg c_{\text{sound}}^2$) and so continues to refract around the null. In fact, as the wings of the (low β) fast wave wrap around below the null point, they encounter the part of the fast wave that travelled through the null. This results in a complicated interference pattern (both constructive and destructive). However, it appears that the two waves passes through each other without affecting each other; due to the linear nature of the system. A full non-linear treatment of the equations may reveal some very different behaviour.

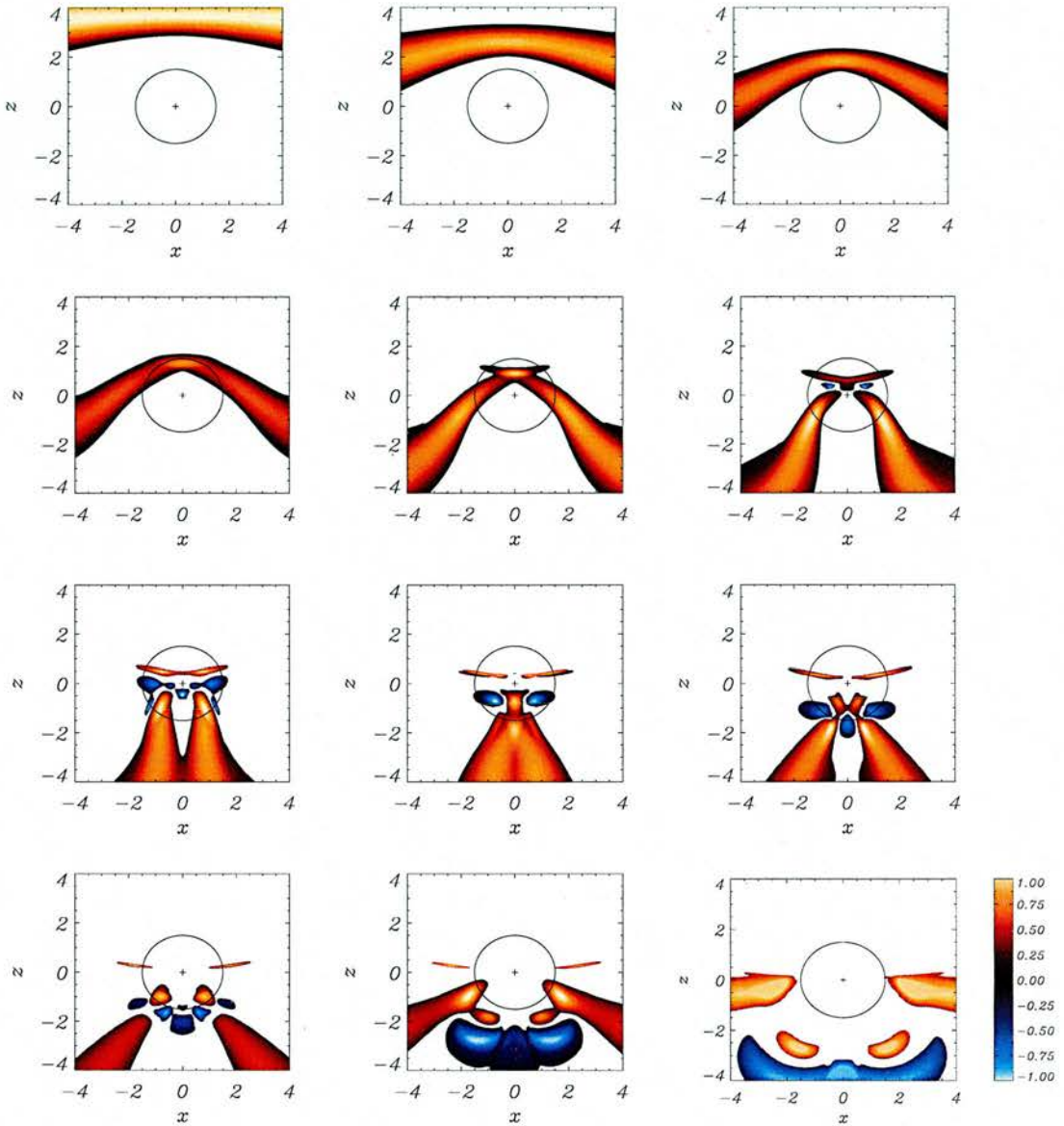


Figure 7.18: Contours of v_{\perp} for numerical simulation for a fast wave sent in from upper boundary for $-4 \leq x \leq 4$ and $\beta_0 = 2.25$ and its resultant propagation at times (a) $t=0.33$, (b) $t=0.67$, (c) $t=1.0$, (d) $t=1.33$, (e) $t=1.67$ and (f) $t=2.0$, (g) $t=2.33$, (h) $t=2.67$, (i) $t=3.0$, (j) $t=3.33$, (k) $t=3.67$ and (l) $t=4.0$, labelling from top left to bottom right. The black circle indicates the position of the $c_s^2 = v_A^2$ layer and the cross denotes the null point in the magnetic configuration.

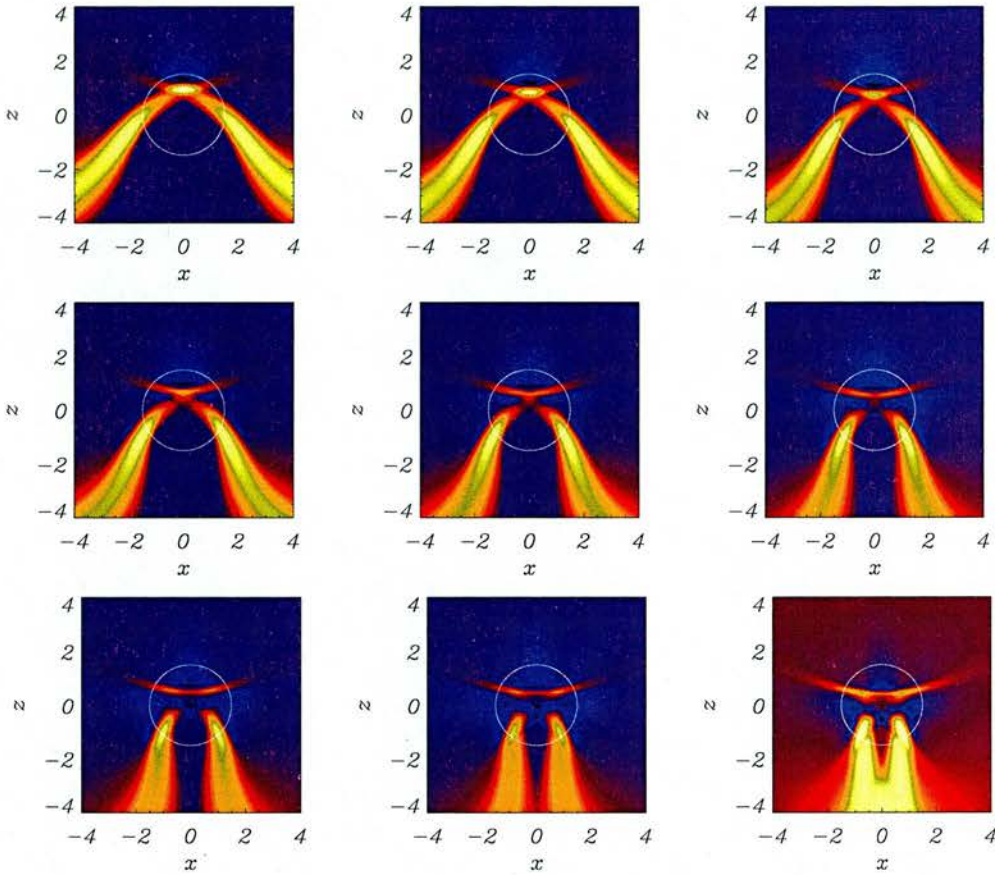


Figure 7.19: Contours of v_{\perp} for numerical simulation for a fast wave sent in from upper boundary for $-4 \leq x \leq 4$ and $\beta_0 = 2.25$ and its resultant propagation at times (a) $t=1.7$, (b) $t=1.8$, (c) $t=1.9$, (d) $t=2.0$, (e) $t=2.1$, (f) $t=2.2$, (g) $t=2.3$, (h) $t=2.4$ and (i) $t=2.5$, labelling from top left to bottom right. The white circle indicates the position of the $c_s^2 = v_A^2$ layer and the cross denotes the null point in the magnetic configuration.

Thus, we have a different behaviour than that seen for the $\beta_0 = 0.25$ case (Figure 7.9). With a large β_0 , the perpendicular component of the velocity has passed through the null (interpreted as a high β fast wave crossing the null), whereas with a small β_0 , we did not see any wave pass through the null. So what is the relationship between the $\beta_0 = 2.25$ and $\beta_0 = 0.25$ cases; are they not just scaled versions of each other?

The part of the fast wave that goes through the null effectively escapes the refraction effect of the null point. It seems as if the smaller the value of β_0 used, the slower the high β fast wave can cross the null. This can be understood since the high β fast wave travels close to the sound speed, which is related to β_0 . Recall the definition of the sound speed in equation (1.24) and the definition of β_0 in Section 7.3:

$$c_s = \sqrt{\frac{\gamma p_0}{\rho_0}}, \quad \beta_0 = \frac{2\mu p_0}{B_0^2} \Rightarrow c_s = \sqrt{\frac{\gamma B_0^2}{2\mu\rho_0}}\beta_0 = \sqrt{\frac{\gamma\beta_0}{2}} \quad (7.9)$$

where we have cancelled a factor of $\sqrt{\frac{B_0^2}{\mu\rho_0}} = \bar{v}$ to non-dimensionalise c_s ($c_s = \bar{v}c_s^*$).

This provides the link between the $\beta_0 = 2.25$ and $\beta_0 = 0.25$ cases; we suspect that in the $\beta_0 = 0.25$ case, the high β fast wave *can* pass through the null, but it travels at such a slow speed (as c_s goes like $\sqrt{\beta_0}$) that the refraction effect dominates. Thus, as the $c_s^2 = v_A^2$ layer gets closer to the null, less and less of the fast wave can pass through the null in a given time, and the parts that can travel through do so at a smaller and smaller speed. Also, these parts that pass through can be swamped by the wings of the rest of the wave wrapping round below the null (repeatedly).

This explains the relationship between our $\beta_0 = 0.25$ and 2.25 investigations. These experiments do not simply show scaled versions of each other, they show two competing phenomena; a *refraction* effect caused by the varying Alfvén speed and a non-zero sound speed at the null which allows the fast wave to pass through, and it is the value of β_0 that dictates which effect dominates. This will be discussed further in Section 7.9.

The two extremes occur as $\beta_0 \rightarrow 0$; in which case the refraction effect infinitely dominates over the other effects (and we recover the results of Chapter 3) or as $\beta_0 \rightarrow \infty$ and the system becomes hydrodynamic. In this case, the fast wave reduces to an acoustic wave and so completely passes through the null (in effect it does not even see the magnetic field, since $v_A^2 \ll c_s^2$).

7.7.2 Numerical Simulation : v_{\parallel} ($\beta_0 = 2.25$)

Figure 7.20 shows the numerical simulation of the parallel component for the wave. Again we have an asymmetric nature to the wave. Here, the wave consists of two parts. Firstly, there is a fast wave part that travels across the separatrix and down and out of the system; we identify this as the high β fast wave in the perpendicular velocity showing up in the parallel component. Secondly, there is a slow wave part that spreads out along the fieldlines and accumulates along the separatrices; we identify this as the high β slow, again from from the perpendicular velocity.

It is also interesting to note that the amplitude of these waves is comparable to the waves in Figure 7.18, which was not the case in the $\beta_0 = 0.25$ experiment. The large value of β_0 means that the parallel velocity has a (noticeable) feedback effect on the perpendicular velocity. It is also interesting that we can see similarities between Figures 7.13 and 7.20, both have very similar behaviour before reaching the $c_s^2 = v_A^2$ layer and both exhibit a lobe like structure (seen in the radial case in Figure 7.6). However, at a later time the two figures are different; the $\beta_0 = 0.25$ parallel wave is focussed at the null, with some slow wave evident, whereas the $\beta_0 = 2.25$ parallel wave has completely split between a slow wave part and a part moving out of the box.

7.7.3 Current ($\beta_0 = 2.25$)

Again, we have a changing perturbed magnetic field whose gradients are increasing in time and so we have a build up of current density. Figure 7.21 shows the buildup of current density as time increases. We see that in this case, it is the thinning of the slow wave aspects of the waves that contribute most to the current accumulation. Thus, we have a large current accumulation along the separatrices, just as for the Alfvén wave (Chapter 4). The high β fast wave aspects also lead to current accumulation, but less so than the slow wave parts (since the fast wave parts are either still refracting around or have passed through the null and are spreading out, they are not really accumulating in a specified location).

Note that in the final few subfigures of Figure 7.21, we begin to run out of numerical resolution. Also note that the current build-up is less so than before, i.e. it reaches a maximum of about 20 units (as opposed to the $\beta_0 = 0.25$ case, Figure 7.16, which got to about 40 units). This is probably because some of the wave has escaped the refraction effect (when the high β fast wave passed through the null) and so some of the wave energy has left the area near the null.

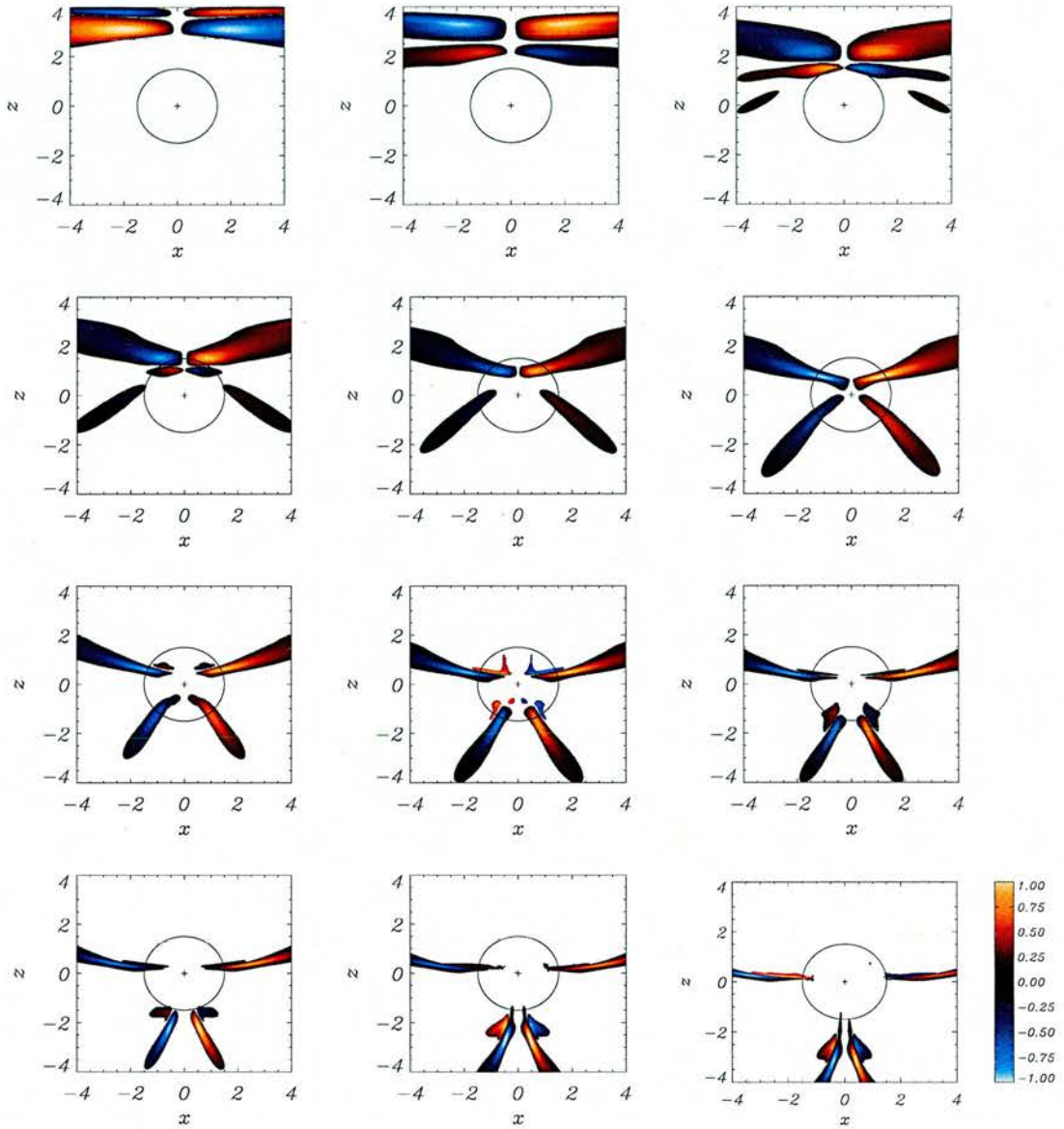


Figure 7.20: Contours of v_{\parallel} for numerical simulation for a fast wave sent in from upper boundary for $-4 \leq x \leq 4$ and $\beta_0 = 2.25$ and its resultant propagation at times (a) $t=0.33$, (b) $t=0.67$, (c) $t=1.0$, (d) $t=1.33$, (e) $t=1.67$ and (f) $t=2.0$, (g) $t=2.33$, (h) $t=2.67$, (i) $t=3.0$, (j) $t=3.33$, (k) $t=3.67$ and (l) $t=4.0$, labelling from top left to bottom right. The black circle indicates the position of the $c_s^2 = v_A^2$ layer. The cross denotes the null point in the magnetic configuration.

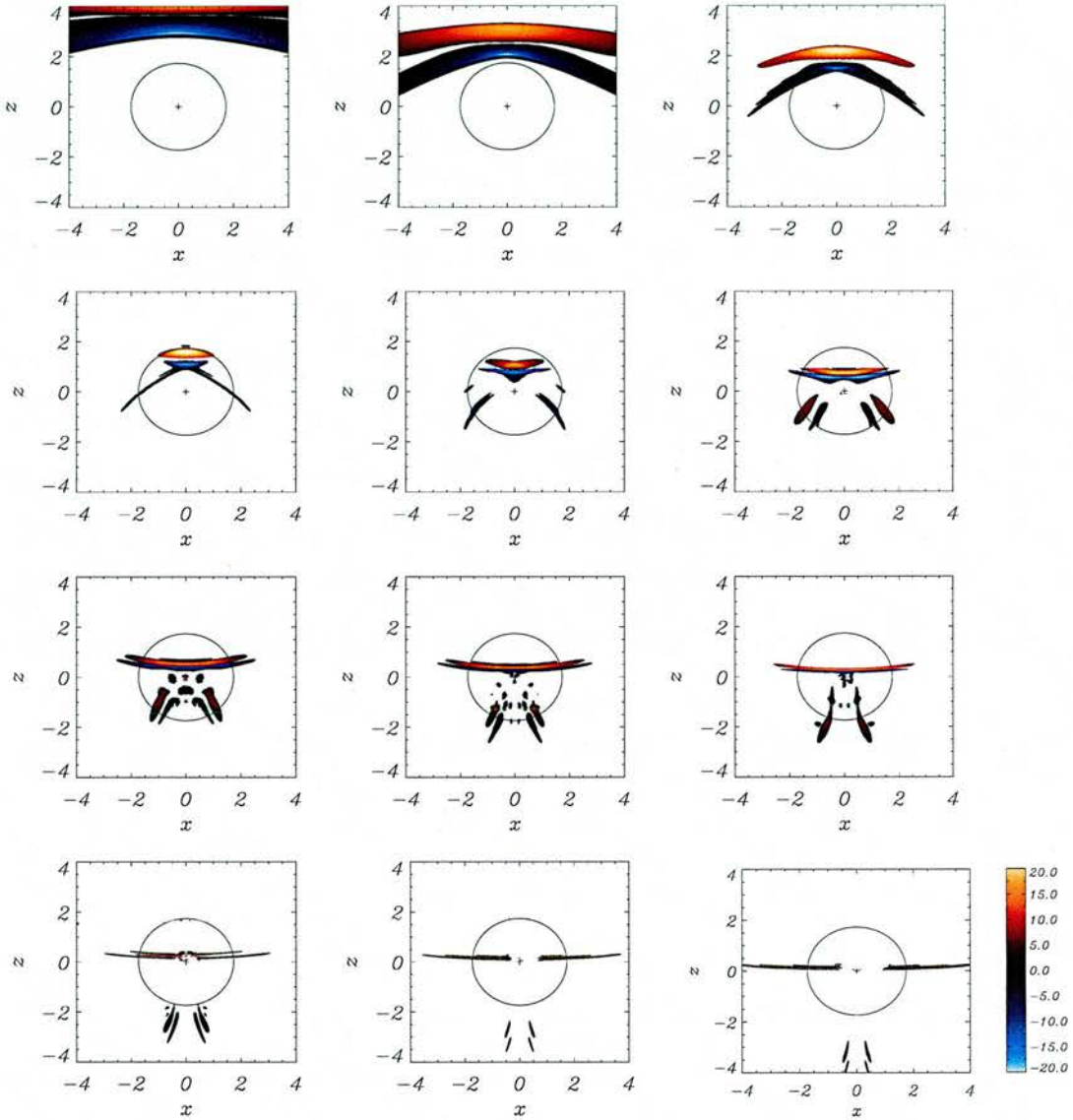


Figure 7.21: Numerical simulation of current for a wave sent in from top boundary for $\beta_0 = 2.25$ and its resultant propagation at times (a) $t=0.33$, (b) $t=0.67$, (c) $t=1.0$, (d) $t=1.33$, (e) $t=1.67$ and (f) $t=2.0$, (g) $t=2.33$, (h) $t=2.67$, (i) $t=3.0$, (j) $t=3.33$, (k) $t=3.67$ and (l) $t=4.0$, labelling from top left to bottom right. The black circle indicates the position of the $c_s^2 = v_A^2$ layer. The cross denotes the null point in the magnetic configuration.

7.8 Analytical work : WKB approximation

We can approximately solve our equations to gain more insight into the numerical simulations. By combining equations (1.14), (1.15) and (1.17), we can form:

$$\frac{\partial^2 \mathbf{v}}{\partial t^2} = \frac{\gamma p_0}{\rho_0} \nabla (\nabla \cdot \mathbf{v}) + \{ \nabla \times [\nabla \times (\mathbf{v} \times \mathbf{B}_0)] \} \times \frac{\mathbf{B}_0}{\mu \rho_0} \quad (7.10)$$

We substitute $\mathbf{v} = \mathbf{a} e^{i\phi(x,z)} \cdot e^{-i\omega t}$ into (7.10) where \mathbf{a} is a constant. We now take the dot product with \mathbf{B}_0 and $\nabla \phi$ to get the two velocity components. This gives:

$$\begin{aligned} \omega^2 (\mathbf{v} \cdot \mathbf{B}_0) - \frac{\gamma p_0}{\rho_0} (\mathbf{B}_0 \cdot \nabla \phi) (\mathbf{v} \cdot \nabla \phi) &= 0 \\ \left[\omega^2 - \left(\frac{\gamma p_0}{\rho_0} + \mathbf{B}_0 \cdot \mathbf{B}_0 \right) (\nabla \phi \cdot \nabla \phi) \right] (\mathbf{v} \cdot \nabla \phi) + (\mathbf{B}_0 \cdot \nabla \phi) (\nabla \phi \cdot \nabla \phi) (\mathbf{v} \cdot \mathbf{B}_0) &= 0 \end{aligned}$$

This can be written as:

$$\begin{bmatrix} \omega^2 & -\frac{\gamma p_0}{\rho_0} (\mathbf{B}_0 \cdot \nabla \phi) \\ (\mathbf{B}_0 \cdot \nabla \phi) |\nabla \phi|^2 & \omega^2 - \left(\frac{\gamma p_0}{\rho_0} + |\mathbf{B}_0|^2 \right) |\nabla \phi|^2 \end{bmatrix} \begin{pmatrix} \mathbf{v} \cdot \mathbf{B}_0 \\ \mathbf{v} \cdot \nabla \phi \end{pmatrix} = \begin{pmatrix} 0 \\ 0 \end{pmatrix}$$

These two coupled equations must have determinant zero so as not to have trivial solution, and so by taking the determinant we obtain:

$$\omega^2 \left[\omega^2 - |\nabla \phi|^2 \left(\frac{\gamma p_0}{\rho_0} + |\mathbf{B}_0|^2 \right) \right] + \frac{\gamma p_0}{\rho_0} (\mathbf{B}_0 \cdot \nabla \phi)^2 |\nabla \phi|^2 = 0$$

This equation is reminiscent of equation (1.40) for magnetoacoustic waves, especially if we view terms like $|\mathbf{B}_0|^2$ as an Alfvén speed and $\frac{\gamma p_0}{\rho_0}$ as a sound speed. Note that $c_s^2 = \frac{\gamma p_0}{\rho_0}$ and thus with our definition of β_0 leads to $\frac{\gamma p_0}{\rho_0} = c_s^2 = \frac{\gamma \beta_0}{2}$. Substituting our magnetic field into this equation gives:

$$\begin{aligned} \omega^4 - \omega^2 \left(\frac{\gamma \beta_0}{2} + x^2 + z^2 \right) \left[\left(\frac{\partial \phi}{\partial x} \right)^2 + \left(\frac{\partial \phi}{\partial z} \right)^2 \right] \\ + \frac{\gamma \beta_0}{2} \left[\left(\frac{\partial \phi}{\partial x} \right)^2 + \left(\frac{\partial \phi}{\partial z} \right)^2 \right] \left(x \frac{\partial \phi}{\partial x} - z \frac{\partial \phi}{\partial z} \right)^2 = 0 \end{aligned}$$

Now we make the WKB approximation such that $\omega \sim \phi \gg 1$. This leads to a first order equation of the form:

$$\begin{aligned} \omega^4 - \omega^2 \left(\frac{\gamma \beta_0}{2} + x^2 + z^2 \right) (p^2 + q^2) + \frac{\gamma \beta_0}{2} (p^2 + q^2) (xp - zq)^2 = 0 \\ \Rightarrow \mathcal{F}(x, z, \phi, p, q) = 0 = \frac{1}{2} \left[\omega^4 - \omega^2 \left(\frac{\gamma \beta_0}{2} + x^2 + z^2 \right) (p^2 + q^2) + \frac{\gamma \beta_0}{2} (p^2 + q^2) (xp - zq)^2 \right] \end{aligned}$$

where $p = \frac{\partial \phi}{\partial x}$ and $q = \frac{\partial \phi}{\partial z}$ and \mathcal{F} is a non-linear PDE (we include a half in the form of \mathcal{F} to make the equations nicer later).

Note that if we write $v_A^2 = x^2 + z^2$ and $c_s^2 = \frac{\gamma \beta_0}{2}$, then $\mathcal{F} = 0$ gives us:

$$2\omega^2 = (c_s^2 + v_A^2) (p^2 + q^2) \pm \sqrt{(p^2 + q^2)^2 (c_s^2 + v_A^2)^2 - 4 c_s^2 (p^2 + q^2) (xp - zq)^2} \quad (7.11)$$

Note that the discriminant vanishes for $c_s^2 = v_A^2$. This equation contains information about two wave types (as hinted by its similarity to equation 1.40). The method to solve this equation is to assume it to be of the form $(\omega^2 - \omega_{\text{slow}}^2)(\omega^2 - \omega_{\text{fast}}^2) = 0$. Considering the fast wave (so $\omega^2 \neq \omega_{\text{slow}}^2$), we can apply the method described in Section 2.4.4 to $\omega^2 - \omega_{\text{fast}}^2 = 0$. Then Charpit's relations (equations 2.24 – 2.28) give:

$$\begin{aligned} \frac{d\phi}{ds} &= 2\omega^2 \\ \frac{dp}{ds} &= -(p^2 + q^2)x - \frac{[(c_s^2 + x^2 + z^2) (p^2 + q^2)^2 x - 2p(p^2 + q^2)(xp - zq)c_s^2]}{\sqrt{(p^2 + q^2)^2 (c_s^2 + x^2 + z^2)^2 - 4(p^2 + q^2)(xp - zq)^2 c_s^2}} \\ \frac{dq}{ds} &= -(p^2 + q^2)z - \frac{[(c_s^2 + x^2 + z^2) (p^2 + q^2)^2 z + 2q(p^2 + q^2)(xp - zq)c_s^2]}{\sqrt{(p^2 + q^2)^2 (c_s^2 + x^2 + z^2)^2 - 4(p^2 + q^2)(xp - zq)^2 c_s^2}} \\ \frac{dx}{ds} &= [c_s^2 + x^2 + z^2] p \\ &+ \frac{[(p^2 + q^2) (c_s^2 + x^2 + z^2)^2 p - 2p(xp - zq)^2 c_s^2 - 2c_s^2 x(p^2 + q^2)(xp - zq)]}{\sqrt{(p^2 + q^2)^2 (c_s^2 + x^2 + z^2)^2 - 4(p^2 + q^2)(xp - zq)^2 c_s^2}} \\ \frac{dz}{ds} &= [c_s^2 + x^2 + z^2] q \\ &+ \frac{[(p^2 + q^2) (c_s^2 + x^2 + z^2)^2 q - 2q(xp - zq)^2 c_s^2 + 2c_s^2 z(p^2 + q^2)(xp - zq)]}{\sqrt{(p^2 + q^2)^2 (c_s^2 + x^2 + z^2)^2 - 4(p^2 + q^2)(xp - zq)^2 c_s^2}} \end{aligned}$$

where ω is the frequency of our wave and s is some parameter along the characteristic and $c_s^2 = \frac{\gamma \beta_0}{2}$.

These five ODEs were solved numerically using our fourth-order Runge-Kutta method. Contours of constant ϕ can be thought of as defining the positions of the edges of the wave pulse, i.e. with correct choices of s , the WKB solution represents the front, middle and back edges of the wave. $s = \omega t$ and so the numerical and analytical work can be directly compared.

Our analytical solution gives extra insight into the nature of the finite β system. In Figure 7.22, we look at the solution to $\omega^2 - \omega_{\text{fast}}^2 = 0$. We compare this to the behaviour of the perpendicular wave seen in Section 7.7.1.

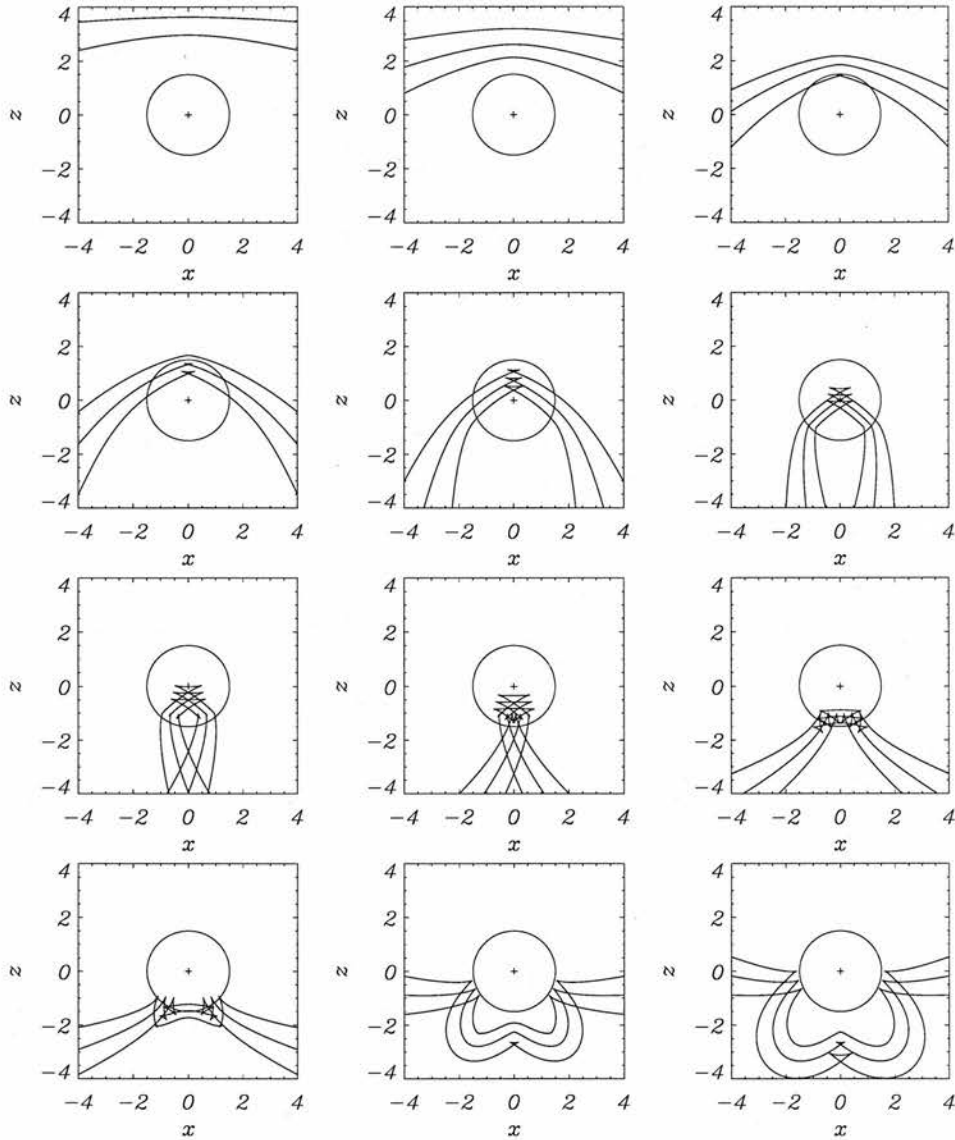


Figure 7.22: Plots of WKB solution for a wave sent in from the upper boundary and its resultant positions at times (a) $t=0.33$, (b) $t=0.67$, (c) $t=1.0$, (d) $t=1.33$, (e) $t=1.67$ and (f) $t=2.0$, (g) $t=2.33$, (h) $t=2.67$, (i) $t=3.0$, (j) $t=3.33$, (k) $t=3.67$ and (l) $t=4.0$, labelling from top left to bottom right. The lines represent the front, middle and back edges of the wave. The black circle indicates the position of the $c_s^2 = v_A^2$ layer and the cross denotes the null point in the magnetic configuration.

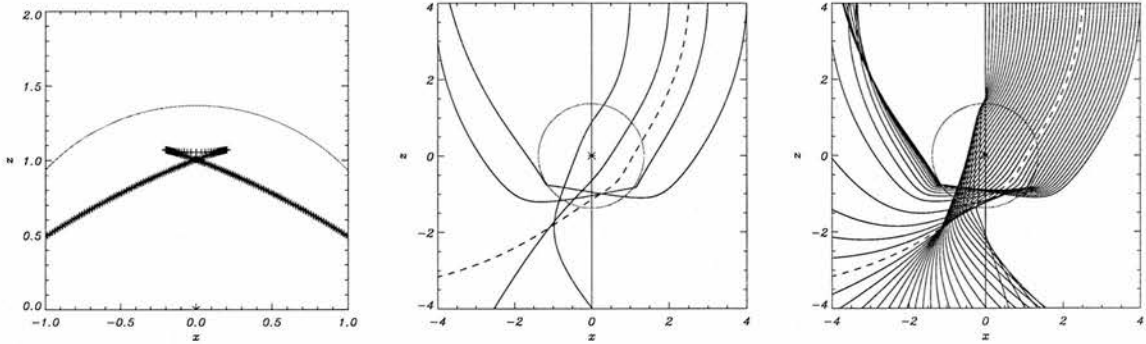


Figure 7.23: Graphs showing various aspects of the analytical WKB approximation. *Left* shows blow-up of wavefront at time $t = 0.65$. *Center* shows rays for WKB solution for a wave sent in from the upper boundary for starting points of $x = 0, 1, 2, 2.5, 3$ and 4 along $z = 4$. *Right* shows same rays but for $x \in [0, 4]$ at intervals of 0.1 . The green circle indicates the position of the $c_s^2 = v_A^2$ layer and the star denotes the null point.

We see that the agreement between the numerical simulation and the analytical approximation is quite good. In Figure 7.22, we see the main features of the numerical simulation; the wave refracts as it approaches the null and that part of the wave passes through the null (at a slower speed than the 'wings' outside the $c_s^2 = v_A^2$ layer). This central part (that passed through the null) then emerges from the $c_s^2 = v_A^2$ layer and expands out isotropically. Meanwhile, the wings continue to refract around the null.

There are also other features; as the wave crosses the $c_s^2 = v_A^2$ layer, the wavefront overlaps with itself (forming small triangular shapes, see Figure 7.23); this may explain why we see the perpendicular wave form a sharp edge as it crosses the $c_s^2 = v_A^2$ layer in Figure 7.18. Also, as mentioned above, we see that the central part travels at a much slower speed than the wings, and that this central part then emerges from the $c_s^2 = v_A^2$ layer and expands out isotropically. Later still, this part overlaps itself; this may explain the wedge-like structures seen in the expanding low β fast wave in the last subfigure of Figure 7.18 (around $(x, z) = (0, -4)$).

The rays of the WKB solution can be seen in Figure 7.23. The left graph shows the small triangular shape formed as the wavefront overlaps with itself when it crosses the $c_s^2 = v_A^2$ layer. This subfigure shows that this is a true structure and not just a discontinuity in the wavefront (i.e. since it can be resolved). The central graph shows the rays for starting points of $x = 1, 2, 2.5, 3$ and 4 along $z = 4$. We see that for a starting point of $x = 3$ and $x = 4$ ($z = 4$), the particle is deflected substantially by the null point, whereas the deflection is less severe for 2 and 1 . A starting point of $x = 2.5$ seems to be the critical starting point that determines if $\frac{dz}{ds}$ changes sign (at least in the range $-4 \leq x \leq 4$). We also see that $x = 0$ is not deflected at all. The right hand graph shows the rays for for $x \in [0, 4]$ in intervals of 0.1 . The dashed line represents $x = 2.5$; for $x > 2.5$, the particle path is deflected so much that $\frac{dz}{ds}$ changes sign. For $x < 2.5$, the rays are deflected but escape from the opposite corner of the system. This nature reflects the numerical solution; part of the wave passes through the null and part refracts around it.

However, the analytical WKB approximation does not give a full description of the numerical simulation. Firstly, though the WKB solution is in good agreement with the numerical simulation, the positions of the waves in the two do not exactly agree. This may be due to the difference between the side and bottom boundary conditions between the two, or due to the fact that the WKB approximation is only valid for a harmonic wavetrain with $\omega \gg 1$.

Secondly, it is difficult to glean information on the coupling between the two wave types. The WKB approximations only give solutions of the form:

$$\begin{aligned} \mathbf{v} \cdot \mathbf{B}_0 &= Av_{\perp} + Bv_{\parallel} \\ \mathbf{v} \cdot \nabla \phi &= Cv_{\perp} + Dv_{\parallel} \end{aligned}$$

where A, B, C and D are unknown functions.

Thirdly, the analytical work does not include resistivity in its equations. Finally, the WKB approximation can also be applied to the $\omega^2 - \omega_{\text{slow}}^2 = 0$ equation but this does not yield any particularly enlightening results.

7.9 Conclusions

This chapter extends the investigations of Chapter 3 into the nature of magnetoacoustic waves in the neighbourhood of a null point. We have conducted two experiments, varying the choice of β_0 in each, where the choice dictated the location of the $c_s^2 = v_A^2$ layer.

In the first experiment (Section 7.6), we set $\beta_0 = 0.25$. We find that the linear magnetoacoustic wave travels towards the neighbourhood of the null point and begins to wrap around it. This occurs due to the spatially varying Alfvén speed, $v_A^2(x, z) = x^2 + z^2$, and has been observed before (McLaughlin & Hood 2004; Nakariakov & Roberts 1995). In this experiment, we drove a wave pulse in the perpendicular velocity coordinate and we identified this pulse as a low β fast wave. However, once the wave reaches and crosses the $c_s^2 = v_A^2$ layer, part of the wave is transformed into a high β slow wave. This slow wave part spreads out along the fieldlines. Meanwhile, the rest of the (low β) fast wave continues to wrap around the origin. This refraction effect continues again and again, but each time part of the fast wave is converted to a slow wave as it crosses the $c_s^2 = v_A^2$ layer. The majority of the current build-up occurs very close to the null.

In our second set of simulations (Section 7.7), we set $\beta_0 = 2.25$, thus placing the $c_s^2 = v_A^2$ layer at a larger radius than before (since in this magnetic geometry, the $c_s^2 = v_A^2$ layer occurs at a radius $r = \sqrt{\frac{\gamma\beta_0}{2}}$). In this experiment, we find that the magnetoacoustic wave travels towards the neighbourhood of the null point and begins to wrap around it (as before). However, when the wave crosses the $c_s^2 = v_A^2$ layer, a secondary wave (high β slow wave) becomes apparent. The propagation now proceeds in three ways. Firstly, the generated slow wave spreads out along the fieldlines and accumulates along the separatrixes. Secondly, the remaining part of the fast wave inside the $c_s^2 = v_A^2$ layer continues to refract and some of it (located close to the null point) *passes through the origin*. We identify this part as a high β fast wave. The high β fast wave can pass through the origin because, although $v_A(0, 0) = 0$, there is now a non-zero sound speed there (and $c_{\text{fast}}^2 = v_A^2 + c_{\text{sound}}^2$). This passing causes a large current accumulation near the origin. After it has crossed the null, the high β fast wave continues downwards and leaves the $c_s^2 = v_A^2$ layer. As it emerges, it becomes a low β fast wave and spreads out (since the low β fast wave propagates almost isotropically). Finally, the fast wave located away from the null and $c_s^2 = v_A^2$ layer (the ‘wings’ of the low β wave) are not affected by the non-zero sound speed (as $v_A^2 \gg c_{\text{sound}}^2$) and so for them the refraction effect dominates. In fact, as these wings wrap around below the null point, they encounter the high β fast wave as it is emerging from the $c_s^2 = v_A^2$ layer. This results in a complicated interference pattern, but it appears that the two waves pass through each other without any lasting effect on each other (due to the linear nature of the system). A full non-linear treatment of the equation may reveal some very different behaviour. The $\beta_0 = 2.25$ numerical simulations also showed good agreement with an analytical WKB approximation. The WKB approximation also gave some other insights into the fast wave behaviour.

From the work in this chapter, it has been seen that extending the model from a cold to a warm plasma introduces many new effects, most noticeably the introduction of fast *and* slow waves to the system. It also appears that the choice of β_0 is of critical importance, since the two experiments yield different results. However, the key choice here is not in picking β_0 , since this just determines where the $c_s^2 = v_A^2$ layer will occur. The choice of β_0 is equivalent to choosing where to set the boundaries of our box, and so the critical parameter in our system is in choosing *the distance between the initial disturbance and the $c_s^2 = v_A^2$ layer*. This is because these experiments do not simply show scaled versions of each other, they show two competing phenomena; a *refraction* effect caused by the varying Alfvén speed, and a non-zero sound speed at the null which allows the fast wave to pass through.

If the $c_s^2 = v_A^2$ layer is close to the null (small choice of β_0 and hence there is not much coupling to the parallel velocity and pressure terms) then the refraction effect will dominate, resulting in a scenario similar to $\beta_0 = 0.25$ and heating will occur close to the null point. The extreme case occurs as $\beta_0 \rightarrow 0$, in which case the refraction effect infinitely dominates over the other effects and we recover the results of Chapter 3.

However, if the $c_s^2 = v_A^2$ layer is far from the null, a portion of the fast wave will be able to pass through the origin and escape the system (i.e. will not deposit its energy near the null point). In this case, the remaining wave energy is dissipated along the separatrices (due to the high β slow wave). So heating will occur in both systems, although the nature will be different. This highlights the importance of understanding the topology in the system.

This is all very interesting for its mathematical sake, but how does the competition of these two effects manifest itself in the corona? As mentioned in Chapter 1, the plasma β parameter is defined as the ratio of the thermal plasma pressure to the magnetic pressure (equation 1.12). In most parts of the corona, $\beta \ll 1$ and hence the pressure gradients in the plasma can be neglected. Values of $\beta = 0.01$ are often quoted (e.g. Priest 1982). However, near null points the plasma β can become very large, so the (true) plasma β varies through the whole region. However as seen above, it is the distance between the initial (planar) pulse and the $c_s^2 = v_A^2$ layer that is of critical importance. We believe that in the corona disturbances that occur will propagate for some time before they encounter a (coronal) null point. Hence, the fast wave part of the disturbance will feel the refraction effect of the null and begin to refract around it. By the time the $c_s^2 = v_A^2$ layer is reached or the sound speed becomes important, the fast wave disturbance will be (almost) circular in nature and will have thinned and dissipation will be extracting the energy from the wave. It is true that some of the wave may pass through the null or be converted into high β slow waves, but the resultant effect will be that all the wave energy will accumulate close to the null and hence we will have large current accumulation and heating there.

Chapter 8

Phase mixing of Alfvén waves near a 2D null point

8.1 Introduction

As mentioned at the start of Chapter 2, recent observations of the solar corona have clearly demonstrated the existence of wave activity. The fact that the three basic waves modes exist, namely Alfvén waves and fast and slow magnetoacoustic waves, is no longer in doubt but the surprising fact is that these are generally rapidly damped. Waves in a uniform magnetic field and plasma have extremely long damping lengths and so the explanation of the observations must lie in the non-uniform nature of the solar corona.

This chapter is concerned with the dissipation of Alfvén waves. One of the most efficient damping mechanism to date is called **phase mixing** and is described by Heyvaerts and Priest (1983) for a harmonic wave train propagating in a uniform vertical magnetic field. They found that the amplitudes decay as the negative exponential depending on the third power of the height and linearly with magnetic resistivity, η . Thus, the damping length depends on $\eta^{-1/3}$. Since observations rarely show more than a few periods at a time, Hood *et al* (2002) investigated the propagation of single pulses and found that the decay was now algebraic in nature but still depended on $\eta^{-1/3}$.

The idea of the mechanism of phase mixing is simple to explain; when the plasma has a density gradient perpendicular to the magnetic field, the Alfvén speed is a function of the transverse coordinate. Thus, the Alfvén waves propagate on each field line with their own local Alfvén speed. After a certain time, the Alfvén wave perturbations on neighbouring field lines become out of phase (Botha *et al.* 2000). It is precisely the Alfvén perturbations oscillating independently from their neighbours that leads to the build up of small length scales and consequently current

generation (and hence dissipation).

In this chapter, we will investigate the behaviour of the linear Alfvén wave in the neighbourhood of a simple 2D X-point geometry, as we did in Chapter 4. However, we shall now consider the behaviour in a non-uniform density plasma. This lifts one of the restrictions imposed back in Chapter 4 (i.e. that $\rho_0 = 1$). This chapter only considers the Alfvén wave. The simplest way to add a non-uniform density profile in our equations is to consider $\rho = \rho(A_0)$, where $\mathbf{A} = (0, A_0, 0) = \nabla \times \mathbf{B}$ is the flux function and A_0 is its y -coordinate. Thus, since ∇A_0 is perpendicular to \mathbf{B}_0 , we have a density gradient perpendicular to the magnetic field. Hence, the Alfvén speed is changing from field line to field line, and thus we may have phase mixing. This is the key question that this chapter addresses; with the addition of a non-uniform density, does the current build-up still occur at the separatrix or does phase mixing now allow the energy to be extracted from a different location?

8.2 Basic Equations

As in Chapter 4, the basic magnetic field structure considered here is a simple 2D X-type neutral point. This simple geometry decouples the fast and Alfvén modes and hence we can investigate their behaviour in depth separately, since $\frac{\partial}{\partial y} = 0$. We again take the magnetic field of equation (3.1), namely:

$$\mathbf{B}_0 = \frac{B_0}{L} (x, 0, -z),$$

where B_0 is a characteristic field strength and L is the length scale for magnetic field variations. Again, this particular choice of magnetic field is only valid in the neighbourhood of the null point located at $x = 0, z = 0$. We can also write $\mathbf{B}_0 = \nabla \times \mathbf{A}$ where $\mathbf{A} = (0, A_0, 0)$ is the flux function. Here, $A_0 = -xz$.

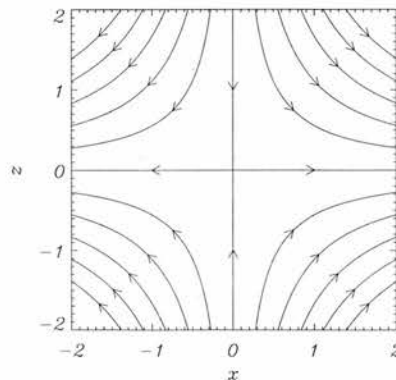


Figure 8.1: Our choice of equilibrium magnetic field.

As before, we use the linearised MHD equations, to study the nature of wave propagation near the X-point. The equations relevant to studying the Alfvén wave are equations (2.12) and (2.13). Defining $\mathbf{B}_0 = (B_x, 0, B_z)$ and $\mathbf{b} = (0, b_y, 0)$ yields:

$$\begin{aligned} \rho_0 \frac{\partial v_y}{\partial t} &= (\mathbf{B}_0 \cdot \nabla) b_y = \left(B_x \frac{\partial}{\partial x} + B_z \frac{\partial}{\partial z} \right) b_y, \\ \frac{\partial b_y}{\partial t} &= (\mathbf{B}_0 \cdot \nabla) v_y + \frac{1}{R_m} \nabla^2 b_y \\ &= \left(B_x \frac{\partial}{\partial x} + B_z \frac{\partial}{\partial z} \right) v_y + \frac{1}{R_m} \left(\frac{\partial^2}{\partial x^2} + \frac{\partial^2}{\partial z^2} \right) b_y, \end{aligned} \quad (8.1)$$

where as defined by equation (2.1), v_y is the velocity out of the plane that \mathbf{B}_0 defines. Hence, waves with this velocity will be transverse waves (energy flow perpendicular to the wavevector).

We will again neglect the magnetic resistivity (η) in our investigations, but will discuss its role in the conclusions. Thus, we consider an ideal plasma ($\eta = 0$ or $R_m \rightarrow \infty$). Since $\rho_0 = \rho_0(\mathbf{x})$, this allows us to write the above equations as:

$$\rho_0 \frac{\partial^2 v_y}{\partial t^2} = (\mathbf{B}_0 \cdot \nabla)^2 v_y, = \left(B_x \frac{\partial}{\partial x} + B_z \frac{\partial}{\partial z} \right)^2 v_y. \quad (8.2)$$

We will now vary the background plasma density. As mentioned above, the simplest variation for ρ is to assume that it is constant along a field line but that it can vary from line to line. Hence, the density is a function of A_0 , namely

$$\rho_0 = \rho_0(A_0) = \rho_0(xz), \quad (8.3)$$

where $A_0 = -xz$. Thus equation (8.2) can be written as:

$$\frac{\partial^2 v_y}{\partial t^2} = \frac{1}{\rho_0(xz)} \left(x \frac{\partial}{\partial x} - z \frac{\partial}{\partial z} \right)^2 v_y. \quad (8.4)$$

This is the primary equation we will be looking at for the Alfvén wave in this chapter. In its derivation, we have assumed linearised behaviour in an ideal 2D plasma. This is the wave equation of the form of equation (1.23), where $\frac{1}{\rho_0}$ is related to the speed. If we define $V_{A0}(xz) = \frac{1}{\sqrt{\rho_0(xz)}}$, then our equation can be written as:

$$\frac{\partial^2 v_y}{\partial t^2} = V_{A0}(xz)^2 \left(x \frac{\partial}{\partial x} - z \frac{\partial}{\partial z} \right)^2 v_y$$

Here $V_{A0}(xz)$ is related to the speed of the system. If we recall we non-dimensionalised our speeds in Section 2.2.2 in units of $\frac{B_0}{\sqrt{\mu \rho}}$, then $V_{A0}(xz)^* = \frac{B_0}{\sqrt{\mu \rho}} \frac{1}{\sqrt{\rho_0(xz)^*}} = \frac{B_0}{\sqrt{\mu \rho}}$, where * indicates a non-dimensional quantity. Thus, we can see that V_{A0} takes a similar form to that of the Alfvén speed (page 12), hence the similar notation. In Chapter 4, we considered uniform background density,

and so V_{A0} was a constant, i.e. $V_{A0} = 1$ (i.e. $V_{A0} = \frac{B_0}{\sqrt{\mu\rho}}$).

It is precisely this non-constant Alfvén speed ($V_{A0} = V_{A0}(xz)$) that now leads to gradients in the Alfvén speed, and hence to (the possibility of) phase mixing. There was no phase mixing argument in Chapter 4 since we had $V_{A0} = 1$.

8.3 D'Alembert solution

As in Section 4.3.1, we can compare $\frac{\partial}{\partial s} = \left(x \frac{\partial}{\partial x} - z \frac{\partial}{\partial z}\right)$ and the original equation with $\frac{\partial v_y}{\partial s} = \frac{\partial x}{\partial s} \frac{\partial v_y}{\partial x} - \frac{\partial z}{\partial s} \frac{\partial v_y}{\partial z}$. This leads to:

$$x = x_0 e^s, \quad z = z_0 e^{-s}, \quad (8.5)$$

where x_0 and z_0 are the starting positions of our characteristics (as in Section 4.3.1). $s = -\log \frac{z}{z_0}$ and in our simulation, $z_0 = 2$. Thus our equation (8.4) can be written:

$$\frac{\partial^2 v_y}{\partial t^2} = \frac{1}{\rho_0(xz)} \frac{d^2}{ds^2} v_y = V_{A0}(xz)^2 \frac{d^2}{ds^2} v_y. \quad (8.6)$$

This characteristic equation can be solved with a D'Alembert solution such that:

$$v_y = \mathcal{F}(t - \sqrt{\rho} s) + \mathcal{G}(t + \sqrt{\rho} s) = \mathcal{F}\left(t - \frac{s}{V_{A0}(A_0)}\right) + \mathcal{G}\left(t + \frac{s}{V_{A0}(A_0)}\right) \quad (8.7)$$

We can implement the D'Alembert solution since $A_0 = -xz$ is a constant along each fieldline.

In the following sections, we will be solving equation (8.4) numerically and comparing it with our analytical solution. In order to compare the analytical and numerical results, we substitute the same initial conditions into the D'Alembert solution, i.e. $\mathcal{F}(t) = \sin(\omega t)$ to get the analytical solution for v_y , namely:

$$v_y(x, z, t) = \sin \omega \left(t + \sqrt{\rho_0(xz)} \log \frac{z}{z_0} \right) \quad \text{for} \quad \begin{cases} 0 \leq t + \sqrt{\rho_0(xz)} \log \frac{z}{z_0} \leq \frac{\pi}{\omega} \\ 0 \leq x_0 \leq 2 \end{cases} \quad (8.8)$$

8.4 Density profiles

We consider a non-uniform background density profile.

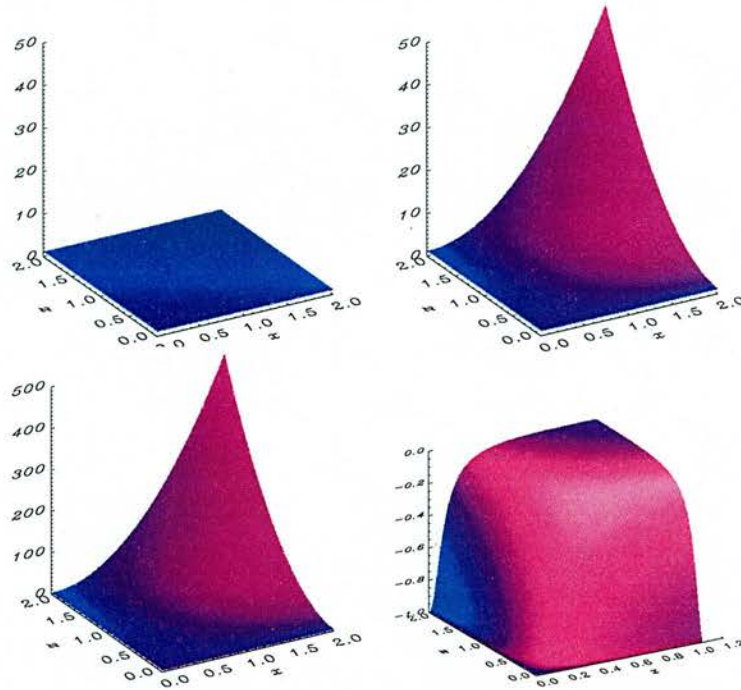


Figure 8.2: *Top left* shows density profile of case 1, i.e. $\rho_0 = 1$. *Top right* shows density profile of case 2, i.e. $\rho_0 = 1 + 3(xz)^2$. *Bottom left* shows density profile of case 3, i.e. $\rho_0 = 1 + 30(xz)^2$; thus the maximum of the z -axis is much greater. *Bottom right* shows density profile of case 4, i.e. $\rho_0 = (1 + 30(xz)^2)^{-1}$. Since $0 < \rho_0 \leq 1$, this bottom right subfigure is shown as a surface of $-\rho_0$, since this shows the profile behaviour clearer.

As mentioned in equation (8.3), the simplest way to consider a (non-uniform) density profile in our equations is to consider $\rho = \rho(A_0)$ and so in this magnetic equilibrium $\rho = \rho(xz)$. We will consider four scenarios. The first three cases will consider a density profile of the form $\rho_0 = 1 + \lambda(xz)^2$, where we vary the parameter λ . Firstly, we will consider a uniform density profile (where $\lambda = 0$). This system is identical to that investigated in Section 4.2, but is worth repeating here as it provides an excellent visual contrast to the other scenarios. Secondly, we consider a weakly changing density profile of the form $\rho = 1 + 3(xz)^2$ ($\lambda = 3$) and thirdly, we consider a more extreme density profile of the form $\rho = 1 + 30(xz)^2$ ($\lambda = 30$). The second and third choices of density profile consider a region of highest V_{A0} , i.e. smallest ρ_0 close to the axes. We will also consider a final scenario where $\rho_0 = \frac{1}{1+30(xz)^2}$, where the maximum V_{A0} is instead away from the axes. Tests show that these four choices of density profile communicate the general results well. These density profiles can be seen in Figure 8.2. Note the axes vary.

We can also use our D'Alembert solution to calculate b_y and hence j_x and j_z . For the first three cases; $\rho_0 = 1 + \lambda(xz)^2$ so using equation (8.8) we can write:

$$b_y = -\sqrt{1 + \lambda x^2 z^2} \sin \omega \left(t + \sqrt{1 + \lambda x^2 z^2} \log \frac{z}{z_0} \right), \quad (8.9)$$

$$j_x = \left[\frac{\omega(1 + \lambda x^2 z^2)}{z} + \omega \lambda x^2 z \log \frac{z}{z_0} \right] \cos \omega \left(t + \sqrt{1 + \lambda x^2 z^2} \log \frac{z}{z_0} \right) \quad (8.10)$$

$$+ \frac{\lambda x^2 z}{\sqrt{1 + \lambda x^2 z^2}} \sin \omega \left(t + \sqrt{1 + \lambda x^2 z^2} \log \frac{z}{z_0} \right) \quad (8.11)$$

$$j_z = - \frac{\lambda x z^2}{\sqrt{1 + \lambda x^2 z^2}} \sin \omega \left(t + \sqrt{1 + \lambda x^2 z^2} \log \frac{z}{z_0} \right) \quad (8.12)$$

$$- \omega \log \left(\frac{z}{z_0} \right) \lambda x z^2 \cos \omega \left(t + \sqrt{1 + \lambda x^2 z^2} \log \frac{z}{z_0} \right) \quad (8.13)$$

The form for b_y , j_x and j_z is slightly different for $\rho_0 = \frac{1}{1+30(xz)^2}$.

8.5 Case 1 : Uniform Density ($\lambda = 0$)

8.5.1 Numerical Simulation

Recall Section 4.2. In that Section, we looked at the propagation of the Alfvén wave in the neighbourhood of a simple 2D X-point in a uniform density plasma. We found that the linear Alfvén wave travels down from the top boundary and begins to spread out, following the field lines. As the wave approaches the lower boundary (the separatrix), it thins but keeps its original amplitude. The wave eventually accumulates very near the separatrix; defined by the x axis. We chose a localised wave pulse because primarily it demonstrated this nature of spreading out more clearly, and secondly we didn't want the boundary conditions to affect the simulation.

These results are reproduced here, but now with the wave pulse along the entire upper boundary. Though we do not learn anything new in this section, it acts as a useful comparison to cases 2 and 3. Equations (8.4) were solved numerically using our two-step Lax-Wendroff scheme. We consider a box ($0 \leq x \leq 2$, $0 \leq z \leq 2$) with a single wave pulse coming in across the top boundary. The boundary conditions were set such that:

$$v_y(x, 2) = \sin \omega t \quad \text{for} \quad \begin{cases} 0 \leq x \leq 2 \\ 0 \leq t \leq \frac{\pi}{\omega} \end{cases},$$

$$v_y = 0 \quad \text{otherwise}$$

$$\left. \frac{\partial v_y}{\partial x} \right|_{x=2} = 0, \quad \left. \frac{\partial v_y}{\partial x} \right|_{x=0} = 0, \quad \left. \frac{\partial v_y}{\partial z} \right|_{z=0} = 0. \quad (8.14)$$

The results can be seen in Figure 8.3 (they demonstrate the same nature as Figure 4.1). The bottom row of subfigures may be deemed unnecessary (the finite resolution of our simulation is inadequate by this point) but all four cases will be shown at the same time slices, so the bottom row is presented for a comparison with later figures.

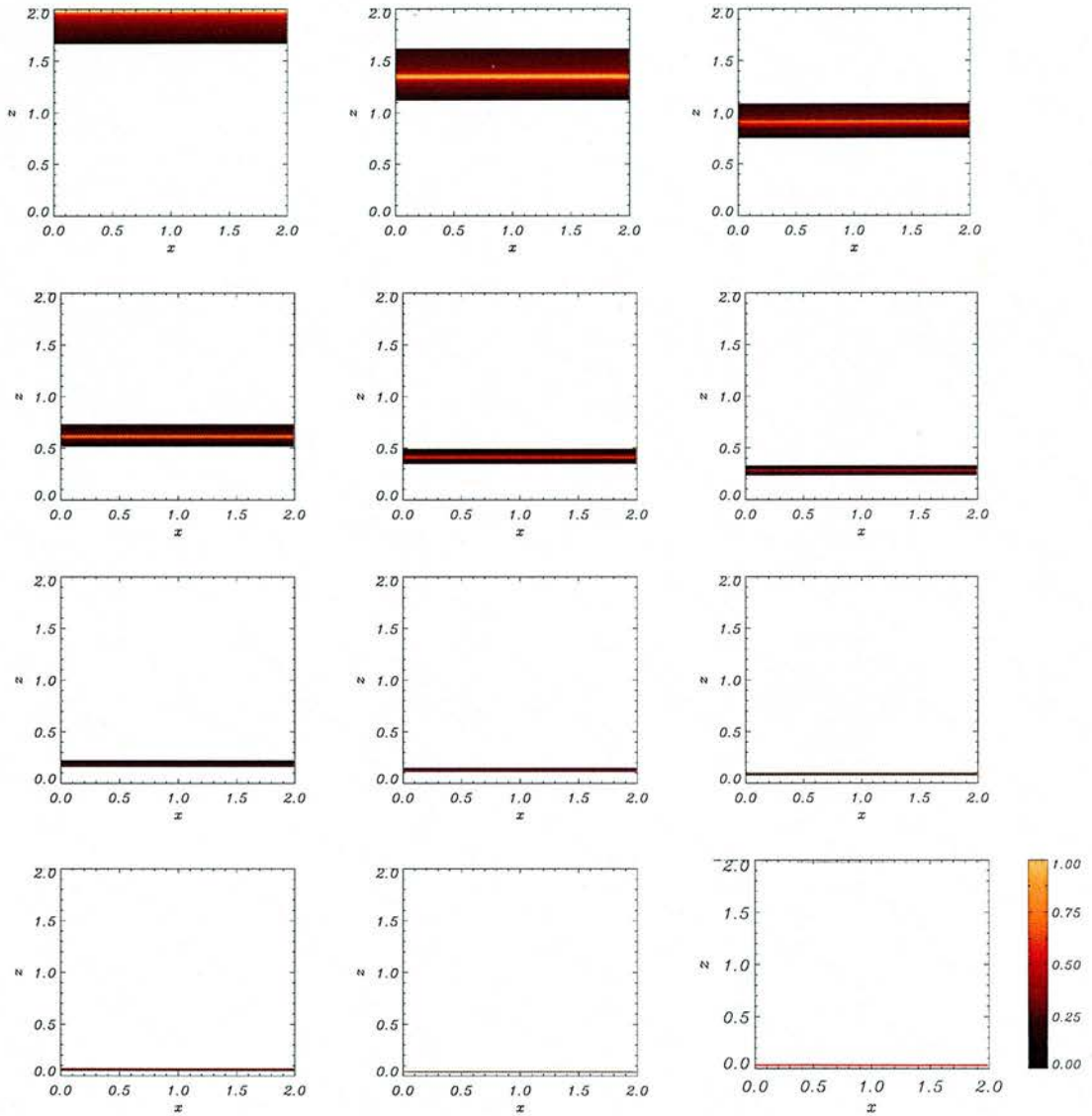


Figure 8.3: Contours of v_y for an Alfvén wave sent in from upper boundary for $0 \leq x \leq 2$ and its resultant propagation at times (a) $t=0.25$, (b) $t=0.6$, (c) $t=1.0$, (d) $t=1.4$, (e) $t=1.8$, (f) $t=2.2$, (g) $t=2.6$, (h) $t=3.0$, (i) $t=3.4$, (j) $t=3.8$, (k) $t=4.2$, (l) $t=4.6$, labelling from top left to bottom right.

8.5.2 Analytical Solution

We can also solve equation (8.4) using our D'Alembert solution (as we did in Chapter 4). The agreement between the numerical and analytical work is (again) excellent. Equations (8.13) can be simplified under $\lambda = 0$ to give:

$$\begin{aligned} b_y &= -\sin \omega \left(t + \log \frac{z}{z_0} \right), \\ j_x &= \frac{\omega}{z} \cos \omega \left(t + \log \frac{z}{z_0} \right) \\ j_z &= 0 \end{aligned}$$

Hence, the Alfvén wave causes current density to build up along the separatrix (j_x builds up). As we have already seen (Section 4.4), this build up is exponential in time. In this simulation, $j_z = 0$ for all time. Figure 8.4 shows the build-up of j_x . This figure shows the same behaviour as Figure 4.5, but is reproduced here for comparison with the work to come.

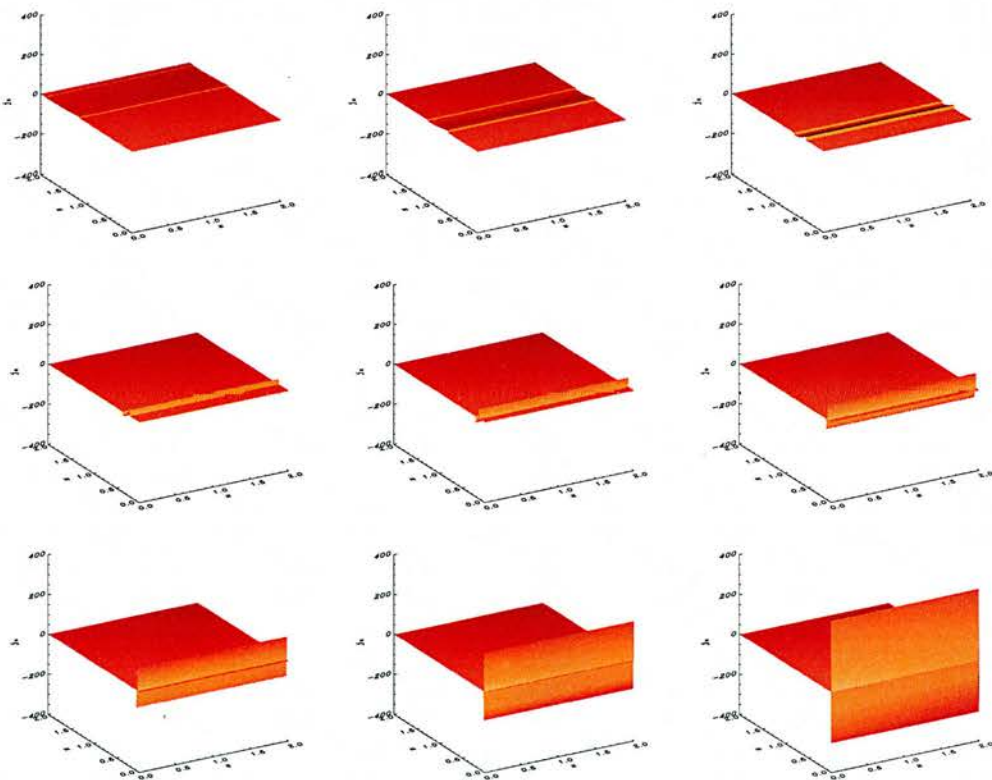


Figure 8.4: Shaded surfaces showing the build-up of j_x at times (a) $t=0.5$, (b) $t=1.0$, (c) $t=1.5$, (d) $t=2.0$, (e) $t=2.5$, (f) $t=3.0$, (g) $t=3.5$, (h) $t=4.0$ and (i) $t=4.5$, labelling from top left to bottom right.

8.6 Case 2 : Weakly non-uniform Density ($\lambda = 3$)

8.6.1 Numerical Simulation

Equation (8.4) were solved again solved numerically using our two-step Lax-Wendroff scheme. The same boundary and initial conditions were used as in Section 8.5 (i.e. equations 8.14), but now solving equation (8.4) with our weakly changing density profile, i.e. solving:

$$\frac{\partial^2 v_y}{\partial t^2} = \frac{1}{1 + 3x^2 z^2} \left(x \frac{\partial}{\partial x} - z \frac{\partial}{\partial z} \right)^2 v_y .$$

The results can be seen in Figure 8.5. We see that the Alfvén wave again descends and accumulates along the separatrix (x -axis), but now the (previously planar) wave is distorted. The varying speed, $V_{A0}(xz)$, means different sections of the wave travel at different speeds. Thus, the parts of the wave closest to the $x = 0$ axis, where $V_{A0}(xz)$ takes its maximum value (or alternatively $\rho_0(xz)$ takes its minimum value) travel at a greater speed than those parts away from the axis (i.e. left hand side travels faster than right). Thus, the wave is distorted and descends at different rates. This is different behaviour to that the uniform density case considered in Figure 8.3. The wave does however still accumulate along the separatrix.

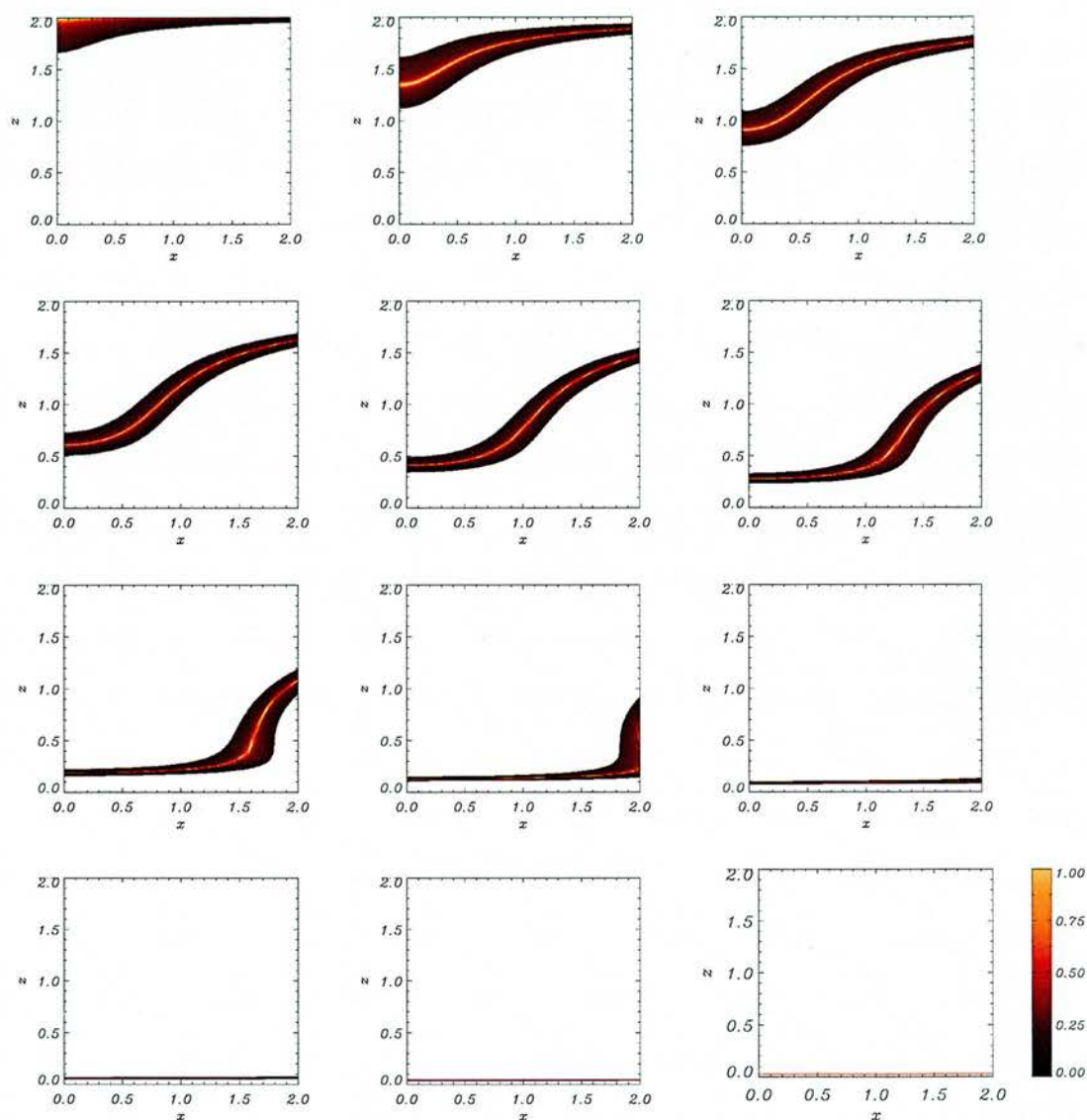


Figure 8.5: Contours of v_y for an Alfvén wave sent in from upper boundary for $0 \leq x \leq 2$ and its resultant propagation at times (a) $t=0.25$, (b) $t=0.6$, (c) $t=1.0$, (d) $t=1.4$, (e) $t=1.8$, (f) $t=2.2$, (g) $t=2.6$, (h) $t=3.0$, (i) $t=3.4$, (j) $t=3.8$, (k) $t=4.2$, (l) $t=4.6$, labelling from top left to bottom right.

8.6.2 Analytical Solution

Again, the D'Alembert solution agrees exactly with the numerical simulation. Substituting $\lambda = 3$ into equations (8.13) gives analytical forms for j_x and j_z . These can be seen in Figures 8.6 and 8.7. In Figure 8.6, we can see that there is a large concentration of j_x initially along the wave, due to the changing density profile. This concentration propagates with the wave and begins to accumulate along the separatrix (x -axis). The build-up of j_x along the separatrix is substantially more than in early subfigures, and hence it appears that the separatrix will still be the location for preferential heating, even with the inclusion of a non-uniform density.

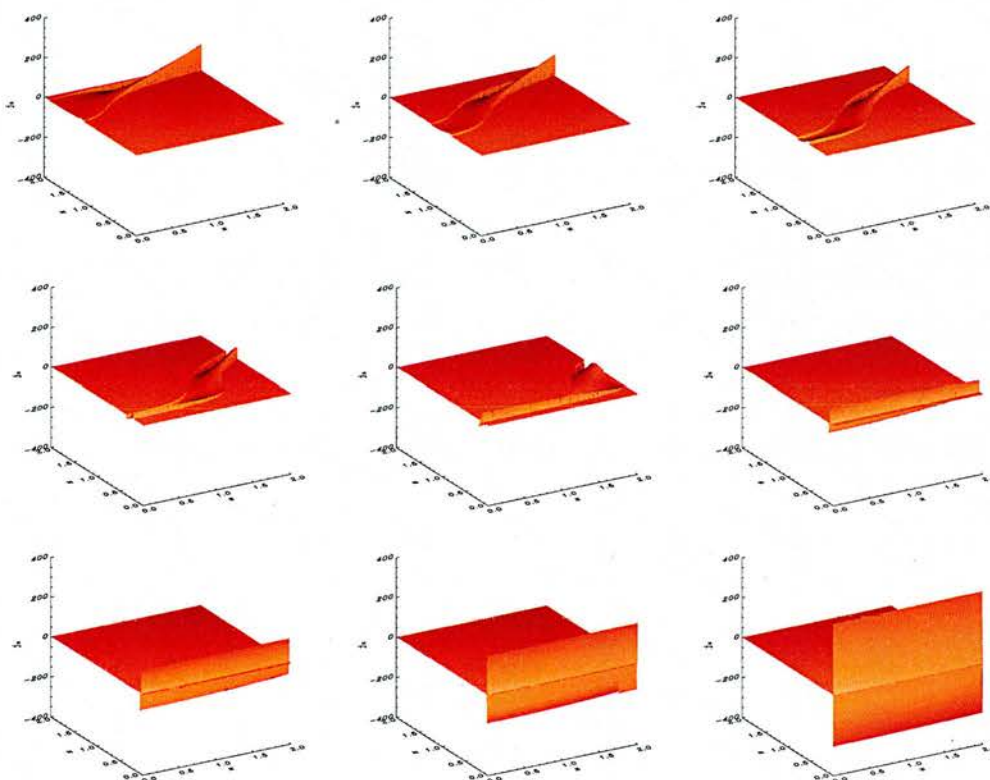


Figure 8.6: Shaded surfaces showing the build-up of j_x at times (a) $t=0.5$, (b) $t=1.0$, (c) $t=1.5$, (d) $t=2.0$, (e) $t=2.5$, (f) $t=3.0$, (g) $t=3.5$, (h) $t=4.0$ and (i) $t=4.5$, labelling from top left to bottom right.

In Figure 8.7, we can see that there is initially a concentration of j_z (due to the changing density profile) but that this decays away as time elapses. Figure 8.7 is similar to Figure 4.7 in that there is an initial profile of j_z that then seems to propagate in the increasing x and decreasing z directions. Like Figure 4.7, j_z in Figure 8.7 also decays away.

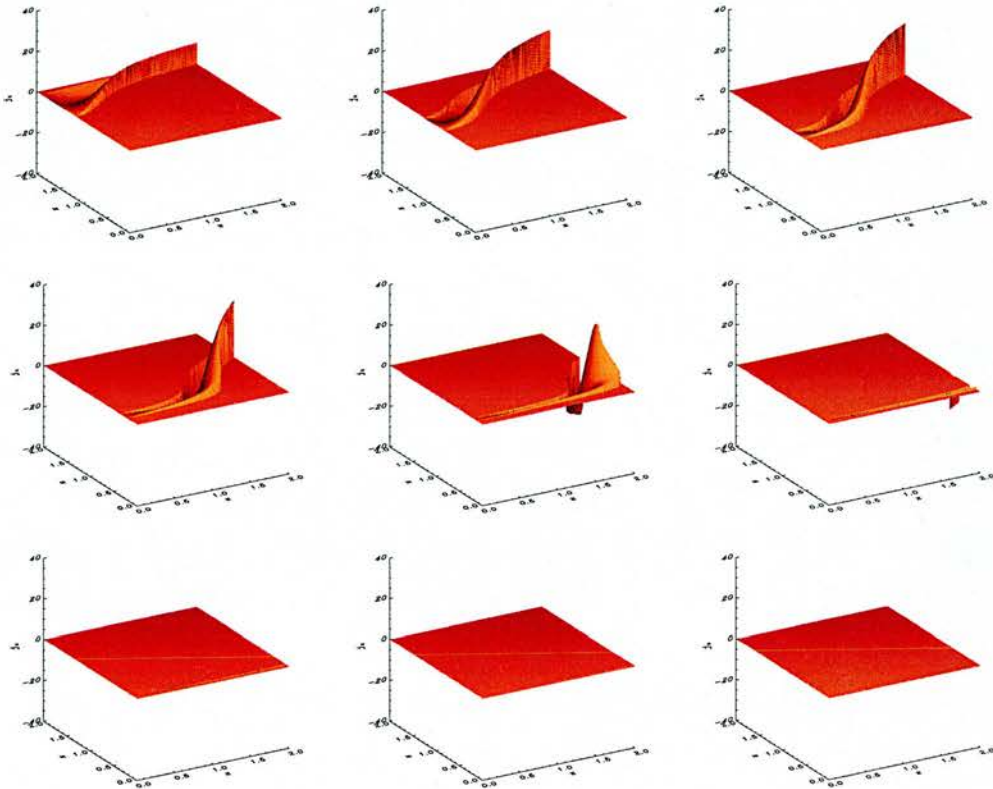


Figure 8.7: Shaded surfaces showing the build-up of j_z at times (a) $t=0.5$, (b) $t=1.0$, (c) $t=1.5$, (d) $t=2.0$, (e) $t=2.5$, (f) $t=3.0$, (g) $t=3.5$, (h) $t=4.0$ and (i) $t=4.5$, labelling from top left to bottom right.

8.7 Case 3 : Strongly non-uniform Density ($\lambda = 30$)

8.7.1 Numerical Simulation

Equation (8.4) were solved again solved numerically using our two-step Lax-Wendroff scheme. The same boundary and initial conditions were used as in Section 8.5 (i.e. equations 8.14), but now solving equation (8.4) with our strongly changing density profile, i.e. solving:

$$\frac{\partial^2 v_y}{\partial t^2} = \frac{1}{1 + 30x^2z^2} \left(x \frac{\partial}{\partial x} - z \frac{\partial}{\partial z} \right)^2 v_y .$$

The results can be seen in Figure 8.8. The behaviour is very similar to that of the weakly changing density profile (Case 2), but with one important distinction. Again, we see that the Alfvén wave descends and accumulates along the separatrix. The wave is distorted from its original planar form by the varying density profile, and hence different parts of the wave descend at different speeds. Thus, the wave travels faster nearer to the z -axis than away from it. However, since the Alfvén wave is confined to the field lines, and propagating along those field lines, there comes a point where elements of the wave as so ahead of other elements of the wave that the wave front (made by joining up all the elements) actually bends back upon itself. This can be seen most clearly in the lower subfigures of Figure 8.8. However, once again the Alfvén wave still accumulate along the separatrix (x -axis).

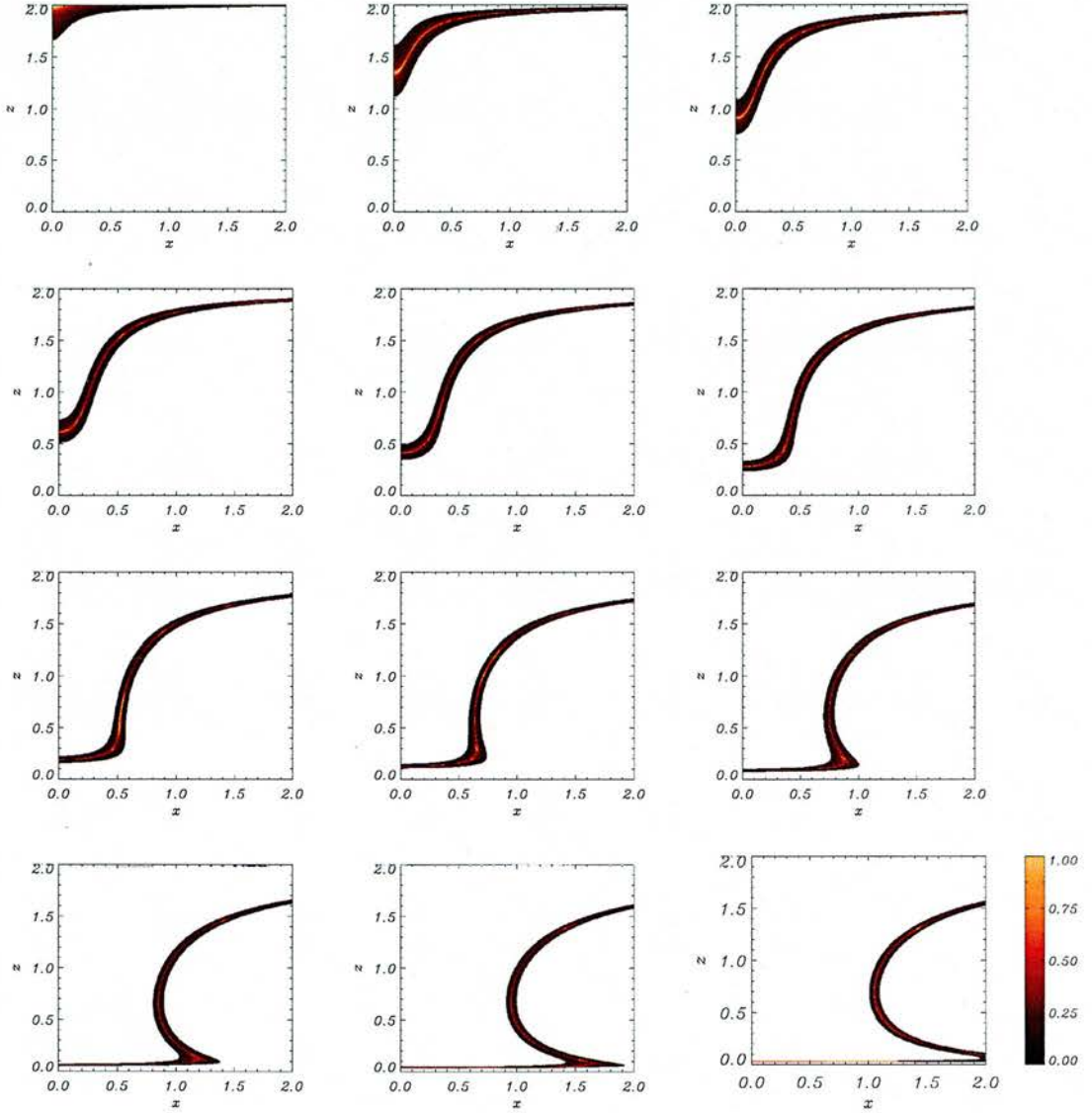


Figure 8.8: Contours of v_y for an Alfvén wave sent in from upper boundary for $0 \leq x \leq 2$ and its resultant propagation at times (a) $t=0.25$, (b) $t=0.6$, (c) $t=1.0$, (d) $t = 1.4$, (e) $t=1.8$, (f) $t=2.2$, (g) $t = 2.6$, (h) $t=3.0$, (i) $t=3.4$, (j) $t = 3.8$, (k) $t=4.2$, (l) $t=4.6$, labelling from top left to bottom right.

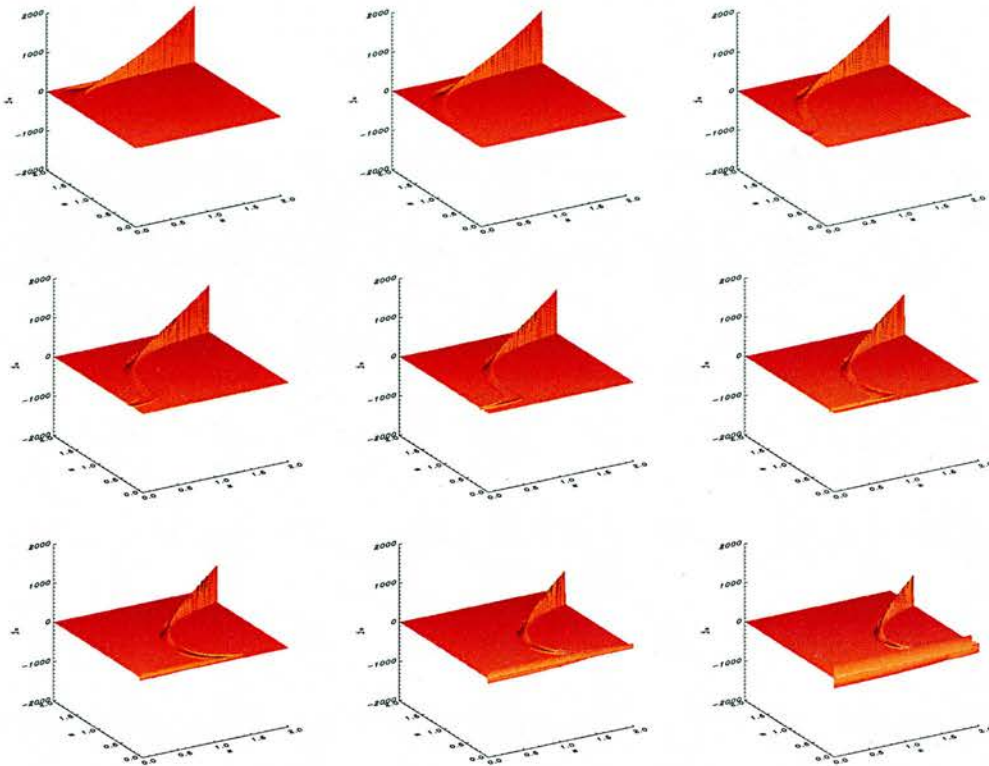


Figure 8.9: Shaded surfaces showing the build-up of j_x at times (a) $t=0.5$, (b) $t=1.0$, (c) $t=1.5$, (d) $t=2.0$, (e) $t=2.5$, (f) $t=3.0$, (g) $t=3.5$, (h) $t=4.0$ and (i) $t=4.5$, labelling from top left to bottom right.

8.7.2 Analytical Solution

Since the wave is so stretched where it forms the spike in the wave front, there may be a great deal of current build-up near this point. Hence, this may provide an extra location for (preferential) heating. We shall have to look at j_x and j_z .

As before, the D'Alembert solution agrees exactly with the numerical simulation. Substituting $\lambda = 30$ into equations (8.13) gives analytical forms for j_x and j_z . These can be seen in Figures 8.9 and 8.10. In Figure 8.9, we can see that there is a very large concentration (note value on axis!) of j_x initially along the wave, due to the changing density profile. This concentration propagates with the wave and begins to accumulate along the separatrix (x -axis). This build-up along the separatrix eventually overtakes the magnitude of current concentrations elsewhere (although this occurs at a time after the time elapsed in the last subfigure). Hence, the separatrix will *still* be the location for the majority of heating, however small η is taken to be, but if η is large, there may be some heating along other parts of the wave. However, the density profile used here has a very extreme distribution (so perhaps under coronal conditions this scenario would not take place and preferential heating would still occur along the separatrices).

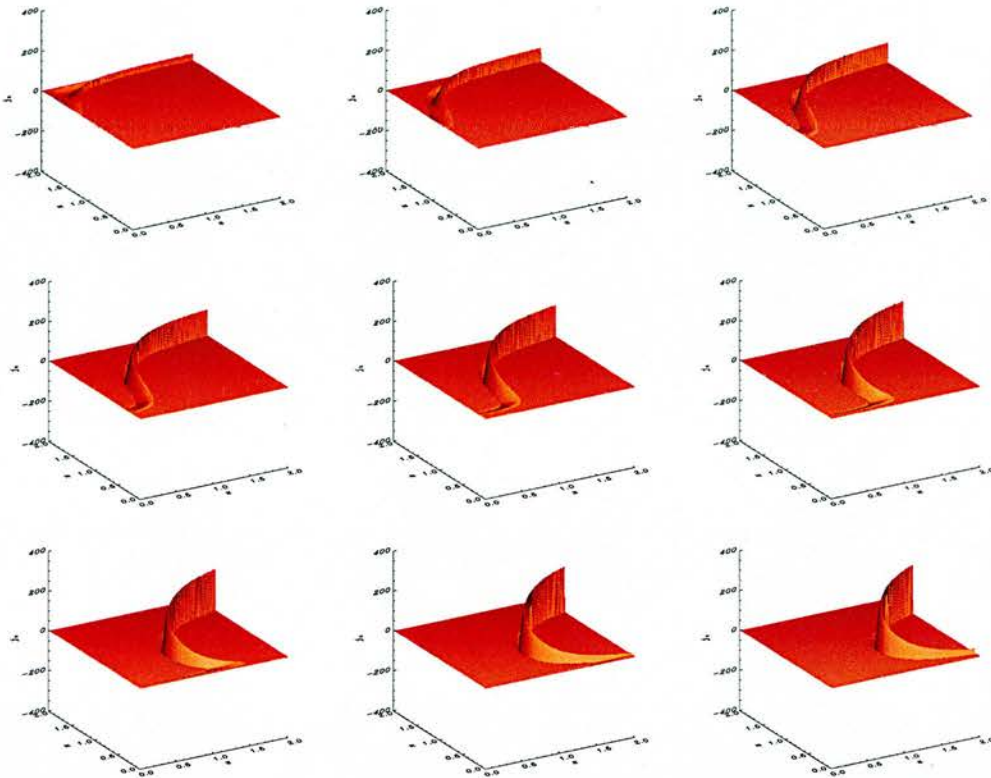


Figure 8.10: Shaded surfaces showing the build-up of j_z at times (a) $t=0.5$, (b) $t=1.0$, (c) $t=1.5$, (d) $t=2.0$, (e) $t=2.5$, (f) $t=3.0$, (g) $t=3.5$, (h) $t=4.0$ and (i) $t=4.5$, labelling from top left to bottom right.

In Figure 8.10, we can see that there is initially a concentration of j_z (due to the changing density profile). This propagates in the increasing x and decreasing z directions, and decays away near the x -axis. The rest of the j_z concentration propagates away and out of our box, but will eventually decay away (like j_z did before). This can be seen in the form of j_z from equations (8.13).

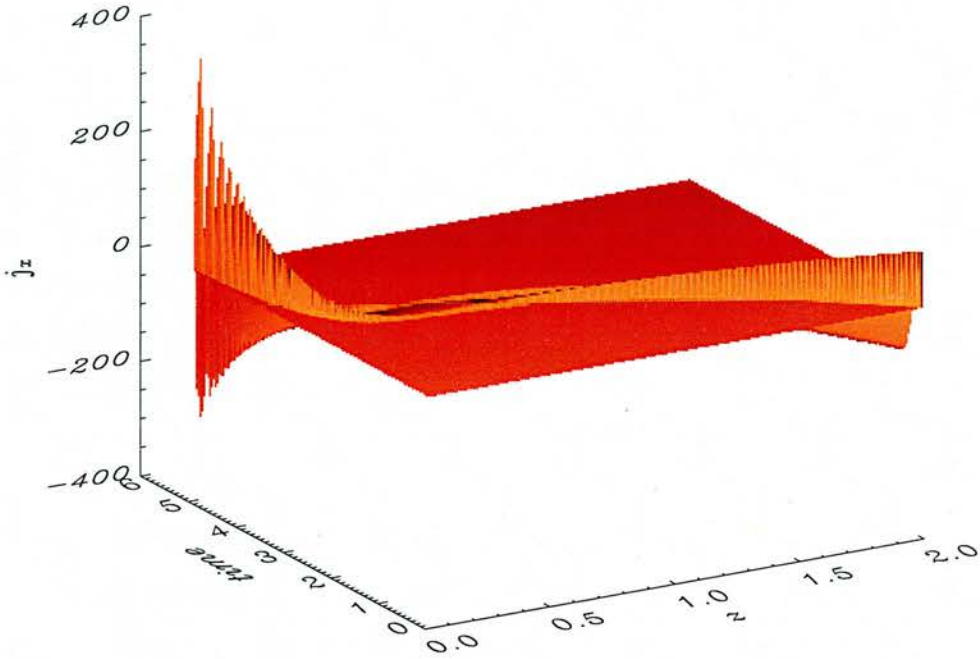


Figure 8.11: Shaded surfaces showing the build-up of j_x plotted against z and time with $x = 0.5$.

It is perhaps not clear from Figure 8.9 that the maximum j_x build-up occurs near the x -axis ($z = 0$ line). Figure 8.11 shows a surface of the build-up of j_x plotted against z and time, along $x = 0.5$. Thus we can see that z decreases from 2 down to near 0 as time elapses and that j_x is building up the closer we are to $z = 0$ and the build-up is increasing in time. Looking back at equations (8.13) and substituting $xz = x_0z_0$ and $x = x_0e^{-s}$, $z = z_0e^{-s}$ gives:

$$\begin{aligned}
 j_x &= e^s \left\{ \left[\frac{\omega\rho_0}{z_0} - (\omega\lambda x_0^2 z_0) s \right] \cos \omega(t - \sqrt{\rho_0} s) + \frac{\lambda x_0^2 z_0}{\sqrt{\rho_0}} \sin \omega(t - \sqrt{\rho_0} s) \right\} \\
 &= e^s [(B - C s) \cos \omega(t - \sqrt{\rho_0} s) + D \sin \omega(t - \sqrt{\rho_0} s)] \\
 j_z &= e^{-s} \left[-\frac{\lambda x_0 z_0^2}{\sqrt{\rho_0}} \sin \omega(t - \sqrt{\rho_0} s) + (\omega\lambda x_0 z_0^2) s \cos \omega(t - \sqrt{\rho_0} s) \right] \\
 &= e^{-s} [-E \sin \omega(t - \sqrt{\rho_0} s) + F s \cos \omega(t - \sqrt{\rho_0} s)]
 \end{aligned} \tag{8.15}$$

where $x_0, z_0, \omega, \lambda, \rho_0, B, C, D, E$ and F are all constants for a field line ($B \dots F$ are just collected constants but are all ≥ 0).

Hence, we can see that the behaviour of j_x and j_z follow complicated forms that depend upon many starting parameters and on s , but that j_x will eventually build-up exponentially and j_z will decay exponentially. Thus, for the linear Alfvén wave, preferential heating will still occur along the separatrices.

8.8 Case 4 : Non-uniform Density $\rho_0 = [1 + 30(xz)^2]^{-1}$

8.8.1 Numerical Simulation

For our final density profile, equation (8.4) was again solved numerically using our two-step Lax-Wendroff scheme, with the same boundary and initial conditions as before (given by equations 8.14) with $\rho_0 = [1 + 30(xz)^2]^{-1}$, i.e. solving

$$\frac{\partial^2 v_y}{\partial t^2} = (1 + 30x^2z^2) \left(x \frac{\partial}{\partial x} - z \frac{\partial}{\partial z} \right)^2 v_y .$$

The results can be seen in Figure 8.12. Here, the greatest V_{A0} occurs away from the axes (in these numerical boxes maximum occurs at $(x, z) = (2, 2)$). Thus, we find that the Alfvén wave is again distorted from its initially planar shape, but that it now travels faster the *further* we are away from the axes. The first subfigure of Figure 8.12 shows the massive speed differential across the wave after a very short time. The linear Alfvén wave then decends and starts to accumulate along the x -axis (separatrix). Here, the wave slows down and thins, but keeps its original amplitude. There is no spike formed, as there was in Case 3. This is a different velocity profile to that seen in the previous three cases, but the phenomenon of different elements of the wave travelling at different speeds due to the density profile is common to all cases.

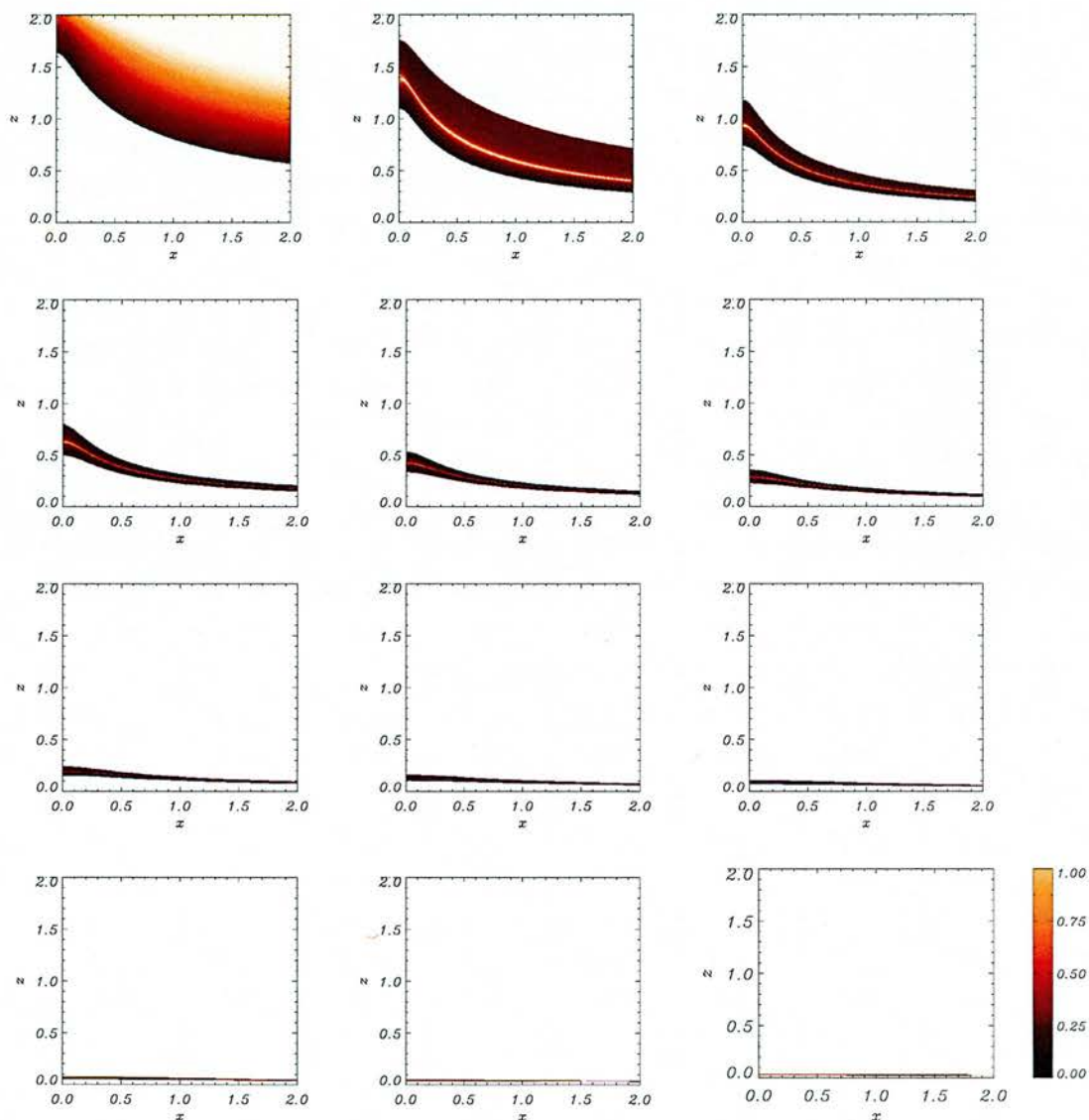


Figure 8.12: Contours of v_y for an Alfvén wave sent in from upper boundary for $0 \leq x \leq 2$ and its resultant propagation at times (a) $t=0.25$, (b) $t=0.6$, (c) $t=1.0$, (d) $t=1.4$, (e) $t=1.8$, (f) $t=2.2$, (g) $t=2.6$, (h) $t=3.0$, (i) $t=3.4$, (j) $t=3.8$, (k) $t=4.2$, (l) $t=4.6$, labelling from top left to bottom right.

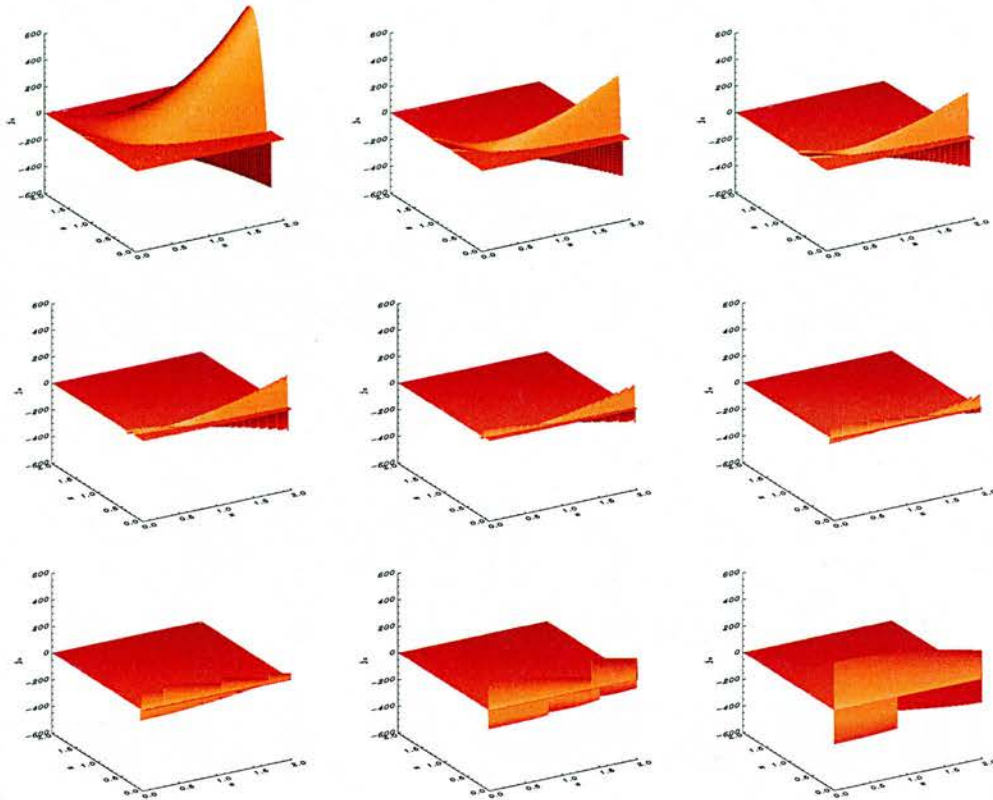


Figure 8.13: Shaded surfaces showing the build up of j_x at times (a) $t=0.5$, (b) $t=1.0$, (c) $t=1.5$, (d) $t=2.0$, (e) $t=2.5$, (f) $t=3.0$, (g) $t=3.5$, (h) $t=4.0$ and (i) $t=4.5$, labelling from top left to bottom right.

8.8.2 Analytical Solution

As before, the D'Alembert solution agrees exactly with the numerical simulation. We can use our D'Alembert solution to work out b_y , j_x and j_z (as we did in equations 8.13) for this final density profile. The analytical forms for j_x and j_z can be seen in Figures 8.13 and 8.14. In Figure 8.13, we can see that there is initially a large concentration of j_x due to the extreme density profile, but that this then decays away (as the wave propagates along the field lines and out of the box). At a later time, after the wave is near the separatrix, j_x starts to grow again. There is a large current accumulation along the separatrix and our key result about Alfvén wave heating seems to hold.

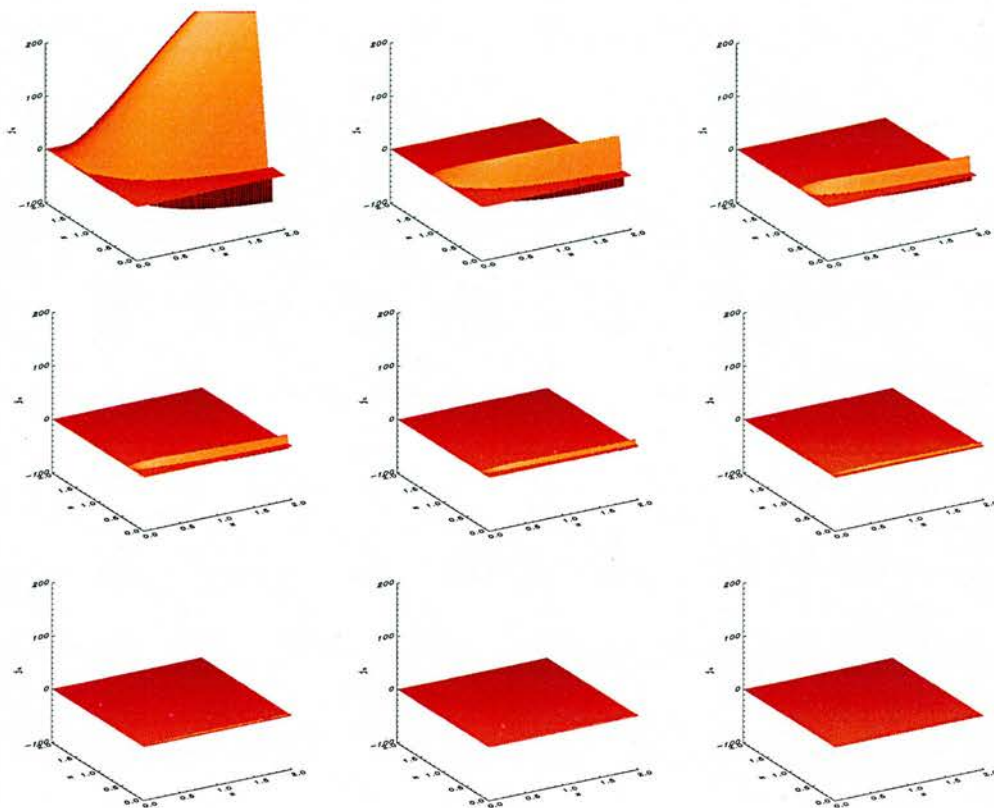


Figure 8.14: Shaded surfaces showing the build up of j_z at times (a) $t=0.5$, (b) $t=1.0$, (c) $t=1.5$, (d) $t=2.0$, (e) $t=2.5$, (f) $t=3.0$, (g) $t=3.5$, (h) $t=4.0$ and (i) $t=4.5$, labelling from top left to bottom right.

In Figure 8.14, we can see that there is initially a large concentration of j_z (due to the changing density profile), but that it very quickly decays away.

As mentioned above, our D'Alembert solution gives us general forms for b_y , j_x and j_z . Substituting $\rho_0 = [1 + \gamma (xz)^2]^{-1}$ into these forms (where $\gamma = 30$ in this study case but γ is used so the result is more general) and substituting $xz = x_0 z_0$ and $x = x_0 e^s$, $z = z_0 e^{-s}$ gives:

$$\begin{aligned}
 j_x &= e^s \left[\left(\omega \gamma x_0^2 z_0^2 \rho_0 s + \frac{\omega}{z_0} \right) \cos \omega (t - \sqrt{\rho_0} s) - \rho_0^{\frac{3}{2}} \gamma x_0^2 z_0 \sin \omega (t - \sqrt{\rho_0} s) \right] \\
 &= e^s [(B + C s) \cos \omega (t - \sqrt{\rho_0} s) - D \sin \omega (t - \sqrt{\rho_0} s)] \\
 j_z &= e^{-s} \left[-s \omega \gamma x_0 z_0^2 \rho_0^2 \cos \omega (t - \sqrt{\rho_0} s) + \gamma x_0 z_0^2 \rho_0^{\frac{3}{2}} \sin \omega (t - \sqrt{\rho_0} s) \right] \\
 &= e^{-s} [+E \sin \omega (t - \sqrt{\rho_0} s) + E s \cos \omega (t - \sqrt{\rho_0} s)]
 \end{aligned}$$

where again x_0 , z_0 , ω , λ , ρ_0 , B , C , D , E and F are all constants for a field line ($B \dots F$ are just collected constants but are all ≥ 0). These equations have a similar form to equations (8.15).

Hence, we can see that the behaviour of j_x and j_z follow complicated forms that depend upon many starting parameters and on s , but that (as we found before) j_x will eventually build-up exponentially and j_z will decay exponentially. Thus, for the linear Alfvén wave, preferential heating will still occur along the separatrices, even when a non-uniform density profile is considered.

8.9 Conclusion

This chapter has investigated the propagation of Alfvénic pulses into an inhomogeneous plasma near a simple 2D X-point. When a uniform plasma density is considered, it is seen that the Alfvén wave front remains purely horizontal, despite the varying Alfvén speed, and the wave collects at the separatrices. In the non-ideal case, these Alfvénic disturbances dissipate their energy there. On the other hand, if a non-uniform density is studied, it is found that the wave front is rapidly stretched. Depending upon the initially density profile, the wavefront is distorted from its initially planar shape and travels along the field lines at different speeds. Depending upon the density profile, the wavefront can stretch so much that it bends back on itself and creates a spike, though this requires an extreme density profile.

This chapter set out to answer a key question; with the addition of a non-uniform density, does the current build-up still occur at the separatrix or does phase mixing now allow the energy to be extracted from a different location? This chapter has been all about the battle between dissipation due to phase mixing and dissipation of the current build-up along the separatrices. From the work above, it appears that current build-up is limited except near the separatrices. This can be seen in Figure 8.11. Thus, the key result of Chapter 4 appears to remain true; **for the linear Alfvén wave, preferential heating occurs along the separatrices, even when a non-uniform density profile is considered.**

Chapter 9

Summary and Further Work

9.1 Summary

In this Thesis, we have looked at the properties and behaviour of MHD waves in the neighbourhood of 2D null points in a variety of magnetic configurations and under various physical assumptions. It is hoped that the work done in this Thesis has contributed to the understanding of how plasma waves behave in complicated magnetic configurations. This work has focussed on wave propagation entering from a boundary and has not considered the initial value problem situation, where there is an initial disturbance everywhere in the neighbourhood of the null point. We will now summarise our main findings.

In Chapter 3, we investigated the behaviour of the fast magnetoacoustic (MA) wave in the neighbourhood of a single 2D null point for a $\beta = 0$ plasma. Through both numerical and analytical techniques in cartesian and polar geometries, we found that when a fast MA wave propagates near a null point, the wave wraps itself around the null point due to *refraction*. This behaviour also causes a large current density to accumulate at the null and this build-up is exponential in time. The physical significance of this is that any fast MA disturbance in the neighbourhood of a neutral point will be drawn towards the region of zero magnetic field strength and focus all its energy at that point. Hence, this is where the build-up of current will occur and where the wave energy will be dissipated. Thus, Chapter 3 concluded that **fast wave heating will naturally occur at $\beta = 0$ coronal null points.**

Chapter 4 looked at the behaviour of the Alfvén wave in the neighbourhood of a single 2D null point. The work, again both numerical and analytical, showed that the Alfvén wave propagates along the field lines and accumulates along the separatrix (and hence, due to symmetry, along the separatrices). This leads to current accumulation along the separatrix in which the j_x component increased exponentially and the j_z component decreased exponentially. Thus, Chapter 4 showed that the Alfvén wave is confined to the field lines in the 2D linear set up and concluded that **Alfvén wave energy will be dissipated along the separatrices**. Thus, the Alfvén wave shows a different behaviour to the fast wave in the sense that the two wave types deposit all their wave energy at different locations, although the phenomenon of depositing wave energy in a specific region is common to both.

Chapter 5 also looked at the propagation of the fast magnetoacoustic wave and Alfvén wave, but now in a more complicated geometry with two null points (but still in a $\beta = 0$ plasma). This chapter questioned whether or not the findings of Chapters 3 and 4 carried through to a configuration of more than just one null point. Due to the 2D linear assumptions, the two wave modes were still decoupled. For the fast wave, it was found that the refraction effect persists but that the wave now splits with part of the wave travelling to each null point. Once near their chosen null, the wave fraction continued to wrap around it, akin to the behaviour seen in Chapter 3. The proportion of fast wave that goes to each null was found to depend on the angle of approach (although the details of only two approach angles were given). However, once again the conclusion was that **fast wave heating would still naturally occur at these $\beta = 0$ null points**. This gives us confidence that the key result from Chapter 3 was a general result (rather than being specific to certain magnetic fields). For the Alfvén wave, the results showed that the wave propagates along the field lines and accumulates along the separatrices. Thus, the Alfvén wave is again confined to the field lines. It was concluded that this would lead to current build-up along those separatrices, and hence that would be where Alfvén wave heating would naturally occur due to dissipation. Thus, Chapter 5 concluded that key findings of Chapters 3 and 4 *do* carry through to a magnetic configuration of two null points.

Chapter 6 again tested the key findings of Chapters 3 and 4, namely to see if they persisted in a more realistic magnetic configuration; a two dipole configuration with a magnetic null point (again still in a $\beta = 0$ plasma). The magnetic field, $\mathbf{B}_0(x, z)$, used in Chapter 3, 4 and 5 had the property that for large x and z , $|\mathbf{B}_0|$ was also large, which is unphysical. Chapter 3 also claimed that a single null point could affect an arbitrarily long fast wave that was a great distance away. Thus, a more realistic magnetic geometry was chosen in which \mathbf{B}_0 tends to zero as x and z tend to infinity. When looking at the behaviour of the fast wave, it was found that the wave splits and only part of it was refracted into the null point. The rest of the wave had its propagation influenced by the null, but eventually escaped and propagated out of the numerical box. Thus, we see that the phenomenon from Chapter 3 persists in this more complicated geometry, but only if the fast

wave is near the null point. This makes intuitive sense; if the wave is far away from the null, it will not be heavily influenced by it until it is much closer. We also looked at the behaviour of the Alfvén wave near the two dipoles. We saw that if the Alfvén wave started straddling a separatrix, it accumulated along that separatrix (or separatrices). However, if the wave did not start across a separatrix, it propagated away from the magnetic region. These two findings were explained by the fact that in the system, the Alfvén wave is confined to the field lines and each fluid element is trapped on the field line it starts on. The chapter concluded by saying that some heating would occur at the null point for the fast wave and that heating would occur along the separatrices for the Alfvén wave.

Chapter 7 considered the behaviour of both fast and slow waves in a non-zero β plasma, lifting the restriction of $\beta = 0$ in previous chapters. The Alfvén wave is unaffected by the plasma pressure term and is hence still decoupled from our equations for the magnetoacoustic waves (so we did not need to consider it in this chapter). We looked at an identical set-up to Chapter 3, except now the plasma pressure introduced slow waves into our system. The plasma pressure also introduced a $c_s^2 = v_A^2$ layer which effectively divides the system into low β and high β regions, in which both the fast and slow waves have differing properties. We found that depending on the choice of β_0 , which is equivalent to choosing the distance between the initial disturbance and the $c_s^2 = v_A^2$ layer, we saw differing results. It is clear, however, that the system showed two competing phenomenon; a refraction effect caused by the varying Alfvén speed and a non-zero sound speed at the null which allows the fast wave to pass through. We found that:

- For $\beta_0 \rightarrow 0$, the refraction effect infinitely dominates and we recover the results of Chapter 3.
- If β_0 is small, then the refraction effect slightly dominates and we get high β slow waves along the separatrices near the null, but the majority of the wave continues wrapping around the neutral point. This leads to current accumulation close to the null and along part of the separatrices nearby.
- However, if β_0 is large, then the sound speed is large enough to allow the high β fast wave to pass through the null in a short time and escape the refraction effect of the null. In this case, we get some current build-up (again due to the high β slow wave) near the null and along the separatrices, but a large fraction of the wave energy escapes the system via the high β fast wave (which changes back to a low β fast wave as it emerges from the $c_s^2 = v_A^2$ layer).
- Finally, for $\beta_0 \rightarrow \infty$, the system becomes hydrodynamic. In this case, the fast wave reduces to an acoustic wave and so completely passes through the null (in effect, it doesn't even see the magnetic field, since $v_a^2 \ll c_s^2$).

The chapter concluded by stating that under coronal conditions, the scenario with a very small value for β_0 seems most physical.

Finally, Chapter 8 looked at the behaviour of the Alfvén wave near a 2D null point with a non-uniform density profile (a modification on the set-up of Chapter 4). It was found that with a non-uniform density profile, the wave front is distorted from its initially planar shape as it propagates. This was explained by the fact that each fluid element was (again) confined to its original field line but now each element travelled at a different speed. Depending upon the density profile, the wavefront can stretch so much that it bends back on itself and creates a spike, though this requires an extreme density profile. Since each field line is travelling at a different speed, it was thought that phase mixing may become important in the system, i.e. that energy could be extracted from a different location than the separatrices. However, the investigation, which involved several density profiles, found that the current build-up was limited except near the separatrices. Thus, the key result of Chapter 4 appears to remain true, i.e. **for the linear Alfvén wave, preferential heating occurs along the separatrices.**

9.2 Further Work

This Thesis has presented detailed work on the behaviour of MHD waves in the neighbourhood of 2D null points in a variety of magnetic configurations and under various assumptions. There are several extensions to this work. Recently, Fruit & Craig (2005) looked at the behaviour of Alfvén waves near a 2D X-point and included viscosity and resistivity in their model. They also imposed fixed boundary conditions which, since the Alfvén waves are confined to the field line they start on, led to standing waves on each field line. These field lines all vibrated with their own frequency and this led to phase mixing in the system.

Here, we present some possible extensions to the work done in this Thesis.

9.2.1 Non-linear wave behaviour

All the wave disturbances looked at in this Thesis were linear. As a further project, it would be interesting to consider how non-linearities effect the system. In the case of the fast wave near a simple 2D X-point for a $\beta = 0$ plasma, the refraction effect will still play a part in the (non-linear) wave propagation, but since the wave is thinning and gradients are increasing, the wave may shock at some point and so extract energy away from the null point.

9.2.2 3D wave propagation near null points

The work conducted in this Thesis was done in 2D, and the obvious extension is to develop the ideas in 3D. Using the knowledge gained in this Thesis, several simple 3D systems could be investigated to gain insights into the 3D behaviour. One of the most important new effects will be the coupling of the fast wave and Alfvén wave (in a $\beta = 0$ plasma) due to the geometry. This has already been looked at in 3D by Galsgaard *et al.* (2003). An extension to this work would be to look at different magnetic configurations, such as two 3D null points, or to include plasma pressure and thus introduce slow waves to the system (which would lead to coupling between all three modes).

9.2.3 MHD disturbances in observed magnetic fields

As mentioned in Chapter 2, potential field extrapolations, using photospheric magnetograms to provide the field distribution on the lower boundary, suggest that there are always likely to be null points in the corona (and, of course, separatrix surfaces in the magnetic topology). An extension to the work done in this Thesis, would be to use these observed magnetic fields as a starting magnetic configuration into which a wave disturbance can be launched. Then, with the aid of the investigations done on simpler 3D systems (see above), the more complicated, but more realistic, wave propagation could be deduced.

These realistic results can then be used to generate synthetic observations by inserting coronal parameters into the model. With the right choice of parameters, the intensity of plasma at a certain temperature (say 1.5MK, which would correspond to a Fe XII 195.1Å line) could be constructed and compared with TRACE or EIT observations. This could then be used as a direct test of the theoretical model through comparison with the observations, and thus the model could be refined. Eventually, the model may have some application in **coronal seismology** where by matching the synthetic observations to real observations, we can gain values for certain parameters in the corona.

Appendix A: Derivation of equation (3.4)

Recall the quantities we are working with in Section 3.3.2:

$$\mathcal{F} = \frac{1}{2} [(x^2 + z^2) (p^2 + q^2) - \omega^2] = 0 \quad (1)$$

$$\frac{d\phi}{ds} = \omega^2 \quad (2)$$

$$\frac{dp}{ds} = (p^2 + q^2) x \quad (3)$$

$$\frac{dq}{ds} = (p^2 + q^2) z \quad (4)$$

$$\frac{dx}{ds} = -(x^2 + z^2) p \quad (5)$$

$$\frac{dz}{ds} = -(x^2 + z^2) q \quad (6)$$

In what follows, $A, B, C, D, E, x_0, z_0, p_0, q_0$ and ϕ_0 are constants. We see that there are two important conserved quantities of the system, namely $\frac{d}{ds} (xp + zq) = 0 \implies xp + zq = A$ and $\frac{d}{ds} (zp - xq) = 0 \implies zp - xq = B$. Rearranging gives

$$p = \frac{Ax + Bz}{x^2 + z^2}, \quad q = \frac{Az - Bx}{x^2 + z^2} \quad (7)$$

Taking $[2p(3) + 2q(4)]$ gives:

$$\frac{d}{ds} (p^2 + q^2) = 2(p^2 + q^2) (px + qz) = 2A(p^2 + q^2) \implies (p^2 + q^2) = De^{2As}$$

Taking $[2x(5) + 2z(6)]$ gives:

$$\frac{d}{ds} (x^2 + z^2) = -2(x^2 + z^2) (px + qz) = -2A(x^2 + z^2) \implies (x^2 + z^2) = Ce^{-2As}$$

From the equation (1) we see that $C \cdot D = \omega^2$. Recall that our initial conditions at $s = 0$ are:

$$\phi = \phi_0 = 0, \quad x = x_0, \quad z = z_0, \quad p = p_0 = 0, \quad q = q_0 = \frac{\omega}{\sqrt{x_0^2 + z_0^2}},$$

where the form of q_0 comes from $\mathcal{F}_{s=0}$. By setting $s = 0$ and using the initial conditions above, we see that

$$A = z_0 q_0 = \frac{z_0 \omega}{\sqrt{x_0^2 + z_0^2}} \quad , \quad B = -\frac{x_0 \omega}{\sqrt{x_0^2 + z_0^2}} \quad , \quad C = x_0^2 + z_0^2 \quad , \quad D = \frac{\omega^2}{x_0^2 + z_0^2}$$

Substituting these into equation (7) gives:

$$p = \frac{z_0 \omega}{\sqrt{x_0^2 + z_0^2}} \left(\frac{x - \frac{x_0 z}{z_0}}{x^2 + z^2} \right) \quad , \quad q = \frac{z_0 \omega}{\sqrt{x_0^2 + z_0^2}} \left(\frac{z + \frac{x_0 x}{z_0}}{x^2 + z^2} \right) .$$

From (5) and (6), we see $\frac{dx}{ds} = -(x^2 + z^2)p$ and $\frac{dz}{ds} = -(x^2 + z^2)q$, so substituting in the forms given above yields:

$$\frac{dx}{ds} = -A \left(x - \frac{x_0}{z_0} z \right) \tag{8}$$

$$\frac{dz}{ds} = -A \left(z + \frac{x_0}{z_0} x \right) \tag{9}$$

Taking $\frac{d}{ds}$ (8) and $\frac{d}{ds}$ (9) gives (after some algebra):

$$\frac{d^2 x}{ds^2} + 2A \frac{dx}{ds} + A^2 \left[1 + \left(\frac{x_0}{z_0} \right)^2 \right] x = 0 \quad , \quad \frac{d^2 z}{ds^2} + 2A \frac{dz}{ds} + A^2 \left[1 + \left(\frac{x_0}{z_0} \right)^2 \right] z = 0$$

Making the substitution $x = e^{\lambda s}$ leads to the auxiliary equation:

$$\lambda^2 + 2A\lambda + A^2 \left[1 + \left(\frac{x_0}{z_0} \right)^2 \right] = 0 \quad \Rightarrow \quad \lambda = -A \pm i \frac{Ax_0}{z_0}$$

So $x = \left[\alpha \cos \left(\frac{Ax_0}{z_0} s \right) + \beta \sin \left(\frac{Ax_0}{z_0} s \right) \right] \cdot e^{-As}$, but at $s = 0$, $x = x_0$ and so $\alpha = x_0$. Similarly, letting $z = e^{\mu s}$ leads to:

$$\mu^2 + 2A\mu + A^2 \left[1 + \left(\frac{x_0}{z_0} \right)^2 \right] = 0 \quad \Rightarrow \quad \mu = -A \pm i \frac{Ax_0}{z_0}$$

So $z = \left[\gamma \cos \left(\frac{Ax_0}{z_0} s \right) + \delta \sin \left(\frac{Ax_0}{z_0} s \right) \right] \cdot e^{-As}$ as above, but at $s = 0$, $z = z_0 = 2$ and so $\gamma = z_0$. We can restrict the remaining constants β and δ using equations (8) and (9). Comparing like terms reveals $\beta = z_0$ and $\delta = -x_0$, which is consistent with $(x^2 + z^2) = (x_0^2 + 36) e^{-2As}$. Hence our final forms are:

$$x = \left[x_0 \cos \left(\frac{Ax_0}{z_0} s \right) + z_0 \sin \left(\frac{Ax_0}{z_0} s \right) \right] \cdot e^{-As}$$

$$z = \left[z_0 \cos \left(\frac{Ax_0}{z_0} s \right) - x_0 \sin \left(\frac{Ax_0}{z_0} s \right) \right] \cdot e^{-As}$$

Appendix B : Contents of CD-ROM

This Thesis contains a CD-ROM (located on the rear inside cover). The CD-ROM contains movies of some of the figures shown in the Thesis.

By entering the folder relevant to the chapter you are interested in, the reader can see the movies labelled as they are in the Thesis, e.g. the movie corresponding to Figure 3.2 in chapter 3 of this Thesis can be found on the CD-ROM in the **chapter3** folder as **Figure3_2.mpeg**. All the movies are in **mpeg** format and will thus work in most movie packages.

Running movies in Linux

To play the movie **Figure3_2.mpeg** in a Linux terminal, type:

- **mplayer Figure3_2.mpeg** (to play movie once), or
- **mplayer -loop 0 Figure3_2.mpeg** (to play movie on a loop)

Once the movie is playing, three useful commands are:

- The commands [and] decrease or increase the current playback speed by 10%.
- Pressing the down arrow (↓) restarts the movie.
- Pressing the space bar pauses the movie at any time.

Other **mplayer** commands can be used to change the properties of watching the movie. A full list of these can be obtained by typing **man mplayer** in a terminal window.

Contents of CD-ROM

The full content of the CD-ROM is as follows (bold face denotes a folder on the CD-ROM):

- **Thesis_Movies**
 - **chapter3**
 - * Figure3_2.mpeg, Figure3_4.mpeg, Figure3_7.mpeg,
Figure3_10.mpeg, Figure3_12.mpeg
 - **chapter4**
 - * Figure4_1.mpeg, Figure4_2.mpeg, Figure4_5.mpeg, Figure4_7.mpeg
 - **chapter5**
 - * **Fast_waves**
 - Figure5_2.mpeg, Figure5_3.mpeg, Figure5_6.mpeg, Figure5_7.mpeg
 - * **Alfven_waves**
 - Figure5_10.mpeg, Figure5_14.mpeg, Figure5_17.mpeg, Figure5_20.mpeg
 - **chapter6**
 - * Figure6_5.mpeg, Figure6_7.mpeg, Figure6_10.mpeg,
Figure6_14.mpeg, Figure6_16.mpeg
 - **chapter7**
 - * **Polar**
 - Figure7_2.mpeg, Figure7_6.mpeg
 - * **Cartesian**
 - Figure7_9.mpeg, Figure7_13.mpeg, Figure7_16.mpeg, Figure7_18.mpeg,
Figure7_20.mpeg, Figure7_21.mpeg, Figure7_22.mpeg
 - **chapter8**
 - * **Case1**
 - Figure8_3.mpeg, Figure8_4.mpeg
 - * **Case2**
 - Figure8_5.mpeg, Figure8_6.mpeg, Figure8_7.mpeg
 - * **Case3**
 - Figure8_8.mpeg, Figure8_9.mpeg, Figure8_10.mpeg
 - * **Case4**
 - Figure8_12.mpeg, Figure8_13.mpeg, Figure8_14.mpeg
- How_to_use_this_CD.ps (this postscript simply repeats what is stated in this Appendix).
- James_McLaughlin_Thesis.txt (this text file again simply repeats what is stated here).

Bibliography

- Alfven, H. (1942). Existence of electromagnetic-hydrodynamic waves. *Nature*, 150:405+.
- Aschwanden, M. J. (2004). *Physics of the Solar Corona: An Introduction*. Springer.
- Bender, C. M. and Orszag, S. A. (1978). *Advanced Mathematical Methods for Scientists and Engineers*. McGraw-Hill Book Company.
- Berghmans, D. and Clette, F. (1999). Active region EUV transient brightenings - First Results by EIT of SOHO JOP80. *Solar Phys.*, 186:207–229.
- Beveridge, C., Priest, E. R., and Brown, D. S. (2002). Magnetic topologies due to two bipolar regions. *Solar Phys.*, 209:333–347.
- Bogdan, T. J., Carlsson, M., Hansteen, V. H., McMurry, A., Rosenthal, C. S., Johnson, M., Petty-Powell, S., Zita, E. J., Stein, R. F., McIntosh, S. W., and Nordlund, Å. (2003). Waves in the Magnetized Solar Atmosphere. II. Waves from Localized Sources in Magnetic Flux Concentrations. *ApJ*, 599:626–660.
- Boyd, T. J. M. and Sanderson, J. J. (2003). *The Physics of Plasmas*. Cambridge University Press.
- Brown, D. S. and Priest, E. R. (1998). The Topology of Coronal Magnetic Fields in Active Regions. In *ASP Conf. Ser. 155: Three-Dimensional Structure of Solar Active Regions*, pages 90+.
- Brown, D. S. and Priest, E. R. (1999). The Topological Behaviour of Stable Magnetic Separators. *Solar Phys.*, 190:25–33.
- Brown, D. S. and Priest, E. R. (2001). The topological behaviour of 3D null points in the Sun's corona. *A & A*, 367:339–346.
- Bulanov, S. V. and Syrovatskii, S. I. (1980). Mhd oscillations and waves near a magnetic null line. *Soviet J. of Plasma Phys.*, 6:661–667.
- Cally, P. S. (2001). Note on an Exact Solution for Magnetoatmospheric Waves. *ApJ*, 548:473–481.
- Cally, P. S. and Bogdan, T. J. (1997). Simulation of f- and p-Mode Interactions with a Stratified Magnetic Field Concentration. *ApJL*, 486:L67+.
- Carlsson, M. and Stein, R. S. (1999). Wave Modes in a Chromospheric Cavity. In *ASP Conf. Ser. 184*, pages 206–210.
- Carrier, G. F. and Pearson, C. E. (1988). *Partial Differential Equations*. Academic Press, inc.

- Courant, R., Friedrichs, K. O., and Lewy, H. (1928). Über die partiellen differenzgleichungen der mathematischen physik. *Math. Ann.*, 100:32–74.
- Craig, I. J. and Watson, P. G. (1992). Fast dynamic reconnection at X-type neutral points. *ApJ*, 393:385–395.
- Craig, I. J. D. and Fruit, G. (2005). Wave energy dissipation by phase mixing in magnetic coronal plasmas. *A & A*, 440:357–366.
- Craig, I. J. D. and McClymont, A. N. (1991). Dynamic magnetic reconnection at an X-type neutral point. *ApJ*, 371:L41–L44.
- Craig, I. J. D. and McClymont, A. N. (1993). Linear theory of fast reconnection at an X-type neutral point. *ApJ*, 405:207–215.
- De Moortel, I., Hood, A. W., Gerrard, C. L., and Brooks, S. J. (2004). The damping of slow MHD waves in solar coronal magnetic fields. III. The effect of mode coupling. *A & A*, 425:741–752.
- De Moortel, I., Ireland, J., and Walsh, R. W. (2000). Observation of oscillations in coronal loops. *A & A*, 355:L23–L26.
- Demoulin, P., Mandrini, C. H., Rovira, M. G., Henoux, J. C., and Machado, M. E. (1994). Interpretation of multiwavelength observations of November 5, 1980 solar flares by the magnetic topology of AR 2766. *Solar Phys.*, 150:221–243.
- Díaz, A. J. (2004). *Fast MHD Waves in Line-tied Solar Coronal Flux Tubes*. PhD thesis, Universitat de les Illes Balears.
- Edwin, P. M. and Roberts, B. (1982). Wave propagation in a magnetically structured atmosphere. III - The slab in a magnetic environment. *Solar Phys.*, 76:239–259.
- Edwin, P. M. and Roberts, B. (1983). Wave propagation in a magnetic cylinder. *Solar Phys.*, 88:179–191.
- Evans, G., Blackledge, J., and Yardley, P. (2001). *Analytical Methods for Partial Differential Equations*. Springer.
- Ferraro, C. A. and Plumpton, C. (1958). Hydromagnetic Waves in a Horizontally Stratified Atmosphere. *ApJ*, 127:459+.
- Fruit, G. and Craig, I. J. D. (2005). Visco-resistive Shear Wave Dissipation in Magnetic X-points. *A & A*, in press.
- Galsgaard, K. and Nordlund, Å. (1997). Heating and activity of the solar corona. 2. Kink instability in a flux tube. *JGR*, 102(11):219–230.
- Galsgaard, K., Priest, E. R., and Titov, V. S. (2003). Numerical experiments on wave propagation towards a 3D null point due to rotational motions. *Journal of Geophysical Research (Space Physics)*, 108(1):10+.
- Galsgaard, K., Reddy, R. V., and Rickard, G. J. (1997a). Energy Release Sites in Magnetic Fields Containing Single Or Multiple Nulls. *Solar Phys.*, 176:299–325.
- Galsgaard, K., Rickard, G. J., Reddy, R. V., and Nordlund, Å. (1997b). Double null points and

- magnetic reconnection. *Advances in Space Research*, 19:1785–1788.
- Galsgaard, K., Rickard, G. J., Reddy, R. V., and Nordlund, A. (1997c). Dynamical Properties of Single and Double 3D Null Points. In *ASP Conf. Ser. 111*, pages 82+.
- Gerrard, C. L. (2001). *Three Dimensional Numerical Simulations of Non-linear MHD Instabilities in the Solar Corona*. PhD thesis, University of St Andrews.
- Goossens, M., Andries, J., and Aschwanden, M. J. (2002). Coronal loop oscillations. An interpretation in terms of resonant absorption of quasi-mode kink oscillations. *ApJ*, 394:L39–L42.
- Harrison, R. A., Hood, A. W., and Pike, C. D. (2002). Off-limb EUV line profiles and the search for wave activity in the low corona. *A & A*, 392:319–327.
- Hassam, A. B. (1992). Reconnection of stressed magnetic fields. *ApJ*, 399:159–163.
- Heyvaerts, J. and Priest, E. R. (1983). Coronal heating by phase-mixed shear Alfvén waves. *A & A*, 117:220–234.
- Hood, A. W. (2003). Asymptotic analysis and perturbation theory. University of St Andrews: MT4511 lectures.
- Lamb, H. (1909). *Proc. London Math. Soc.*, 7:122.
- Lamb, H. (1932). *Hydrodynamics*. Cambridge University Press.
- Lang, K. R. (2001). *The Cambridge Encyclopedia of the Sun*. Cambridge University Press.
- Longcope, D. W. and Cowley, S. C. (1996). Current sheet formation along three-dimensional magnetic separators. *Phys. Plasmas*, 3:2885–2897.
- McClymont, A. N. and Craig, I. J. D. (1996). Dynamical Finite-Amplitude Magnetic Reconnection at an X-Type Neutral Point. *ApJ*, 466:487+.
- McLaughlin, J. A. and Hood, A. W. (2004). MHD wave propagation in the neighbourhood of a two-dimensional null point. *A & A*, 420:1129–1140.
- McLaughlin, J. A. and Hood, A. W. (2005). MHD wave propagation in the neighbourhood of two null points. *A & A*, 435:313–325.
- Murray, D. A. (1927). *Differential Equations*. Longmans, Green and Co.
- Nakariakov, V. M. and Verwichte, E. (2005). Coronal waves and oscillations. *Living Rev. Solar Phys. (Online Article)*.
- Nakariakov, V. M. and Ofman, L. (2001). Determination of the coronal magnetic field by coronal loop oscillations. *A & A*, 372:L53–L56.
- Nakariakov, V. M., Ofman, L., Deluca, E. E., Roberts, B., and Davila, J. M. (1999). TRACE observation of damped coronal loop oscillations: Implications for coronal heating. *Science*, 285:862–864.
- Nakariakov, V. M. and Roberts, B. (1995). On Fast Magnetosonic Coronal Pulsations. *Solar Phys.*, 159:399–402.
- Nakariakov, V. M., Roberts, B., and Murawski, K. (1997). Alfvén Wave Phase Mixing as a Source of Fast Magnetosonic Waves. *Solar Phys.*, 175:93–105.

- Parker, E. N. (1991). The phase mixing of Alfvén waves, coordinated modes, and coronal heating. *ApJ*, 376:355–363.
- Paterson, A. R. (1983). *Fluid Dynamics*. Cambridge University Press.
- Piaggio, H. T. H. (1937). *Differential Equations and their applications*. G. Bell and sons, Ltd.
- Priest, E. and Forbes, T. (2000). *Magnetic Reconnection*. Cambridge University Press.
- Priest, E. R. (1982). *Solar magnetohydrodynamics*. D. Reidel Publishing. Company.
- Priest, E. R., Heyvaerts, J. F., and Title, A. M. (2002). A Flux-Tube Tectonics Model for Solar Coronal Heating Driven by the Magnetic Carpet. *ApJ*, 576:533–551.
- Priest, E. R. and Hood, A. W. (1991). Book-Review - Advances in Solar System Magnetohydrodynamics. *Journal of the British Astronomical Association*, 101:300+.
- Priest, E. R., Longcope, D. W., and Heyvaerts, J. (2005). Coronal Heating at Separators and Separatrices. *ApJ*, 624:1057–1071.
- Priest, E. R. and Titov, V. S. (1996). Magnetic reconnection at three-dimensional null points. *Phil. Trans. R. Soc. Lond. A*, 354:2951–2992.
- Rae, I. C. and Roberts, B. (1982). Pulse propagation in a magnetic flux tube. *ApJ*, 256:761–767.
- Rae, I. C. and Roberts, B. (1983). MHD wave motion in magnetically structured atmospheres. *A & A*, 119:28–34.
- Rickard, G. J. and Titov, V. S. (1996). Current Accumulation at a Three-dimensional Magnetic Null. *ApJ*, 472:840+.
- Roberts, B. (1985). *Solar System Magnetic Fields (editor: E. R. Priest)*, chapter 3. Reidel.
- Roberts, B. (1991). *Advances in Solar System Magnetohydrodynamics (eds. Priest & Hood)*, pages 105+. Cambridge University Press.
- Roberts, B. (2004). Mhd waves in the solar atmosphere. In *SOHO 13: Waves, Oscillations and Small Scale Transient Events in the Solar Atmosphere*.
- Roberts, B., Edwin, P. M., and Benz, A. O. (1983). Fast pulsations in the solar corona. *Nature*, 305:688–690.
- Roberts, B., Edwin, P. M., and Benz, A. O. (1984). On coronal oscillations. *ApJ*, 279:857–865.
- Roberts, B. and Nakariakov, V. M. (2003). *Turbulence, Waves and Instabilities in the Solar Plasma (eds. Erdelyi, Petrovay, Roberts and Aschwanden)*, pages 167–191. Kluwer.
- Rosenthal, C. S., Bogdan, T. J., Carlsson, M., Dorch, S. B. F., Hansteen, V., McIntosh, S. W., McMurry, A., Nordlund, Å., and Stein, R. F. (2002). Waves in the Magnetized Solar Atmosphere. I. Basic Processes and Internetwork Oscillations. *ApJ*, 564:508–524.
- Ruzmaikin, A. and Berger, M. A. (1998). On a source of Alfvén waves heating the solar corona. *A & A*, 337:L9–L12.
- Sears, F. W. and Salinger, G. L. (1986). *Thermodynamics, Kinetic Theory and Statistical Thermodynamics*. Addison-Wesley Publishing Company.

- Smith, M. G. (1967). *Theory of Partial Differential Equations*. D. Van Nostrand Company Ltd.
- Sneddon, I. N. (1957). *Elements of Partial Differential Equations*. McGraw-Hill Book Company.
- Taylor, A. B. (1986). *Mathematical Models in Applied Mathematics*. Clarendon Press.
- Taylor, R. J. (1970). *The Stars: their structure and evolution*. Cambridge University Press.
- Vekstein, G. and Bian, N. (2005). Forced Magnetic Reconnection at a Neutral X-point. *ApJ*, 632:L151–L154.
- Zhugzhda, I. D. and Dzhalilov, N. S. (1982). Transformation of magnetogravitational waves in the solar atmosphere. *A & A*, 112:16–23.